UNIVERSITY OF HULL


# The Creation of 3D Thyroid Models to Investigate the Effects of Sorafenib on Thyroid Tumour Tissue

being a Thesis submitted for the Degree of Masters by Research in Biomedical Sciences at the University of Hull

by

Przemyslaw Marek Golebiewski

BSc (Hons) Biomedical Science

August 2024

## Acknowledgements

Firstly, I would like to express my deepest gratitude to my supervisors for their patience and guidance throughout this journey, especially as they endured my relentless stream of thesis sections.

Dr. Victoria Green, I am profoundly thankful for the time and effort you invested in helping me succeed. Your genuine care and commitment have made a tremendous difference in my academic journey. You were always approachable and never hesitant to offer guidance or assistance, even in challenging times.

Prof. John Greenman, your insightful feedback and mentorship throughout both my undergraduate and master's studies have profoundly shaped my academic growth. Your ability to keep spirits high and foster enthusiasm in the lab has been truly inspiring.

I owe a debt of gratitude to Por and Stephen for their extraordinary hospitality. Por, your constant check-ins and unwavering belief in me were crucial in keeping me focused and motivated.

I am also incredibly grateful to all my lab colleagues for making my time in the team so enjoyable and fulfilling. Thank you for your encouragement, collaboration, and for creating such a positive and productive environment.

I am immensely grateful to Dr. Tom, Mr. England, and the entire surgical/clinical team at Castle Hill Hospital. Your generosity in allowing me to glimpse the clinical world has reinforced my passion for medicine and provided invaluable real-world context to my research.

To my family and friends, thank you for enduring my endless "I'm almost finished" speeches—your patience has been truly heroic, and your limitless support has kept me going.

Finally, I extend my sincere thanks to Help for Health for their generous sponsorship, without which this work would not have been possible.

# Abstract

Thyroid cancer (TC) is the most common endocrine malignancy globally. While surgery and radioactive iodine (RAI) therapy generally yield favourable outcomes, prognosis worsens in RAI-refractory or resistant cases, highlighting the need for alternative therapies such as tyrosine kinase inhibitors (TKI). High attrition rates in anti-cancer drug discovery often result from inadequate representation of the tumour microenvironment (TME) in traditional 2D culture models. Spheroids and organoids (3D models), which better replicate *in vivo* tumour conditions, have demonstrated superior predictive capabilities by exhibiting dose-dependent drug responses and $IC_{50}$ values comparable to 2D studies, despite greater drug diffusion distances.

The current study established, optimised and demonstrated the effectiveness of 3D cultures from two TC cell lines, papillary (K1) and anaplastic (8305c), as reliable drug screening platforms. The aim was to evaluate the efficacy of sorafenib, a commonly-used TKI, in TC spheroids and organoids, under both static and dynamic conditions. Consistently well-defined spheroids were created, displaying reproducible sizes, shape and viability. Spheroids were subjected to sorafenib treatment for a duration of 48 h, with the drug medium replenished at the 24 h mark to simulate the pharmacokinetic profile of clinical patient dosing regimens. Post-treatment, spheroids were evaluated using viability assays, microscopy analysis and diameter measurements. Both papillary and anaplastic spheroids, with and without necrotic cores, were successfully developed. The addition of the 3D matrix, Matrigel® to the spheroids, resulted in a doubling in overall size and greater viability compared to those without the additive. The 8305c spheroids displayed greater sensitivity to sorafenib compared to K1 spheroids.

Preliminary trials involving spheroids maintained on a microfluidic chip, with a constant flow of nutrients and removal of waste, validated their potential by demonstrating dose-dependent drug responses resembling those observed in static 3D models within this study. Furthermore, the spheroids within the microfluidic devices displayed heightened sensitivity to sorafenib, aligning with findings in the literature that dynamic culture systems often exhibit greater drug sensitivity compared to static models.

Patient-derived thyroid tissues, both malignant (n = 7) and benign (n = 4), were dissociated into primary cells and plated in either Matrigel® or VitroGel® matrices for generation of organoids or primary spheroids. Of the 11 primary cultures, 6 formed spheroids or spheroid-like structures. Notably, co-cultures with K1 cells resulted in more defined and stable spheroidal formations, suggesting a supportive role of immortalised cell lines in enhancing primary spheroid development. However, the success of organoid cultivation was limited, with issues such as inadequate aggregation and variability across different matrices.

This study highlights the potential use of spheroids for high throughput testing of both mono and combination therapies. It is clear that the consistent generation of organoids and spheroids from patient-derived tissue will require additional work, however the promise that these cultures offer, being more closely representative of the *in vivo* situation, for personalised medicine makes this work a priority.

## Thesis associated poster presentations

Beattie H., **Golebiewski** P., Green V., Greenman J, England J., The creation of 3D thyroid models to investigate the effect of Tyrosine Kinase Inhibitors on thyroid tumour tissue (**Allam lecture**; *research celebration event, May 2023, Kingston upon Hull, United Kingdom)*

Beattie H., **Golebiewski** P., Green V., Greenman J, England J., The creation of 3D thyroid models to investigate the effect of Tyrosine Kinase Inhibitors on thyroid tumour tissue (**HYMS**; *Hull York Medical School Postgraduate Research Conference, July 2023, Kingston upon Hull, United Kingdom)*

**Golebiewski** P., Beattie H., Green V., Greenman J, England J., (2023) The creation of 3D thyroid models to investigate the effect of Tyrosine Kinase Inhibitors on thyroid tumour tissue. (**BAETS**; *43rd Annual Scientific meeting of the British Association of Endocrine and Thyroid Surgeons, October 2023, Athens, Greece)*

# Contents

Acknowledgements ..... ii
Abstract ..... iii
Thesis associated poster presentations ..... iv
Contents ..... v
List of Figures ..... ix
List of Tables ..... xii
Abbreviations ..... xiii
**Chapter 1 Introduction ..... 1**
1.1 Thyroid Gland Anatomy ..... 1
1.1.1 The Sodium-Iodide Symporter ..... 1
1.1.2 Thyroid Hormone Synthesis and Release ..... 2
1.1.3 Thyroid Hormone Distribution ..... 3
1.2 Thyroid Cancer ..... 6
1.2.1 Epidemiology ..... 6
1.2.2 Differentiated Thyroid Cancer (DTC) ..... 7
1.2.3 Papillary Thyroid Cancer ..... 8
1.2.4 Follicular Thyroid Cancer ..... 10
1.2.5 Anaplastic Thyroid Cancer ..... 10
1.3 Thyroid Cancer Risk Factors ..... 12
1.3.1 Significance of Iodine ..... 12
1.3.2 Iodine Inadequacy ..... 13
1.3.3 Hypothyroidism ..... 14
1.3.4 Iodine Abundance ..... 15
1.3.5 Hyperthyroidism ..... 15
1.3.6 Radiation Exposure ..... 16
1.4 Thyroid cancer treatment ..... 18
1.4.1 Surgery and Radioiodine (RAI) Therapy ..... 20
1.4.2 RAI Therapy Resistance ..... 21
1.4.3 Dedifferentiated Thyroid Cancer ..... 21
1.4.4 NIS Dysfunction ..... 21
1.5 Tyrosine Kinase Inhibitors ..... 23
1.5.1 Sorafenib ..... 24
1.5.2 Sorafenib resistance ..... 26
1.6 Thyroid cancer models ..... 28
1.6.1 Spheroids and Organoids in Preclinical Drug Testing ..... 32
1.6.2 Microfluidics ..... 35

1.7 Thesis Aims ..... 36
**Chapter 2 Materials and Methods ..... 37**
2.1 Culture of thyroid cancer cell lines ..... 37
2.1.1 Culture of K1 cell lines ..... 38
2.1.2 Culture of 8305c cell lines ..... 38
2.1.3 Cell counting with Trypan blue exclusion ..... 38
2.2 Spheroid generation ..... 39
2.2.1 Generation of 1000 cells/well spheroids with and without Matrigel® ..... 40
2.2.2 Measuring spheroids ..... 40
2.3 Inducing Cell Death with $H_2O_2$, $NaN_3$, and TKI in Spheroids ..... 41
2.3.1 Inducing cell death using $H_2O_2$ ..... 42
2.3.2 Inducing cell death using $NaN_3$ ..... 43
2.3.3 MTS assay ..... 43
2.3.4 CellTiter-Glo® (CTG) 3D Cell Viability Assay ..... 44
2.3.5 Fluorescence microscopy ..... 45
2.3.6 OCT embedding and Cryostat sectioning ..... 46
2.3.7 Immunohistochemistry (IHC; Ki67) ..... 47
2.3.8 Spheroid treatment with sorafenib ..... 49
2.4 Acquisition of thyroid biopsies from patients ..... 53
2.4.1 Dissociation of thyroid tissue into single cells ..... 54
2.4.2 Generation of thyroid organoids ..... 55
2.4.3 Generation of primary thyroid spheroids ..... 58
2.5 Microfluidic device set-up ..... 61
2.6 Statistical analysis ..... 65
**Chapter 3 Optimisation of Spheroids for Experimental Use ..... 66**
3.1 Introduction ..... 66
3.2 Aims ..... 69
3.3 Methods ..... 69
3.4 Statistical analysis ..... 70
3.5 Optimisation of K1 spheroids ..... 72
3.5.1 Optimisation of K1 spheroids seeded at 1000 cells/well ..... 76
3.6 Optimisation of 8305c spheroids ..... 79
3.6.1 Optimisation of 8305c spheroids seeded at 1000 cells/well ..... 81
3.7 Discussion ..... 85
3.7.1 K1 Spheroids ..... 85
3.7.2 8305c Spheroids ..... 86
3.7.3 K1 and 8305c ..... 87

3.7.4 Use of Matrigel® ..... 88
**Chapter 4 Optimising Experimental Parameters for K1 and 8305c Spheroid Viability ..... 90**
4.1 Introduction ..... 90
4.1.1 $H_2O_2$ ..... 92
4.1.2 $NaN_3$ ..... 92
4.2 Aims ..... 93
4.3 Methods ..... 93
4.3.1 Optimisation of cell death assay/agent on K1/8305c spheroids ..... 93
4.3.2 Assessment of cell viability ..... 94
4.4 Statistical analysis ..... 95
4.5 Measuring the effects of $H_2O_2$ on K1 spheroids ..... 96
4.5.1 Trialling $NaN_3$ as a potential cell death agent alternative on K1 spheroids ..... 104
4.5.2 Effects of $NaN_3$ Treatment on K1 1000 cell/well Spheroids with and without Matrigel® 110
4.6 Investigating $NaN_3$ treatment on 8305c spheroids seeded at 10,000 cells/well ..... 116
4.7 Discussion ..... 119
4.7.1 $H_2O_2$ and Its Challenges in Spheroid Models ..... 119
4.7.2 $NaN_3$ as a Spheroid Cell Death Inducer ..... 120
4.7.3 Limitations of the spheroid models ..... 121
4.7.4 Chosen Experimental Parameters ..... 121
**Chapter 5 Investigating sorafenib-Induced Cytotoxicity in Thyroid Cancer Spheroids ..... 125**
5.1 Introduction ..... 125
5.2 Aims and Objectives ..... 128
5.3 Methods and Materials ..... 128
5.3.1 Spheroid generation ..... 128
5.3.2 Sorafenib treatment ..... 129
5.3.3 $IC_{50}$ calculation ..... 129
5.3.4 On-chip setup ..... 129
5.3.5 Cell viability analysis ..... 130
5.4 Statistical Analysis ..... 130
5.5 Assessing sorafenib effects on thyroid cell line spheroids ..... 131
5.5.1 Analysing sorafenib potency on K1 spheroids seeded at 20,000 cells/well ..... 131
5.5.2 Analysing sorafenib potency on K1 spheroids seeded at 1,000 cells/well ..... 140
5.5.3 Investigating sorafenib effects on 8305c 10K spheroid viability ..... 147
5.5.4 Investigating sorafenib effects on 8305c 1K spheroid viability ..... 154
5.5.5 Calculation of $IC_{50}$ values ..... 161
5.6 Spheroid On-chip investigations ..... 163

5.7 Discussion ..... 168
5.7.1 Effects of sorafenib on Thyroid Carcinoma Spheroids ..... 168
5.7.2 Comparison of $IC_{50}$ values ..... 171
5.7.3 On-chip investigations ..... 173
5.7.4 Limitations ..... 174
**Chapter 6 Generation of Thyroid Organoids from Patient-Derived Tissue ..... 177**
6.1 Introduction ..... 177
6.1.1 Applications and advantages of organoids ..... 178
6.1.2 Challenges surrounding organoid development ..... 179
6.1.3 Matrigel® and VitroGel® ..... 180
6.2 Aims ..... 180
6.3 Materials and Methods ..... 182
6.3.1 Sample Collection ..... 182
6.3.2 Organoid generation protocol ..... 182
6.3.3 Primary spheroid generation protocol ..... 183
6.3.4 Cell viability analysis ..... 184
6.4 Statistical Analysis ..... 184
6.5 Characterisation of patient-derived organoids and primary spheroid growth and morphology ..... 185
6.6 Using VitroGel® as an alternative to Matrigel® in generating thyroid organoids ..... 187
6.7 Discussion ..... 200
6.7.1 A Comparative Analysis of VitroGel® and Matrigel® for the Generation of Organoids 200
6.7.2 Thyroid tissue-derived primary spheroids ..... 203
6.7.3 Implications of thyroid organoid generation ..... 205
6.7.4 Future applications ..... 207
**Chapter 7 Discussion ..... 209**
7.1 Future work ..... 211
7.2 Conclusion ..... 214
**References ..... 215**
**Appendix 1 ..... I**

# List of Figures

Figure 1.1 Location and structure of the thyroid gland ..... 1
Figure 1.2 Diagram illustrating the process of thyroid hormone synthesis ..... 3
Figure 1.3 Thyroid-Pituitary feedback loop and hormone regulation ..... 5
Figure 1.4 US Thyroid cancer incidence rates by age at diagnosis between the years, 2017-2021 ..... 7
Figure 1.5 Simplified MAPK/ERK Signalling Pathway ..... 9
Figure 1.6 Main histological types of thyroid cancer ..... 12
Figure 1.7 Illustration depicting a healthy thyroid gland and the formation of a goitre ..... 16
Figure 1.8 Overview of the decision-making process for Anti-VEGF TKI prescription ..... 19
Figure 1.9 Summary of clinically used TKI and their targets ..... 23
Figure 1.10 Multi-Kinase Inhibition by sorafenib ..... 24
Figure 1.11 Comparison of Cancer Research Models ..... 31
Figure 1.12 Main mechanisms of tumour resistance to TKI ..... 34
Figure 2.1 Diagram of a haemocytometer grid ..... 39
Figure 2.2 Measuring spheroids using the software ImageJ ..... 41
Figure 2.3 Plate setup for cell viability investigations with $H_2O_2$ or $NaN_3$ ..... 42
Figure 2.4 Reduction reaction of MTS into Formazan product by viable cells ..... 44
Figure 2.5 Reaction of CellTiter-Glo® 3D lytic reagents. ..... 45
Figure 2.6 ULA Plate Setup for sorafenib Treatment ..... 50
Figure 2.7 Serial dilution of sorafenib for use in spheroid treatment (static/on-chip). ..... 51
Figure 2.8 24-Well Plate Setup for Organoid Generation with Matrigel® ..... 55
Figure 2.9 96-Well flat-bottom plate Setup for Organoid Generation with Vitrogel® ..... 57
Figure 2.10 Photographs and schematic diagram of microfluidic chip. ..... 62
Figure 2.11 Photographs of the microfluidic device set-up ..... 64
Figure 3.1 Diagram illustrating the zones within a tumour spheroid model ..... 68
Figure 3.2 Images of FDA/PI stained K1 10/15/20K spheroids ..... 73
Figure 3.3 Images of irregularly shaped K1 10/15K spheroids . ..... 73
Figure 3.4 Diameter measurements for K1 10/15/20 spheroids ..... 74
Figure 3.5 Images of K1 20K spheroids ..... 75
Figure 3.6 Diameter measurements for K1 20K spheroids ..... 76
Figure 3.7 Images of K1 1K spheroids ..... 77
Figure 3.8 Diameter measurements for K1 1K spheroids ..... 78

Figure 3.9 Images of 8305c 10/20/30K spheroids ..... 79
Figure 3.10 Diameter measurements for 8305c 10/20/30K spheroids ..... 81
Figure 3.11 Images of 8305c 1K spheroids ..... 82
Figure 3.12 Diameter measurements for 8305c 1K spheroids ..... 84
Figure 4.1 Schematic representation of a 96-well ULA plate set-up for the cell death assays ..... 95
Figure 4.2 MTS absorbance values for untreated and treated K1 20K spheroids with $H_2O_2$ ..... 97
Figure 4.3 Worked example for determining the live/dead cell percentages in a spheroid. ..... 98
Figure 4.4 Fluorescent images of FDA/PI stained K1 20K spheroids post $H_2O_2$ treatment ..... 99
Figure 4.5 MTS absorbance values for untreated and treated K1 20K spheroids ..... 101
Figure 4.6 Fluorescent images of FDA/PI stained K1 20K spheroids post $H_2O_2$ treatment ..... 102
Figure 4.7 K1 20K spheroids post 48 h $H_2O_2$ treatment stained with marker Ki67 for IHC. ..... 103
Figure 4.8 Z-stack of K1 Hoechst-stained spheroids un/treated with $NaN_3$ ..... 105
Figure 4.9 MTS absorbance values for untreated and treated K1 20K spheroids with $NaN_3$. ..... 106
Figure 4.10 Fluorescent images of FDA/PI stained K1 20K spheroids post $NaN_3$ treatment ..... 107
Figure 4.11 K1 20K spheroids $NaN_3$ treatment stained with marker Ki67 for IHC ..... 108
Figure 4.12 CTG assay results for $NaN_3$ untreated and treated K1 20K spheroids ..... 110
Figure 4.13 MTS absorbance values for untreated and treated K1 1K spheroids with $NaN_3$ ..... 111
Figure 4.14 Fluorescent images of FDA/PI stained K1 20K spheroids post $NaN_3$ treatment ..... 113
Figure 4.15 CTG luminescent values for untreated and treated K1 1K spheroids with $NaN_3$ ..... 115
Figure 4.16 CTG luminescent values for untreated and treated 8305c 10K spheroids with $NaN_3$. 117
Figure 4.17 Fluorescent images of FDA/PI stained 8305c 10K spheroids post $NaN_3$ treatment. ..... 118
Figure 5.1 CTG assay results for untreated and treated (sorafenib) K1 20K spheroids. ..... 132
Figure 5.2 CTG assay results for untreated and treated (sorafenib) K1 20K spheroids ..... 134
Figure 5.3 Diameter measurements for K1 20K spheroids post sorafenib treatment. ..... 135
Figure 5.4 Live/Dead percentage readings for K1 20K spheroids post sorafenib treatment ..... 137
Figure 5.5 Fluorescent images of FDA/PI stained K1 20K spheroids post sorafenib treatment ..... 139
Figure 5.6 CTG assay results for untreated and treated (sorafenib) K1 1K spheroids ..... 141
Figure 5.7 Diameter measurements for K1 1K spheroids post sorafenib treatment ..... 142
Figure 5.8 Live/Dead percentage readings for K1 1K spheroids post sorafenib treatment ..... 144
Figure 5.9 Fluorescent images of FDA/PI stained K1 1K spheroids post sorafenib treatment ..... 146
Figure 5.10 CTG assay results for untreated and treated (sorafenib) 8305c 10K spheroids ..... 148
Figure 5.11 Diameter measurements for 8305c 10K spheroids post sorafenib treatment ..... 150
Figure 5.12 Live/Dead percentage readings for 8305c 10K spheroids post sorafenib treatment .. 151

Figure 5.13 FL images of FDA/PI stained 8305c 10K spheroids post sorafenib treatment .....153
Figure 5.14 CTG assay results for untreated and treated (sorafenib) 8305c 1K spheroids.....155
Figure 5.15 Diameter measurements for 8305c 1K spheroids post sorafenib treatment .....156
Figure 5.16 Live/Dead percentage readings for 8305c 1K spheroids post sorafenib treatment. ...158
Figure 5.17 FL images of FDA/PI stained 8305c 1K spheroids post sorafenib treatment .....160
Figure 5.18 Calculated $IC_{50}$ values for K1 and 8305c spheroids .....162
Figure 5.19 CTG assay results for untreated and treated (sorafenib) K1 20K spheroids on-chip ...164
Figure 5.20 FL images of FDA/PI stained K1 20K spheroids post sorafenib treatment on-chip.....165
Figure 5.21 CTG assay results for un/treated (sorafenib) 8305c 10K spheroids on-chip.....166
Figure 5.22 FL images of FDA/PI stained K1 20K and 8305c 10K spheroids post sorafenib treatment on-chip .....167
Figure 6.1 Overview of the organoid generation process.. .....183
Figure 6.2 Images of primary thyroid tissue cultures emedded in Matrigel® .....186
Figure 6.3 Images of primary thyroid tissue cultures seeded in VitroGel® .....188
Figure 6.4 Images of primary thyroid tissue cultures seeded in VitroGel® following Cytospin .....189
Figure 6.5 Images of primary thyroid spheroid cultures .....190
Figure 6.6 Images of primary thyroid tissue cultures .....192
Figure 6.7 Primary spheroid MTS/CTG results after treatment with sorafenib .....193
Figure 6.8 Images of primary thyroid tissue cocultured with CFSE stained K1 cells .....195
Figure 6.9 Images of primary thyroid tissue cocultured with CytoPainter green stained K1 cells..196
Figure 6.10 Images of primary thyroid tissue cocultured with CytoPainter green stained K1 cells198
Figure 6.11 FL images of a K1 1K spheroid following labelling with CytoPainter and Hoechst.....199

# List of Tables

Table 1.1. Main mechanisms of sorafenib resistance.....27
Table 2.1 Sample types obtained from patients undergoing thyroidectomy. .....53
Table 3.1 Seeding densities from various publications exploring thyroid cancer spheroids .....67
Table 6.1 Recent studies investigating human derived thyroid tissue.....181
Table 6.2 Ongoing clinical trials involving organoids.....208

# Abbreviations

| | |
|---|---|
| **2D** | Two-Dimensional |
| **3D** | Three-Dimensional |
| **ADSC** | Adipose-Derived Stem Cells |
| **ATC** | Anaplastic Thyroid Cancer |
| **BRAF** | B-Raf Proto-Oncogene |
| **CFSE** | Carboxyfluorescein Succinimidyl Ester |
| **CSC** | Cancer Stem Cells |
| **CTG** | CellTiter-Glo® 3D |
| **DAPI** | 4',6-Diamidino-2-Phenylindole |
| **DDTC** | Dedifferentiated Thyroid Cancer |
| **DIT** | Diiodotyrosine |
| **DMEM** | Dulbecco's Modified Eagle Medium |
| **DMF** | Digital Microfluidics |
| **DMSO** | Dimethyl Sulfoxide |
| **DTC** | Differentiated Thyroid Cancer |
| **EC** | Endothelial Cells |
| **ECM** | Extracellular Matrix |
| **EMT** | Epithelial-Mesenchymal Transition |
| **FDA/PI** | Fluorescein diacetate/Propidium Iodide |
| **FITC** | Fluorescein Isothiocyanate |
| **FL** | Fluorescence |
| **FTC** | Follicular Thyroid Cancer |
| **GD** | Graves' Disease |
| **$H_2O_2$** | Hydrogen Peroxide |
| **HO** | Hydro-Organoid |
| **HT** | Hashimoto's Thyroiditis |
| **$IC_{50}$** | Half-Maximal Inhibitory Concentration |
| **ID** | Iodine Deficiency |
| **IHC** | Immunohistochemistry |
| **ITD** | Iodide Transport Defect |
| **MCT8** | Monocarboxylate Transporter 8 |
| **MIT** | Monoiodotyrosine |
| **MNG** | Multinodular Goiter |
| **MPTC** | Papillary Thyroid microcarcinoma |
| **MSC** | Mesenchymal Stem Cells |
| **MTS** | 3-(4,5-Dimethylthiazol-2-Yl)-2,5-Diphenyltetrazolium Bromide |
| **NaI** | Sodium Iodide |
| **$NaN_3$** | A chemical inhibitor used in research |
| **NIS** | Sodium Iodide Symporter |
| **OCT** | Optimal Cutting Temperature |
| **OR** | Odds Ratio |
| **PBS** | Phosphate-Buffered Saline |
| **PDTC** | Poorly Differentiated Thyroid Cancer |
| **PFS** | Progression-Free Survival |

| | |
|---|---|
| **PMMA** | Polymethyl Methacrylate |
| **PTC** | Papillary Thyroid Cancer |
| **RAI** | Radioactive Iodine |
| **RAI-R** | Radioactive Iodine Refractive/Resistant |
| **RBC** | Red Blood Cells |
| **ROS** | Reactive Oxygen Species |
| **RR** | Relative Risk |
| **T3** | Triiodothyronine |
| **T4** | Thyroxine |
| **TBS** | Tris-Buffered Saline |
| **TC** | Thyroid Cancer |
| **TERT** | Telomerase Reverse Transcriptase |
| **TG** | Thyroglobulin |
| **TH** | Thyroid Hormone |
| **TKI** | Tyrosine Kinase Inhibitor |
| **TME** | Tumour Microenvironment |
| **TPO** | Thyroid Peroxidase |
| **TRAB** | Thyroid Receptor Antibodies |
| **TSH** | Thyroid-Stimulating Hormone |
| **TT** | Total Thyroidectomy |
| **UIC** | Urinary Iodine Concentration |
| **ULA** | Ultra-Low Adherence |

# Chapter 1 Introduction

## 1.1 Thyroid Gland Anatomy

The thyroid, a butterfly-shaped organ is the largest endocrine gland within the human body, located in the anterior neck (Figure 1.1). Consisting of two lobes connected by an isthmus; it is largely composed of flattened epithelial cells called follicular cells, also referred to as thyrocytes, which are responsible for producing the essential thyroid hormones (TH): triiodothyronine (T3) and thyroxine (T4) (Kapral & Khot, 2022). Thyrocytes are polarised, with a basolateral side where iodide ions ($I^-$) are taken up into the cell via the $Na^+/I^-$ symporter (NIS) and an apical face, where TH is secreted (Nilsson and Fagman, 2017). The process of thyroid hormonogenesis within follicular cells can be separated into three primary steps: iodine uptake, oxidation and organification, combined with the subsequent secretion of TH (Benvenga *et al.,* 2018).

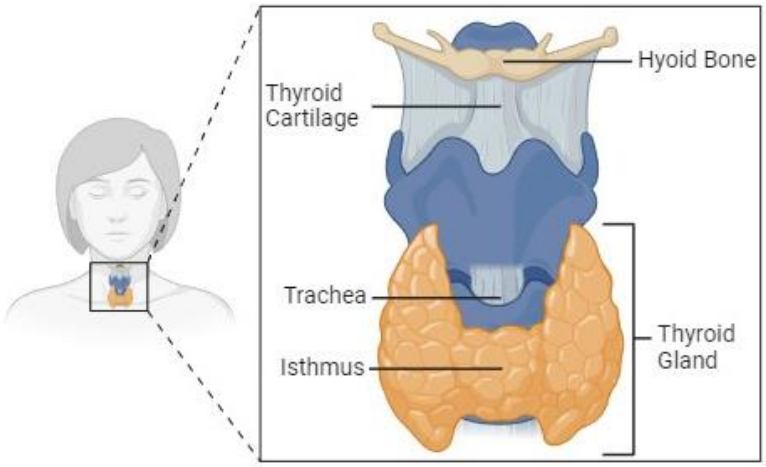


***Figure 1.1 Location and structure of the thyroid gland.*** *Created using Biorender.*

### 1.1.1 The Sodium-Iodide Symporter

A key component of the TH manufacturing process is the NIS, a plasma membrane glycoprotein mainly found in the thyroid gland, but which is also expressed, to a lesser extent, in tissue located in the stomach, small intestine, mammary and salivary glands (Ravera *et al.,*

2022). The primary role of the NIS is the active transport of $I^-$ from the bloodstream, into follicular cells for hormone synthesis. The NIS glycoprotein consists of 13 transmembrane domains, forming a channel through which $I^-$ can pass. A functional NIS operates via secondary active transport, coupling the movement of 2 $Na^+$, down a concentration gradient, along with 1 $I^-$, against its gradient into the cell. This process is mediated by a $Na^+/K^+$ ATPase pump also located on the basolateral side of the follicular cell, which works simultaneously with the NIS. The pump generates an electrochemical gradient through the transport of 3 $Na^+$ out of the cell while allowing 2 $K^+$ inside, maintaining a high extracellular and low intracellular $Na^+$ concentration (Riesco-Eizaguirre *et al.,* 2021).

### 1.1.2 Thyroid Hormone Synthesis and Release

The synthesis pathway begins with the uptake of $I^-$ via the NIS (Figure 1.2). Once in the cytosol $I^-$ is transported through the apical membrane of the follicular cell, facilitated by the carrier protein pendrin into the colloid (Babić Leko *et al.,* 2021). $I^-$ is subsequently oxidised by thyroid peroxidase (TPO) utilising hydrogen peroxide ($H_2O_2$), which is supplied by dual oxidase (DUOX2); both enzymes being located between the colloid and the apical membrane (Sorrenti *et al.,* 2021). In addition to this, TPO attaches the oxidised iodine to the tyrosyl residues of thyroglobulin (TG) to form monoiodotyrosine (MIT) and diiodotyrosine (DIT). TPO then catalyses the coupling of the two iodinated tyrosyl residues (MIT and DIT) to form T3 and T4 TH (Jonklaas, 2021). At the organification stage, the two hormones are stored within the colloid in an inactive form, which is covalently linked to TG. TH release is initiated by TG which is endocytosed into thyroid follicular cells and broken down by lysosomes, releasing T3 and T4 in the process (Koibuchi, 2018). The liberated hormones are transported out of the cell, across the membrane aided by the Monocarboxylate Transporter 8 (MCT8) which also facilitates their uptake into target cells (Groeneweg *et al.,* 2019).

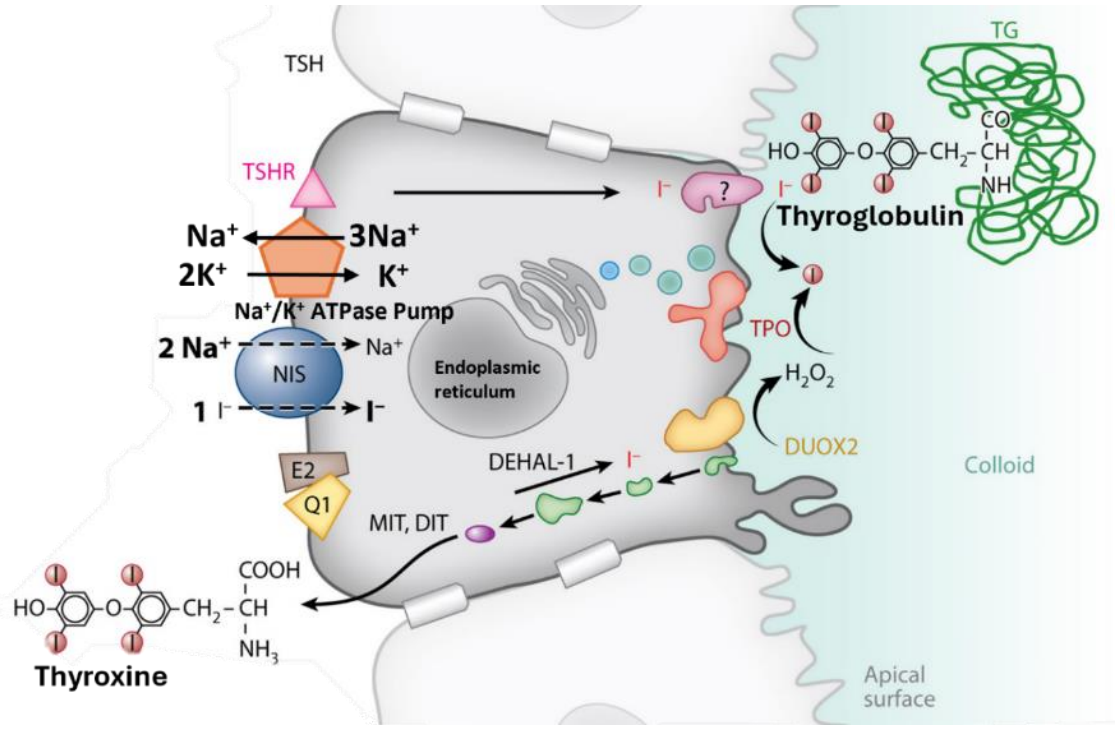


***Figure 1.2 Diagram illustrating the process of thyroid hormone synthesis including location of NIS within the cell.*** *The Sodium-Iodide Symporter (NIS) protein (blue circle), located on the basolateral side of the thyrocyte, transports sodium ions ($Na^+$) and iodide ions ($I^-$) into the cell with a 2:1 stoichiometry. This process is driven by the electrochemical gradient created by the $Na^+/K^+$ ATPase pump (orange pentagon). $I^-$ crosses the apical membrane via a carrier protein pendrin (pink structure labelled with a question mark) and is then oxidised and added to thyroglobulin (TG, green structure inside the colloid) by the enzyme thyroid peroxidase (TPO, red structure) with $H_20_2$ produced by dual oxidase (DUOX2, yellow structure). The maturation of DUOX2 is supported by its chaperone DUOXA2 (small blue circle near the endoplasmic reticulum). The iodinated thyroglobulin is then taken back into the cell, broken down in endocytic/lysosomal vesicles (green structures), and the thyroid hormones (TH) are released into the bloodstream. Any iodide attached to monoiodotyrosine (MIT) and diiodotyrosine (DIT) is recycled by a deiodination reaction. Adapted from Ravera et al., (2017).*

### 1.1.3 Thyroid Hormone Distribution

The release of thyroid hormones is controlled by a tightly regulated feedback loop; in low circulating T3/T4 conditions (Figure 1.3), the anterior pituitary gland is stimulated by the uptake of thyrotropin-releasing hormone (TRH) released by the hypothalamus, in turn secreting thyroid-stimulating hormone (TSH). TSH is supplied to thyrocytes by the fine

capillary network that surrounds each follicle (Suzuki *et al.,* 2011). TSH stimulates the thyroid gland to produce more TH. Within the hypothalamus and pituitary gland, the inactive T4 hormone is converted into the more biologically active form T3 by 5'-deiodinase type 2 (D2) enzyme during episodes of higher metabolic demands. The more potent T3 hormone has an effect on every nucleated cell in the body, regulating: metabolic rate, body temperature, maintaining heart and nervous system function as well as controlling growth and development (Armstrong *et al.,* 2023). Once TH reaches the maximal level in the bloodstream, it inhibits the release of TSH from the pituitary and TRH from the thyroid gland through a negative feedback loop. In a healthy thyroid with a functional NIS, this highly sensitive feedback system allows for the maintenance of a delicate equilibrium (Arrojo e Drigo & Bianco, 2011). Residual iodine is recycled through the action of iodotyrosine dehalogenase (DEHAL1). This recycling process helps maintain the iodine pool necessary for continued TH synthesis between meals, but also during events in which there is a fluctuation or lack in the intake of dietary iodine for extended periods (e.g. multiple days).

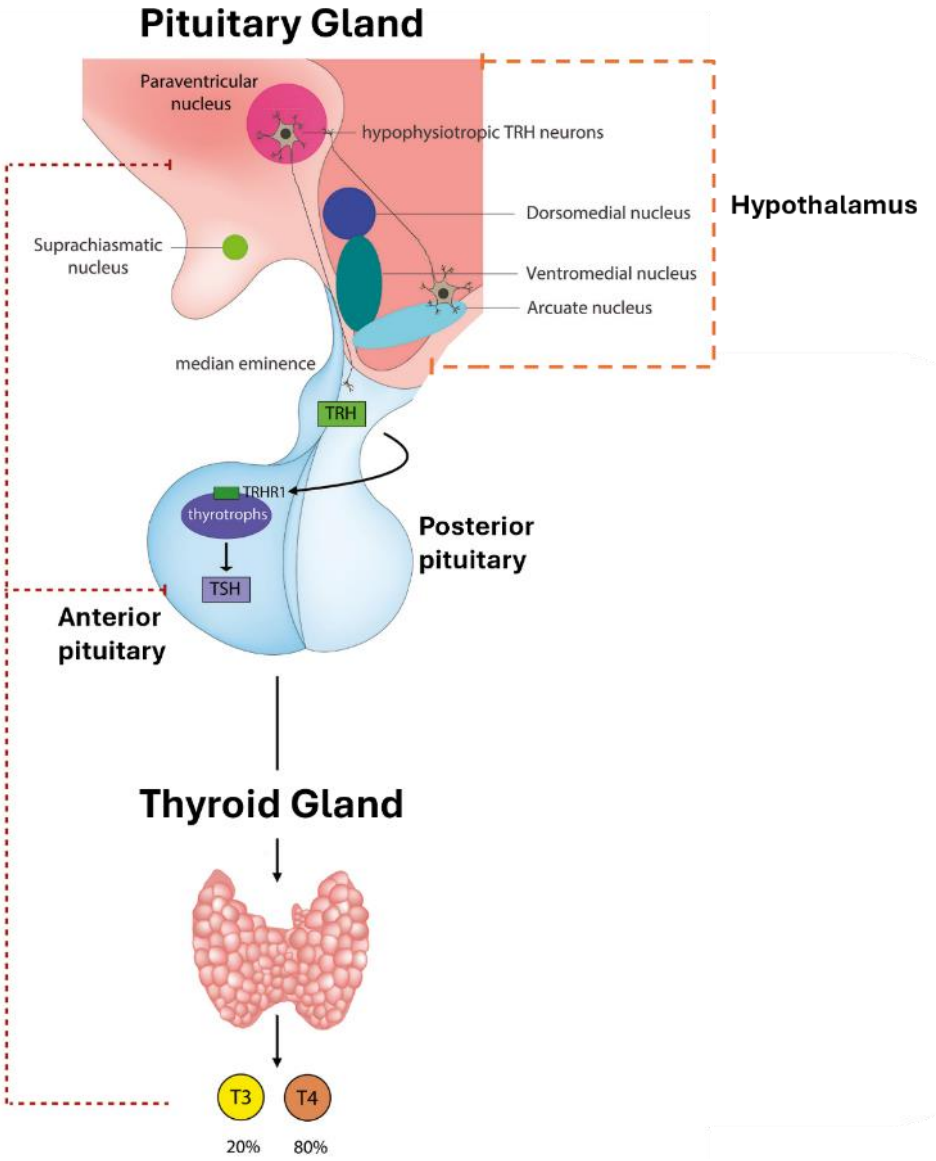


***Figure 1.3 Thyroid-Pituitary feedback loop and hormone regulation.*** *Thyrotropin-releasing hormone (TRH), synthesised by neurons in the paraventricular nucleus of the hypothalamus, is released into the median eminence and travels via the portal system to the anterior pituitary. Here, TRH binds to TRH receptors (TRHR1) on thyrotroph cells, inducing the release of thyroid-stimulating hormone (TSH). TSH then prompts thyrocytes to secrete thyroid hormones (TH), including thyroxine (T4) and triiodothyronine (T3). Elevated levels of T4 and T3 in the bloodstream exert negative feedback on both the hypothalamus and anterior pituitary, reducing the release of TRH and TSH, respectively. This feedback mechanism ensures the fine-tuning of thyroid hormone levels. Adapted from Feldt-Rasmussen et al., (2021).*

## 1.2 Thyroid Cancer

Thyroid cancer (TC) cases in the United Kingdom (UK) continue to rise annually, marking a notable surge in incidence rates, 65% in females and 68% in males between 2008-2018 with 4,040 new cases documented based on recent data (2017-2019, Cancer Research UK, 2024). Currently, thyroidectomy followed by radioiodine therapy (RAI) remains the gold standard treatment for TC (Naoum *et al.,* 2018). However, in rare cases a differentiated thyroid cancer (DTC) can transition into a dedifferentiated state, defined by loss of specialisation and heightened cell proliferation, representing 5–10% of all TC patients. This phenomenon often compromises the functionality of the NIS, a crucial component of successful RAI treatment. Reduced NIS activity due to DTC dedifferentiation (DDTC) correlates with a diminished response to therapy and heightened invasiveness (Liu *et al.,* 2019). The major challenges posed by RAI-refractory (RAI-R) cancers, along with rising cases every year, underscores the need for research into the processes of tumorigenesis, better diagnostic approaches, and more effective therapies (Shen *et al.,* 2024).

### 1.2.1 Epidemiology

TC is a rising problem worldwide that disproportionally affects women predominantly between the ages of 22-60 years. Since the 1990s, the UK has witnessed a significant increase in TC incidence rates, reporting an increase of approximately 175% (from 2.2 cases per 100,000 in 1993-1995 to 6.1 in 2016-2018, Cancer Research UK, 2024). The prevalence of TC cases has a projected upward trajectory, likely due, at least in part, to the advancements in diagnostic technologies, namely ultrasonic scans, and biopsies, enabling earlier detection and diagnosis (Zhai *et al.,* 2021). Approximately three-quarters of TC cases occur in women, a gender disparity believed to stem from innate differences in the effects of male and female sex hormones (Rahbari *et al.,* 2010). Oestrogen has been shown to be a potent growth factor in both malignant and benign thyroid tissue, displaying a correlation with TC incidence rates that surge after the onset of puberty and decline post menopause, a trend observed in females only (Derwahl & Nicula., 2014, Liu *et al.,* 2021 and Zhang *et al.,* 2023). This is visualised in Figure 1.4, which shows a rapid increase in TC incidence starting at ages in which puberty usually begins (age 10-19 years), the trend steadily continues to rise up until the

menopausal age range of 40-55 years, after which, TC incidence displays an observable decrease. In contrast, the incidence in men only gradually increases peaking in the 70s followed by a subsequent decline.

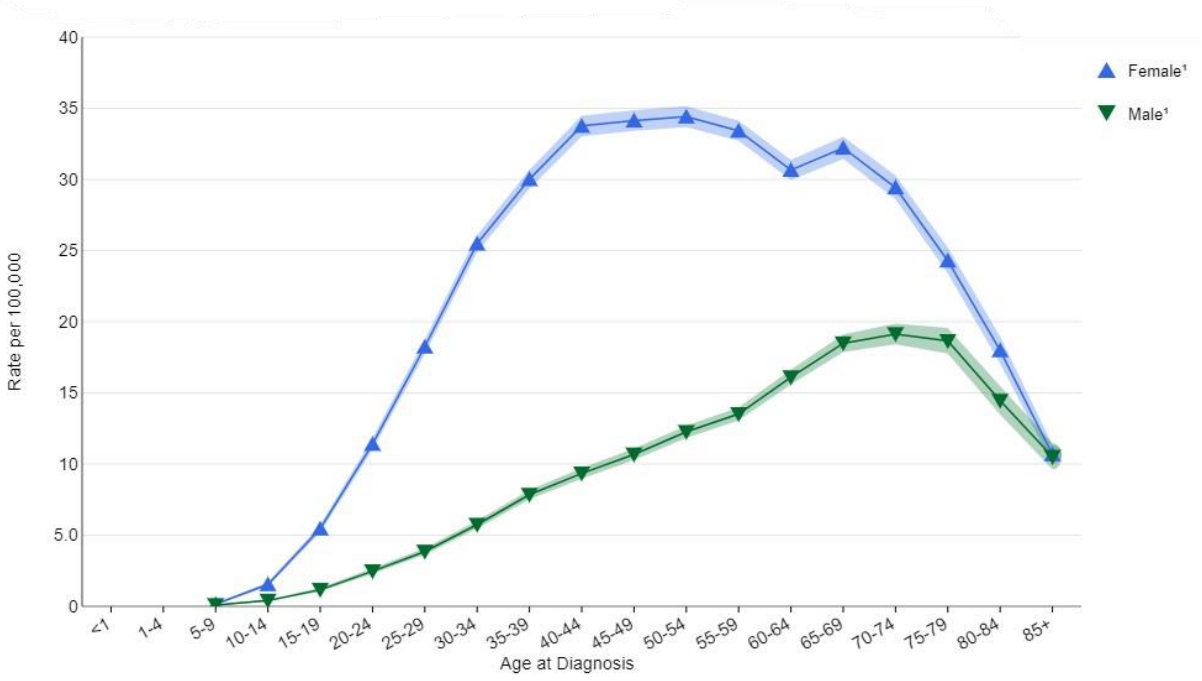


***Figure 1.4 US Thyroid cancer incidence rates by age at diagnosis between the years, 2017-2021.*** *Graph created using interactive SEER cancer statistics, (National Cancer Institute, 2024).*

### 1.2.2 Differentiated Thyroid Cancer (DTC)

Differentiation in tumours refers to how closely cancer cells resemble normal cells in structure and function; for instance, in DTC, which make up 90% of thyroid cancer cases, the cancer cells retain most of the characteristics of normal thyroid tissue, and tend to exhibit slow growth and an excellent prognosis (Schmidbauer *et al.,* 2017). The most frequent types being papillary (~60-85%) and follicular (10-15%) carcinomas which tend to respond well to conventional treatments such as surgery and RAI therapy, as they are capable of iodine uptake (Chou *et al.,* 2022). Carcinogenesis generally encompasses three main phases; Initiation, this stage typically involves genetic point mutations and rearrangements that activate signalling pathways, promoting cell growth and survival. Secondly, progression which

involves additional mutations and lastly, escape, where the tumour reaches immortality and a greater growth rate via further mutations (Williams, 2015).

### 1.2.3 Papillary Thyroid Cancer

PTC is the most prevalent type of DTC, originating from follicular cells of the thyroid gland (Coca-Pelaz *et al.,* 2020). The MAPK/ERK signalling pathway (Figure 1.5) is involved in cell proliferation, differentiation, development, and apoptosis and plays a major role in PTC tumorigenesis. Common additional genetic alterations include BRAF V600E, which is present in 66.54% of PTC cases (Niciporuka *et al.,* 2021), and RET/PTC rearrangements, which are present in 20-40% of PTC cases (Ciampi & Nikiforov, 2007). Radiation exposure heightens the chances of these genetic aberrations. The point mutation activates the BRAF protein through the substitution of valine with glutamic acid at position 600, driving the persistent stimulation of the MAPK/ERK pathway leading to uncontrolled cell proliferation and survival (Wei *et al.,* 2022). The fusion of the RET tyrosine kinase domain with the coiled-coil domain-containing protein 6 (CCDC6) gene is the most common type of RET/PTC rearrangement, accounting for approximately 90% of RET fusion-positive cases leading to further promotion of the MAPK/ERK pathway (Santoro *et al.,* 2020). Together, BRAF mutations and RET/PTC rearrangements drive the malignant transformation and proliferation of thyroid cells through persistent activation of the MAPK/ERK pathway.

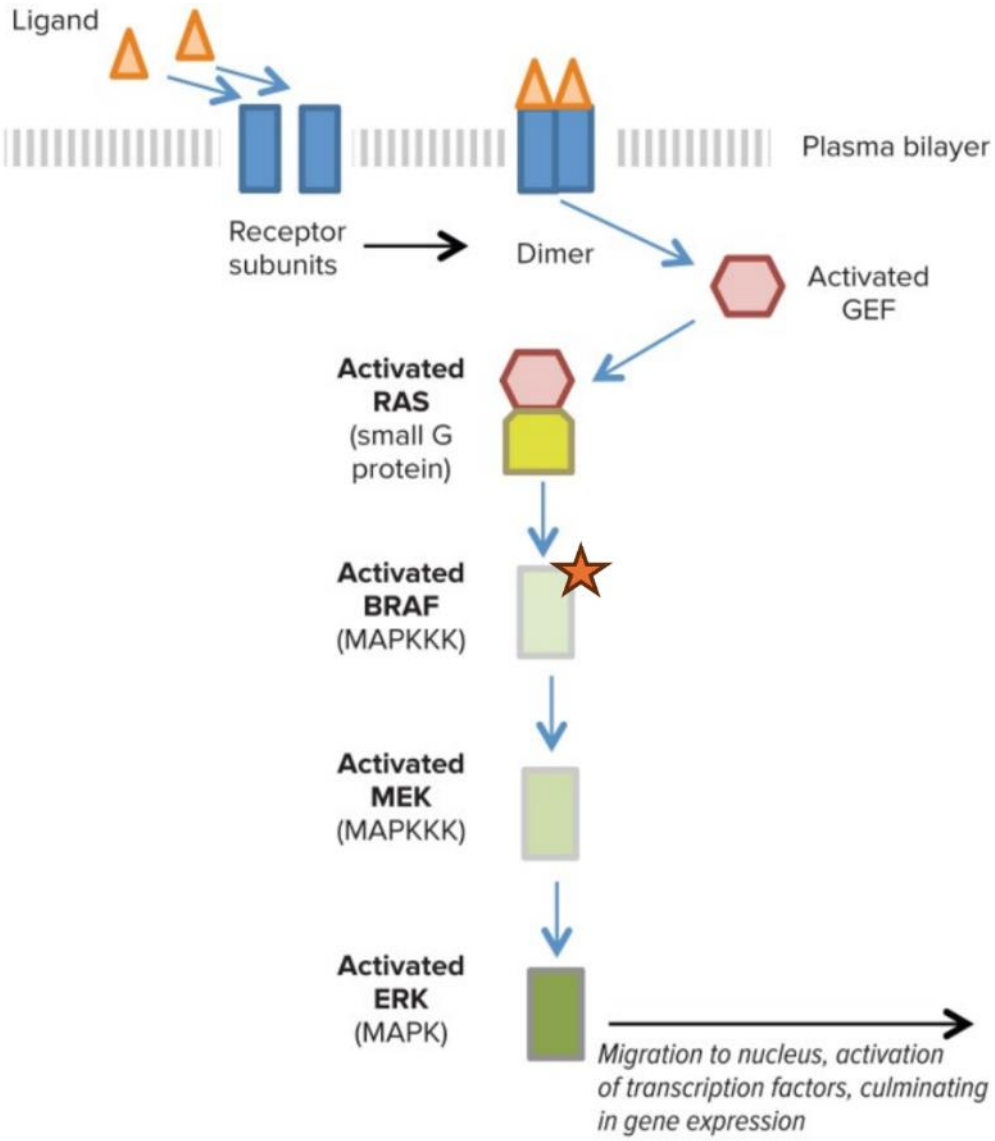


***Figure 1.5 Simplified MAPK/ERK Signalling Pathway.*** *The MAPK/ERK signalling pathway is initiated once a ligand, such as a growth factor or hormone, binds to the extracellular domain of a receptor tyrosine kinase (RTK). This binding induces dimerization of the RTK subunits and subsequent phosphorylation of their cytoplasmic domains. Activated RTK recruits cytoplasmic adaptor proteins, which in turn attract guanine-nucleotide exchange factors (GEFs) to the plasma membrane. GEFs activate the small G protein RAS by facilitating the exchange of guanosine diphosphate (GDP) for guanosine triphosphate (GTP). Activated RAS then phosphorylates and activates BRAF, a mitogen-activated protein kinase kinase kinase (MAPKKK). Majority of PTC cases that exhibit aberrant MAPK/ERK signalling are caused by BRAF V600E mutations (Star). BRAF phosphorylates MEK (MAPK/ERK kinase), which is the next kinase in the cascade. MEK, a dual-specificity kinase, phosphorylates ERK (extracellular signal-regulated kinase) on both tyrosine and threonine residues, leading to ERK activation. Activated ERK moves to the nucleus to phosphorylate transcription factors, influencing gene expression related to cell growth and differentiation. In thyroid cancer, aberrations in the MAPK/ERK pathway such as mutations in genes like BRAF and RAS lead to persistent activations of the pathway, driving uncontrolled cell proliferation and tumorigenesis which can influence treatment response and disease aggressiveness. Adapted from McCain (2013).*

### 1.2.4 Follicular Thyroid Cancer

FTC is the second most prevalent type of DTC which also originates from follicular cells of the thyroid gland but unlike PTC, RET/PTC rearrangements and BRAF mutations are rarely discovered (Cipriani *et al.,* 2015). Instead, tumorigenesis is primarily driven by mutations within the family of RAS oncogenes (HRAS, NRAS, and KRAS), which are found in approximately 50% of all FTC (Prabhash *et al.,* 2022). The presence of these RAS mutations subsequently stimulate the activation and overexpression of both the MAPK and PI3K/AKT signalling pathways, responsible for regulating cell growth, proliferation, and survival. Fusion of Paired Box Gene 8 (PAX8) with Peroxisome Proliferator-Activated Receptor Gamma (PPARγ) is observed in ~30-35% of FTC cases, promoting abnormal cell growth and survival (Raman & Koenig, 2014). This fusion results from a chromosomal translocation between the PAX8 gene, involved in thyroid follicular cell development and differentiation, and the PPARG gene, which encodes the receptor PPARγ, involved in adipogenesis and glucose metabolism. The resulting product disrupts the PI3K/AKT pathway facilitating the malignant transformation of follicular cells. Another crucial genetic alteration in FTC is the PIK3CA mutation, found in approximately 10% of cases, which combined with loss of the PTEN tumour suppressor gene, further enhances the activation of PI3K/AKT signalling, promoting heightened cell proliferation (Singh *et al.,* 2021).

### 1.2.5 Anaplastic Thyroid Cancer

ATC is an incurable and rare TC accounting for less than 2% of TC diagnoses, characterised by its fast-growing nature, early metastasis, and resistance to conventional therapies (Amaral *et al.,* 2020). Despite the relatively low number of cases, ATC is responsible for a disproportionately high disease-specific mortality of nearly 100% (Rao & Smallridge, 2023), with a median survival time of only 6 to 8 months post-diagnosis, it is responsible for 40% of all thyroid cancer related deaths (Liu *et al.,* 2016). ATC has a strong tendency to spread to distant parts of the body with around 50% of patients diagnosed with ATC experiencing metastasis (Pavlidis *et al.,* 2023). ATC is classified as an undifferentiated TC, often arising from pre-existing well-differentiated DTC, which evolves to bear no resemblance to its tissue of origin, gifting the malignancy resistance to RAI therapy due to impaired NIS activity (Figure

1.6). This transformation process is facilitated through the accumulation of genetic and epigenetic alterations. Notably, the loss of the TP53 tumour suppressor gene, occurring in approximately 27-78% of ATC cases, causing cell cycle dysregulation and genomic instability, which has also been shown to negatively influence the efficacy of RAI therapy. In about 32-73% of cases, a mutation in the Telomerase Reverse Transcriptase (TERT) promoter leads to an increase in telomerase activity, granting the cells a proliferative advantage (Abe & Lam, 2021).

Epigenetic changes include DNA methylation and histone modifications, silencing thyroid specific genes, further supporting the loss of differentiated features and greater resistance to therapies. Several genes including PTEN, RAP1GAP, RASAL1, REC8, RASSF1, and RASSF2, which have been implicated as potential tumour suppressors, exhibit promoter hypermethylation in ATC, typically leading to decreased expression or functional inactivation. Moreover, thyroid-specific genes like TSHR and NKX2-1, critical for normal thyroid function and TH production, can also undergo hypermethylation in ATC, disrupting their regulatory roles and contributing to other thyroid related disorder such as hypothyroidism (Ravi *et al.,* 2020). ATC patients with hypothyroidism have been reported to experience poorer survival outcomes (Kasemsiri *et al.,* 2021). Conversely, hypomethylation of genes such as NOTCH4, MAP17, and TCL1B often results in increased expression, altering regulatory functions and enhancing tumorigenic capabilities (Ravi *et al.,* 2020). Whereas histone modifications play a critical role in facilitating the dedifferentiation process observed in ATC through the overexpression of histone methylation modifiers like EZH2 suppresses PAX-8 transcription, a key regulator of thyroid differentiation thus promoting loss of differentiated features in ATC cells. In addition, histone deacetylation significantly alters the expression of genes involved in the NIS, impairing its functionality thereby granting ATC resistance to RAI therapy (Volante *et al.,* 2021).

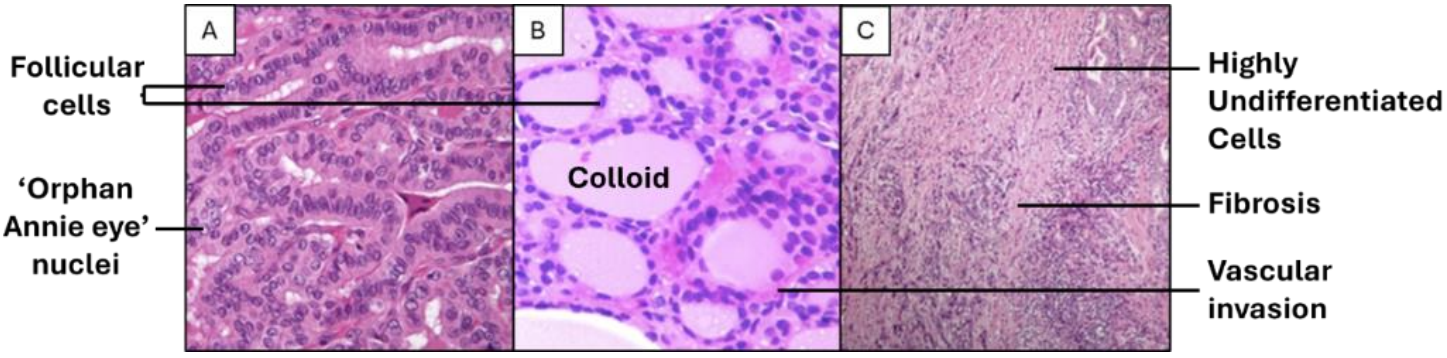


***Figure 1.6 Main histological types of thyroid cancer.*** *A – Papillary thyroid carcinoma comprising of characteristic "Orphan Annie eye" nuclei, with clear, empty-appearing chromatin, and nuclear grooves. B – Follicular thyroid carcinoma with uniform follicular structures filled with colloid and evidence of vascular invasion and C – Anaplastic thyroid carcinoma consisting of highly undifferentiated cells with numerous mitotic figures and areas of fibrosis and necrosis. Adapted from Yale Rosen.*

## 1.3 Thyroid Cancer Risk Factors

The aetiology of TC remains elusive, primarily due to the intricacies of its origins (Horgan *et al.,* 2022). However, certain factors have been proposed to elucidate how they may predispose individuals to TC. Notably, the influence of iodine and radiation.

### 1.3.1 Significance of Iodine

The importance of Iodine in thyroid functionality cannot be overstated, it is essential for the adequate production of TH, and in turn is heavily involved in various cell proliferation pathways. The availability of iodine, therefore, is interlinked with thyroid carcinogenesis (Guigon & Cheng, 2009).

Iodine must be obtained from external sources, sufficient levels can be maintained most commonly through iodine-rich foods such as seaweed, cod, dairy products, and eggs (Bath *et al.,* 2022). A prolonged state of iodine deficiency (ID) can lead to the development of a goitre and thyroid nodules, conditions which are frequently observed in ID populations (Zimmermann & Galetti, 2015). ID is classified as a Urinary Iodine Concentration (UIC) below 99 µg/L (WHO, 2013). In the UK, the recommended daily intake of iodine for adults is 150 µg, with the amount rising to 200 µg for pregnant and lactating women (British Dietetic Association, 2021).

### 1.3.2 Iodine Inadequacy

Boltze *et al.* (2002) found that ID in rats significantly increased thyrocyte proliferation by 5 to 30-fold, resulting in elevated serum TSH levels. This chronic overstimulation led to marked hyperplasia and hypertrophy leading to heightened susceptibility to mutagenic agents such as radiation, chemical carcinogens, and oxidative stress. In contrast, no carcinomas were observed in rats with normal iodine intake post-radiation, indicating that ID plays a crucial role in the emergence of thyroid cancer . Zimmerman and Galetti (2015) reviewed multiple studies involving rats on either ID or normal iodine diets. In female rats, ID diets over 6 to 20 months increased serum TSH levels and led to thyroid tumours in 54-100% of subjects across four studies, confirming the adverse effects of inadequate iodine intake.

A longitudinal study in the UK found that pregnant women had a median urinary iodine concentration (UIC) of 85 µg/L, indicating mild iodine deficiency when compared against WHO standards for iodine sufficiency in pregnant women (Bath *et al.,* 2013). Insufficient maternal/foetal thyroid hormone levels are associated with significant neurodevelopmental defects in children, potentially persisting into adulthood (Alemu *et al.,* 2016). This underscores the importance of monitoring and nutritional interventions, as sufficient iodine intake through diet or supplements can prevent these adverse effects. However, thyroid enlargement due to ID may take months or years to revert to its original size after iodine levels are corrected (Zimmermann, 2008).

Public health initiatives, like the iodised salt program first introduced in Switzerland in 1922, have been crucial in reducing ID-related disorders. The program, aimed at promoting the production and consumption of iodine-fortified salt, led to the lowest prevalence of ID (10.6%) in the Americas, where iodised salt consumption was the highest (~90%) (Zimmermann, 2008). Globally, the number of countries with adequate iodine intake rose from 67 in 2003 to 118 in 2020, reducing the global prevalence of ID-related disorders from 13.1% to 3.2% and preventing 720 million cases, a 75.9% reduction (Gorstein *et al.,* 2020). However, it is yet to be implemented in the UK, where iodine deficiency remains a concern (Apostolou *et al.,* 2020).

Despite these successes, some countries have seen an increase in PTC. It remains unclear whether this rise is due to the failure of iodised salt programs, hesitation to incorporate

iodised salt into diets (especially with recent movements in the UK to reduce salt consumption), overconsumption of iodine (section 1.3.4), or improved screening and overdiagnosis of TC in recent years (Zimmermann, 2009; Aravindan, 2017).

### 1.3.3 Hypothyroidism

When the thyroid gland fails to produce sufficient quantities of TH, either due to a lack of essential resources or damage to the organ, individuals will experience the consequences of an underactive thyroid (hypothyroidism). Hashimoto's thyroiditis (HT) results from chronic inflammation of the thyroid gland, leading to its gradual deterioration and is a common cause of hypothyroidism, second only to dietary ID (Ralli *et al.,* 2020). HT is associated with TC, although the exact relationship remains unclear. A 36-study review (64,628 subjects) from 13 countries, with data between 1955 and 2016, found a significant risk of PTC among patients with HT (Resende de Paiva *et al.,* 2017). Moreover, another study involving 839 patients with HT did identify the disease as an independent risk factor for developing TC (Cappellacci *et al.,* 2022). Furthermore, a meta-analysis involving 11 case-control and 12 cohort studies, indicated that HT patients have an increased risk of TC. The overall risk of HT patients developing TC was significantly higher compared to non-HT patients, with an odds ratio (OR) of 1.82 from case-control studies and a relative risk (RR) of 1.49 from cohort studies (Hu *et al.,* 2022).

Interestingly, a study examining the association of HT with PTC in a cohort of 9,210 participants, found that patients with HT had better outcomes and lower disease-related morbidity compared to those without the disease (Xu *et al.,* 2021). They also mentioned that countries are reporting rising trends in TC regardless of having implemented iodised salt programs. Meaning it is uncertain whether deficient levels of dietary iodine are directly related to the increase in TC prevalence, although mechanisms have been brought forward to explain how low iodine intake can result in TC (mentioned in section 1.3.2). Most of aforementioned studies had collected data across multiple continents, however they did not analyse ethnic differences as a risk factor although it was mentioned by Hu *et al.,* (2022), that more studies should investigate ethnicity, region and lifestyle as potential risk factors in HT

patients to develop TC. This showcases the complex interplay between thyroid functionality, dietary iodine intake and related disease outcomes/risks.

### 1.3.4 Iodine Abundance

In cases of iodine overconsumption, a physiological reflex known as the Wolff-Chaikoff effect takes place whereby the thyroid transiently inhibits TH production in response to the large quantities of iodine in the system (Campos *et al*., 2023) A healthy thyroid can tolerate chronically high iodine intakes and adapt to handle up to 2 g/day, which is substantially above the UK Department of Health's daily recommendation of 150 µg/day for adults (Bath *et al.,* 2022). Through protective autoregulation within the thyroid gland, TH production normalises after approximately 10 days. However, individuals with autoimmune thyroid disease, may experience persistent suppression, necessitating intervention. While there is insufficient evidence to directly link iodine excess to malignancies, it can lead to thyroiditis by generating oxidative stress in thyrocytes, which causes cell damage and triggers an immune response against thyroid auto-antigens (Luo *et al.,* 2014). Groups that include the elderly, pregnant and those with pre-existing thyroid disorders, such as goitres are most vulnerable  Prolonged excess of iodine can lead to thyroid autoimmune disorders, which themselves carry an increased risk of malignancy (Smyth, 2021).

### 1.3.5 Hyperthyroidism

An overstimulated thyroid (hyperthyroidism) can be triggered by various thyroid-related disorders, including thyroiditis, thyroid nodules, and iodine excess. Graves' disease (GD), an autoimmune disorder, accounts for the majority of cases which lead to hyperthyroidism, every year globally around 50 cases per 100 000 are reported (Chaker *et al.,* 2024). In the UK, approximately 4 out of 5 individuals with GD are diagnosed with an overactive thyroid gland (NHS, 2023). Individuals with GD experience the overexpression and release of thyrotropin receptor-specific autoantibodies (TRAB), which act as agonists, leading to the hypersecretion of TH (Soares *et al.,* 2023). This disruption in thyroid function may induce an enlargement of the gland, resulting in a goitre (Figure 1.7). While thyroid nodules are common in the general population (~4%), the presence of multiple nodules indicates the development of a multinodular goitre (MNG), also referred to as a toxic diffuse goitre (Geraldo, 2016). MNG is

more prevalent in populations with low iodine intakes and is associated with a higher risk of TC compared to individuals with a non-toxic diffuse goitre (Apostolou *et al.,* 2020). Although benign, MNG come with a 5% cancer rate (Yildirim Simsir *et al.,* 2019) with no significant differences in risk among different ethnicities (Horn-Ross, 2001). However, conflicting findings exist regarding the higher incidence of TC in MNG patients compared with non-toxic diffuse goitres or single nodules, which both tend to be benign, with lower chances of developing into TC. As indicated by a meta-analysis by Brito *et al.,* (2013) involving 23,565 patients with MNG and 20,723 patients with single nodules. Based on the cohort, they found MNGs exhibited a 20% lower risk of TC compared to single nodules. Consequently, the association between MNG and TC incidence remains undetermined.

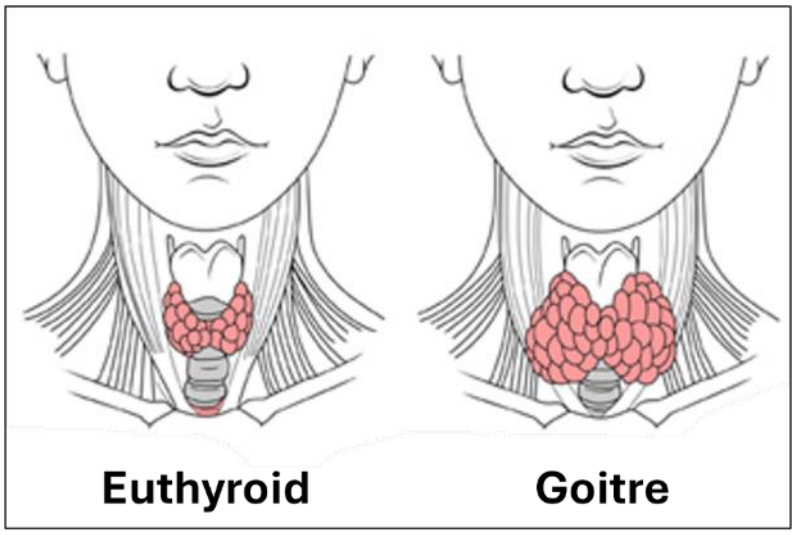


***Figure 1.7 Illustration depicting a healthy thyroid gland (Left) and the formation of a goitre (Right).*** *Presence of a goitre caused by swelling of the thyroid gland creates a visible protrusion in the neck. Adapted from What is a goiter? (2015).*

### 1.3.6 Radiation Exposure

Radiation is a well-established and documented risk factor for TC (Iglesias *et al.,* 2017). In the event of ionising radiation exposure, two main considerations are examined to determine the chances of developing TC: the dose and age at time of exposure. Ionising radiation causes DNA double-strand breaks, resulting in genetic mutations and chromosomal rearrangements.

For instance, RET/PTC rearrangements and BRAF mutations in PTC. These genetic alterations disrupt normal cellular pathways and functions, leading to uncontrolled cell proliferation and ultimately the development of TC (Albi *et al.,* 2017).

Exposure to radiation doses exceeding 0.05-0.1 Gy heightens the risk of TC, especially with childhood exposure carrying a greater risk. The latency period before TC manifestation ranges from 5 to 10 years, with PTC being the most common subtype. In the instance of childhood exposure, a distinct form, radiation-induced PTC is predominantly observed in younger children, which tend to be more aggressive and have shorter latency periods compared to typical PTC observed in adults (Iglesias *et al.,* 2017). This is thought to be due to children exhibiting a higher thyrocyte proliferation rate and lower DNA repair capacity compared to adults. Furthermore, medical treatments involving radiation, such as radio/chemotherapy for childhood cancers, have also been linked to an elevated risk of TC later in life (Inskip, 2001). For instance, treatment with doses of 20 Gy or less, along with alkylating agents, was linked to a significant 2.4-fold increased risk of TC, with the cumulative incidence of TC 30 years after childhood cancer treatment being 1.3% for females and 0.6% for males (Veiga *et al.,* 2012). Highlighting the need for careful monitoring and protective measures for younger individuals exposed to radiation.

The association between radiation exposure, age, and TC development has been extensively documented in the aftermath of the Chernobyl (1986) and Fukushima (2011) nuclear disasters, which witnessed a notable rise in TC cases in the local regions (Cléro *et al.,* 2021). Aware of the relationship between radiation exposure and TC, thyroid ultrasound screenings were implemented within the Fukushima Health Management Survey for residents under 18 years (38,114 children) at the time of the accident, revealing no significant spikes in TC cases (Yasumura *et al.,* 2022). However, a comparison of radiation exposure and TC incidence between Chernobyl and Fukushima revealed a marked increase in TC cases among younger age groups, particularly those aged 0-5 years at the time of the Chernobyl accident. Conversely, post-Fukushima observations displayed a higher prevalence of TC cases in the older age groups, however this could be attributed to improved screening methods in the Japan disaster, which occurred 25 years after the Chernobyl melt-down, rather than radiation-induced malignancy (Takamura *et al.,* 2016).

## 1.4 Thyroid cancer treatment

Given the limitations of RAI therapy in refractory cases, secondary treatment options are essential. Tyrosine Kinase Inhibitors (TKI, see section 1.5) have exhibited great potential, namely sorafenib and Lenvatinib. Although TKI have demonstrated promising results in clinical trials, they are not as effective as RAI therapy and typically yield only partial responses, with complete responses being extremely rare (Oba *et al.,* 2020), despite that side effects are commonplace underscoring the importance of managing their toxicity through careful monitoring, dose adjustments, and patient education (Figure 1.8). Moreover, the presence of multiple TC subtypes necessitates a personalised approach for each patient which is further complicated by the prevalence of primary and secondary drug resistance (Zhang *et al.,* 2022). Thus, highlighting the continued need for research in the area of chemoradiotherapy.

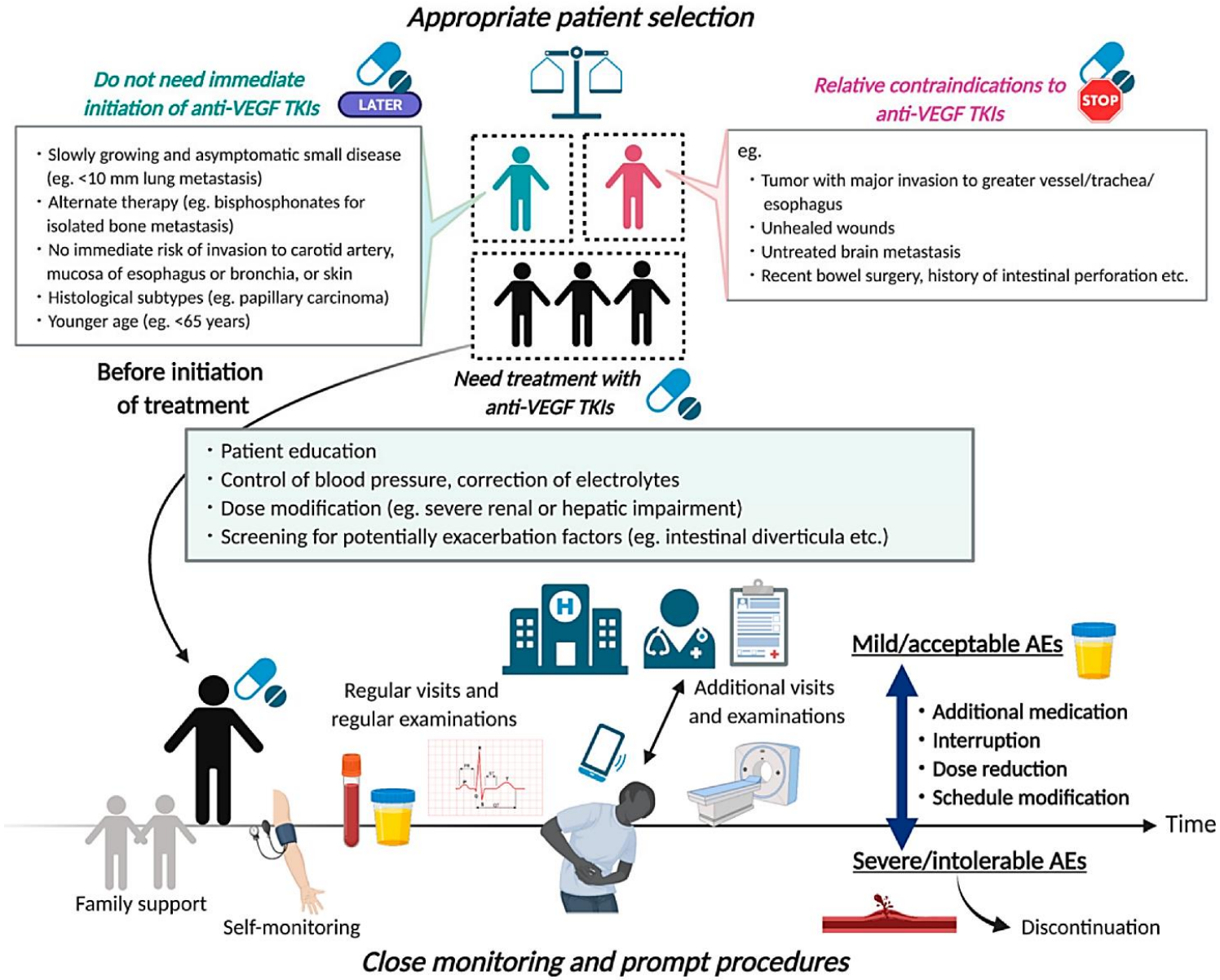


***Figure 1.8 Overview of the decision-making process for Anti-VEGF TKI prescription.*** *Careful examination of patient history, age, tumour status and susceptibility to side effects are considered when determining the patient's suitability for anti-VEGF TKI (e.g. sorafenib) treatment. VEGF - Vascular Endothelial Growth Factor, TKI – Tyrosine Kinase Inhibitor and AE – adverse events (Enokida & Tahara, 2021).*

### 1.4.1 Surgery and Radioiodine (RAI) Therapy

For DTC, the primary therapeutic approach involves thyroidectomy, which is the partial or complete surgical removal of the thyroid gland, with the aim of excising as much of the tumour as possible to reduce the risk of recurrence and possibility of metastasis. This is followed by RAI therapy which involves the NIS transporting radioactive iodine ($I^{131}$) into DTC cells, ablating them through the release of high-energy β particles that damage and kill remnant thyroid tissue and/or residual cancer cells that were not removed during surgery. Patients who had their entire thyroid gland extracted are put on mandatory and lifelong thyroxine supplementation and TSH suppressive therapy (Mayson *et al.,* 2021). The combination of surgery and RAI treatment has been established as the worldwide gold standard for managing DTC for more than 60 years, but is heavily dependent on ability of the thyroid gland in each individual, to uptake and concentrate iodine, which is facilitated by the NIS (Schmidbauer *et al.,* 2017). Specifically, during the iodine organification process which increases iodine retention time within the thyroid gland, enhancing the efficacy of RAI therapy.

Papillary thyroid microcarcinomas (mPTCs) account for ~50% of classified PTC cases and are often identified incidentally during routine examinations. These small tumours present a diagnostic challenge in the management of PTC due to their small size (typically 1 cm or less) and very slow growth rate, as although regarded as a malignancy, they do have a favourable prognosis. Kaliszewski *et al.* (2019) proposed a classification system categorising microcarcinomas into "true cancers" (tumours >0.5 mm in diameter) and "precancers"(<0.5 mm in diameter), facilitating different treatment planning. While true cancers may necessitate more aggressive interventions such as thyroidectomies, smaller tumours (<0.5 mm) may benefit from less invasive methods like hemithyroidectomies (HT) or active surveillance to monitor disease progression**.** Conversely, Williams (2015) cautions against labelling microcarcinomas, which have not yet achieved full immortality, as fully-fledged "cancers," warning of the potential for overtreatment and its associated risks to patient well-being. In a systematic review and meta-analysis of 17 studies involving 1,416 patients who underwent HT and 2,411 patients who underwent total thyroidectomy (TT) done by Hsiao *et al.,* (2022), they discovered that complications associated with the surgical management of mPTCs increased with the extent of surgery performed. Specifically, HT was associated with

lower risks of temporary vocal fold paralysis (VFP) (2.0% vs. 4.2%), temporary hypoparathyroidism (2.2% vs. 21.3%), and permanent hypoparathyroidism (0% vs. 1.8%) compared to TT. Despite, observing lower rate of post operative complications, the HT group did show greater rates of recurrence compared to the TT group (3.9% vs 1.3%, respectively). Ultimately, personalised treatment strategies tailored to individual patient needs and preferences are required, considering the multitude of benefits and drawbacks associated with any intervention.

### 1.4.2 RAI Therapy Resistance

Unfortunately, around 10-20% of patients with DTC exhibit local recurrence and/or distant metastasis within 5-10 years of initial treatment, 2/3 of which experience gradual or complete loss of iodine uptake capabilities, making them RAI-R (Karapanou *et al.,* 2022). This resistance to RAI therapies primarily stems from a dysfunctional NIS, thus little or no $I^{131}$ can enter the follicular cells.

### 1.4.3 Dedifferentiated Thyroid Cancer

In addition to the loss of function of the NIS during dedifferentiation other characteristic thyroid-specific molecules such as TG and TPO can also suffer loss of expression (Aashiq *et al.,* 2019). These molecules are essential for the normal function of thyrocytes through their contribution in iodine metabolism processes, and their loss further contributes to the aggressive nature and treatment resistance of dedifferentiated DTC's (Zhao *et al.,* 2019).

These cancers forfeit their ability to uptake iodine rendering RAI therapy ineffective (Luo *et al.,* 2021). An intermediate subset between DTC and ATC are the poorly differentiated thyroid carcinomas (PDTC) which are more aggressive and carry a poorer prognosis compared to DTC but less so in contrast to ATC (Fallahi *et al.,* 2015). Currently, the best secondary treatment for RAI-R cancer are TKI such as sorafenib (De Leo *et al.,* 2020).

### 1.4.4 NIS Dysfunction

Mutations in the SLC5A5 gene, which encodes the NIS can lead to structural alterations that decrease NIS expression and impair its ability to transport iodine into cells, a condition known

as iodide transport defect (ITD, Reyna-Neyra *et al.,* 2021). Mutations in the NIS gene itself are relatively uncommon; however, mutations of the BRAF V600E gene and aberrant MAPK/ERK signalling are more frequently associated with NIS dysfunction than due to ITD (section 1.2.3). BRAF mutations can disrupt the post-translational processing and trafficking of the NIS protein, resulting in misfolding, and improper cellular localisation, thereby impeding its iodine uptake capability (Ge *et al.,* 2020).

Impairments in NIS function, such as reduced mRNA levels or disruptions in plasma membrane trafficking, are linked to poor prognosis in TC (Gaohong & Lijun, 2020). Epigenetic modifications, such as hypermethylation of the NIS promoter region, hinder the binding of essential transcription factors, effectively silencing NIS expression. Additionally, histone deacetylation contributes to this by creating a more condensed chromatin structure, preventing NIS gene transcription (Zhang *et al.,* 2013). These modifications are found to be influenced by race, environment, lifestyle, and nutrition, which play a critical role in the malfunction of NIS and its response to treatment, again underscoring the need for targeted therapies to address these epigenetic changes (Zarkesh *et al.,* 2022).

## 1.5 Tyrosine Kinase Inhibitors

TKI are a type of targeted therapy that block the activity of tyrosine kinases involved in cell signalling pathways which, as described previously, are commonly dysregulated in TC. By competitively attaching to the ATP binding sites of these enzymes, TKI aim to restore normal levels of cell proliferation, inhibit angiogenesis and potentially limit metastatic spread. They are generally employed to treat TC that are RAI-R (Jannin *et al.,* 2019). Several TKI, including sorafenib, lenvatinib, vandetanib, and cabozantinib, are approved for the treatment of TC (Figure 1.9), targeting various pathways involved in tumour growth (such as BRAF, RAS, and RET) and angiogenesis (i.e. VEGFR2 and PDGFR) (Enokida & Tahara, 2021).

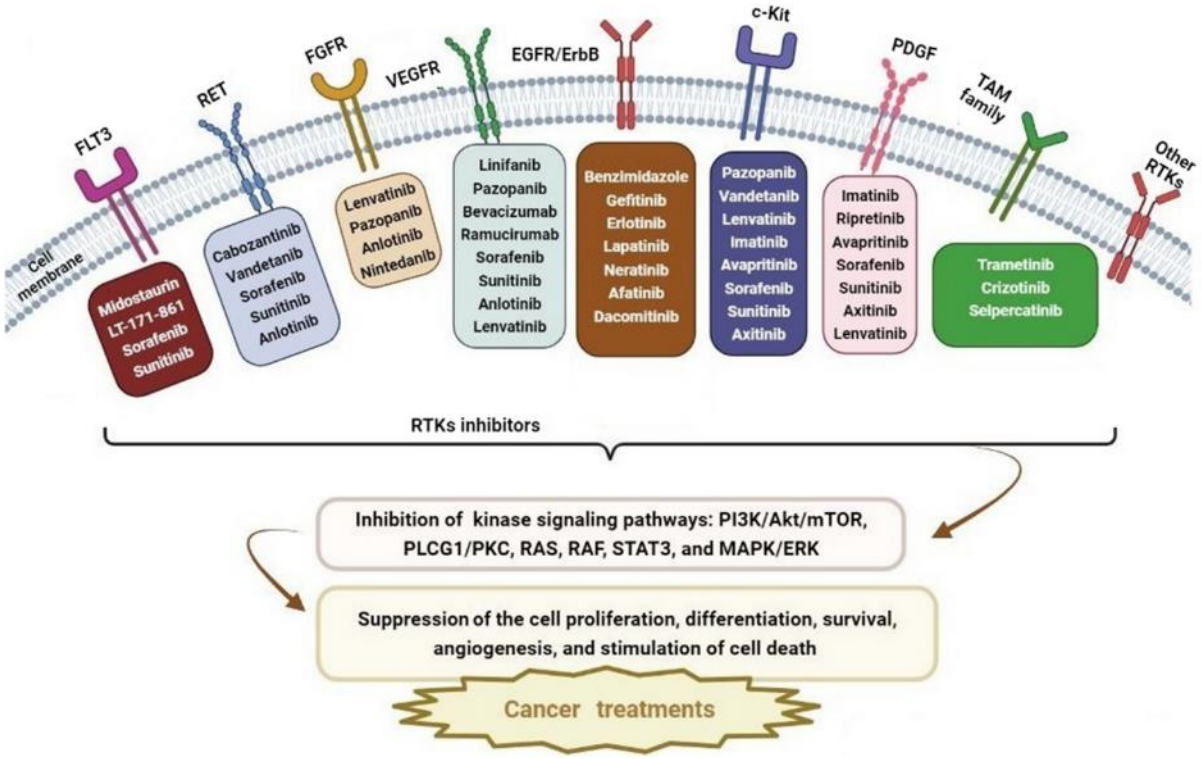


***Figure 1.9 Summary of clinically used Tyrosine Kinase Inhibitors (TKI) and their targets.*** *The diagram highlights how small molecule TKI target the ATP-binding site in the intracellular domain of Receptor Tyrosine Kinases (RTK), blocking phosphorylation and subsequent signalling cascades. Abbreviations: FLT3 (FMS-like tyrosine kinase-3); RET (rearranged during transfection); FGFR (fibroblast growth factor receptor); VEGFR (vascular endothelial growth factor receptor); EGFR (epidermal growth factor receptor); c-KIT (Mast/Stem Cell Growth Factor Receptor Kit); PDGFR (platelet-derived growth factor receptor); PI3K (phosphoinositide 3-kinase); Akt (V-Akt murine thymoma viral oncogene homolog); mTOR (mammalian target of rapamycin); PLCG1/PKC (phospholipase C gamma 1/protein kinase C); RAS (rat sarcoma virus); RAF (rapidly accelerated fibrosarcoma); STAT3 (signal transducer and activator of transcription 3); MAPK/ERK (mitogen-activated protein kinase/extracellular signal-regulated kinase). Adapted from Ebrahimi et al., (2023).*

### 1.5.1 Sorafenib

Sorafenib is an orally administered (starting dose of 400 mg twice a day) multi-TKI which is usually considered after the failure of RAI therapy (Cabanillas *et al.,* 2019). It targets serine/threonine kinase RAF1 and various tyrosine-kinase receptors, such as RET, VEGFR2, VEGFR3, PDGFR beta, c-KIT, and Flt-3 (Figure 1.10). These factors play key roles in tumour cell proliferation, metastasis, and neovascularisation. Moreover, it inhibits both wild-type and mutant BRAF V600E, a genetic alteration frequently observed in PTC as discussed previously (section 1.2.3). Sorafenib induces tumour shrinkage due to its anti-proliferative and anti-angiogenic properties (Huang *et al.,* 2021).

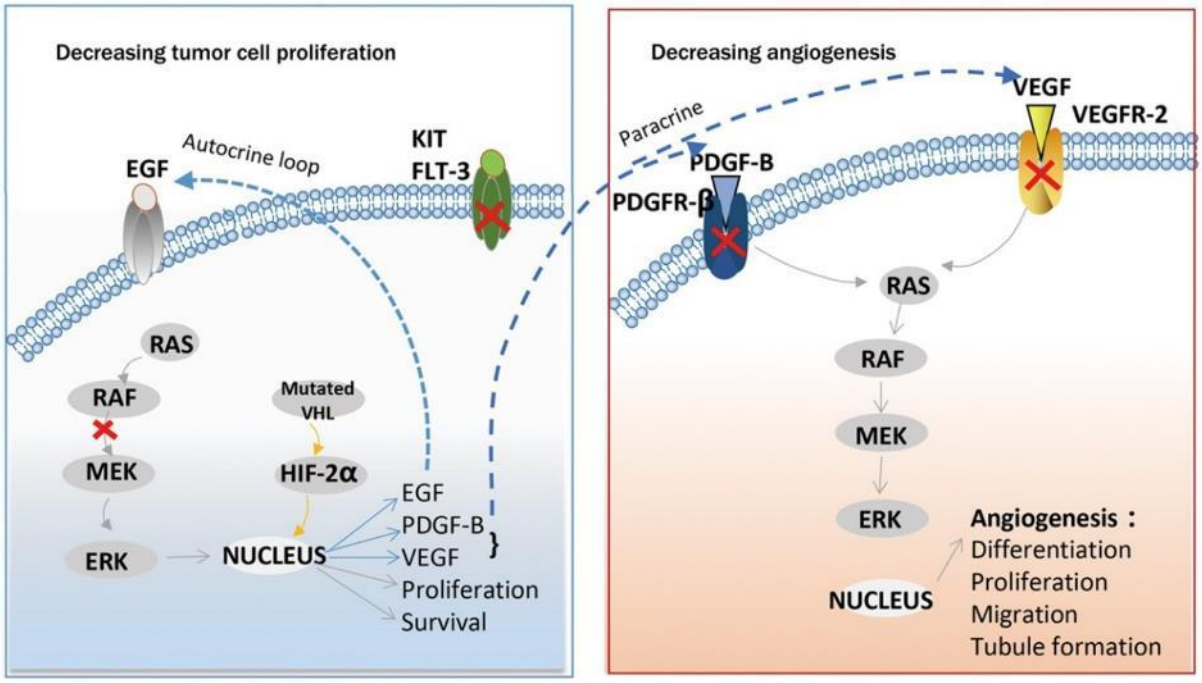


***Figure 1.10 Multi-Kinase Inhibition by sorafenib.*** *Sorafenib targets multiple cellular pathways by inhibiting Receptor Tyrosine Kinases (RTK), such as VEGFR, PDGFR, c-Kit, and RET. This inhibition disrupts the downstream Raf/MEK/ERK signalling pathway, resulting in decreased tumour growth through anti-angiogenic, antiproliferative, and pro-apoptotic effects. Abbreviations: VEGFR (vascular endothelial growth factor receptor, which promotes blood vessel formation); PDGFR (platelet-derived growth factor receptor, involved in cell growth and division); c-Kit (Mast/Stem Cell Growth Factor Receptor Kit, essential for cell survival and proliferation); RET (rearranged during transfection, a receptor linked to cell differentiation and growth); Raf/MEK/ERK (rapidly accelerated fibrosarcoma/mitogen-activated protein kinase kinase/extracellular signal-regulated kinase). Adapted from Zhu et al., (2017).*

Unfortunately, side effects are very common with almost 80% of patients requiring a dose reduction due to developing Hand-Foot syndrome, characterised by redness, swelling, and pain in the palms of the hands and soles of the feet. Furthermore, breaks in sorafenib treatment are required due to the severity of the adverse effects in 63–82% of patients. Sorafenib has also been shown to induce cutaneous squamous cell carcinomas in up to 5% of patients (Zygulska *et al.,* 2013). Despite this, most reactions to the cytotoxic agent are mild and sorafenib remains as one of the top TKI treatment options for treating RAI-DTC to date (Oba *et al.,* 2020;Enokida & Tahara, 2021).

Clinical studies have demonstrated that sorafenib significantly prolongs progression-free survival (PFS) in patients (Brose *et al.,* 2014; Fierro-Maya *et al.,* 2021). A randomised phase III trial, totalling 417 patients with RAI-R locally advanced or metastatic DTC, with 207 patients receiving sorafenib and 209 patients assigned a placebo. The median PFS was 10.8 months in the sorafenib group, compared to 5.8 months in the placebo group (Brose *et al.,* 2014). A phase II study examined the safety and efficacy of sorafenib in 19 patients with advanced TC revealing an 18-month PFS, however this study did not include a placebo group (Fierro-Maya *et al.,* 2021).

It is pertinent to note that many TKI including sorafenib, although having shown efficacy in clinical trials, lack the potency of RAI therapy and typically yield only partial responses; complete responses are highly uncommon (Pitoia *et al.,* 2022). There are a plethora of TKI available that target a variety of specific tyrosine kinases, but these generally produce weak results on their own. Many *in vitro/in vivo* studies have consistently shown that combination therapies involving TKI with other inhibitors and molecules, offer greater responses compared to monotherapies, with some already completed while others are on-going in clinical trials (Laetitia *et al.,* 2020). For instance, the combination of sorafenib with a steroidal lactone, withaferin A (which has shown to exhibit anti-Inflammatory/cancer cell properties) to treat a PTC cell line (BCPAP) and an ATC cell line (SW1736), significantly enhanced response to the treatment compared to sorafenib monotherapy. Sorafenib alone showed moderate efficacy with $IC_{50}$ values of 6.3 µmol/L in BCPAP cells) and 7.6 µmol/L in SW1736 cells, whereas combination therapy achieved significantly lower $IC_{50}$ values of 0.055 µmol/L inBCPAP cells and 1.4 µmol/L in SW1736 cells (Cohen *et al.,* 2012).

Nude BALB/c mice have been used to generate xenograft tumour models using 8505c (ATC) and FTC133 (FTC) cell lines, which were subsequently treated with either sorafenib, chloroquine (CQ) an autophagy inhibitor (reported to heighten sensitivity to cancer treatments) or a combination of both every day for 21 days. Sorafenib alone reduced tumour sizes significantly compared to controls (698.61 $mm^3$ for 8505C and 697.07 $mm^3$ for FTC133 *vs*. 1,280.93 $mm^3$ and 2,176.57 $mm^3$, respectively). CQ alone also decreased tumour sizes (602.36 $mm^3$ for 8505C and 600.42 $mm^3$ for FTC133). Combining sorafenib with CQ resulted in even smaller tumours (358.99 $mm^3$ for 8505C and 344.36 $mm^3$ for FTC133), significantly smaller than either treatment alone or controls ($p<0.01$) showing the efficacy of this dual therapy (Yi *et al.,* 2017).

Combination therapy of sorafenib and onalespib, a heat shock protein 90 (HSP90, a molecular chaperone involved in cancer cell growth and survival) inhibitor, significantly reduced tumour growth and improved median survival times in BHT-101 (anaplastic thyroid cancer cell line) xenograft mice, when compared to monotherapy and control groups. The median survival times for the combination therapy group was 24 days in contrast to monotherapies which was 17 for both inhibitors and only 13 days for the control group (Mortensen *et al.,* 2023). These studies underscore the ongoing efforts aimed at developing enhanced therapies for patients afflicted with RAI-R cancers, reflecting promising prospects for future treatment strategies. However, the models for testing these drugs in TC need to be further refined to better mimic the complexity and heterogeneity of human tumours, as all of the mentioned studies in this section utilised monolayers.

### 1.5.2 Sorafenib resistance

Understanding tumour resistance mechanisms to sorafenib is particularly critical, as many patients eventually develop resistance over time, diminishing its effectiveness. The study outlined in Table 1.1 details the main resistance mechanisms to sorafenib. The latest theory on how tumours can gain resistance to sorafenib is via a process called vessel co-option. In essence, it is believed that tumours may be capable of hijacking existing nearby blood vessels, rather than producing their own, thus the anti-angiogenic properties of sorafenib have little impact. For instance, a study investigating sorafenib treatment on tumour-bearing mice

(hepatocellular carcinoma) which had acquired resistance to sorafenib had shown that up to 75% of blood vessels in resistant tumours were co-opted from existing liver vessels, compared to 23.3% in untreated controls (Kuczynski *et al.,* 2016). This shift from angiogenesis to vessel co-option in response to treatment, allows tumours to sustain growth despite anti-angiogenic therapies. While preclinical studies support vessel co-option as a resistance mechanism, further clinical studies are needed to validate its importance and potentially improve patient treatment strategies. These may include the combination of anti-angiogenic drugs with inhibitors of identified co-option pathways (Kuczynski & Reynolds, 2020).

***Table 1.1. Main mechanisms of sorafenib resistance (Hofmann et al., 2022).***

| Mechanism of Resistance | Description |
|---|---|
| **Activation of Alternative Pathways** | **Activation of pathways that bypass the effects of sorafenib** |
| PI3K/AKT Pathway | Activation promotes cell survival and growth, helping tumour cells evade sorafenib's effects |
| JAK-STAT Pathway | STAT3 phosphorylation aids in tumour cell survival and proliferation despite sorafenib treatment |
| **Epigenetic Changes** | **Genetic aberrations aiding tumour resistance by altering the expression of regulatory genes** |
| EZH2 Upregulation | EZH2, a histone methyltransferase is upregulated, leading to the silencing of tumour suppressor genes: miR-124 and miR-506 |
| **Activation of Pro-Survival Factors** | **Tumours can activate factors that allow them to resist sorafenib** |
| Exportin 1 (XPO1) | Upregulation of XPO1 aids in exporting pro-apoptotic factors out of the nucleus, promoting tumour survival |
| PAK Activation | Activation of PAK promotes cell proliferation, survival, motility, and invasion, processes that help tumours resist sorafenib |

## 1.6 Thyroid cancer models

Various models for studying cancer are currently available; monolayers, spheroids, organoids, On-Chip systems, and xenografts, each possessing distinct properties with specific strengths and limitations that influence their suitability for various research needs (Figure 1.11).

Traditional monolayers, composed of cells grown on flat surfaces have been a cornerstone in cancer research for decades. Their use has been monumental in drug discovery, the simple and relatively cheap set-up, has allowed for a cost-effective model for examining drug efficacy via high-throughput screening (Moya-Garcia *et al.,* 2022). However, due to their simplicity, they offer limited predictive value due to the lack of a tumour microenvironment (TME) and oversimplified culturing conditions.

TC research in recent years has seen great strides in the enhancement of the predictive qualities of models in drug screening, spheroids in particular have played a pivotal role in advancing the understanding and treatment of this complex disease. Spheroids are three-dimensional (3D) aggregates of either homogeneous or heterogeneous cells that closely mimic the microenvironment of avascular tumours. Compared to traditional two-dimensional (2D) cell cultures, spheroids provide a more precise model for investigating cancer biology and drug responses (Sant & Johnston, 2017). They can be grown to develop necrotic cores when sizes exceed 500 µm, where the dense collection of cells restricts oxygen and nutrient supply, creating a hypoxic environment that lowers pH and leads to necrotic cell death (Pinto *et al.,* 2020). This accurately recapitulates *in vivo* tumour hypoxia and therapy resistance, which is not possible in 2D monolayers that lack the ability to generate oxygen and nutrient gradients (Lukowski & Hummon, 2019). Currently, multiple immortalised cell lines are available for each TC type which not only more closely mimic *in vivo* tumours, providing more accurate biological models, but also compete with the high-throughput capabilities of traditional 2D models (Saiselet *et al.,* 2012).

However, these models face notable limitations; preparation and maintenance of spheroids require more specialised techniques to ensure consistent growth thus incurring greater costs compared to traditional monolayers. Moreover, production of spheroids is inconsistent

between batches with variability in size, shape, and internal structure which greatly impacts reproducibility (Aguilar Cosme *et al.,* 2021). Additionally, spheroids lack vascularisation, hampering the accurate recapitulation of interactions between cancer cells and blood vessels which is a highly important component of assessing drug efficacy (Anthon & Valente, 2022). Due to their more complex structure, analysing spheroids can be challenging, necessitating more specialised assays that can penetrate the dense structure. This in turn, also highlights how drug penetration may not accurately reflect clinical drug distribution (Han *et al.,* 2021).

Spheroids are generally homogeneous cell aggregates that provide simplified models, which tend to lack the genetic, phenotypic and physiological complexity of the original tumour. In contrast, organoids derived from patient tissue have emerged as a cutting-edge tool in cancer research, offering a novel approach to studying TC at a personalised level (Sakalem *et al.,* 2021). These miniature 3D structures are cultivated from cells obtained directly from patient biopsies or surgical samples, allowing them to closely replicate the complex cellular interactions, heterogeneity and functions of the thyroid gland as seen with *in vivo* tumours (Samimi *et al.,* 2021). The ability of these models to recapitulate real-life conditions provides researchers with a unique platform to explore the intricate dynamics of TC progression and response to treatments, which is not possible in 2D models. By preserving the genetic and phenotypic characteristics of the original tumour, organoids hold immense promise for tailoring therapies specific to each individual patient (Zhao *et al.,* 2022). Organoids generally provide a more precise representation of tumour behaviours and responses compared to spheroids. However, a significant current limitation lies in their reproducibility, which is hampered by increased costs and a lack of high-throughput capability (LeSavage *et al.,* 2021).

In an attempt to overcome the shortcomings of both spheroids and organoids, namely the lack of vascularisation and recapitulation of cellular interactions between the tumour and surrounding cells, xenografts have been shown to be a promising model. Xenografts, involve the implantation of human cancer tissue/cells into immunocompromised animals such as mice and porcine (Chen *et al.,* 2021). Unlike the previously mentioned models, xenografts provide a living system that closely mimics the human tumour microenvironment allowing for detailed insights into how the malignancy progresses and metastases in a living organism. Moreover, the recent introduction of patient-derived xenografts (PDX) allows for a more

personalised approach to drug screening, researchers can examine how tissue which is genetically and phenotypically similar to those in the patient, responds to various treatments and thus determine the most appropriate regimen for the patient (Byrne *et al.,* 2017).

Nonetheless, these models employ animals with compromised immune systems, which heavily impacts how the tumour behaves within the host organism. Consequently, the evaluation of treatments, especially immunotherapies, may be limited in reliability due to the altered immune response (Abdolahi *et al.,* 2022). Furthermore, the biological differences between humans and mice for example can lead to variations in how drugs interact with tumours, potentially resulting in discrepancies between preclinical drug efficacy observed in murine models and clinical outcomes in humans. The setup process for these models is lengthy, requiring significant investments to maintain controlled environments and care for the laboratory animals. In addition, obtaining ethical approval for these studies can be a protracted process, involving rigorous scrutiny to ensure the humane treatment of these animals and justification of their use (Garcia *et al.,* 2020). This interplay between the extensive time and resources required and the ethical considerations underscores the complexity of employing xenograft models in research.

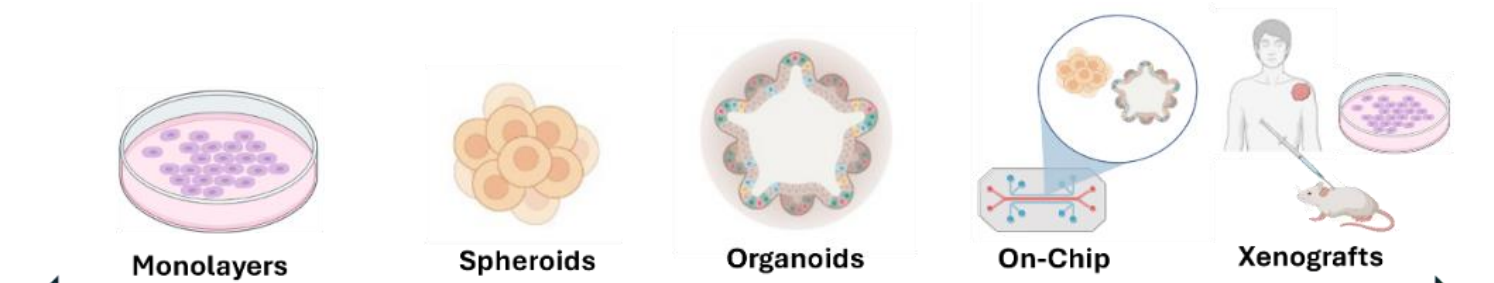


| | Monolayers | Spheroids | Organoids | On-Chip | Xenografts |
|---|---|---|---|---|---|
| **Strengths** | - Low cost<br>- Simple and cost-effective<br>- Controlled environment<br>- Easy observation<br>- Well-characterised models | -Cell-cell interactions<br>- Mimics 3D tumor architecture<br>- Better represents tumor microenvironment<br>- Intermediate between monolayers and organoids | - Complex tissue architecture<br>- Includes multiple cell types<br>- Better mimics *in vivo* conditions<br>- Cell-matrix interactions | - Mimics dynamic microenvironments<br>- Integrates multiple biological processes<br>- Real-time monitoring<br>- Reduction in animal use | - *In vivo* model<br>- Mimics human tumor microenvironment<br>- Useful for studying growth and metastasis<br>- High clinical relevance |
| **Limitations** | - Lacks 3D tumor microenvironment<br>- Altered cell behavior compared to *in vivo*<br>- Limited heterogeneity<br>- Short-term growth<br>- Low clinical relevance | - Variability in size and structure<br>- no vascularisation<br>- Difficult internal analysis<br>- Necrotic core dependent on size | - Complex set-up and costly<br>- Limited scalability<br>- High variability in formation efficiency<br>- Diffusion gradient dependent on size | - High technical complexity<br>- Requires specialised technology<br>- High cost<br>- Early-stage technology | - Expensive and time-consuming<br>- Ethical concerns<br>- Species differences may affect drug response<br>- Limited immune system interaction |
| **HTS capacity/ complexity** | - High reproducibility<br>- Very high throughput<br>- Low complexity | - Moderate reproducibility<br>- Moderate throughput<br>- Moderate complexity | - Low to moderate reproducibility<br>- Low to moderate throughput<br>- High complexity | -Moderate to high reproducibility<br>- Low to moderate throughput<br>- Very high complexity | - Moderate reproducibility<br>-Low throughput<br>- Very high complexity |

***Figure 1.11 Comparison of Cancer Research Models.*** *The table summarises the main strengths and limitations along with an assessment on the reproducibility, throughput capacity and clinical relevance for each cancer research model. HTS – High-Throughput Screening. Created using Biorender.*

The increasing prevalence of RAI-R TC, alongside the rising annual incidence of TC underscores significant treatment challenges. This highlights the pressing need for in-depth research into the mechanisms underlying the resistance to TKI such as sorafenib, which remains one of the very few last resort treatment options for patients unresponsive to conventional therapies. Recent advancements in spheroid and organoid technologies offer promising approaches for more personalised treatment regimens. In particular patient-derived organoids which closely mimic the biological and genetic characteristics of the parental tumour, enable the possibility of personalised medicine by predicting individual responses to treatments (Wu *et al.,* 2022).

A study on PTC organoids found that the models closely recapitulated the histopathological, molecular, and genetic profiles of the parental tumours and demonstrated patient-specific drug responses, which were consistent with their respective mutational profiles (Chen *et al.,* 2021). Moreover, Nuciforo *et al*., (2018) showcased that liver cancer organoids from various patients exhibited distinct dose-dependent reactions to sorafenib, highlighting the potential of cancer organoids to predict individual patients' sensitivity to targeted therapies. In addition, Lee *et al.,* (2018) found that the patient-derived bladder tumour organoids retained the key mutations present in the parental tumours and exhibited similar responses to therapy when compared to response *in vivo* (xenografts). These 3D culture systems provide a more physiologically relevant environment compared to traditional 2D monolayer cultures, enabling more accurate evaluations of drug efficacy and toxicity (Brancato *et al.,* 2020).

### 1.6.1 Spheroids and Organoids in Preclinical Drug Testing

There is a critical need for improved models to better understand and overcome TKI resistance. Traditional models often fail to capture the complex interactions within the tumour microenvironment and the nuanced mechanisms of resistance. This is where spheroids and organoids become invaluable. The high-throughput capabilities of spheroid models can facilitate rapid screening of various drug combinations, potentially accelerating the discovery of effective multi-drug regimens to enhance drug sensitivity but also limit the risk of the patient developing resistance. Moreover, 2D cultures when compared with 3D models tend to exhibit increased drug sensitivity in part due to their inability to maintain normal morphology and possess different cell surface receptor organisation, which differs

significantly from that in 3D cultures (Habanjar *et al.,* 2021). This limitation underscores the importance of using 3D models for more reliable predictions of therapeutic outcomes in preclinical studies, thereby advancing the development of effective treatments.

TKI resistance presents a significant challenge in the treatment of thyroid cancers, as it undermines the efficacy of these targeted therapies. The mechanisms by which tumours gain resistance to TKI are multifaceted and complex (Figure 1.12). The most common being, alterations in the drugs target binding sites facilitated though mutations, nullifying their ability to interact with their specific target receptor. Some tumour cells possess the ability to limit intracellular TKI concentrations via drug efflux mechanisms, such as overexpressing transport proteins that actively pump TKI molecules out of the cell, or sequestering the drugs in lysosomes, preventing them from reaching their targets.

The tumour microenvironment plays an important role in drug response by regulating signalling pathways, for instance it can provide additional growth signals to malignant cells whereas it can also create an immunosuppressive environment, hindering the function of immune cells in destroying cancer cells (Chen *et al.,* 2023). The TME actively adapts to changes in its surroundings and can respond to those disruptions accordingly, in the absence of oxygen, the tumour will switch to anaerobic glycolysis for energy production, allowing for the continuation of growth. This in turn allows for cells to undergo epithelial-to-mesenchymal transition (EMT), which enhances the cells' ability to survive and migrate (Chen *et al.,* 2022). These processes enable tumour cells to evade the effects of TKI and continue proliferating despite treatment.

Furthermore, unlike genetic mutations, which alter the DNA sequence itself, epigenetic changes involve modifications to the DNA or histones that affect gene expression without changing the underlying genetic code. Epigenetic changes within cancer cells have a crucial role in TKI resistance by modifying the expression of genes involved in drug metabolism, resistance mechanisms, and cellular stress responses, thereby influencing how effectively a TKI can combat tumour growth (Wajapeyee & Gupta, 2021).

In addition to TKI resistance, a prevalent issue associated with TKI is the occurrence of side effects, which can affect patient well-being and limit the effectiveness of treatment. Common

adverse effects of TKI include hypertension, gastrointestinal and hepatic disorders, dermatologic toxicities, kidney dysfunction, and interstitial lung diseases. Additionally, TKI can impair thyroid function, leading to conditions such as dysthyroidism, which includes both thyrotoxicosis and hypothyroidism (Basolo *et al.,* 2022). This further highlights the need for better screening models such as spheroids and organoids which allow for more detailed studies of drug efficacy and safety, including the impact of TKI on both tumour cells and normal tissues, ultimately guiding the development of more effective and less toxic treatment strategies.

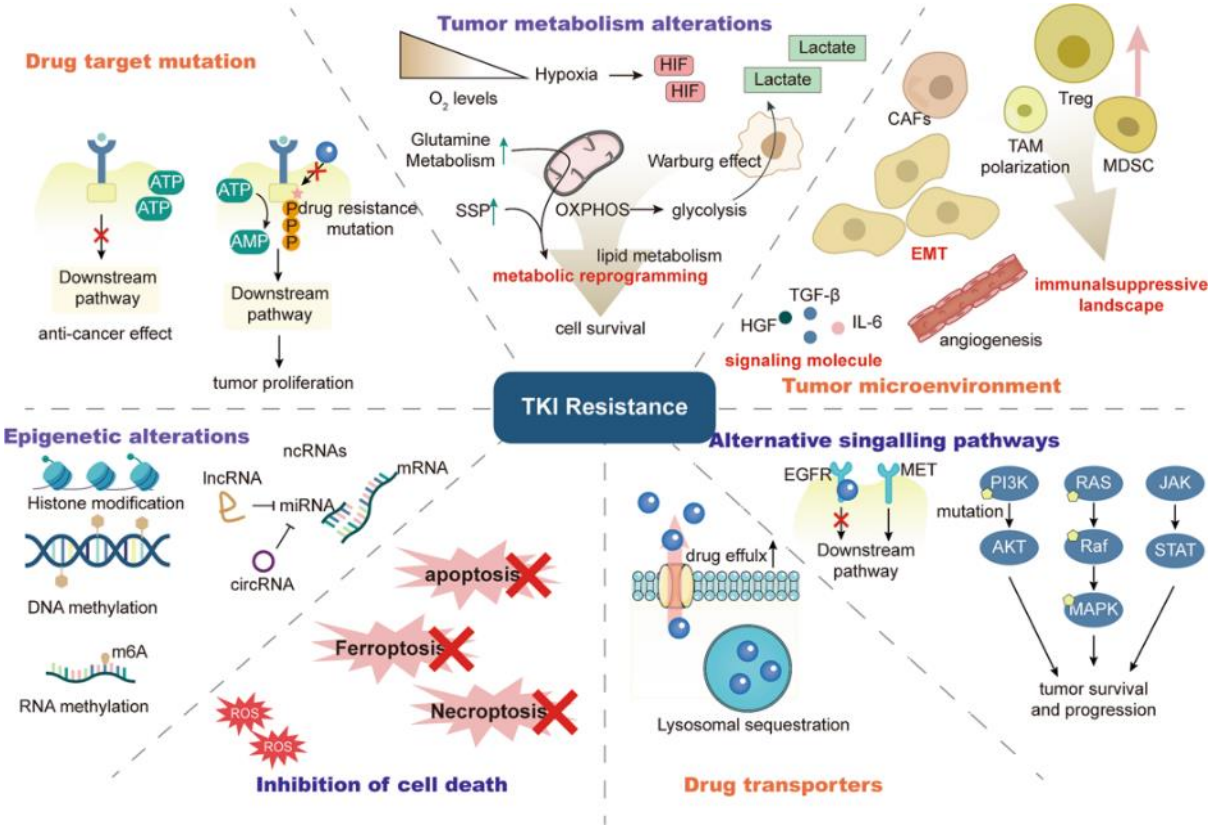


***Figure 1.12 Main mechanisms of tumour resistance to tyrosine kinase inhibitors (TKI).*** *Tumour cells can acquire resistance to TKI treatment through various processes; Target Binding Site Alterations - mutations in the drug's target binding site reduce the drug's ability to interact with its receptor, Drug Efflux Mechanisms - Tumour cells overexpress transport proteins that pump TKI out of the cell or sequester them in lysosomes, Tumour Microenvironment (TME) Adaptation - the TME can provide growth signals and create an immunosuppressive environment, influencing drug efficacy, Hypoxia-Induced Metabolic Shift - Tumours switch to glycolysis under low oxygen conditions, supporting continued growth and epithelial-to-mesenchymal transition (EMT), escaping the effects of the drug, Epigenetic Modifications - Changes in DNA or histones affect gene expression related to drug metabolism and resistance, influencing TKI effectiveness, and cell death inhibition – tumour cells can become unaffected by cell death pathways induced by the TKI including ferroptosis, autophagy, and apoptosis, resulting in survival and resistance (Yang et al., 2022).*

### 1.6.2 Microfluidics

Microfluidic devices represent a transformative technology in biomedical research, particularly in the realms of drug delivery systems and screening methodologies. These devices are particularly beneficial as some are capable of addressing the limitations associated with static 3D models, namely the lack of vascularisation and precise control over microenvironmental conditions, two components that are crucial in simulating how tumours *in vivo* may respond to treatment (Tevlek *et al.,* 2023).

Unlike static spheroids and organoids, which often struggle to replicate the complex dynamics of nutrient and oxygen gradients seen *in vivo*, microfluidic platforms integrate microchannels that simulate blood vessels and lymphatic systems (LeSavage *et al.,* 2021). This innovation enables researchers to mimic physiological conditions accurately by controlling flow rates, pH and temperature, to optimise drug delivery systems and enhance the biological relevance of their experiments (Damiati *et al.,* 2018). This is exemplified in a recent study whereby Riley *et al.,* (2019) successfully maintained viable human thyroid tissue explants for up to 96 h using a microfluidic device. They demonstrated that the device preserved tissue morphology, viability, and functionality of the tissue, enabling detailed investigations into TC mechanisms and therapeutic responses, thus advancing the promising development of personalised therapeutic approaches. Moreover, prolonged incubation times exceeding 28 days have been reported when utilising human liver and skin tissue. This extended incubation period is particularly significant for drug screening, as it adheres to the OECD guidelines for dermal sub-systemic repeated dose toxicity testing in animals, which mandate a 21–28 day exposure period (Wagner *et al.,* 2013). The ability to maintain tissue cultures for extended durations not only highlights the potential of these models as more ethically sound alternatives to animal use but also enhances their relevance as more physiologically accurate representations of human biology.

Additionally, microfluidic systems hold promise in transforming TC diagnostics by enabling sensitive and specific detection of biomarkers from small patient samples, such as blood or fine needle aspiration specimens (Bargahi *et al.,* 2022). These devices offer rapid and accurate analysis capabilities, potentially allowing for much earlier detection, disease monitoring, and

personalised treatment decision-making. Ultimately, the integration of microfluidic technology into TC research and diagnostics promises to advance both scientific understanding and clinical outcomes for patients. (Akgönüllü *et al.,* 2021). Overall, integrating 3D models with microfluidic devices which can simulate vascularization and microenvironmental conditions can yield more insightful responses to treatments and holds significant potential for preclinical drug research (Fritschen & Blaeser, 2021).

## 1.7 Thesis Aims

This project aims to develop and characterise robust *ex vivo* TC models using cancer cell lines (spheroids) and patient-derived tissue samples (organoids), evaluating the efficacy of sorafenib on these models as an exemplar of TKI therapy. Response of the models to treatment will be determined using image analysis following staining of both live and dead cells and biochemical assessments of cytotoxicity. Furthermore, the project explores the feasibility of maintaining and treating spheroid cultures within microfluidic chip devices, which help mimic *in vivo* scenarios even more closely. The main research objectives of the study are outlined as follows:

1. To establish a spheroid generation protocol using two distinct thyroid cancer cell lines (K1 - PTC and 8305c - ATC cell line), to determine optimal seeding densities and generation time.
2. To evaluate the efficacy of sorafenib on K1, 8305c and primary spheroids to observe how different tumour types respond to treatment, using $H_2O_2$ or $NaN_3$ as positive control reagents, establishing the optimal timing of treatment.
3. Comparing the potential of utilising (cell line) spheroid cultures within microfluidic chip devices for drug testing, to that in static culture.

# Chapter 2 Materials and Methods

## 2.1 Culture of thyroid cancer cell lines

Cells derived from a papillary thyroid carcinoma cell line (K1, ECACC 92030501) and undifferentiated human thyroid anaplastic carcinoma (8305c, ECACC 94090183) were purchased from the European Collection of Authenticated Cell Cultures (ECACC, Culture Collections UK Health Security Agency, Porton Down, Salisbury, UK). Cell lines were handled in a class II biological safety cabinet following the guidelines of the Advisory Committee on Dangerous Pathogens (ACDP), ensuring sterile conditions. Reserves of each cell line were stored in liquid nitrogen at a low passage number in 90% Foetal Bovine Serum (FBS; Labtech, Heathfield, UK) and 10% Dimethyl sulfoxide (DMSO; Thermo Fisher Scientific, Loughborough, UK).

The subculture protocol was based on the recommendations from the ECACC for each cell line. K1 cells were split 1:2 to 1:4, once they reached sub-confluence (70-80%), while 8305c were split 1:3 to 1:6. Both cell lines were cultured up to passage number of 50, at which point they were replaced with a lower passage number from the frozen stores. Both cell lines when split 1:4 took 3 days to reach 70% confluency, incubated at 37°C with 5% $CO_2$ in 75 $cm^2$ cell culture flasks (Sarstedt, Leicester, UK). After achieving optimal confluency, confirmed by light microscopy (10x magnification), the supernatant from the monolayer was disposed of into 1% Rely+On™ Virkon™, and the monolayer was washed with 5 mL of phosphate-buffered saline (PBS, Thermo Fisher Scientific).

For the detachment of cell monolayers, 2 mL of 1% Trypsin EDTA (TE, Thermo Fisher Scientific) was added into the 75 $cm^2$ flask, followed by incubation at 37°C, 5% $CO_2$ for approximately 10 min. After which the flask was firmly tapped using the palm of the hand to free any remaining cells. Then, 8 mL of appropriate medium was added to the flask, inhibiting the Trypsin and the cell suspension was centrifuged at 400 x *g* for 5 min, to pellet the cells. The supernatant was carefully decanted into Virkon without disturbing the cell pellet, which was then resuspended in 5 mL of medium using a serological pipette (Sarstedt) until fully dispersed. The appropriate volume of cell suspension was transferred into a new flask, topped with a suitable volume of

fresh medium (e.g., 1.5 mL in 18.5 mL medium for a 1:6 split). Flasks were checked daily using light microscopy, monitoring growth and signs of contamination.

### 2.1.1 Culture of K1 cell lines

K1 cells were cultured in a 2:1:1 mixture of Dulbecco's Modified Eagle's Medium (DMEM) with 4.5 g/L glucose, and L-glutamine (0.4 mM; GE healthcare, Yeovil, Somerset, UK), Ham's F-12 Nutrient Mixture (Fisher Scientific) and MCDB 105 Medium (Sigma-Aldrich, Gillingham, UK). Additionally, the final culture medium was supplemented with 1x Penicillin-Streptomycin solution (100 U/mL and 100 mg/mL respectively; Corning, Flintshire, UK) and 10% FBS (Labtech).

### 2.1.2 Culture of 8305c cell lines

The 8305c cells were cultured in Minimum Essential Medium (MEM; Fisher Scientific) including 2 mM Glutamine and initially supplemented with Hanks Balanced Salts (HBSS) in accordance with the suppliers' recommendations, however due to slow proliferation, medium containing Earles Balanced Salts (EBSS) was used as it produced the desired results after performing a comparative growth test. Medium was also supplemented with 10% FBS, 1x Penicillin-Streptomycin solution (as described previously) and 1% Non-Essential Amino Acids (NEAA, Fisher Scientific).

### 2.1.3 Cell counting with Trypan blue exclusion

Cell counting was performed utilising an improved Neubauer haemocytometer (Hawksley, Sussex, UK) under 10x magnification. Cell suspension (20 µL), formed from the trypsinisation of cells (section 2.1), was mixed with 20 µL Trypan Blue (Sigma-Aldrich, Gillingham, UK) in a 0.5 mL Eppendorf tube (Eppendorf, Hamburg, Germany). Subsequently, 20 µL of the resulting solution was transferred to both counting chambers of the haemocytometer. Only the viable (unstained) cells were counted within the two 1 mm x 1 mm squares of the haemocytometer grid (Figure 2.1). The total number of cells per mL were calculated by multiplying the average cell count by a factor of 2 to account for the trypan blue dilution, and then by 10,000 to adjust the volume to 1 mL.

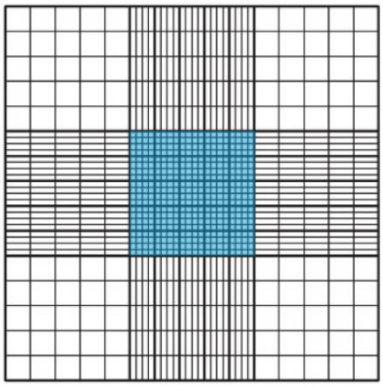

***Figure 2.1 Diagram of a haemocytometer grid with counted area highlighted blue.***

## 2.2 Spheroid generation

Spheroid optimisation and generation was aided through literature, which contained many conflicting propositions on the optimal seeding densities for each cell line. Therefore, to conduct optimisation tests, a range was formulated by compiling the densities obtained from these publications. For K1 investigations the range consisted of 1000, 10,000, 15,000 and 20,000 cells/well and for 8305c: 1000, 10,000, 20,000 and 30,000 cells/well were trialled.

Post trypsinisation, counting and resuspension (section 2.1 and 2.1.3), K1 and 8305c cells were seeded in 96-well ultra-low attachment plates (ULA, Corning) encouraging spheroid formation. Optimal seeding densities were established using results from the optimisation investigations (section 3.5 and 3.6). A 100 µL cell suspension comprised of the appropriate medium and cell density of K1 and 8305c cells was added to each well, excluding the outer ones, which sometimes suffer from medium evaporation. Spheroids were observed for a total of 13 days and imaged every 2 days after a 3 day incubation (3, 5, 7, 9, 11, and 13, section 3.3). Spheroids were allowed to grow and mature for three days, after which 100 µL of fresh medium was added to each well, this was repeated every three days whereby 100 µL of medium would be removed from each well, without disturbing the spheroid and replaced with 100 µL of fresh medium. The optimal time for treatment was optimised (section Chapter 4), once K1 and 8305c spheroids reached 5 and 7 days they were ready for experimentation with sorafenib. The resupply of fresh medium, with or without drug, every three days continued during investigations.

### 2.2.1 Generation of 1000 cells/well spheroids with and without Matrigel®

For the smaller spheroids (1000 cells/well), 1% Matrigel® (corning) was incorporated into the cell suspension based on the protocol supplied by our partner company CN-BIO, with the aim of providing additional support to cells aggregating into a 3 dimensional (3D) spherical structure. The inclusion of Matrigel® was compared to spheroids prepared without the hydrogel. Matrigel® was not needed for the generation of the larger spheroids. The preparation for the smaller spheroids required the process to be carried out on ice and prior to starting, the centrifuge was precooled down to 4°C and ULA plates were stored in a fridge.

Two aliquots of medium (both 8 mL) in a 50 mL falcon tube were labelled w/wo Matrigel® and placed on ice. To thaw the Matrigel®, an ice slush was created (ice with added water) with the Eppendorf containing Matrigel® placed into the slush. The precooling of the centrifuge and thawing of the Matrigel® would take around 30 min, once fluid, Matrigel® was placed on regular ice. Then, 80 µL of medium was removed from the labelled falcon tube (w Matrigel®) and replaced with 80 µL of Matrigel® (1%) and mixed thoroughly by vortexing for 20 sec and returning it to the ice. Cell detachment was carried out (section 2.1), the cells were counted (section 2.1.3) and the appropriate volume of cell suspension was added to the prepared Matrigel® and the tube without Matrigel®, to provide 5000 cells/mL. Rapidly, but carefully, 200 µL of the mixture (1000 cells) were dispensed into each well using a multichannel pipette. The plates with and without Matrigel® were immediately transferred for centrifugation at 300 x *g* for 5 min. For these smaller spheroids, frequent changes of medium were not necessary and only required supplementation with fresh medium after 10-14 days.

### 2.2.2 Measuring spheroids

In order to determine the optimal age of spheroids for use in testing, light microscope (10x) images were taken on days 3, 5, 7, 9, 11 and 13 to enable measurement of the diameter of each spheroid. The software ImageJ (v1.53t, https://imagej.net/) was used to measure the vertical and horizontal diameters of the spheroids allowing for an average size to be established throughout its growth span (Figure 2.2).

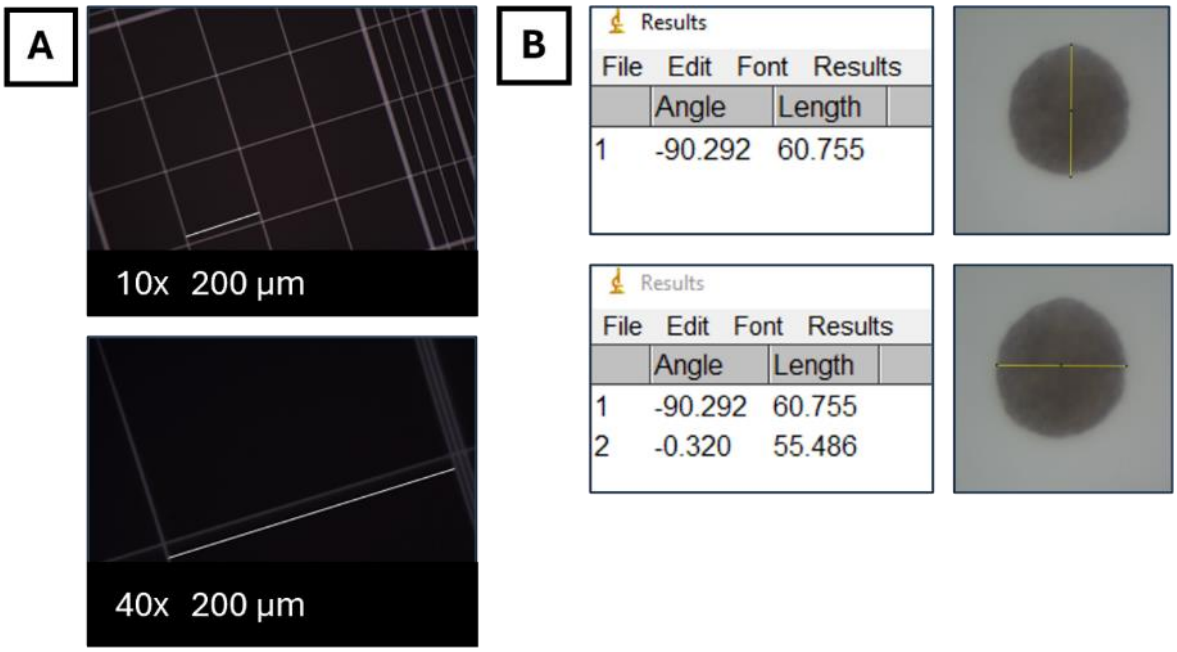


***Figure 2.2 Measuring spheroids using the software ImageJ.*** *A – images of a haematocytometer with measurements of the length of a single small square for calibration of the measuring tool. B – using the known length on the haemocytometer, measurements of the vertical and horizontal planes of the spheroids were taken in µm to calculate the average diameter.*

## 2.3 Inducing Cell Death with $H_2O_2$, $NaN_3$, and TKI in Spheroids

The study aimed to determine whether cell death occurred in spheroids as a result of the natural aging process or due to the cytotoxic effects of the TKI. To achieve this, spheroids were treated with hydrogen peroxide ($H_2O_2$) and sodium azide ($NaN_3$) to induce cell death and assess their response to these cytotoxic agents. Thereby, establishing a baseline for cell death and identifying the optimal age of spheroids for further experimentation with the TKI.

$H_2O_2$ was initially chosen for its common use in cell research as a cytotoxic agent, but it primarily affected only the outer cell layers of the spheroids, even with extended incubation from 24 to 48 h. As a result, $NaN_3$ was adopted as the primary cytotoxic agent for the cell death assay investigations. Initially, viability was assessed using the MTS assay (section 2.3.3), but later replaced by the 3D Cell Titre Glo Assay™ (section 2.3.4).

Due to limited structural integrity and sample scarcity, organoid viability optimisations were confined to growth assessments, and only primary spheroids were treated with TKI.

### 2.3.1 Inducing cell death using $H_2O_2$

For the $H_2O_2$ investigations, two 96-well ULA plates were populated with 20,000 K1 cells per well and cultured for a total of 13 days, with tests performed on the spheroids on days 3, 5, 7, 9, 11 and 13. The control spheroids, located in the top half of the inner wells (Figure 2.3) did not undergo any treatment except for medium exchange, (section 2.2). In contrast, the spheroids in the bottom half of the plate received treatment 24 h before the assessment day. For instance, analysis on day 3 meant that spheroids were treated with $H_2O_2$ on day 2. Due to the insufficient death of cells observed in treated spheroids, the incubation period for the treatment was then extended to 48 h, meaning that for day 3 analysis, spheroids were treated following 1 day of generation.

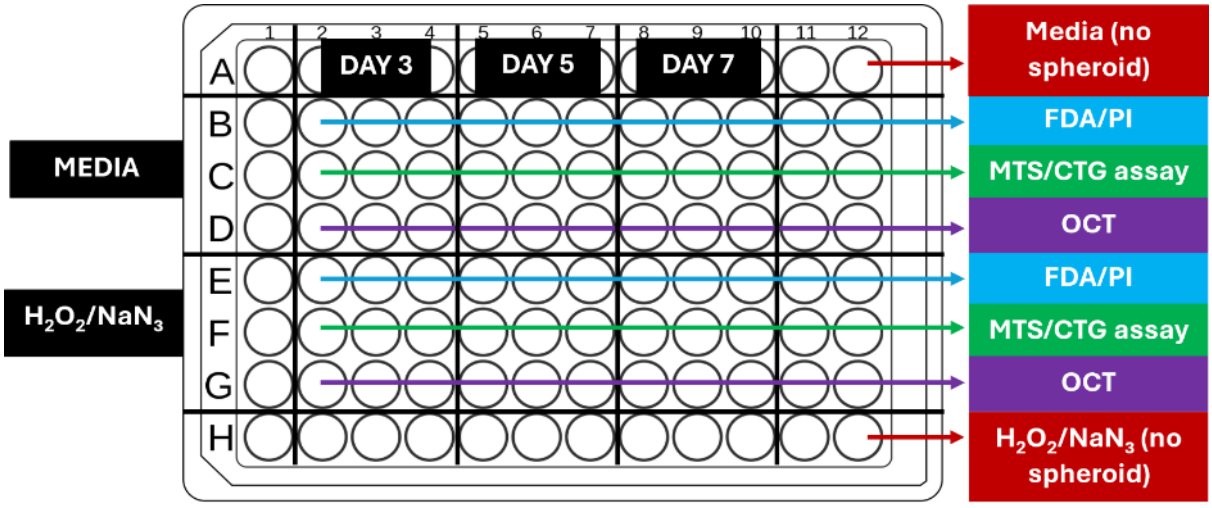


***Figure 2.3 Plate setup for cell viability investigations with $H_2O_2$ or $NaN_3$.*** *Top half of the plate only received a fresh medium exchange, bottom half was treated with either $H_2O_2$ or $NaN_3$. Nine control and 9 treated spheroids for each designated assay day, 3 for each assay. Two additional controls containing no spheroids in the corner wells of the plate consisting of either medium or the $H_2O_2$/$NaN_3$ mixture. Another plate for days 9, 11 and 13 was also set up at the same time.*

The treatment procedure was performed as follows; 10 mL of fresh K1 medium was combined with 8 µL of 30% $H_2O_2$ for a final concentration of 1.6 mM (established in section 4.1.1). The spheroids designated for treatment had as much of their medium removed which was replaced with 200 µL of the $H_2O_2$ mixture, whereas the control spheroids simply had a fresh medium change. Two additional control wells were established: one containing 200 µL of fresh K1 medium and the other, 200 µL of the $H_2O_2$ mixture, both wells lacked any spheroids and served as negative controls.

### 2.3.2 Inducing cell death using $NaN_3$

Cells were similarly set up as in section 2.3.1 with two 96-well ULA plates populated with either 20,000 K1 cells /well or 10,000 cells/well (two plates for each cell line) and cultured for a total of 13 days, with tests performed on the spheroids on days 3, 5, 7, 9, 11 and 13. Treatment with $NaN_3$ was prepared by adding 195 µL of 10% $NaN_3$ to 10 mL of the appropriate medium for a final concentration of 30 mM (established in section 4.1.2). Both the $H_2O_2$ and $NaN_3$ mixtures were made up fresh for each treatment day. Additionally, single repeats for both cell lines were conducted at a seeding density of 1000 cells per well (with 1% Matrigel®). The culture and plating of these cells followed the protocol outlined in section 2.2.1. Both the larger and smaller sized spheroids were imaged using light microscopy for growth analysis. Following treatment, the spheroids were assessed for viability using either the MTS, CTG assay, or by fluorescent microscopy of live/dead cells (sections 2.3.3, 2.3.4, and 2.3.5 respectively). Spheroids were also placed into optimum cutting temperature medium (OCT, Tissue Tek; Fisher Scientific) and frozen for immunohistochemical analysis of cell death/proliferation markers.

### 2.3.3 MTS assay

The CellTiter 96® Aqueous One Solution Cell Proliferation Assay (Promega, Southampton, UK) assay is a colorimetric method used to determine cell viability by detecting the coloured soluble formazan product formed during the reduction of tetrazolium compound (3-(4,5-dimethylthiazol-2-yl)-5-(3-carboxymethoxyphenyl)-2-(4-sulfophenyl)-2H-tetrazolium) by the viable cells (Figure 2.4). When spheroids had reached their 24/48 h of incubation with either $H_2O_2$ or $NaN_3$, they were transferred into a new 96-well flat bottom plate. MTS reagent was

thawed at room temperature for approximately 30 min before adding 20 µL to each well containing 200 µL of medium including the spheroid. The plate was incubated for 4 h at 37°C, 5% $CO_2$. The absorbance was measured and recorded at 492 nm using a Multiskan™ FC Microplate Photometer (Thermo Fisher). A bar chart was constructed with the average absorbances from the triplicate wells.

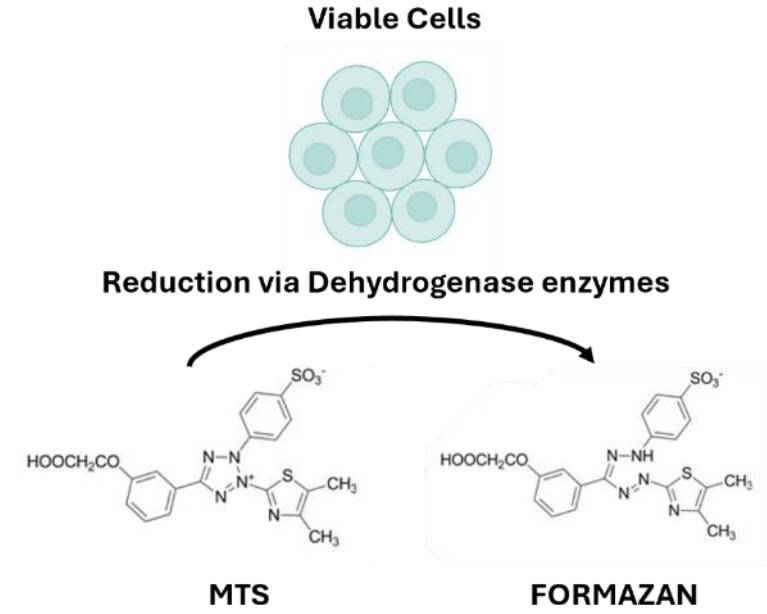


***Figure 2.4 Reduction reaction of MTS into Formazan product by viable cells.*** *Schematic created using Biorender and images adapted from Riss et al., (2004).*

## 2.3.4 CellTiter-Glo® (CTG) 3D Cell Viability Assay

The CellTiter-Glo® 3D Cell Viability Assay (CTG; Promega) is a single-step method used to determine cell viability by measuring the quantity of ATP present in the 3D culture. This involves lysis of the cells in the spheroid and subsequent measurement of the ATP released (Figure 2.5) which allows for a more sensitive approach to assessing 3D models compared to traditional assays (Giczewska *et al.,* 2023). The CTG reagent was thawed at room temperature for approximately 30 min prior to starting. Firstly, only 100 µL of the culture medium including the spheroids, which had reached their 24/48 h of incubation with either $NaN_3$ or sorafenib were transferred into an opaque-white walled 96 well plate (Thermo Fisher). The reagent and

the sample were equilibrated to room temperature (~21–25°C) before an equal volume of the CTG reagent (100 µL) was added to each well. The plate was placed onto a plate shaker for 5 min at 1200 rpm to induce cell lysis. The plate was then incubated for 25 min at room temperature. The luminescence generated from the reaction was measured and recorded using a luminometer (Luminoskan®, Thermo Fisher). A bar graph was constructed with the average of the triplicate readings for each treatment.

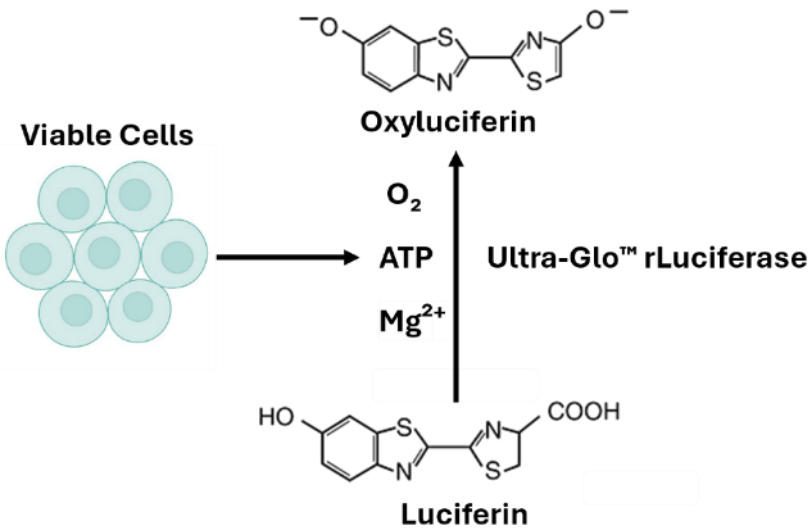


***Figure 2.5 Reaction of CellTiter-Glo® 3D lytic reagent forming a luminescent product of Firefly Luciferase by supply of ATP by viable cells.*** *Schematic created using Biorender and images adapted from Reproducible drug screening assays using single organoids (2023).*

## 2.3.5 Fluorescence microscopy

### 2.3.5.1 Fluorescein diacetate (FDA)/Propidium Iodide (PI) staining Principle

Fluorescein diacetate (FDA) is a non-fluorescent compound which easily penetrates the cell membrane of viable cells and undergoes hydrolysis by nonspecific esterase's, present in live cells, resulting in the production of a fluorescein molecule that fluoresces green. In contrast, propidium iodide (PI) is a cell membrane impermeable molecule which fluoresces a red colour when intercalated with DNA. This only occurs in dead or damaged cells where the membrane is compromised allowing the PI access to the nucleus. Cells with a healthy cell membrane are stained green by FDA signifying that these cells are alive, on the other hand dead cells are stained red by PI (Xiao *et al.,* 2011).

#### 2.3.5.2 FDA/PI Staining protocol

Fluorescence microscopy was utilised to characterise and visualise cell viability and cell death in spheroids post treatment. Three spheroids post treatment with $H_2O_2$, $NaN_3$ and sorafenib, as described in section 2.3, were transferred from their ULA plates into a µ-Slide 8 Well plate (Corning), and as much of the medium as possible was aspirated without disturbing the spheroids. The wells were then washed with 200 µL fridge-cold PBS and all liquid was removed before the FDA-PI staining solution was added [3.2 µL FDA (5 mg/mL), 20 µL PI (2 mg/mL) and 4 mL PBS was prepared and 200 µL added to each well] and incubated for 5 min at room temperature in the dark. As much of the staining solution was removed and each well was washed three times with 200 µL of fresh PBS. The plate was wrapped with aluminium foil and transported to the microscope suite avoiding light exposure. The spheroids were imaged immediately after the staining procedure was complete, using an epifluorescence microscope (Zeiss, Germany), with pre-set filters for FDA (495 nm excitation, 517 nm emission) and PI (596 nm excitation, 614 nm emission).

#### 2.3.5.3 Confocal microscopy

To confirm whether $NaN_3$ was truly penetrating the spheroid a confocal microscopy test was also conducted in a 96-well ULA plate (section 4.5.1). The spheroids treated with $NaN_3$ had their medium removed and replaced with 100 µL of Hoechst 33342 Solution (20 mM, Thermo Fisher), prepared by adding 6 µL Hoechst 33342 to 5 mL of medium. The spheroids were incubated overnight with the stain at 37°C, 5% $CO_2$. On imaging day, the medium was removed, spheroids were transferred into a µ-Slide 8 Well plate and washed with PBS three times. A Z-stack image was captured using an LSM 980 confocal microscope (Zeiss).

### 2.3.6 OCT embedding and Cryostat sectioning

For the immunohistochemistry (IHC) investigations 6 spheroids (e.g. 6 spheroids from day 3; 3 from the control and 3 from the treated, section 2.3), were transferred into labelled plastic embedding moulds (Fisher Scientific) using a 1000 µL blue tip following the treatment experiment. Spheroids were allowed to settle to the bottom of the mould and using a 200 µL yellow pipette tip, as much medium as possible was removed. Spheroids were washed with 200 µL of PBS before 200 µL of erythrosine B (Sigma; 40 µL 1% + 1 mL PBS) was added for 5

min at room temperature, to stain the spheroid in order to aid visualisation in the OCT. The stain was removed, and the spheroids were washed with PBS followed by the removal of as much of the solution as possible. OCT was added using a plastic Pasteur pipette, starting at the edges to encourage the spheroids into the centre of the mould. The mould was subsequently transferred to a -80°C freezer and allowed to solidify.

The spheroids were then sectioned at 8 µm, using a cryotome (Leica Biosystems, Wetzlar, Germany). Prior to collecting the frozen OCT sample, the cryotome was precooled to -20°C. A small amount of OCT was applied to a chuck and attached to the open-ended side of the mould and allowed to solidify within the cooled cryotome. Once solid, the sample was pressed out of the mould and the chuck was secured into the holder. The samples were cut into 8 µm sections and carefully recovered onto Starfrost™ glass slides (Scientific Laboratory Supplies, Nottingham, UK). Three slides, with at least four sliced sections on each were collected for each sample, placed into a slide storage container and stored in a -20°C freezer prior to IHC. Only the spheroids treated with $H_2O_2$ and $NaN_3$ were analysed via IHC (section 2.3.7), as the surplus of spheroids allowed for additional analyses for these optimisation experiments.

### 2.3.7 Immunohistochemistry (IHC; Ki67)

Prior to starting the IHC procedure, the fixative (100% methanol) was pre-cooled to -20°C for at least 30 min. The frozen section slides obtained from the cryotome (section 2.3.6) were allowed to warm to room temperature for 5 min and labelled with a pencil.

The slides were sorted into a staining rack and placed into a glass container filled with the pre-cooled methanol fixative for 10 min, ensuring the slides were completely submerged. All sections were rinsed in Tris Buffered Saline (TBS, appendix 1.1) for 5 min, before endogenous peroxidase activity was blocked by placing the rack of slides into a glass staining jar containing 400 mL methanol and 40 mL 30% $H_2O_2$ (Sigma; 3% final concentration) for 15 min. The slides were rinsed in tap water and assembled into a Sequenza™ rack by first dipping the cover plate in TBS, placing the section face to the cover plate and clicking the slide into position. Using fresh TBS, the sections were washed 3 times. A blocking serum was prepared by adding 1 drop of horse serum (provided in the Vectorstain Elite kit, 2B scientific, Kirtlington, UK #PK-6200)

into a mixing bottle containing 5 mL of TBS. Sections were incubated for 20 min with diluted blocking serum and immediately after, 3 drops of Avidin D solution were added to each section and incubated for 15 min, before rinsing with TBS 3 times. Three drops of Biotin solution were then added to each slide and incubated for 15 min, before being rinsed a further 3 times with TBS. This was done to block any nonspecific binding of the avidin/biotin system reagents. Once all the blocking steps had been completed, 100 µL of diluted primary antibody Ki67 (MIB-1 clone; 2B Scientific, diluted in TBS 1:100) was added to all sections except for the negative control, to which 100 µL of isotype control, IgG1 (Insight Biotechnology, Wembley, UK), 1:100 in TBS was added. A cover was placed on the Sequenza™ rack and incubated at 4°C overnight.

The slides were rinsed again with TBS 3 times, before diluted secondary antibody (provided with the Vectorstain Elite universal kit) was prepared; 2 drops (100 µL) of normal blocking serum was added to 5 mL TBS in a mixing bottle followed by 2 drops of biotinylated horse antibody stock. The antibody solution was applied to the sections evenly (100 µL/slide) and incubated for 30 min. During the incubation, Vectorstain Elite, ABC reagent (Supplied with the kit) was prepared (2 drops reagent A and 2 drops of reagent B added to 5 mL TBS in a mixing bottle) and allowed to stand for 30 min before use. Following secondary antibody incubation, slides where rinsed 3 times with TBS before ABC reagent was added to all slides and incubated for a further 30 min. Following further washes slides were transferred into a slide rack and placed into a pot of tap water. SIGMAFAST™ 3,3'-Diaminobenzidine (DAB; Sigma) solution was prepared by adding 1 gold tablet of DAB and one silver tablet of $H_2O_2$ to 1 ml of $dH_2O$ and mixed using a vortex until both tablets were completely dissolved. The sections were removed from the tap water and a circle was drawn around them using an isolator pen. The sections were placed on a staining rack and 100 µL of the DAB solution was applied to each section for 5 min. The slides were then placed back into a slide rack and rinsed under running tap water for 2 min. The sections were counterstained by placing them into a jar containing Harris Haematoxylin (filtered prior to use; Sigma) for 20 sec and then immediately rinsed under running tap water.

Sections were dehydrated through a series of graded alcohols (70%, 90%, 100% ethanol) for 2 min each, then 3 changes of Histoclear II (Scientific Laboratory Supplies), 2 min each. The sections were then mounted with a glass coverslip using Pertex® mounting medium (Cell Path, Newtown Powys, UK). Once fully dry the staining was visualised using light microscopy to determine positivity.

### 2.3.8 Spheroid treatment with sorafenib

Sorafenib (Signalchem Biotech, Richmond, British Columbia, Canada),was selected as the cytotoxic agent for this study, representing a prevalent targeted therapy administered to patients afflicted with various cancers, including those with radioactive iodine-resistant thyroid carcinomas (Fullmer *et al.,* 2021; section 1.5.2).

The initial optimisation employed a serial dilution starting at 200 µM down to 25 µM. This range was based on previous work done at the University involving TKI treatment on monolayers and literature that had used K1 and 8305c cell lines and treated them with sorafenib (more details in section 5.1). Subsequently, due to the observed significant cytotoxic effects at each concentration, the highest concentration was set at 100 µM and the range was extended to encompass lower concentrations down to 3.13 µM. Based on the data obtained from the spheroid viability assessments, it was determined that the optimal duration for experimentation ranged from 7 to 9 days, during which the spheroids exhibited peak viability (section 4.7.4). A noticeable decline in viability was typically observed after 11 days. Consequently, spheroids were cultured for 5 or 7 days prior to the initiation of 48 h treatment with sorafenib. During treatment, the agent was replenished every 24 h to simulate a clinical environment, mirroring the oral intake of the drug by patients.

#### 2.3.8.1 Sorafenib dose optimisation

Sorafenib was obtained in powdered form and 10 mg was resuspended in 1 mL of DMSO, to give a final concentration of 21,500 µM. Aliquots of 50 µL were generated from this 1 mL solution and stored at -20°C. K1 spheroids were generated by plating 20,000 cells/well in a ULA plate (section 2.1 and Figure 2.6) and allowed to proliferate for 5 days, maintaining regular medium changes every 3 days.

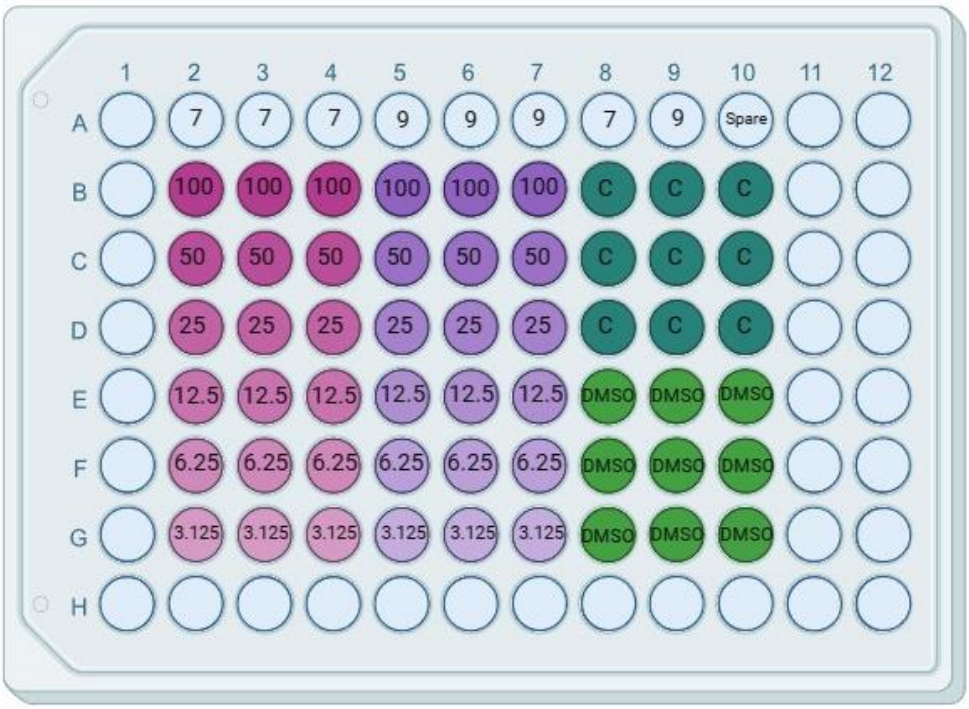


***Figure 2.6 ULA Plate Setup for sorafenib Treatment of 5/7 Day-Old Spheroids.*** *Wells in the columns labelled '7,' contained 5-day-old spheroids treated with sorafenib, with treatment replenished after 24 h. Analysis was conducted once the spheroids reached 7 days of maturity. The same protocol was applied for day 9 spheroids, which were 7 days old at the commencement of treatment. The numerical values assigned to wells, such as '100,' indicate the concentration (µM) of sorafenib added to the respective well. C: control well, medium only. DMSO: dimethyl sulfoxide, diluted to match the highest concentration of sorafenib [1% (v/v)].*

A frozen 50 µL aliquot of sorafenib was thawed at room temperature, and a stock concentration of 200 µM was prepared by adding 27.9 µL of sorafenib (21.5 mM) to 2972.1 µL of K1 medium, under sterile conditions. Prior to serial dilution, the 200 µM stock was filtered. Three vials were labelled with concentrations of 25, 50, and 100 µM, and 800 µL of medium was added to each. The dilution process involved adding 800 µL of the 200 stock to the 100 µM labelled bottle, followed by thorough mixing via pipetting the solution up and down. Then, 800 µL of this solution was transferred to the 50 µM labelled bottle, and the process was repeated until the 25 µM labelled bottle reached a final volume of 1600 µL (Figure 2.7). Two additional vials were prepared: one containing 800 µL of fresh medium and another containing 27.9 µL of DMSO in 2972.1 µL of K1 medium, matching the top concentration of sorafenib. This step ensured that observed cytotoxic effects were attributed to the agent rather than the solvent used for dilution.

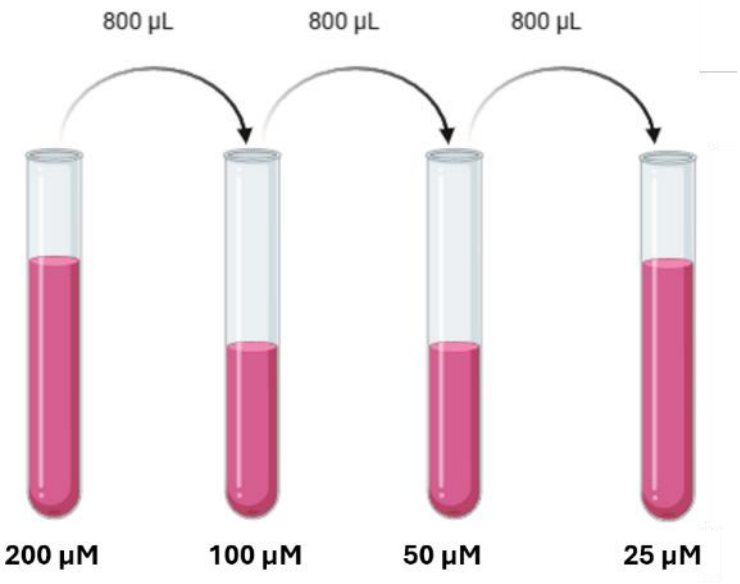


***Figure 2.7 Serial dilution of sorafenib for use in spheroid treatment (static/on-chip).***

#### 2.3.8.2 Sorafenib optimisation - spheroid treatment

Once K1 spheroids seeded at 20,000 cells/well on a ULA plate, reached either 5-day or 7-day maturity, medium was removed from the wells. The prepared serially diluted concentrations (starting with 200 µM) of sorafenib were added to appropriate wells (100 µL/well), and medium only or DMSO containing medium was added to the control wells (Figure 2.6). The plate was incubated at 37°C with 5% $CO_2$ for 24 h before replenishment of sorafenib.

After the initial 24 h incubation period, the treated wells underwent complete sorafenib/medium removal without disturbing the spheroids. A fresh batch of sorafenib was then prepared following the procedure outlined in section 2.3.8.1 and added to appropriate wells. This process ensured the continuous exposure of spheroids to sorafenib, which has a half-life of approximately 25 h (Huh *et al.,* 2021). The plate was once again incubated at 37°C with 5% $CO_2$, for a further 24 h. The spheroids were carefully transferred to an opaque-white walled plate, and a CTG assay was conducted (section 2.3.4). CTG values obtained from both sets of spheroids (5-day-old and 7-day-old) were compiled in Microsoft Excel for subsequent analysis and interpretation in GraphPad (v9.5.1).

#### 2.3.8.3 Subsequent sorafenib treatment of K1 and 8305c spheroids

Following optimisation using the 20,000 cells/well K1 spheroids, further experiments were performed using K1 spheroids generated from 1,000 cells/well (grown with 1% Matrigel®) and 20,000 cells/well. The same was true for the 8305c cells except these were seeded at 1,000 (w/ 1% Matrigel®) and 10,000 cells/well seeded in ULA plates. A top concentration of 100 µM sorafenib was used with doubling dilutions down to 3.13 µM. The sorafenib treatment investigations for each cell line and seeding density was repeated three times, meaning 6 sets of data sets for each cell line. The appropriate medium was used based on the cell line. In addition, a supplementary plate was also prepared exclusively for staining the spheroids with FDA/PI and subsequent imaging using fluorescent microscopy (section 2.3.5).

## 2.4 Acquisition of thyroid biopsies from patients

Thyroid tissue samples (n = 7 malignant; n = 4 benign; Table 2.1) were obtained from patients scheduled for various thyroid resection operations following written informed consent. The research ethics committee that approved this project was North East-Newcastle & North Tyneside (15/NE/0412) and Hull and East Yorkshire NHS Trust R&D (R1925).

***Table 2.1 Sample types obtained from patients undergoing thyroidectomy.***

| No. | Tissue Type | Patient age range (years) | Tissue Received |
|---|---|---|---|
| **1** | Follicular adenoma | 60-70 | B |
| **2** | Papillary carcinoma (Follicular variant) | 60-70 | B+C |
| **3** | Papillary carcinoma (PT3 N1B) | 20-30 | C |
| **4** | Papillary carcinoma (PT3a) | 70-80 | C |
| **5** | Benign | 70-80 | B |
| **6** | Follicular adenoma | 30-40 | B |
| **7** | Papillary carcinoma (micro) | 70-80 | C |
| **8** | Papillary carcinoma (micro) | 50-60 | C |
| **9** | Medullary Carcinoma (PT3a N1B R1) | 70-80 | C |
| **10** | Papillary carcinoma | 20-30 | C |

**B –** Benign

**C –** Cancer

### 2.4.1 Dissociation of thyroid tissue into single cells

The biopsy sample acquired from the operating theatres at Castle Hill Hospital was transported to the laboratory in complete medium (K1 medium as described in section 2.1.1 but exosome-depleted). It was then immediately transferred onto a petri dish containing 1 mL of medium and mechanically dissociated via mincing, using two scalpels in a criss cross action, non-uniformly until the sample resembled a gel-like consistency.

The digestion mixture was prepared by adding 100 µL of DNase (10 mg/mL stock, SLS/Sigma, Dorset, UK) and 130 µL of Collagenase IV (10 mg/mL stock, SLS/Sigma) to 5 mL of complete medium, in a 50 mL universal tube and the minced sample was transferred using a 25 mL stripette into the digestion mix. The 50 mL tube was then placed onto a tube rotator (MACSmix™, Miltenyi Biotech, Woking, UK) for 2 h on constant rotation at 37°C.

After incubation, the sample was triturated using a 25 mL serological stripette and then a 10 mL stripette, to disperse any clumps that remained. Using a 10 mL stripette the sample was passed through a 70 µm cell strainer (Falcon/VWR, Lutterworth, UK), into a 50 mL falcon tube, removing larger clumps of cells.

The dispersed sample was centrifuged for 5 min at 400 x *g*, to pellet the cells, the supernatant was decanted into 2% Virkon solution, leaving the cell pellet behind. A red blood cell lysis solution was prepared by adding 500 µL of FACS lyse (BD Biosciences, Wokingham, UK) to 4.5 mL $dH_2O$ and sterilised through a 0.2 µm filter. The cell pellet was resuspended by adding the full 5 mL of the FACS lyse solution followed by incubation for 10 min at room temperature. The solution was centrifuged at *400 x g* for 5 min to pellet the cells. The supernatant was removed, and the cell pellet was resuspended in the residual medium before adding 5 mL of complete medium.

A cell count was performed with trypan blue exclusion (section 2.1.3). The cell concentration was calculated, and the cell suspension was diluted in the appropriate amount of complete medium to generate a cell concentration relevant for either organoid or spheroid generation (section 2.4.2 and 2.4.3, respectively).

## 2.4.2 Generation of thyroid organoids

### 2.4.2.1 Organoids using Matrigel®

Initially Matrigel® (10 mg/mL) was used in an attempt to generate thyroid organoids following the manufacturers protocol for 3D culture. The following steps were performed on ice and prior to starting, the 24-well plate and pipette tips were stored in a cold room (4°C). Matrigel® was thawed on ice during cell preparation. Firstly, 200 µL of Matrigel® was added into the 8 central wells (Figure 2.8) and incubated for 30 min at 37°C, to allow the Matrigel® to polymerise into a matrix. After which, 250 µL of cell suspension (section 2.4.1) at 300,000 cells/mL was added into the 8 central wells and incubated again for 30 min at 37°C. Finally, 250 µL of Matrigel® matrix medium (0.5 mL of Matrigel® and 4.5 mL of complete medium) was added to the 8 central wells. The plate was incubated at 37°C, 5% $CO_2$ and 0.5 mL medium was replaced with 0.5 mL of fresh complete medium every three days. In addition, the plate was imaged using light microscopy every 2-3 days, monitoring the growth of the organoids, noting any formation of organoid structures.

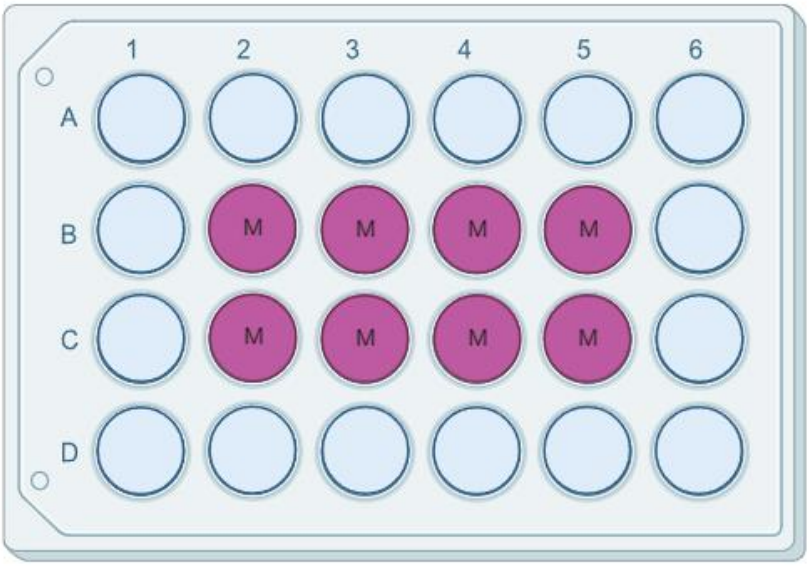


***Figure 2.8 24-Well Plate Setup for Organoid Generation with Matrigel®. M - wells consisting of Matrigel®-Cell mixture.*** *Outer wells did not contain any cells to avoid medium evaporation.*

#### 2.4.2.2 Organoids using Vitrogel®

During the MSc project there was a shortage of Matrigel®, therefore an alternative was sought. Four distinct Vitrogel® (Thewell Bioscience, North Brunswick, NJ, USA) samples from the VitroGel® ORGANOID Discovery Kit (Cat# VHM04-K) differing in formulations (specifications not revealed by manufacturer) were trialled.

Following the manufacturers protocol for 3D culture , the Vitrogel® samples were brought to room temperature and 400 µL of cell suspension (section 2.4.1) at 800,000 cells/ml was prepared. Vitrogel® 1 (150 µL) was added into a 1 mL Eppendorf along with 75 µL of the cell suspension. Once properly mixed, 50 µL was added into four wells (avoiding the outer ones) of a 96-well flat bottom plate (Figure 2.9*)*. This was repeated for the remaining three Vitrogel® samples consecutively so as to ensure the Vitrogel® did not harden prior to addition into the wells. The plate was incubated at 37°C, 5% $CO_2$ and 50 µL of medium was removed carefully so as to not disrupt the hydrogel and replaced with 50 µL of fresh complete medium, every three days. Initially, regular complete medium was used, however due to slow/little growth, a 50 mL falcon tube containing 50 mL of complete medium was supplemented with 63.3 µL of Thyroid Stimulating Hormone (2 mIU/L) and 0.7 µL of sodium iodide (NaI, 0.1µL/ml) subsequently used for the remaining organoid investigations.

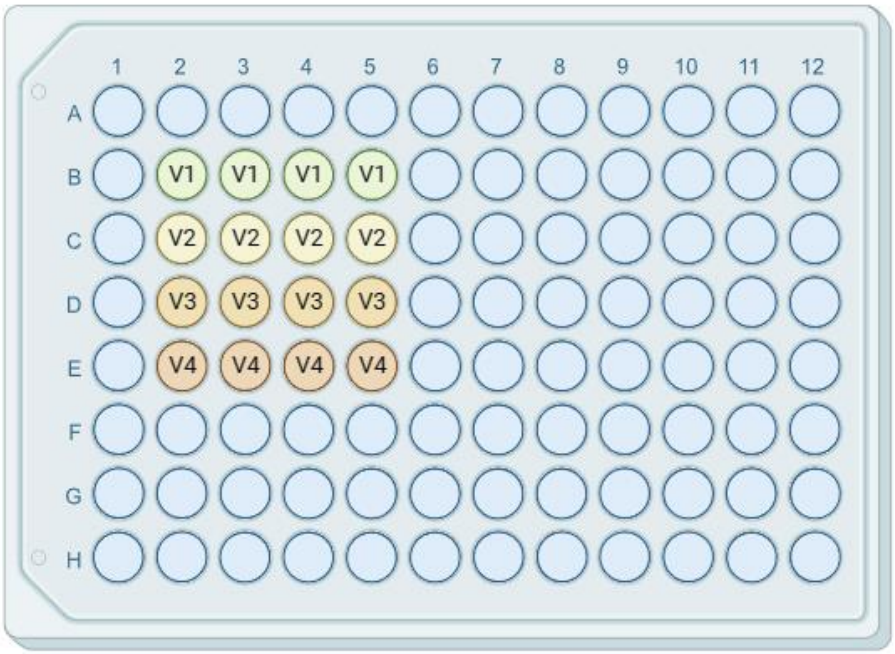


***Figure 2.9 96-Well flat-bottom plate Setup for Organoid Generation with Vitrogel®.*** *V followed by a number denotes the presence of a Vitrogel-Cell mixture and which Vitrogel® sample was used.*

#### 2.4.2.3 Vitrogel® recovery

The Vitrogel® cell recovery solution (provided with the kit), was placed in an incubator to bring it to 37°C. Medium covering the top of the hydrogel was removed from the wells that were chosen for testing, and the organoids were subsequently washed with PBS twice. Warm Vitrogel® recovery solution (200 µL), was added to the appropriate wells and gently using a 1000 µL pipette with a blue tip, the hydrogel was broken down into smaller pieces by gently pipetting the solution up and down. The plate was incubated at 37°C for 10 minutes to ensure the hydrogel had detached form the walls of the well. A further 700 µL of warm recovery solution was added to a 1 mL microfuge tube and the 200 µL cell-recovery solution mixture was transferred from the wells to their respective microfuge tube. The wells were washed with 100 µL of recovery solution and this was added to the appropriate microfuge tube. Using a 1000 µL pipette the solution within the microfuge tube was pipetted up and down 3-5 times and then placed into the 37°C incubator for 5 min, this mix and incubate cycle was repeated 3 times. The cell solution was then centrifuged at 400 x *g* for 5 min. The supernatant was

decanted, and the cell pellet was resuspended in 200 µL of PBS. The recovered solution was then ready for Cytospin investigations (section 2.4.2.4).

#### 2.4.2.4 Cytospin of primary tumour organoids

The four different Vitrogel® 1 mL samples containing tumour organoids post Vitrogel® recovery (section 2.4.2.3) were centrifuged at 400 x *g* for 3 min, forming a cell pellet. As much of the solution was removed without disturbing the cell pellet and 200 µL of the FDA/PI staining solution was added (section 2.3.5.2), this was repeated for all four samples. The samples were incubated for 5 min at room temperature in the dark and centrifuged again at 400 x *g* for 5 min. The solution was again carefully removed without interfering with the cell pellet, before resuspension in 200 µL of PBS.

Prior to Cytocentrifugation the cell suspension, 100 µL of PBS was added to each Cytospin funnel and centrifuged at 1500 rpm for 3 min to wet the filter paper. Then, 100 µL of the recovered cell suspension/organoids was added to each Cytospin funnel and the Cytocentrifugation process was repeated. The slides were air dried for 10 min before the application of a droplet of Vectashield® mounting medium containing the DNA binding dye 4',6-diamidino-2-phenylindole (DAPI), which acts as a blue nuclear counterstain. A coverslip was placed on top of the section and the samples viewed under a fluorescent microscope using the same protocol and settings as described previously (section 2.3.5).

### 2.4.3 Generation of primary thyroid spheroids

For comparison, the remaining cells, from the tissue dispersal, were used to attempt to generate primary spheroids. The dispersed cell suspension (varying in range from 300,000 - 1,800,000 cells/mL depending on the tissue) was added to the wells (100 µL) of a 96-well round-bottom ULA plate without Matrigel® or Vitrogel®, growth was observed with light microscope images taken every 2-3 days.

#### 2.4.3.1 Combination of thyroid cell lines and primary cells

In response to the limited growth observed in the organoids, additional measures were explored involving the supplementation of K1 cells to the primary cells, as the use of cocultures to form multicellular spheroids have shown to possess improved adhesion and

growth, with simple distinguishment between cells through the use of fluorescent microscopy and markers (Xin *et al.,* 2019).

A ULA plate was prepared with each well initially seeded with 100 µL containing 1,000 K1 cells, following the protocol outlined in section 2.2.1. Any remaining primary cells from the procedures detailed in section 2.4.2 were introduced to each well at a volume of 100 µL, containing either 1,000, 10,000 or 20,000 cells (3 wells per density), resulting in a final volume of 200 µL per well. This was done to see which primary seeding density responded best in forming spheroids when cocultured with 1,000 K1 cells. To facilitate the differentiation between K1 cells and primary cells, an initial attempt involved labelling K1 cells with carboxyfluorescein succinimidyl ester (CFSE).

#### 2.4.3.2 CFSE labelling

To prepare the stock, 18 µL of DMSO was added to a vial of CFSE staining solution to give a 10mM stock solution (ThermoFisher). The stock was then diluted in 20 mL of warm PBS to produce a 5 µM staining solution. The K1 cell pellet (section 2.2.1), was resuspended in 2 mL of CFSE staining solution and incubated for 20 min at 37°C. Cells were centrifuged at 300 x g for 5 min and resuspended in the appropriate volume of medium needed for 100 µL to contain 1,000 K1 cells, ready to be seeded along with the primary cells.

However, due to challenges associated with background staining, an alternative approach was explored. A Green Cell Tracking Dye Kit, – CytoPainter, was employed, yielding improved images upon examination using a fluorescent microscope. Both labelling solutions fluoresced a green colour identifying K1 cells.

#### 2.4.3.3 CytoPainter Cell Tracking Dye Green labelling

This staining solution became the primary labelling method for K1 due to the numerous advantages of using CytoPainter (ab138891, Abcam, Cambridge, UK) over CFSE. It is claimed that after multiple replications the cells retain the CytoPainter dye, meaning cells could be cultured for the required time and allowed to mature before fluorescent imaging. In addition, the fluorescent tag is compatible with the Fluorescein isothiocyanate (FITC) filter that was used for the other fluorescent imaging investigations and, CytoPainter did not suffer from the

efflux drawback (higher incidence of background staining) that comes with CFSE, reducing the chances of background staining.

Prior to starting, the 1,000x CytoPainter green stock solution was prepared; 100 µL of DMSO (component c, provided in kit) was added into a vial of CytoPainter green and mixed thoroughly. The 1,000x tracking solution was then diluted in assay buffer at 1:1000 (1 µL 1,000x CytoPainter solution + 999 µL assay buffer, provided in kit) establishing the working solution.

K1 cells were trypsinised and centrifuged to form a cell pellet containing a count of 35,000 cells (following protocol in section 2.2.1), resuspended in 3.5 mL of CytoPainter green working solution (3.5 mL + 7 µL tracking working solution) and incubated for 30 min in a 37°C incubator. Following incubation, cells were centrifuged at 300 *x g* for 5 min and washed with PBS, this was repeated 3 times, after which the cell pellet was resuspended in 3.5 mL of medium. Then, 100 µL containing 1,000 CytoPainter labelled K1 cells were seeded into a ULA plate in combination with primary cells.

## 2.5 Microfluidic device set-up

Based on extensive work done on microfluidic/tissue-on-chip devices at the University of Hull, sorafenib treatment was repeated on spheroids maintained on these devices to more accurately replicate the *in vivo* environment, including factors like blood flow, nutrient supply and lymphatic removal of waste, which are crucial for assessing the drug's efficacy in a setting that closely mimics physiological conditions (Tevlek *et al.,* 2023).

The chip, designed and manufactured at the University of Hull (Figure 2.10), is constructed of laser cut acrylic (10 mm thick) consisting of a basal and apical chamber, each with a 50 µm deep channel enclosed by an O-ring gasket. Stainless steel clips are used to fasten the top and bottom chambers securely. In addition, silicone tubing (#MFLX95718-26 Masterflex® Ismatec® Pump Tubing, C-Flex®, 0.89 mm ID; 50 ft, VWR) was inserted into the chambers via screw Idex Adapter Fit connectors (Cole Palmer WZ-02014-08, Natural ETFE, 0.040" Bore, 1/16" Hose Barb x Male 1/4-28 Flat Bottom), consisting of two inlets and two outlets (3 mm x 10 mm). Poly methyl methacrylate (PMMA) inserts (24 mm) were laser-cut, pressed out of their frames and plastic films lining the back of the inserts were removed. Each insert has 3 central wells 3 mm in diameter, each of which can house 3 spheroids comfortably without reaggregation, whilst being maintained under constant flow (2 µL/min). Inside a fume hood, membranes (10x22 mm, PET, Sabeu), were aligned on to the etched face and using a small paint brush, a layer of Chloroform (288306, Sigma-Aldrich) was applied ensuring no bubbles were created, to bond the membrane to the insert. Once airdried, a second coat of chloroform was applied. The dry inserts were then placed in 70% ethanol for 20 min. In a class II biological safety cabinet, the inserts were placed inside the lid of a petri dish, washed twice with sterile PBS and then allowed to dry.

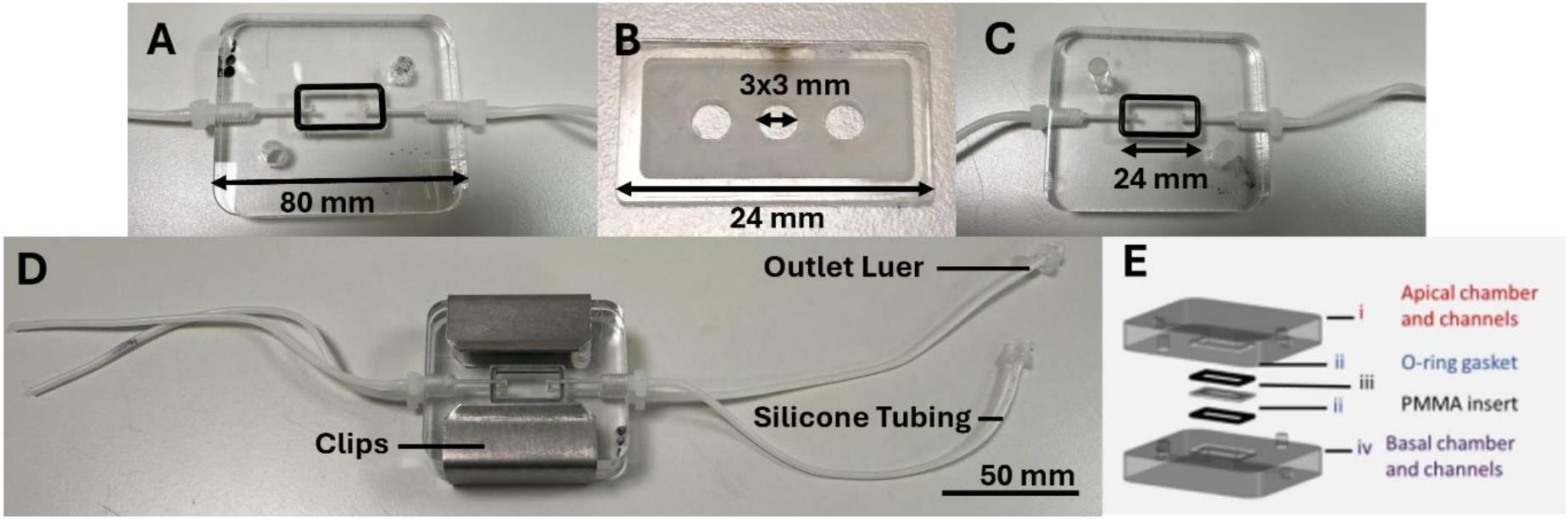


***Figure 2.10 Photographs and schematic diagram of microfluidic chip.*** *A – acrylic apical chamber with channel and O-ring gasket, B – PMMA insert, C – acrylic basal chamber also with a channel and O-ring gasket, D – assembled chip with protruding inlet/outlet silicone tubing secured with stainless steel clips and E – schematic representation of the chip.*

For the sorafenib investigations, 5 µL of Matrigel® was added into each of the three designated cell culture areas. The inserts were sealed in the petri dish and placed into a 37°C, 5% $CO_2$ incubator for 30 min, allowing the Matrigel® to solidify. Spheroids were established following the protocol in section 2.2, K1 cells were seeded at 20,000 and 8305c at 10,000 cells/well. K1 and 8305c spheroids were ready to be placed into the devices following 7 and 5 days of initial growth, respectively.

During incubation of the inserts with Matrigel®, 10 mL syringes (BD Plastipak Luer Slip) were prepared. Each cell line required 4 devices meaning 8 syringes, two for each chip. Sorafenib was prepared in the same way as outlined in section 2.3.8 starting with a top concentration of 100 µM serially diluted to 50 µM and 25 µM, the final two syringes contained medium only (based on the cell line used). The final volume in each syringe amounted to 5 mL and 0.2 µm filters were added to the inlets before attaching the syringes.

After incubation with Matrigel®, inserts were checked for any bubbles before 3 spheroids were added per well using a blue tipped pipette, equating to 9 for each insert, 27 in total across the 4 devices. The inserts containing spheroids were inspected making sure the spheroids did not touch each other, in the case they were, sterile forceps were used to carefully adjust the positioning of the spheroids. Once spheroids had settled in their designated places, the inserts were ready to be placed onto the microfluidic chip.

The inlet plunger of the syringe was gently pressed down to fill the tubing of both the apical and basal chambers. After which, the insert was placed in the central channel and the top chamber was carefully manoeuvred into position, sandwiching the insert between the two chambers, creating a seal with the O-ring. Two stainless steel clips were simultaneously attached to both sides of the device, to ensure the chambers remained intact. The device was inspected for any missing spheroids, bubbles and leaks before being transferred onto a Harvard syringe pump (Harvard apparatus, Cambridge, USA, Figure 2.11).

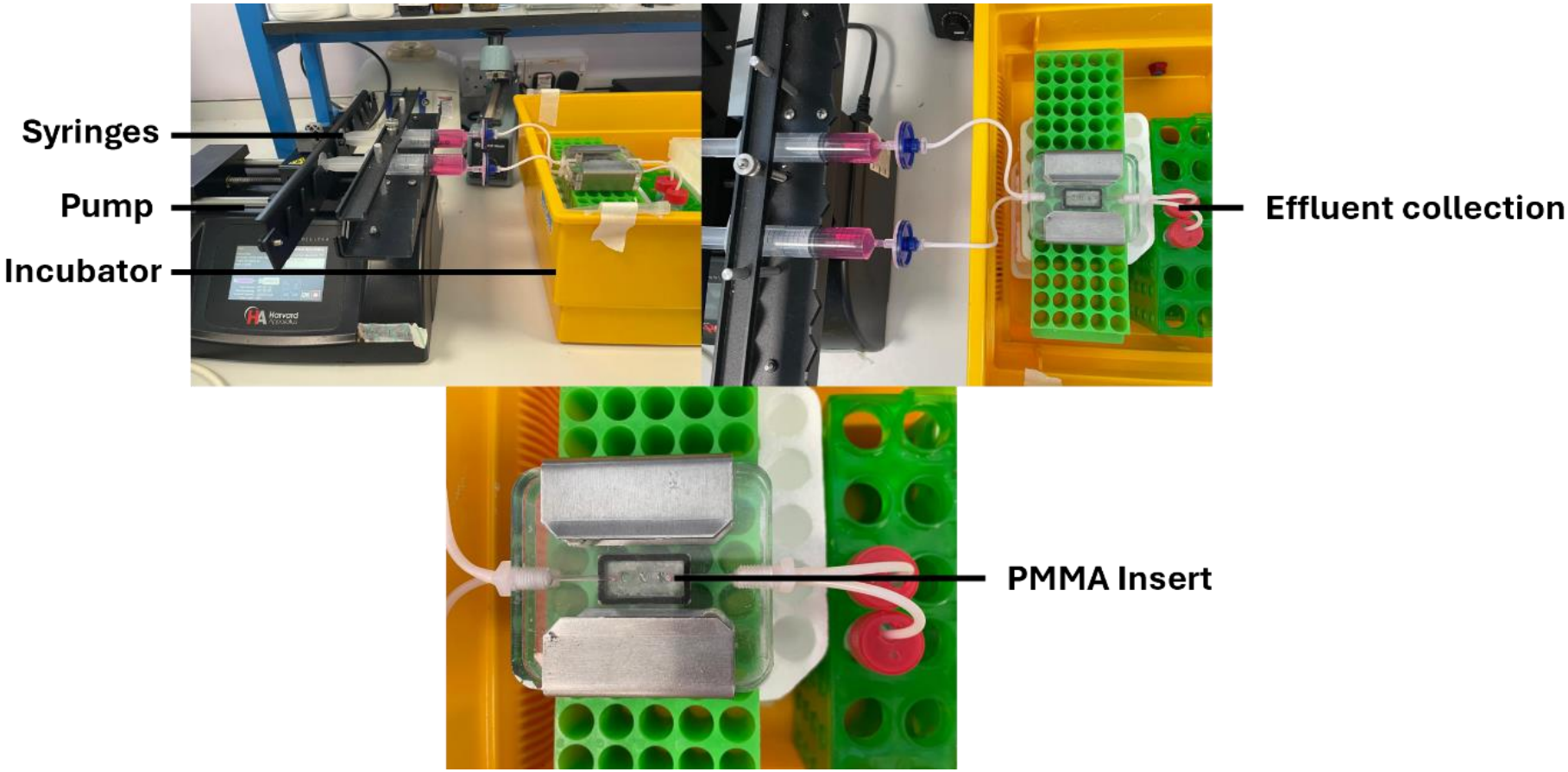


***Figure 2.11 Photographs of the microfluidic device set-up.*** *Chips were placed inside a 37°C incubator with effluent collection in 15 mL tubes. Syringes were mounted on to a Harvard pump and medium with and without sorafenib was perfused over the chips for 48 h (2µL / min) with replenishment after 24 h.*

Syringes were secured onto the pump and the devices were placed inside a 37°C incubator (Novital Covatutto 24 Manual ECO Incubator, Amazon), outlet tubing was placed into 15mL tubes to collect the effluent. Devices were perfused with and without sorafenib (100, 50, 25, and 0 µM) for 24 h (2µL / min), after which, syringes were changed under sterile conditions. This involved carefully removing the syringe connected to the inlet tubing and replacing it with a new syringe, with and without sorafenib (100, 50, 25, and 0 µM), ensuring no bubbles were introduced. The devices were returned to the pump and incubator and set running for a further 24 h.

On completion of the experiment, devices were taken off the pump and dismantled in a class II cabinet. Spheroids were transferred from the insert into a ULA plate by adding 50 µL of medium to the cell culture area using a blue pipette tip and gently pipetting the spheroids into the plate, sterile forceps were used when spheroids were difficult to separate from the Matrigel® base. The spheroids in the plate were then available for CTG (section 2.3.4) or fluorescent microscopy (section 2.3.5) examinations, respectively.

## 2.6 Statistical analysis

All data analysis and generation of graphs was conducted using Graph pad software (v9.5.1) Statistical analysis was performed based on the available data from the specific investigation; for analysis consisting of a singular variable, a one-way ANOVA was conducted along with Tukey's post hoc analysis. Whereas, for comparisons of concentrations/time against the control groups, 2-way ANOVA tests were performed followed by Dunnet's post hoc examination. Further details on why specific tests were chosen is provided in sections where they were used. Data was considered to be significant if $p$ <0.05 with error bars reported as mean ± SD unless otherwise stated. Asterisks plotted on the graphs denote the level of significance; * ($P \leq 0.05$), ** ($P \leq 0.01$), *** ($P \leq 0.001$) and **** ($P \leq 0.0001$).

# Chapter 3 Optimisation of Spheroids for Experimental Use

## 3.1 Introduction

Spheroids are 3D structures, formed from the aggregation of cells, defined by their rounded mass and uniform shape (Han *et al.,* 2021). The 3D interactions of cells within these models better recapitulate the *in vivo* tumour microenvironment, more closely mimicking the functions of the cells from which they were derived (Gunti *et al.,* 2021). Spheroids offer a distinct advantage over standard, flat, monolayers in drug response studies and have become integral to cancer research due to their superior predictive capabilities, yielding more accurate and reliable results (Zhang *et al*., 2016).

In this study, spheroids were assessed on their ability to consistently configure into uniform and spherical structures, maintain viability for the desired duration and have the structural integrity necessary to undergo the treatment and analysis processes. Studies utilising the same cell lines for spheroid generation served as benchmarks for the expected structures and sizes of spheroids, as well as their responses to treatments. This assured not only that the spheroids produced for this work would be reliable for drug testing but also allowed for meaningful comparisons with both 2D and 3D published data. While monolayers underrepresent the complexity of the *in vivo* situation, spheroids address this limitation by simulating crucial features such as drug diffusion distances and hypoxic cores, making them a superior predictive tool. This is especially important in the context of oncological drug development in which there is an attrition rate for new agents exceeding 95% (Jentzsch *et al*., 2023). This is believed to be in most part due to the poor translation of results from 2D models/laboratory animals in preclinical testing to use in human subjects (Antunes *et al*., 2022), necessitating the development of better pre-clinical models.

Spheroids can be formed from various types of cells, these being cancer cell lines, stem cells and primary cells derived from tissue. Cells are commonly supplemented with specialised matrices such as Matrigel® or VitroGel®, which provide a scaffold for cell attachment and support for growth (Flores-Torres *et al.,* 2021), although cancer cell lines when seeded at greater seeding densities (>1000 cells/well) generally do not require such additives due to

their self-assembly capabilities. Cancer cells do, however, exhibit variability in size and behaviour, emphasising the importance of optimising cell parameters and conditions for spheroid formation. By determining optimal seeding densities for each cell line, the production of consistently uniform spheroids in shape and size can be achieved, which is essential for reducing variability between experimental repeats and avoiding the introduction of experimental artefacts. This optimisation enables high throughput testing, while maintaining reproducible results. An issue in the literature in the scope of generating spheroids is the lack of a standardised seeding density protocol for each cell line (Table 3.1).

***Table 3.1 Seeding densities from various publications exploring thyroid cancer spheroid generation.***

| Author | Cell Line | Seeding Density (96-well ULA) |
|---|---|---|
| **Lee *et al.,* 2020** | K1 | $8 \times 10^3$ cells/well |
| **Oh *et al.,* 2022** | K1 | $1 \times 10^3$ or $5 \times 10^3$ cells/well |
| **Sekhar *et al.,* 2022** | K1 | $1 \times 10^4$ cells/well |
| **Caria *et al.,* 2018** | K1 | $2 \times 10^4$ cells/well |
| **Abols *et al.,* 2015** | 8305c | $2 \times 10^3$ cells/well |
| **Hasse, 2020** | 8305c | $1 \times 10^4$ cells/well |
| **Mortensen *et al.,* 2023** | 8305c | $1 \times 10^3$ cells/well |

**K1** - Papillary carcinoma cell line

**8305c** - Anaplastic carcinoma cell line

The reason for the lack of consistency in spheroid generation protocols may be due to the contention between researchers on what makes a good spheroid for drug analysis. This debate revolves around the inclusion of a necrotic core, created by the hypoxic environment at the centre of a spheroid, generally seen with larger seeding cell densities (Zhang *et al.,* 2016). Spheroids are composed of multiple layers; an outer proliferating area, an inner quiescent zone and depending on the seeding density, a necrotic centre (Figure 3.1). The fabrication of a necrotic core is thought to be important in drug resistance studies, as it simulates a common property of the *in vivo* tumour microenvironment, providing an insight

on how this interacts with, or interferes with, certain therapies (Hamilton & Rath, 2019). The inclusion of a necrotic core however can be seen as counterproductive as it essentially involves killing cells which are already dead. This underscores the importance of carefully considering the benefits and drawbacks before incorporating a necrotic core into spheroids for drug analysis protocols, particularly, when it has the potential to alter spheroid behaviours to external stresses, along with influencing the interplay between tumour remodelling and growth within the spheroid (Giverso & Preziosi, 2019).

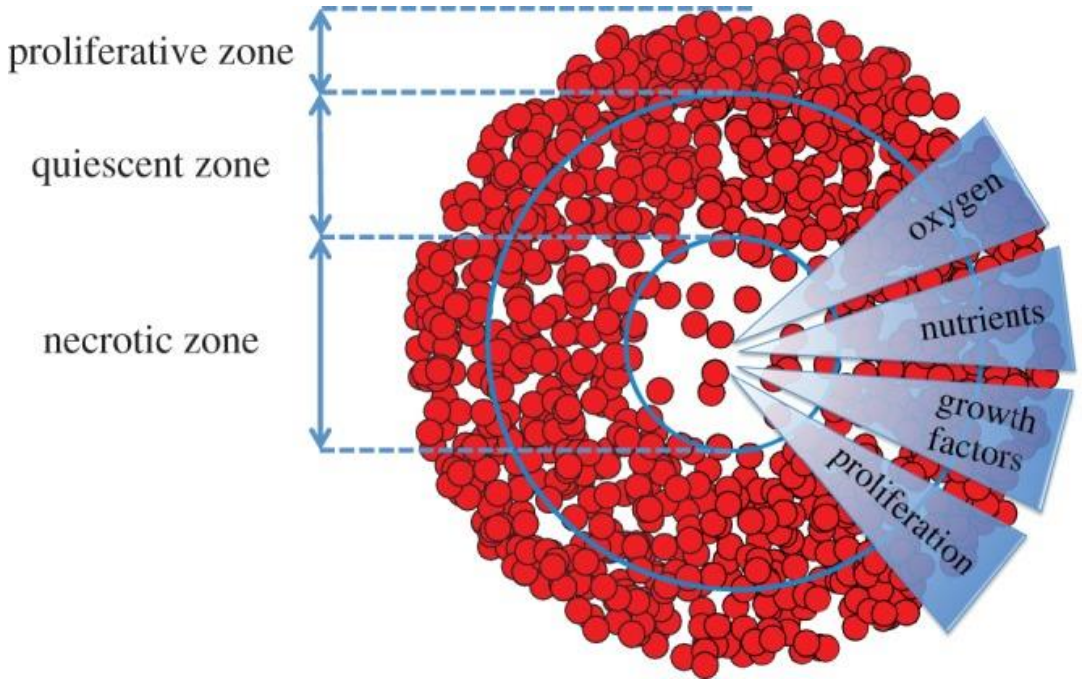


***Figure 3.1 Diagram illustrating the necrotic, quiescent, and proliferative zones within a tumour spheroid.*** *Inner necrotic core – composed of non-viable cells due to lack of nutrients, oxygen, and accumulation of toxic waste. Quiescent zone – non-proliferative but viable cells. Outer proliferative zone – consists of proliferating cells with access to an abundance of nutrients, oxygen, and growth factors. Adapted from Dini et al., 2016.*

To try and address this issue, a consultation was held with a partner company CN-BIO (Cambridge), a Biotech company specialising in organ-on-a-chip, who had experience using spheroids generated from significantly fewer cells than used in the literature. The reason for this was to ensure that a necrotic core was not formed, so the focus would be on killing live

cells. CN-Bio had previously maintained these small spheroids on their organ-on-a-chip device for a more accurate measurement of cell death post-treatment (Petreus *et al.,* 2022). Based on their recommendations it was decided that spheroids would be generated with a density of 1000 cells/well, devoid of a necrotic core. In addition, it was determined that it would be useful to compare the effects of treatment on spheroids with a necrotic core, for that reason the optimal cell density that could consistently induce a necrotic core in spheroids was also investigated. To observe and better understand the multifaceted aspects of the spheroidal structure, fluorescent imaging was utilised to visualise the different regions of the structure.

As previously mentioned, cancer cell lines exhibit considerable variability, which influences their response to treatment. Therefore, it was important to compare the response of the slow-growing PTC (K1 cell line), which typically carries a favourable clinical prognosis, with the fast-growing ATC (8305c cell line), associated with high metastatic potential and resistance to conventional therapies, heralding a poor prognosis (Capdevila *et al.,* 2018). Moreover, both cell lines were chosen based on the genetic mutations that are most commonly associated with the respective malignancy, for instance the common BRAF mutation was present in the PTC line and the suppression of TP53 in ATC (section 1.2.3 and 1.2.5). The comparison of these two cell lines will provide valuable insights on how different cell types, numbers and their unique growth behaviours might impact their responses to therapy.

## 3.2 Aims

To establish a spheroid generation protocol for two thyroid cancer cell lines (K1 and 8305c), determining the optimal seeding density, ensuring the formation of a consistently uniform shape and sized spheroid (with and without a necrotic core), enabling high throughput testing, while maintaining reproducible results. Finally, to investigate differences between spheroids supplemented with and without Matrigel®.

## 3.3 Methods

The K1 and 8305c cell lines were both purchased from the ECACC and cultured in medium based on recommendations by the supplier (section 2.1). Once confluent, cells were seeded into a 96-well ULA plate at varying cell quantities to determine the optimal cell density

required for a viable spheroid (section 2.2). The range of plating densities was selected based on what had been used in thyroid spheroid literature. As a result, an experimental range was established for both cell lines with triplicates for each seeding density. For K1; 1000, 10,000, 15,000 and 20,000 cells/well as for 8305c, 1000, 10,000, 20,000 and 30,000 cells/well.

Once plated, the ULA plates were incubated at 37°C, 5% $CO_2$ for a total of 13 days, with medium replenishment every 3 days. Imaging took place on days: 3, 5, 7, 9, 11 and 13; three spheroids were imaged at each time point, using a brightfield light microscope (Nikon E800). Images were analysed using ImageJ to measure the diameter of each spheroid over the chosen time period (section 4.5). This technique allowed for non-invasive monitoring ensuring spheroids were undisturbed throughout their growth phase. For confirmation of a necrotic core, FDA/PI staining and fluorescence imaging was utilised (section 2.3.5).

The seeding procedure for the 1000 cells/well spheroid generation was based on the protocol provided by our partner company CN-BIO (section 2.2.1). Two ULA plates were prepared, with the only distinction being that one plate included 1%(v/v) Matrigel®, to assess the benefit of its addition to spheroids. The plates were incubated at 37°C, 5% $CO_2$ for a period of up to 13 days. Imaging followed the identical process as described previously with the larger spheroids.

Seeding procedures for the 8305c cell line were identical to the ones outlined for the K1 cell line. However, due to unforeseen supply delays for this cell line, only very basic optimisation observations were carried out to determine its suitability for the sorafenib treatments (Chapter 5). The K1 cell line had already been optimised and in the process of being investigated with $H_2O_2$/$NaN_3$ and MTS/CTG (Chapter 4) once the 8305c cell line had been received where initial culturing difficulties were encountered. Consequently, only single repeats were carried out and the presence/lack of a necrotic core for this cell line could not be determined at this stage but this was identified and confirmed in Chapter 5.

## 3.4 Statistical analysis

Analyses were conducted using GraphPad Prism v9.5.1. A 2-way ANOVA followed by a Tukey's multiple comparisons test was performed on the diameter readings, to determine whether there was a significant difference in average sizes across the varying seeding densities at each

time point. As for the smaller spheroids, seeded at 1000 cells/well, identical tests were conducted to determine whether the inclusion of 1% (v/v) Matrigel® into the wells had any significant impact on average spheroidal size between the two groups (+/- 1% Matrigel®) over the course of incubation.

# Results

## 3.5 Optimisation of K1 spheroids

To determine the optimal seeding density for the K1 cell line, ULA plates were seeded in triplicates with 10,000, 15,000, and 20,000 cells/well. The goal was to identify the density that produced spheroids of consistent shape and size with a necrotic core. Plates were initially incubated at 37°C, 5% CO2, for 7 days to establish which density produced the best spherical structures before extending to 13 days for further studies. Imaging occurred on days 3, 5, and 7, with FDA/PI staining and fluorescent imaging on day 7. Diameter measurements were taken at each time point and averaged using ImageJ software.

Images of the spheroids revealed that all the tested cell densities were capable of producing spherical bodies, however only the 20,000 cells/well spheroids, presented a necrotic core, as shown by a red fluorescence generated by the binding of PI to the DNA in compromised cells in the centre of the spheroid (Figure 3.2). In addition, it was found that the 10,000 and 15,000 cells/well spheroids would more frequently generate irregular and asymmetrical spheroids, compared to those spheroids plated at 20,000 cells/well (Figure 3.3).

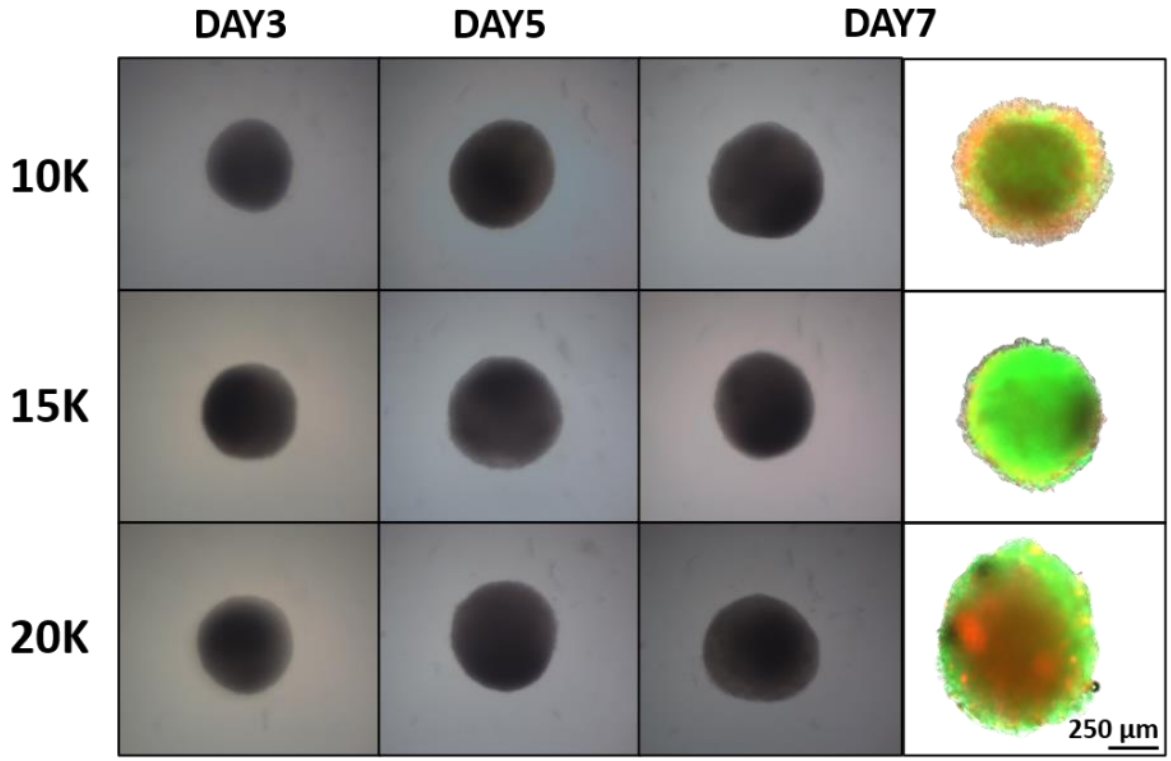


***Figure 3.2 Brightfield and Fluorescent images of Fluorescein Diacetate and Propidium Iodide (FDA/PI) stained K1 spheroids (seeded at 10,000, 15,000 and 20,000 cells/well).*** *Images were taken using either a brightfield light or a Zeiss fluorescent microscope (Day 7) at 10x magnification. Images are representative of a single experiment consisting of triplicates for each seeding density.*

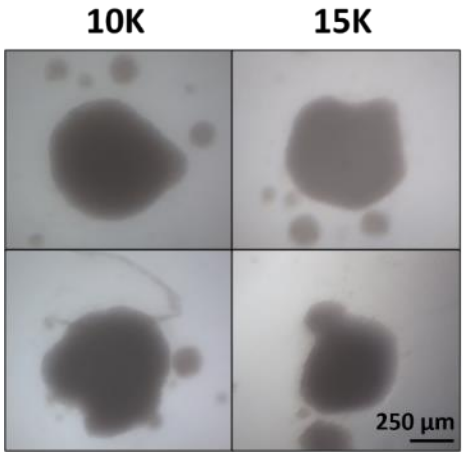


***Figure 3.3 Images of irregularly shaped Day 7 K1 spheroids (seeded either at 10,000 or 15,000 cells/well).*** *Images were taken using a brightfield light microscope at 10x magnification. Images are representative of a single experiment consisting of triplicates for each seeding density.*

In terms of average diameters across the groups, the lowest seeding density spheroids (10,000 cells/well) had an average diameter of 670 ± 48 µm at day 3, with a gradual increase in size to around 900 ± 27 µm by day 7 (Figure 3.4). The 15,000 and 20,000 cells/well spheroids started with similar values at day 3, with an average diameter of 740 ± 69 and 760 ± 25 µm respectively and reaching a size of 870 ± 25 and 890 ± 22 µm by day 7. It was noticed that regardless of seeding density, spheroids reached a similar size ranging between 870-900 µm by the 7$^{th}$ day of incubation. After conducting a 2-way ANOVA followed by a Tukey's multiple comparisons test, the observations were confirmed, revealing no statistical difference in the mean spheroidal sizes for each time point regardless of seeding density.

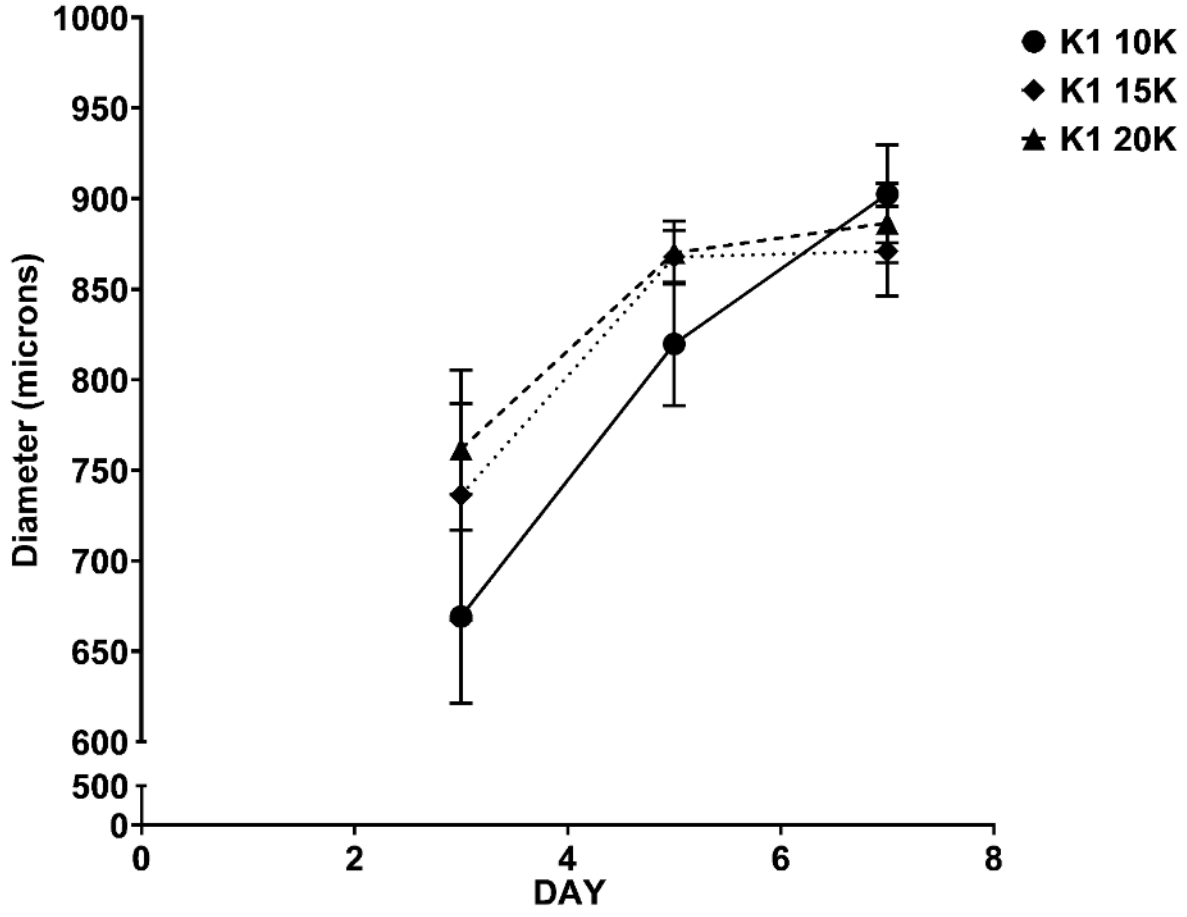


***Figure 3.4 Diameter measurements for K1 spheroids (seeded at 10,000, 15,000 and 20,000 cells/well).*** *Images were taken using a brightfield light microscope at 10x magnification and then average diameter readings of spheroids on days 3, 5 and 7 were determined using ImageJ, triplicates for each analysis day. A single experiment consisting of triplicates for each seeding density was conducted, n=1. Values are mean ± SD. Diameter (microns) on Y axis.*

As a result, a seeding density of 20,000 cells/well was chosen as the optimal seeding density based on the production of consistently uniform spheroids and the presentation of a necrotic core. A further trial was conducted with an extended observation timeframe out to 13 days for just the spheroids seeded at 20,000 cells /well, with imaging taking place on days 3, 5, 7, 9, 11 and 13 to understand the growth trend.

Imaging of the 20,000 cells/well spheroids revealed that a symmetrical and spherical shape was maintained throughout the incubation period up to day 13 (Figure 3.5). Diameter measurements revealed an average size ranging from 700-800 µm on days 3, 5 and 7 with a steep increase to around 1000 µm on day 9, before steadily dropping back down to the 800 µm mark by day 13 (Figure 3.6).

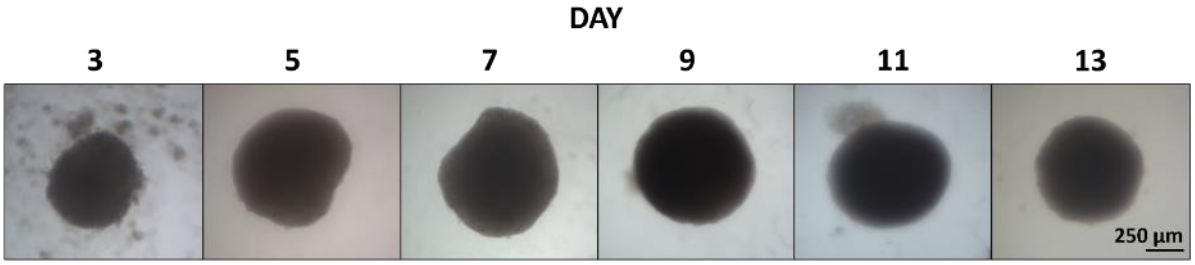


***Figure 3.5 Images of K1 spheroids (seeded at 20,000 cells/well).*** *Images were taken using brightfield light microscope at 10x magnification. Images are representative of a single experiment consisting of triplicates.*

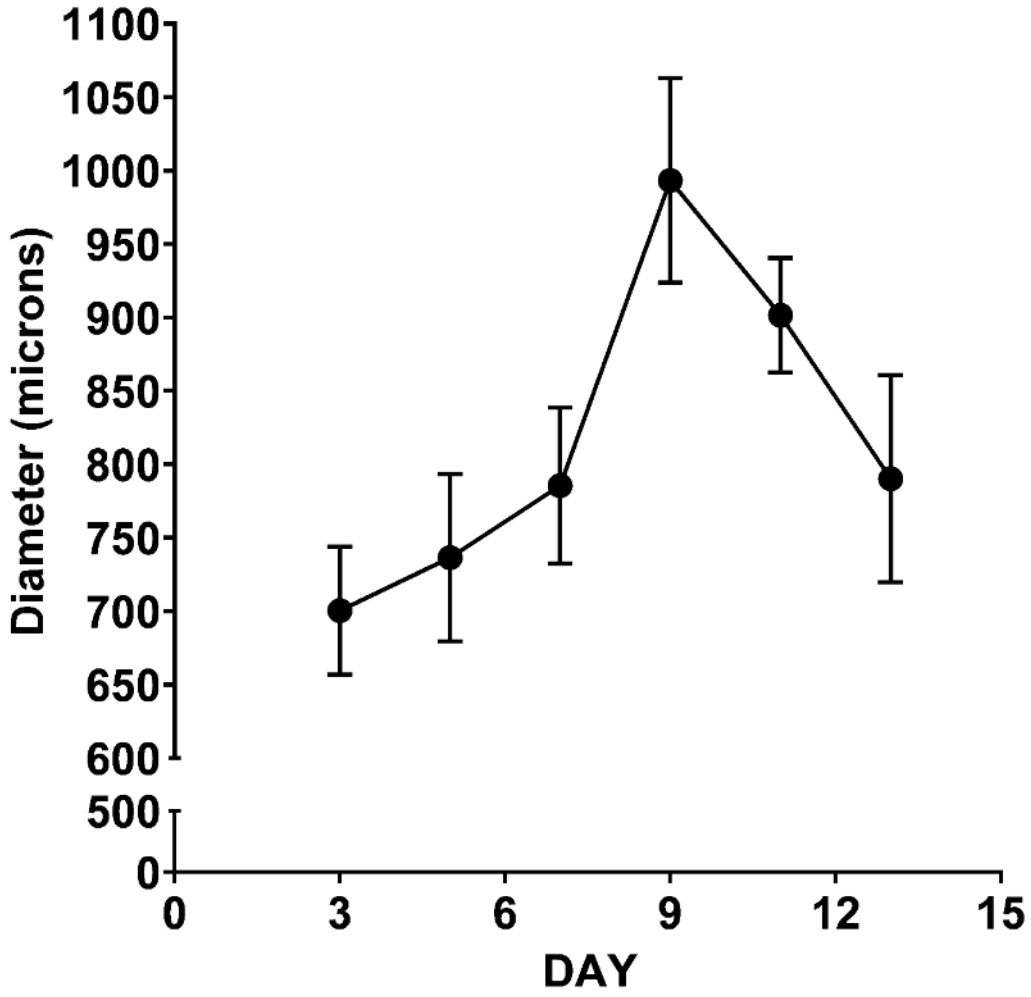


***Figure 3.6 Diameter measurements for K1 spheroids (seeded at 20,000 cells/well).*** *A single experiment consisting of triplicates was conducted, n=1. Images were taken using a brightfield light microscope at 10x magnification and then average diameter readings of triplicate spheroids on days 3, 5, 7, 9, 11 and 13 were determined using ImageJ. Values are mean ± SD. Diameter (microns) on Y axis.*

### 3.5.1 Optimisation of K1 spheroids seeded at 1000 cells/well

As mentioned previously, based on recommendations from our collaborators (CN-BIO), spheroids were also generated by plating two ULA plates at 1000 cells/well, wherein one plate also contained 1% (v/v) Matrigel® per well. Spheroids were incubated for 13 days and images taken on days 3, 5, 7, 9, 11, and 13, with no media change as it was not necessary for such a small cell population and duration.

Images revealed an observable difference in size between the spheroids supplemented with 1% (v/v) Matrigel® and the ones devoid of it (Figure 3.7). It appeared that the spheroids with Matrigel® were more spread out, possibly due to the ECM scaffolds allowing for expanded growth, whereas the other set of spheroids generated more compact structures.

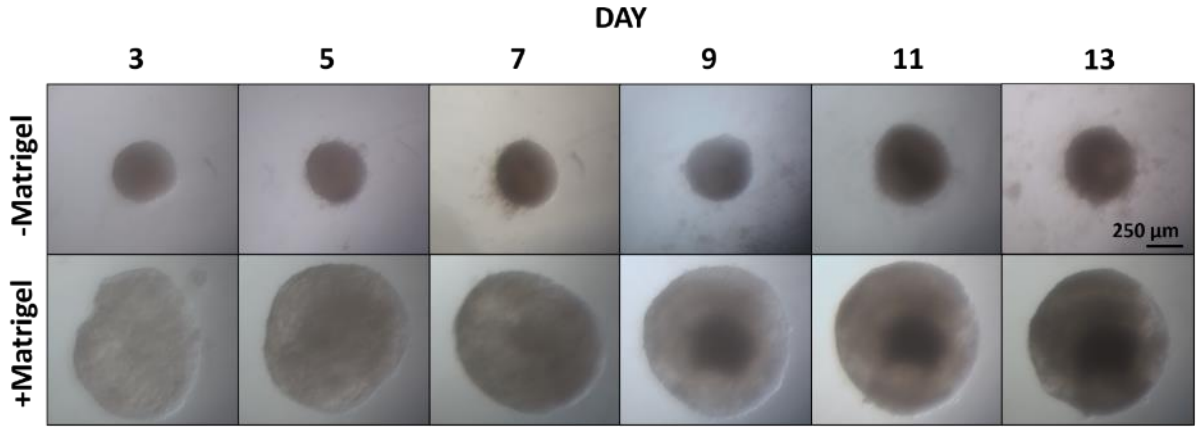


***Figure 3.7 Images of K1 spheroids (seeded at 1000 (with and without 1%(v/v) Matrigel®) cells/well).*** *Images were taken of each spheroid (on days: 3, 5, 7, 9, 11 and 13) using a brightfield light microscope at 10x magnification. Images are representative of two independent experiments (with and without Matrigel®) consisting of triplicates.*

The observation was confirmed with diameter measurements, which proved that spheroids with Matrigel® were significantly larger on average compared to spheroids lacking Matrigel® at each time point when analysed using a 2-way ANOVA with Tukey's post hoc test (Figure 3.8). Spheroids with Matrigel® showed a consistent size with little variation over the full observation term being between 1100-1200 µm. Similarly, albeit considerably smaller (127% smaller when comparing the mean size of spheroids between the two groups), the spheroids without Matrigel® displayed a consistent size with an average diameter of 500-600 µm throughout.

Spheroids seeded with 1% (v/v) Matrigel® were notably larger and easier to identify under the microscope along with the associated ease of transport out of the well, it was therefore decided to include Matrigel® supplementation for the 1000 cells/well K1 spheroids. Moreover, the smaller spheroids were confirmed to not manifest a necrotic core as shown in section

5.5.2 post treatment with or without sorafenib, as the 1000 cells/well spheroids were incorporated later into the protocol post consultation with our partner company CN-BIO which occurred during the cell death investigations (Chapter 4).

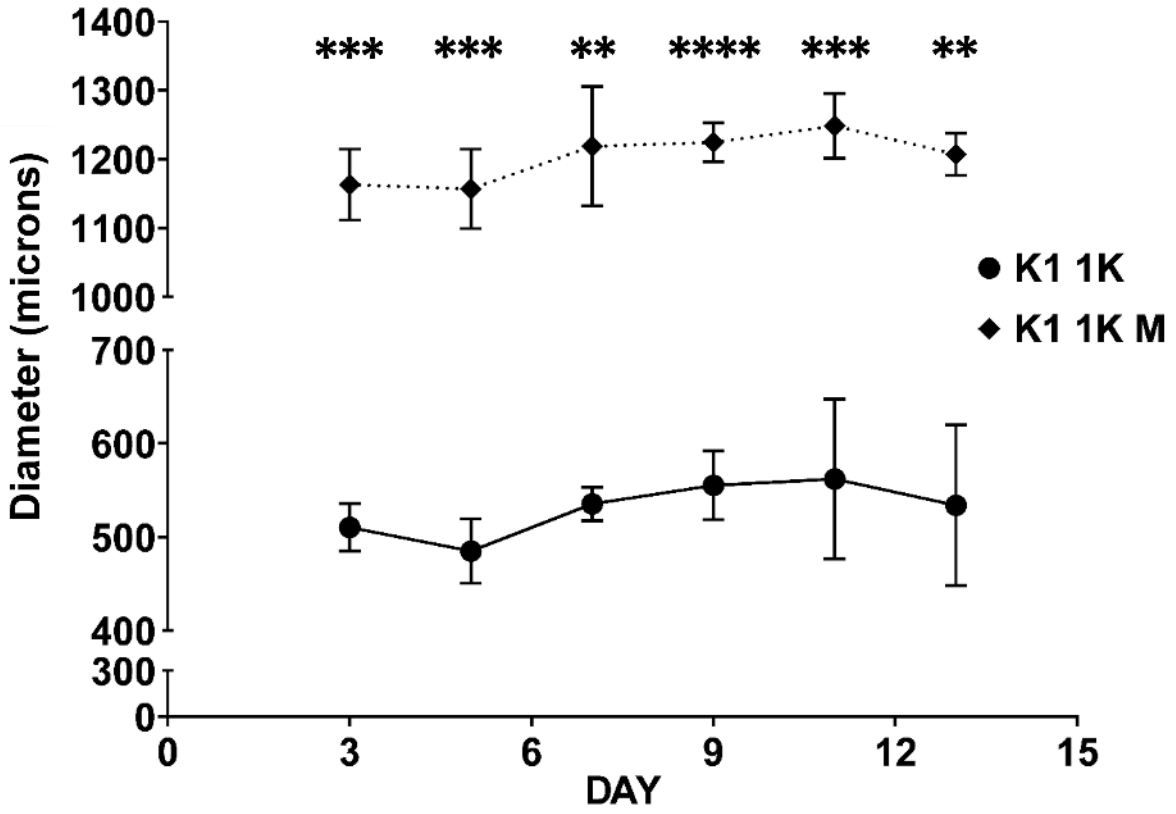


***Figure 3.8 Diameter measurements for K1 spheroids seeded at 1000 (with or without 1% (v/v)Matrigel®) cells/well.*** *Images were taken using a brightfield light microscope at 10x magnification and then average diameter readings of spheroids on days 3, 5, 7, 9, 11 and 13 were determined using ImageJ, triplicates for each analysis day. M = spheroids with 1% (v/v) Matrigel®. Values are mean ± SD, ** (P ≤ 0.01), *** (P ≤ 0.001) and **** (P ≤ 0.0001), n=3, meaning three repeats for each group (with or without Matrigel®) consisting of triplicates. Diameter (microns) on Y axis. Analysed using a 2-way ANOVA with Tukey's multiple comparisons test: spheroids with Matrigel® vs spheroids without it (mean spheroid size for each analysis days).*

## 3.6 Optimisation of 8305c spheroids

The 8305c spheroids were seeded at 10,000, 20,000 and 30,000 cells/well, to determine the optimal seeding density. Plates were incubated at 37°C, 5% $CO_2$, for a total of 13 days, with imaging taking place on days: 3, 5, 7, 9, 11 and 13. Diameter measurements were taken at the selected time points and averages were determined using ImageJ software.

Figure 3.9 displays the effects of seeding density on spheroid formation. At a plating density of 10,000 cells/well, spheroids consistently formed spherical and symmetrical structures. However, as the seeding density increased to 20,000 and 30,000 cells/well, spheroids often exhibited elongated and irregular shapes. Even though the best images were selected for each seeding density, it was challenging to find symmetrical spheroids at the higher densities. This trend highlighted that the lower plating density was more effective for generating consistent, spherical spheroids.

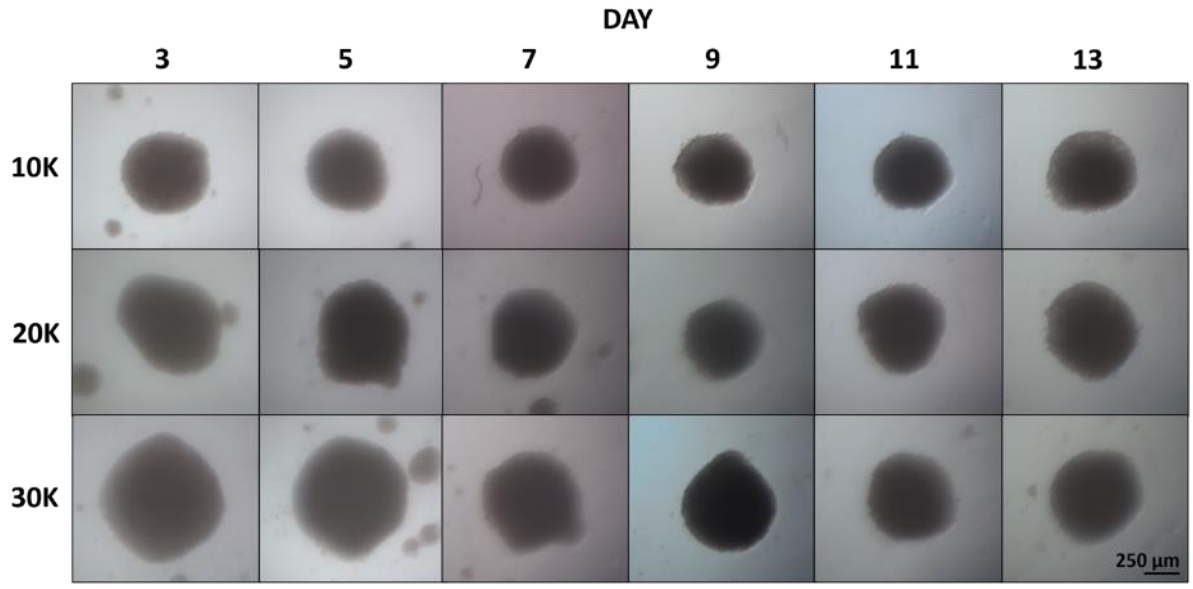


***Figure 3.9 Images of 8305c spheroids (seeded at 10,000, 20,000 and 30,000 cells/well)**. Images are representative of a single experiment consisting of triplicates for each seeding density. Images were taken using a brightfield light microscope at 10x magnification (on days: 3, 5, 7, 9, 11 and 13). 10K: At 10,000 cells/well, spheroids are consistently spherical and symmetrical. 20K: At 20,000 cells/well, spheroids display more elongated and irregular shapes. 30K: At 30,000 cells/well, spheroids show further deviations from a spherical shape, with increased irregularity and elongation.*

In terms of diameter readings, the 10,000 cells/well spheroids started at approximately 700 ± 33 µm on day 3 and 5, and unexpectedly dropped slightly to an average of 650 µm between days 7-11 with a final increase to 750 ± 31 µm by day 13 (Figure 3.10). The 20,000 cells/well group displayed a similar pattern, starting off with, as expected, a slightly larger size of 825 ± 31 µm with a small dip in the mean diameter around the midpoint of the timescale down to around 710 ± 12 µm on day 9, before increasing in size to 805 ± 19 µm before the final day. The diameter of the spheroids plated at 20,000 were larger on average compared to the 10,000 cells/well spheroids at each time point. The largest seeding density group (30,000 cells/well) exhibited a much more pronounced drop in size, from an average diameter of 1000-1050 ± 54 µm on days 3 and 5 down to a consistent reading between 800-850 ± 41 µm for the remaining analysis days, similar to the size of the 20,000 cells/well group.

A 2-way ANOVA, followed by a Tukey's multiple comparisons test revealed significant differences in average spheroidal sizes between the seeding groups from days 3-11. Interestingly, despite all three groups displaying these differences in average diameters from one another, the average fell within 100 µm of each other by day 13, in the range of 750-850 µm. This was also observed and thus supported by fact that no significant differences in mean diameters across all seeding densities were seen on the final day of measurements.

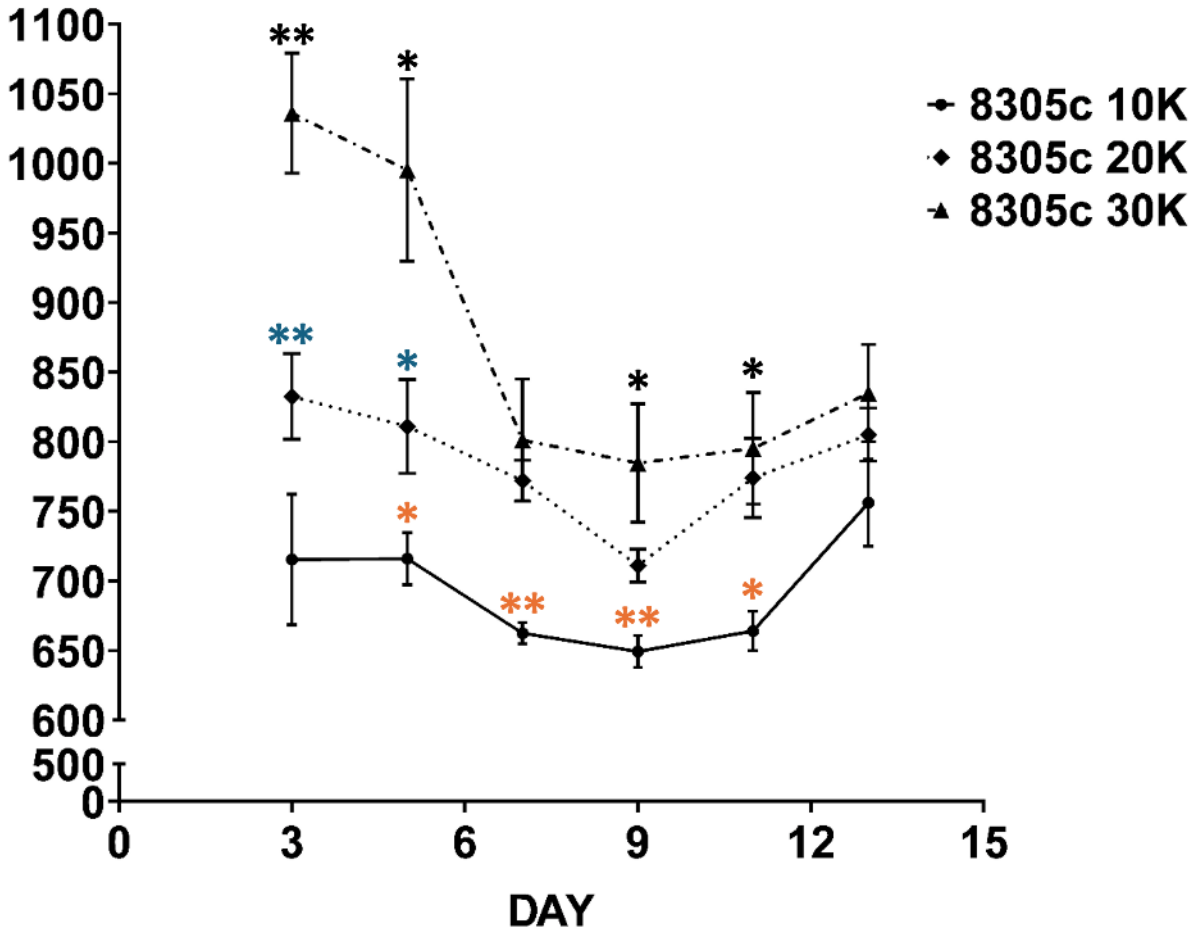


***Figure 3.10 Diameter measurements for 8305c spheroids (seeded at 10,000, 20,000 and 30,000 cells/well).*** *Images were taken using a brightfield light microscope at 10x magnification and then average diameter readings of spheroids on days 3, 5, 7, 9, 11 and 13 were determined using ImageJ, triplicates for each analysis day. A single experiment was conducted consisting of triplicates for each seeding density n=1, values are mean ± SD, * (P ≤ 0.05), and ** (P ≤ 0.01). Diameter (microns) on Y axis. Analysed using a 2-way ANOVA with Tukey's multiple comparisons test: mean spheroid size comparisons for each analysis day between the seeding densities, *: 10K vs 20K, *: 20K vs 30K and *: 10K vs 30K.*

### 3.6.1 Optimisation of 8305c spheroids seeded at 1000 cells/well

8305c spheroids were generated by plating two ULA plates (one with and one without 1% (v/v) Matrigel® per well) at 1000 cells/well following the procedure outlined for the smaller K1 cell line. Spheroids were incubated for 13 days and images taken on days 3, 5, 7, 9, 11, and 13. The same observations regarding the seeding of 1000 cells/well spheroids were made for

the 8305c cell line as was seen with the K1 cells, in that the, 8305c cells supplemented with 1% (v/v) Matrigel®, exhibited on average an observably greater size (Figure 3.11). With both groups regardless of supplementation with Matrigel® having produced uniform and spherical bodies.

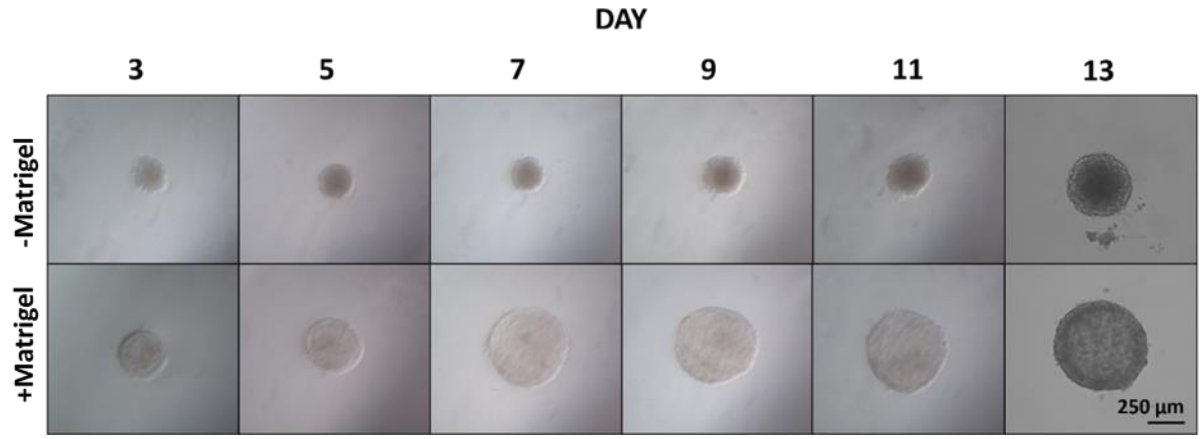


***Figure 3.11 Images of 8305c spheroids seeded at 1000 (with or without 1% (v/v) Matrigel®) cells/well.*** *Images were taken of each spheroid (on days: 3, 5, 7, 9, 11 and 13) using a brightfield light microscope at 10x magnification. Images are representative of two independent experiments (with and without Matrigel®) consisting of triplicates. An identical secondary repeat of these experiments was conducted to attain day 13 images.*

As with the K1 spheroids plated at 1000 cells/well, diameter measurements once again confirmed the considerable differences in sizes observed between the spheroids supplemented with Matrigel® and those without (Figure 3.12). Starting from an average diameter of 430 ± 44 µm on day 3, for spheroids grown with 1% Matrigel®, a pronounced increase was observed by day 11 up to 675 ± 6 µm, however by day 13 the growth of the spheroid began to plateau followed by a considerable drop to 490 ± 13 µm. In contrast, spheroids lacking Matrigel® displayed a much more gradual increase in average size, beginning with an average diameter of just below 300 ± 12 µm and maintaining an average size of 310 µm throughout the observation term.

Moreover, average mean diameter readings revealed significant differences in spheroidal sizes for each analysis day between the Matrigel® supplied spheroids and those without it, post analysis using a 2-way ANOVA with Tukey's multiple comparisons test. The intensity of the disparity in sizes between the two groups gradually increased across the 11 days where

spheroidal size had peaked around 675 µm and was approximately 93% larger than spheroids without Matrigel® sat around 350 µm. Before dropping on the final day, closing down the size difference to around 59%. Overall, the spheroids supplemented with Matrigel® were on average 77% larger than those without it.

As with the K1 cell line, 8305c spheroids seeded with 1% (v/v) Matrigel® showed enhanced growth compared to spheroids lacking Matrigel®. In addition, these spheroids were notably larger and easier to identify under the microscope along with the ease of transportation out of the well for further testing. For those reasons it was decided to also supplement the 1000 cell/well 8305c spheroids with 1%(v/v) Matrigel®. As for the larger spheroids the seeding density of 10,000 cells/well was chosen due to the consistency of generating spherical and symmetrical spheroids compared to the other seeding densities. As before, necrotic core assessment was not available during these investigations but the presence of such a formation was noted during the sorafenib investigations (section 5.5.3 and 5.5.4).

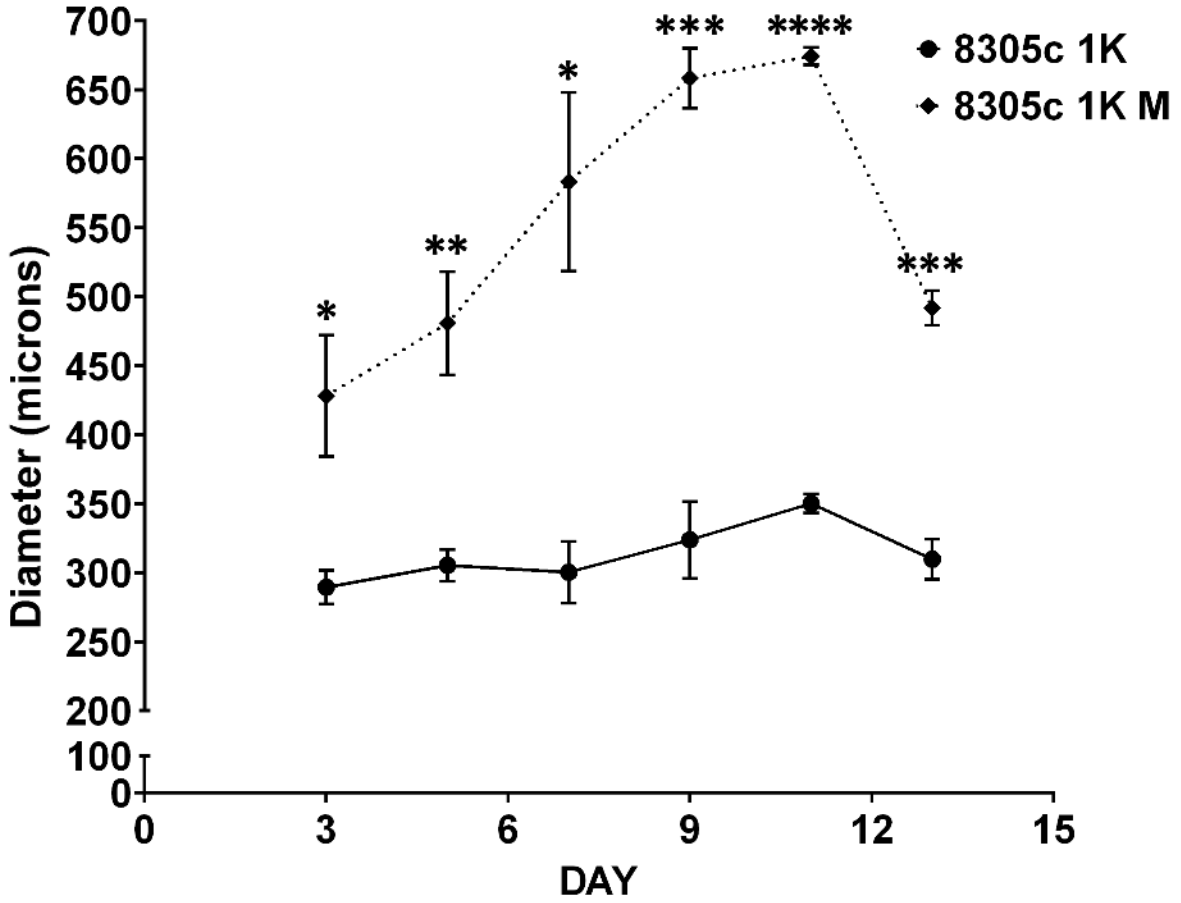


***Figure 3.12 Diameter measurements for 8305c spheroids seeded at 1000 (with or without 1% (v/v) Matrigel®) cells/well.*** *Images were taken using a brightfield light microscope at 10x magnification and then average diameter readings of spheroids on days 3, 5, 7, 9, 11 and 13 were determined using ImageJ, triplicates for each analysis day. M = spheroids with 1% (v/v) Matrigel®. Values are mean ± SD, * (P ≤ 0.05), ** (P ≤ 0.01), *** (P ≤ 0.001) and **** (P ≤ 0.0001), n=1 meaning a single experiment for each group (with or without Matrigel®) consisting of triplicates was conducted. Diameter (microns) on Y axis. Analysed using a 2-way ANOVA with Tukey's multiple comparisons test: spheroids with Matrigel® vs spheroids without it (mean spheroid size for each analysis days).*

## 3.7 Discussion

The objective of seeding both cell lines at different densities (10-30,000 cells/well) was to assess their ability in producing uniformly shaped spheroids with a necrotic core, to mimic the tumour microenvironment. In addition, the aim was to examine the growth patterns of these spheroids at low seeding densities (1000 cells/well ± 1% (v/v) Matrigel®), which would better simulate the situation of a live growing tumour without any necrosis. This evaluation would determine the suitability of these spheroids for experimental use.

### 3.7.1 K1 Spheroids

Varying seeding densities of K1 cells were examined for their ability to aggregate into spheroidal structures, with all densities capable of generating spherical and symmetrical bodies when plated in ULA plates. However, the literature reports differing outcomes for K1 cells under similar conditions. One study by Oh *et al*., (2022), investigated two seeding densities of 1000 and 5000 cells/well across nine TC cell lines. Their findings indicated that regardless of seeding density, K1 cells failed to exhibit aggregation or any formation of viable spheroids. A result that contrasts with findings in this study where K1 spheroids at 1000 cells/well formed compact structures consistently. This discrepancy could be due to the minor differences in methodologies used for spheroid formation, as Oh *et al.,* used 1% (w/v) agarose, while the current study used 1% (v/v) Matrigel®. Regardless, it was demonstrated that even without the incorporation of a hydrogel, K1 spheroids at this seeding density and greater, were perfectly capable of forming viable and uniform shaped spheroids. Additionally, the use of flat-bottom plates in Oh *et al.*'s study may have influenced their results, as ULA plates are designed to facilitate the aggregation of TC cells (Sekhar *et al.,* 2022; Brüningk *et al.,* 2020; Hagemann *et al.,* 2017).

The current study's observations support the findings of Sekhar *et al.* (2022)*,* who observed consistent spheroid formation by K1 cells seeded at 10,000 cells/well in ULA plates, without the use of any additives such as Matrigel®, which was also identified in the current to be unnecessary for higher seeding densities. Images of the spheroids at 10, 000 cells/well by this group show similarities morphologically to the ones seen in the current investigation, with many irregular structures. This shared observation justified the decision to expand the

seeding density range to 20,000 cells/well which ultimately produced more uniform and symmetrical bodies compared to the 10,000 cells/well density.

Brüningk *et al.,* (2020) and Hagemann *et al.,* (2017) had investigated the use of ULA plates in generating spheroids against other popular methods using several head and neck cancer cell lines. They found enhanced spheroid formation and more consistent production of homogenous structures when compared to commonly used approaches, such as the hanging drop technique. Furthermore, the use of ULA plates has been shown to be optimal for forming tight spheroidal structures, regardless of the cell line, as demonstrated in a review by de Souza *et al.,* (2021), who analysed various methods of generating spheroids commonly used in 3D culture studies across multiple different cancer cell lines. They found that ULA plates provided reproducible spheroids, while also being the simplest to set up, requiring only a single step of seeding cells into each well.

### 3.7.2 8305c Spheroids

For the 8305c cells, only the lowest seeding density of 10,000 cells/well (including the 1000 cells/well) spheroids, consistently produced uniform shapes and sizes, whereas higher seeding densities (20/30,000 cells/well), frequently resulted in irregular and asymmetrical spheroids. Oh *et al.,* (2022) had also investigated an ATC cell line, 8505c, at two seeding densities of 1000 and 5000 cells/well in a flat bottomed plate. They reported that the 8505c spheroids had formed very tight and compact spheroids that shrunk in size over time (10-day observation). In contrast, better spheroid aggregation and symmetrical structures at the lower seeding densities were observed in the current study. Moreover, a very similar trend of a gradual decline in size over time observed in the Oh *et al.,* (2022) study was also seen with the larger spheroids (10/20/30,000 cells/well) produced in the current study, whereby a pronounced drop in average diameter size was recorded, before levelling out. These observation are most likely due to the self-limiting nature of spheroids once they pass a certain cell count, that causes “starving” of the inner most cells of access to vital nutrients (Wallace & Guo, 2013). Conversely, 1000 cells/well spheroids in the current study did not shrink in size over time, instead spheroids supplemented with 1% (v/v) Matrigel® showed a significant increase in size whereas the spheroids without Matrigel® showed a very consistent

and stable size throughout the incubation period (13-day observation). Again, this may be due to the use of 1% agarose coated flat-bottom plates by Oh and colleagues previously.

In contrast, Mortensen *et al.,* (2023), reported steady growth in 8305c spheroids (seeded at 1000 cells/well) even by the final 25$^{th}$ day of observation; they had also used flat-bottom plates supplemented with 1% (w/v) agarose gel. The current study's findings align with Mortensen *et al.,* (2023), as the 8305c spheroids did show enhanced growth overtime but only when supplemented with 1% (v/v) Matrigel®. Mortensen *et al.,* (2023) and Oh *et al.,* (2022), used very similar techniques and yet reported very differing growth patterns – perhaps due to alterations in the cell line being grown in different laboratories under subtly different conditions, akin to antigenic drift (Pavlacky & Polak, 2020) albeit the differences between cell lines may have influenced the outcomes.

Finally, Abols *et al.* (2015), who also investigated 8305c spheroids seeded at 2,000 cells/well further demonstrates the superiority of using ULA plates to generate spheroids as they reported continued proliferation over time (7-day observation), without the use of any hydrogel additives. These findings corroborate the observations of sustained growth (in the case of spheroids lacking Matrigel®) in this study, highlighting the fact that hydrogels are not necessary for the generation of viable spheroids, but the plating conditions and apparatus may have an adverse influence on the production of these complex structures.

### 3.7.3 K1 and 8305c

In the current study the K1 (10/15/20,000 cells/well) and 8305c (10/20/30,000 cells/well) spheroids all had reached an average diameter of 800-850 µm by day 13 despite differing greatly in seeding densities and cell types. Likewise, Browning *et al.,* (2021) had looked at changes in spheroid size over 24 days using melanoma cell lines WM793b and WM983b seeded at either 2500, 5000, and 10,000 cells/well in flat-bottomed 96-well plates coated with 1.5% (w/v) agarose. They also found that regardless of seeding density, spheroids would cease to grow any larger once they reached a certain size and maintained it for the remaining observation period; in their case once spheroids were on average 700 µm in diameter. Based on their observations it is possible that spheroids in the current study would have maintained

this size for up to 24 days as well, however there could be different growth patterns between the two cell lines thyroid vs. melanoma.

Another similarity in growth patterns exhibited by both cell lines was the sudden drop in spheroidal size before levelling out. This observed growth pattern can be attributed to the effects of compressive stress. As described by Delarue *et al.,* (2014) who investigated spheroid growth across 27 days using a variety of cell lines: HT29 cells (human colon carcinoma), CT26 cells (mouse colon adenocarcinoma), BC52 cells (human breast cancer), AB6 cells (mouse sarcoma) seeded at 20,000 cells/well in 48-well plates were coated with 1% (w/v) agarose gel. They observed rapid spheroidal expansion before reaching a steady size of around 900 µm in diameter but in the presence of stress factors spheroid growth was impeded and did not reach the usual size, however when these factors were removed, spheroids were able to reach and maintain the 900 µm size. A potential source of stress that could explain what was seen in the current study could be nutrient deprivation through the induction of a necrotic core that reduces proliferation, leading to a decrease in overall spheroid size before reaching a new steady state. Browning *et al.,* (2021), had also mentioned this in their findings, that although the outer layers of the spheroid continued to proliferate the core became necrotic through the accumulation of waste products leading to an initial loss in overall mass and subsequently levelling out via an equilibrium of proliferating and dying cells.

### 3.7.4 Use of Matrigel®

Following the protocol provided by the partner company, CN-BIO, the smaller spheroids seeded at 1000 cells/well were supplemented with 1% (v/v) Matrigel®, to determine if the matrix provided any significant aid in the growth and morphology of the spheroids.

Both cell lines exhibited noticeably greater sized spheroids when supplemented with Matrigel® compared to those grown without it. This aligns with studies by de Souza *et al.* (2021) and Hagemann *et al.* (2017), who demonstrated that Matrigel® supplementation supports spheroid integrity, resulting in more rigid structures less prone to external stresses. Moreover, the hydrogel mimics the ECM environment found *in vivo*, thereby enhancing the physiological relevance of the 3D culture model. Unfortunately, no studies have looked at size differences with and without Matrigel® supplementation following a similar protocol to the

current study in the realm of thyroid cancer. However, researchers working with breast cancer spheroids (with and without 2.5% (v/v) Matrigel®, seeded at 2500, 5000, and 8000 cells/well in ULA plates) found that spheroids supplied with Matrigel® presented with an average diameter of 700 µm compared to 350 µm for spheroids without Matrigel® by day 6 of incubation (6-day observation), a doubling in overall size. Moreover, images of their spheroids closely resembled the 1000 cells/well spheroids from the current study, ones with Matrigel® having a more spacious arrangement of cells whereas non-supplemented spheroids being more compact (Badea *et al.,* 2019).

To conclude, conflicts in findings and protocols across multiple studies, clearly demonstrates the importance of seeding densities and plating conditions, which significantly impacts cell aggregation and subsequently success in forming viable spheroids. Especially with some researchers having used the same lines with similar seeding densities and additives but reporting contradictory findings. This emphasises the need for a standardised protocol for each TC cell line for generating spheroids. Such protocols would enable reproducible results and allow for more reliable comparisons between studies, providing greater advancements in the use of these models in the hope that they can become established as a viable preclinical tool in the near future.

# Chapter 4 Optimising Experimental Parameters for K1 and 8305c Spheroid Viability

## 4.1 Introduction

Cell viability assays form a crucial component when investigating drug effectiveness as they verify whether cell death has occurred due to the cytotoxic effects of the agent (Kamiloglu *et al.,*2020). Firstly, it is important to establish the behaviour and natural cycle of the cells within a spheroid, as understanding when cells begin to undergo programmed cell death is key when assessing the proficiency of a drug. $H_2O_2$ and $NaN_3$ were used in the first instance, to investigate the usefulness of different assays in the assessment of spheroid viability, as these are known cell death inducing agents (Ji *et al.,* 2011; Xiang *et al.,* 2016). The data compiled from these assays with known metabolic inhibitors underpinned the creation of the sorafenib experiment plan (Chapter 5). A literature review showed that many different viability assays have been used for testing the effects of adding sorafenib to cell lines or spheroids (as summarised in Table 4.1). This makes comparisons between studies more challenging, but not impossible. For this reason, investigations were conducted to compare two of the most popular assays. Starting with the MTS assay, a newer and more convenient soluble alternative to the MTT assay, which is widely used for assessment of proliferation in cell cultures to quantify the number of viable cells by assessing the amount of formazan crystals produced via the reduction of the MTS (section 2.3.3/Buranaamnuay, 2021). CellTiter-Glo® 3D (CTG) was also investigated as it is specifically designed for use on 3D models by measuring ATP production as an indicator of cell viability (section 2.3.4). This was coupled with live/dead staining as it provides a visual representation of the damage induced allowing for an insight whether the agent is capable of penetrating the spheroid (section 2.3.5). In addition, IHC staining was used to identify areas of proliferation in spheroids pre/post treatment.

***Table 4.1 Cell viability assays used in sorafenib investigations on either K1 or 8305c cell lines.***

| Study | Aim | Cell Line | Assay | Findings |
|---|---|---|---|---|
| **Ruan *et al.*, 2015** | To evaluate the impact of sorafenib on the expression of genes related to iodide and glucose handling in BHP 2-7 cells carrying a RET/PTC1 rearrangement. | K1 | CCK8 | Sorafenib significantly inhibited cell proliferation, induced cell cycle arrest, and modulated signal transduction pathways in PTC cells with RET/PTC1 rearrangement, while enhancing iodide-handling gene expression and reducing glucose transporter gene expression. |
| **Lin *et al.*, 2018** | To investigate the effectiveness of combining Roniciclib with sorafenib in treating well-differentiated TC compared to monotherapies. | K1 | CytoTox96® | Combination therapy involving Roniciclib and sorafenib was more effective in treating follicular TC xenografts than using either drug alone. |
| **Celano *et al.*, 2019** | To evaluate whether co-administering Quercetin with lower doses of sorafenib could sustain anticancer effects of sorafenib against TC cells. | K1 | MTT | Combination therapy of Quercetin and sorafenib significantly enhanced anticancer effects, leading to greater reductions in cell proliferation, adhesion, and migration, and improved markers of epithelial-mesenchymal transition compared to sorafenib alone. |
| **Kim *et al.*, 2020** | To evaluate the effects of the HIF-1α inhibitor IDF-11774 on TC progression *in vitro* as a potential alternative to TKI therapy. | K1 | CTG | IDF-11774 effectively reduced HIF-1α expression and inhibited cell proliferation, migration, and anchorage-independent growth showing promise as potential therapeutic agent. |
| **Oh *et al.*, 2022** | To investigate the differences in TC cell differentiation and related iodide-metabolising proteins under 2D versus 3D culture conditions. | K1 | CTG 3D/CCK8 | TC cells exhibited reduced differentiation and altered cellular behaviours in spheroid cultures compared to monolayer culture providing more reliable models for drug discovery. |
| **Zhu *et al.*, 2022** | To investigate the antitumor effects of PLK4 inhibitor Centrinone on ATC cell lines and to evaluate its potential synergistic effect with sorafenib. | 8305c | CCK8 | Combination of centrinone and sorafenib significantly enhanced antitumor effects in ATC cell lines compared to using either drug alone. |
| **Shirazi *et al.*, 2022** | To evaluate whether combining Eugenol with sorafenib enhances apoptosis in undifferentiated TC | 8305c | MTT | Combination of Eugenol and sorafenib induced a synergistic apoptotic effect which was greater than using either drug alone. |
| **Mortensen *et al.*, 2023** | To evaluate whether combining sorafenib with the HSP90 inhibitor onalespib enhances the efficacy of treatment in TC, both *in vitro* and *in vivo*. | 8305c | XTT | Combination of sorafenib and onalespib significantly enhanced the efficacy of treatment in TC. |
| **Mortensen *et al.*, 2023** | To evaluate the potential of targeted therapies for TC by investigating the effectiveness of targeting BRAF, EGFR, and CD44v6 markers using antibody 131I-AbN44v6 without or in combination with sorafenib. | 8305c | XTT | Targeting CD44v6 with antibody 131I-AbN44v6, either alone or in combination with sorafenib, significantly impaired the growth ATC spheroids. |
| **Jingtai *et al.*, 2023** | To evaluate the synergistic effect of combining Aurora-A inhibitor, Alisertib with sorafenib in treating advanced TC. | 8305c | CCK8 | Alisertib enhanced the efficacy of sorafenib by upregulating PFKFB3-mediated glycolysis, which increases ATP supply and promotes cancer progression. This combination therapy was effective both *in vitro* and in xenograft models |

**K1 –** Papillary thyroid carcinoma cell line
**8305c –** Anaplastic thyroid carcinoma cell line
**CCK-8 -** Cell Counting Kit - 8
**MTT –** 3-(4,5-Dimethylthiazol-2-yl)-2,5-Diphenyltetrazolium Bromide Assay
**XTT –** 2,3-Bis(2-Methoxy-4-Nitro-5-Sulfophenyl)-2H-Tetrazolium, Inner Salt Assay
**CTG** - CellTiter-Glo® Assay

### 4.1.1 $H_2O_2$

$H_2O_2$ is widely utilised as a cytotoxic agent in cell viability assays due to its ability to induce oxidative stress/damage in cells due to the production of reactive oxygen species (ROS), in this case; hydroxyl radicals (•OH) and superoxide anions ($O_2$•−) capable of reacting with DNA, proteins, sugars and lipids (ref). In normal homeostatic conditions there is a balance between levels of ROS and antioxidant defences within the cell (Chidawanyika & Supattapone, 2021). However, once these ROS molecules exceed homeostatic concentrations, they overwhelm the cellular antioxidant defences resulting in genomic instability due to perturbed cellular functions such as lipid peroxidation which through a chain of reactions leads to cellular damage and functional impairment (Sies & Jones, 2020).

Both the concentration of $H_2O_2$ and the type of cell, influences the death mechanism. In thyroid cells a moderate concentration (~0.1 mM) invokes a programmed cell death pathway, known as apoptosis, whereas higher concentrations (>0.4 mM) induce uncontrollable cell death via necrosis (Song *et al.,* 2007). A literature review of 5147 publications, investigating the $H_2O_2$ concentration used in 2D cell death assays revealed a general range of 0.1-1 mM (Ransy *et al.,* 2020). Based on spheroidal work done previously at the university, compiled with the understanding that a more potent dose might be required for a 3D model, a concentration of 1.6 mM was chosen.

### 4.1.2 $NaN_3$

$NaN_3$ is another commonly used cell death agent in cell viability investigations due to its ability to inhibit cytochrome c oxidase in the mitochondrial electron transport chain, leading to apoptosis and necrosis (Tarabanis *et al.,* 2024). The inhibitor is especially potent in thyroid cells which tend to exhibit high mitochondrial activity due to these cells producing TH, a process which is very energy demanding (Villanueva *et al.,* 2013). Mitochondria allow for ATP production via oxidative phosphorylation which is impaired in the presence of $NaN_3$ inducing cellular stress and ultimately cell death (Fernández-Moncada & Barros, 2014). A literature review investigating the most common $NaN_3$ concentrations is not available to the best knowledge of the author, a range was generated based on several recent studies investigating thyroid/other cell viability utilising $NaN_3$ as a cell death inducer. It was determined that $NaN_3$

was most effective at concentrations ranging from 10-15 mM (Chen *et al.,* 2023; Gandhirajan *et al.,* 2018, Srivastava *et al.,* 2014, Mass *et al.,* 2012, *Ji et al*., 2011) with one recent study using a much higher concentration of 76 mM (Eiermann *et al.,* 2022). As done with the $H_2O_2$ dose choice, due to most of the work having been done on monolayers a concentration of 30 mM was chosen.

## 4.2 Aims

The first aim was to establish a cell death dose-response curve for both $H_2O_2$ and $NaN_3$ in K1 and 8305c spheroids created with varying seeding densities. These results would then inform the experimental plan for the optimal time point at which to start treatment, ensuring the cells forming the spheroids have not begun natural cell death processes during the treatment period, which may otherwise obscure the cell death induced by the treatment agents.

## 4.3 Methods

### 4.3.1 Optimisation of cell death assay/agent on K1/8305c spheroids

Initial viability assays were carried out on K1 cells seeded at 20,000 cells per well in a ULA plate (section 2.3.1), using $H_2O_2$ as the cell death inducing agent. Spheroids were incubated with $H_2O_2$ (1.6 mM) for 24 h on days 2, 4, 6, 8, 10 and 12 followed by MTS analysis on days 3, 5, 7, 9, 11 and 13; triplicate spheroids were treated at each time point. Triplicates of controls were also analysed as a baseline for each treatment day, where they had their media replenished, without $H_2O_2$ being added. Following the initial set of results, the incubation period with $H_2O_2$ was increased to 48 h and remained as such for all subsequent experiments.

The same protocol was utilised for treatment of the 8305c spheroids, except that 10,000 cells/well (ULA plate) were used to generate the spheroids, based on optimisation data described in Chapter 3. For the 8305c spheroids only $NaN_3$ with 48 h incubation was used. The $H_2O_2$ solutions were freshly prepared prior to each treatment day due to rapid decomposition (Schieber and Chandel, 2014). For consistency, $NaN_3$ was also made up on the days of treatment.

As mentioned previously (Chapter 3), the inclusion of the 1,000 cells/well spheroids into the protocol occurred during the final experiments involving $NaN_3$. Due to supply issues involving the 8305c cell line and initial culture, spheroids seeded at 10,000 cells/well were the only model to be tested in these investigations ($NaN_3$ only), with the 1,000 cells/well 8305c spheroids being incorporated into the sorafenib experiments (Chapter 5) without in depth optimisations.

### 4.3.2 Assessment of cell viability

Cell viability post $H_2O_2$/$NaN_3$ treatment was analysed using MTS, CTG, FDA/PI staining and IHC on each of the set time points, as described in section 2.3. MTS was initially used to assess the number of living cells based on the quantity of formazan produced. CTG was also trialled as it was claimed to be a more reliable assay specifically designed for assessing the viability of 3D microtissues by measuring ATP production (Riss *et al.,* 2014). Figure 4.1 demonstrates the layout of the plates for spheroid growth, treatment allocation and subsequent analysis.

In addition to the functional assays, a secondary tool to confirm and visualise cell death within the spheroids was FDA/PI staining (section 2.3.5). Images of three spheroids were taken for each analysis day on a Zen fluorescence microscope using pre-set filters (FDA – 495 nm and PI – 596 nm excitation) at 10x magnification and analysed using ImageJ software to determine the percentages of live to dead cells.

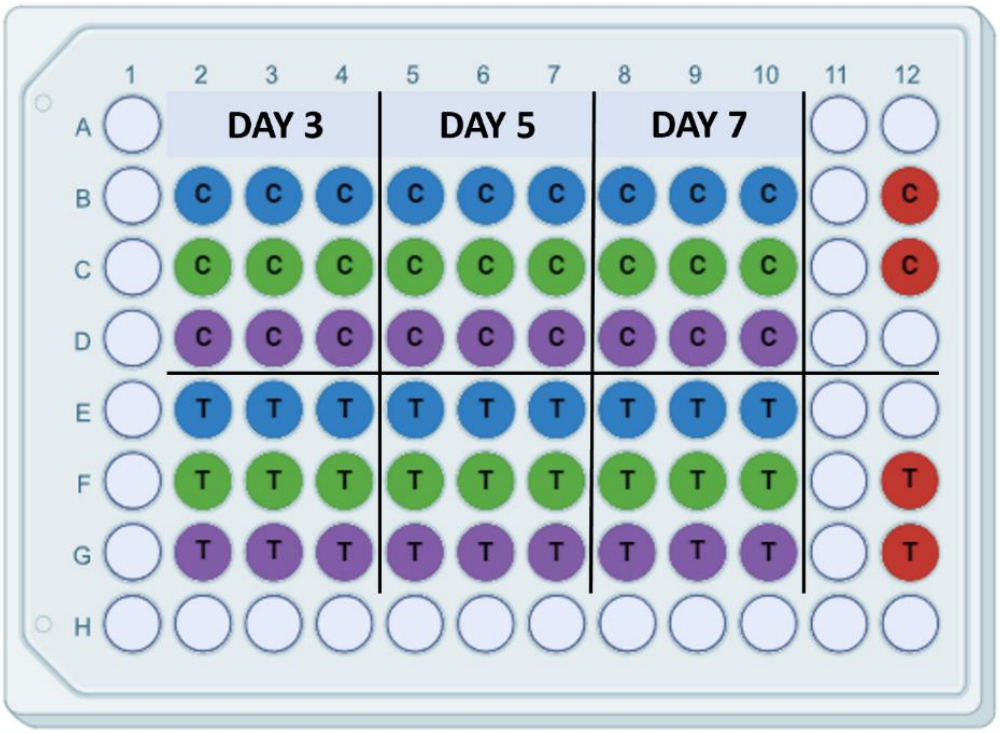


***Figure 4.1 Schematic representation of a 96-well ULA plate set-up for the cell death assays.*** *C – control wells consisting of a spheroid with media; T – treated wells consisting of a spheroid with media containing either $H_2O_2$/$NaN_3$. Colour coded wells display spheroids designated for a specific analysis assay, Blue – Fluorescent microscopy (FDA/PI), Green – MTS/CTG assay, Purple – IHC and Red – additional control wells lacking any spheroid. An additional plate would be set-up alongside this one for the remaining analysis days (9-13). Image generated using Biorender.*

## 4.4 Statistical analysis

Data was analysed using Graph pad software (v9.5.1). A two-way ANOVA with Tukey's multiple comparisons test was performed for each experiment, as it has the ability to compare the individual and combined effects of time and treatment as independent variables on the viability of the spheroids.

# Results

## 4.5 Measuring the effects of $H_2O_2$ on K1 spheroids

Post-MTS analysis of spheroid viability showed that the values for $H_2O_2$ (1.6 mM) treated spheroids were very similar to those of the untreated control group. The data showed a slight, yet discernible, decrease in the formazan product detected among the treated spheroids compared to the controls, suggesting a minor reduction in spheroid viability following treatment (Figure 4.2). Although a large decline in values was seen from day 3 to 5, this trend was observed in both control and treatment groups therefore this drop in viability is most likely not attributable to the cell death agent. The only statistically significant difference in spheroid viability between treated and control groups was recorded on day 7. This suggests that $H_2O_2$ had a minimal effect on spheroid viability following a 24 h incubation period.

The lack of any indication that cells were being killed was further supported through the analysis of FDA/PI staining (worked example, Figure 4.3). Before any analysis was performed it was noted that very little cellular damage had taken place as evidenced by the abundance of green (viable cells) staining with very little red (dead cells; Figure 4.4). ImageJ measurements revealed very high live cell percentages which clearly comprised the majority of the spheroid with the only case of dead cells surpassing the living being seen on day 13 in the treated group. The percentage of viable cells in the control group did not fall below 80% across the observation period, which is similar to what was seen in the treated group where it did not drop below 70%, until the last day. Despite the dead cell percentage exceeding that of the live, ImageJ does struggle with images that are out-of-focus and thus can provide misleading results. Which is why it serves as a confirmatory tool rather than a standalone assessment, especially when working with 3D models which can make clear image capture more challenging unless using confocal microscopy (North, 2006). Regardless, $H_2O_2$ did not induce the expected cell death and as a result incubation with the cell death agent was increased to 48 h.

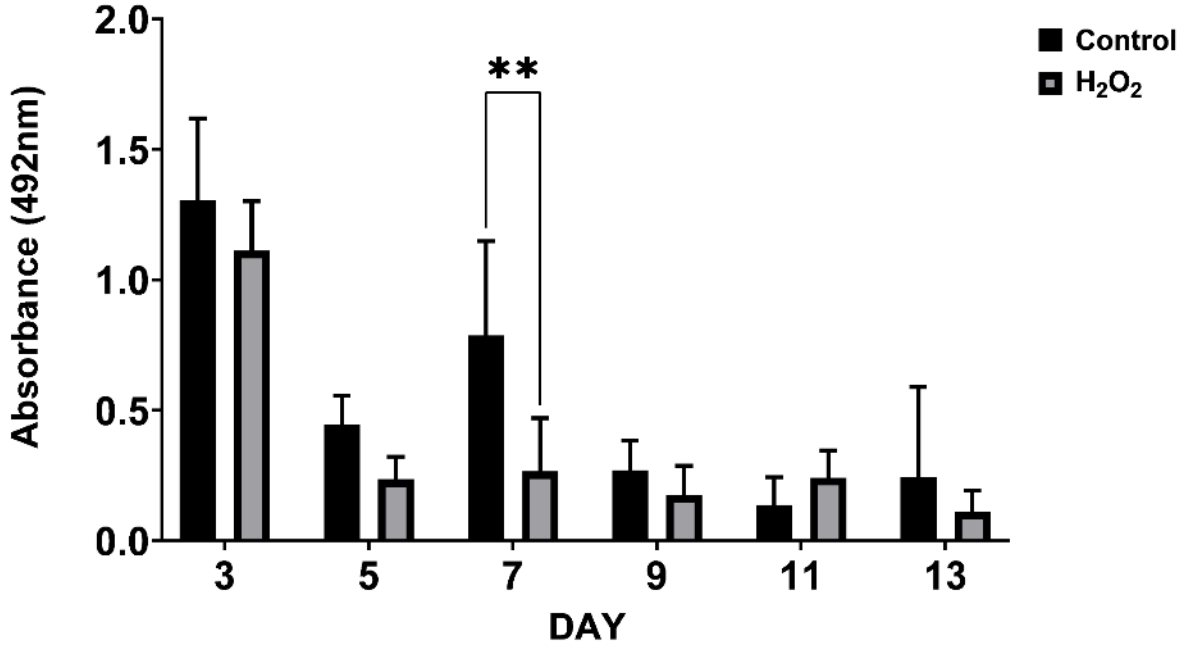


***Figure 4.2 MTS absorbance values (492nm) for untreated (black) and treated K1 (grey) spheroids (seeded at 20,000 cells) with $H_2O_2$ (1.6 mM) for 24 h.*** *MTS analysis took place on spheroid maturity days 3, 5, 7, 9, 11 and 13. A single experiment consisting of triplicate spheroids were analysed on each day. Analysed using a 2-way ANOVA with Tukey's multiple comparisons test: control vs treated (for each analysis day). Values are mean ±SD, ** (P ≤ 0.01), n=1.*

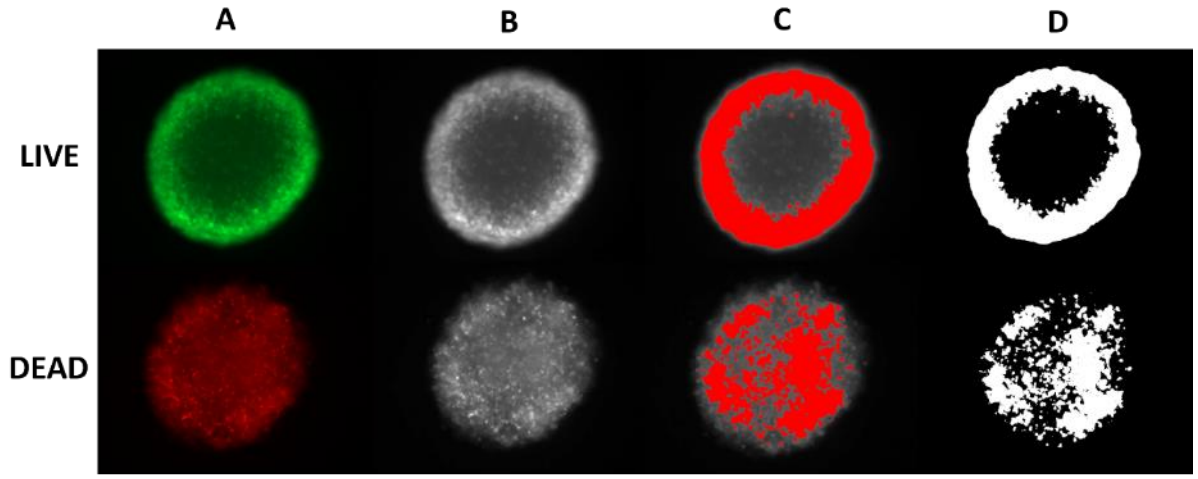


| LIVE | TOTAL | DEAD |
|---|---|---|
| 94063 | | 70110 |
| | 164173 | |
| 57.295 | | 42.705 |

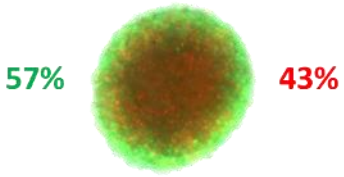


***Figure 4.3 Worked example for determining the live/dead cell percentages in a spheroid using ImageJ.*** *A – fluorescent images of the spheroid stained with FDA (green) and PI (red) markers. B – images were converted into grayscale. C – individual cells were then highlighted. D – highlighted cells were confirmed and measured. The values were exported into Microsoft Excel and totalled to reveal the overall percentages of live/dead cells within that particular spheroid. Triplicates for each timepoint (days 3, 5, 7, 9, 11 and 13) for both treated and control groups were analysed using this method, images are representative.*

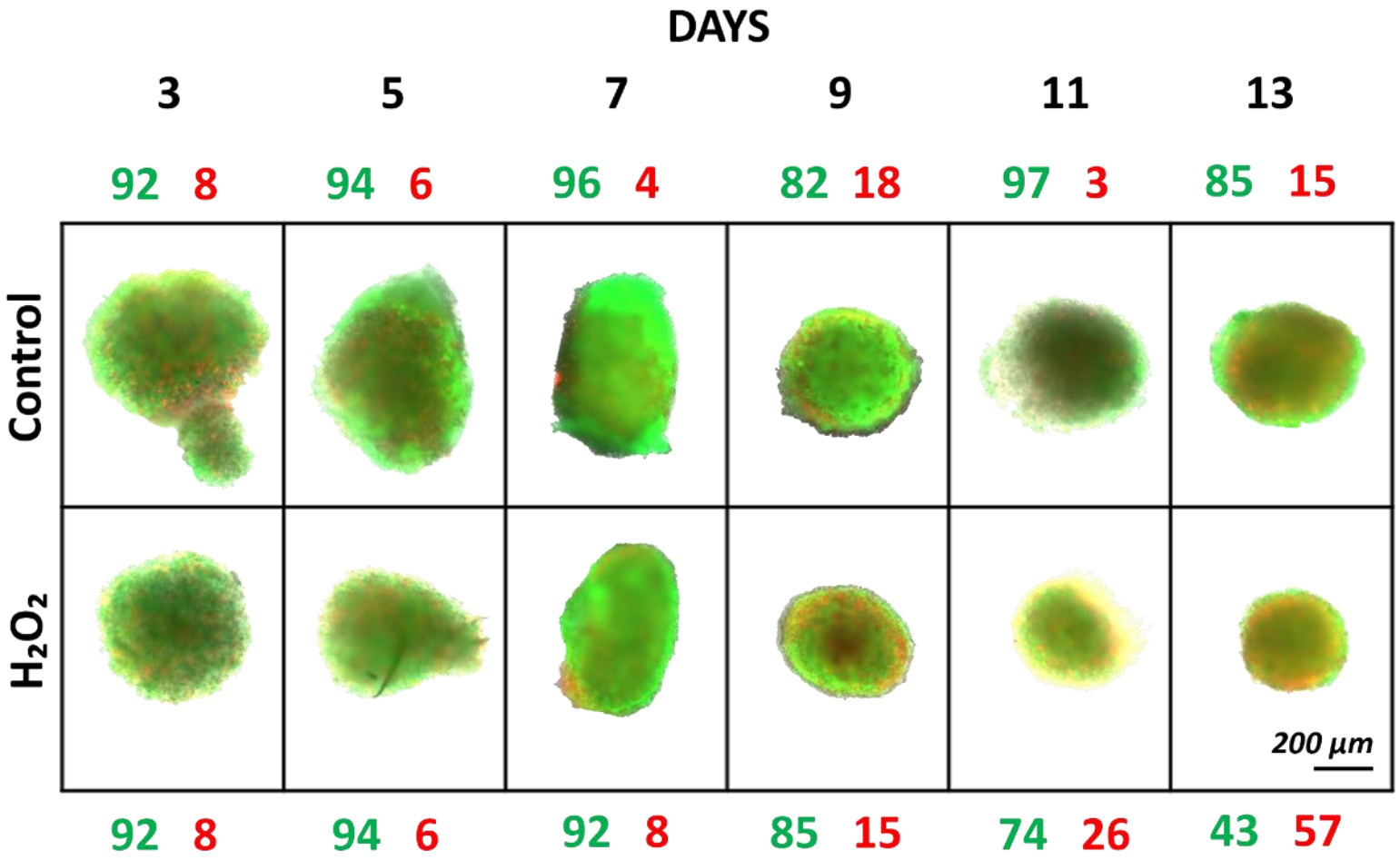


***Figure 4.4 Fluorescent images of FDA/PI stained K1 spheroids (seeded at 20,000 cells) post 24 h $H_2O_2$ (1.6 mM) treatment.*** *Images were taken using a Zeiss fluorescent microscope at 10x magnification. Untreated spheroids (top row) and treated spheroids (bottom row). Images are representative of a single investigation with triplicates for each timepoint (days 3, 5, 7, 9, 11 and 13). ImageJ was used to produce the percentages of live to dead cells (green – live, red – dead).*

Increasing the incubation time resulted in more pronounced reductions in the metabolic activity of the spheroid at all time points compared to the control. All analysis days (apart from day 7) demonstrated a similar trend between the treated and control groups, the former consistently displaying approximately half of the MTS absorbance values compared to their respective control group. Significant reductions in metabolic activity in the treated group were recorded on days 5, 11, and 13 (Figure 4.5). Although less cell viability was seen in the 48 h treated spheroids compared with those incubated for 24 h, fluorescent image analysis still did not show convincing evidence of $H_2O_2$ penetration throughout the spheroids.

Day 13 displayed the closest values to complete cell death whereby the analysed spheroid displayed that 80% of its structure was comprised of dead cells (Figure 4.6). Initially, the dead cell percentage was at 17% on day 3 analysis, gradually increasing to 38-49% between days 5-9, finally reaching 71 and 80% on day 11 and 13, respectively. The MTS did coincide with the fluorescent images for the final two analysis days whereby significant drops in viability had been recorded, but it did not agree at day 5 where, although the live cell percentage dropped from 83 to 63%, it did retain a majority population of live cells. This suggested that the age of the spheroid had a major influence on the spheroid's susceptibility to the cell death agent. Comparing fluorescent images to the 24 h treated spheroids it was revealed that $H_2O_2$ appeared to majorly affect only the outer lining of the structure, with red staining mostly concentrated on the outer layers.

An IHC investigation was carried out to confirm what was seen in the fluorescent images using Ki67, a well-known marker for proliferating cells (Aung *et al.,* 2021). When examining the images of $H_2O_2$ treated spheroids it was clear that staining was present throughout the sample, bearing strong resemblance to the untreated spheroid, indicating cells continued to proliferate even in the presence of $H_2O_2$ (Figure 4.7). Regardless, this further highlighted the inconsistency in the action of $H_2O_2$ and inability to effectively permeate the spheroid structure so for this and the aforementioned reasons, a new cell death agent was trialled.

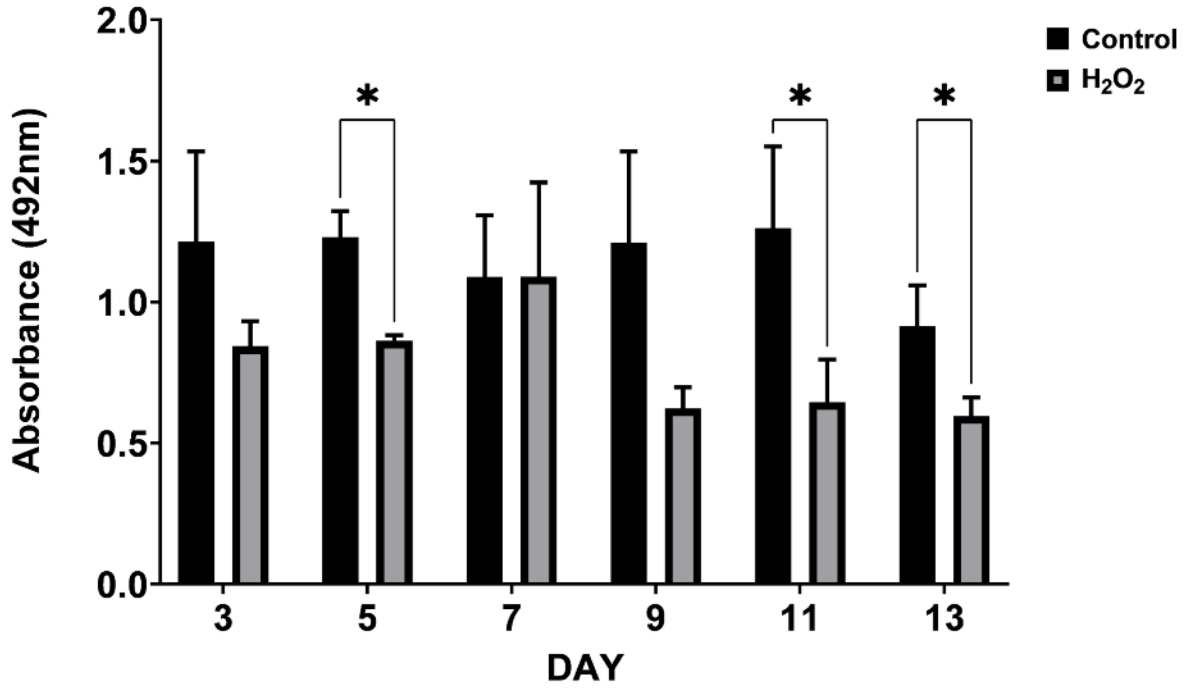


***Figure 4.5 MTS absorbance values for untreated and treated K1 (20,000 cells/well) spheroids with $H_2O_2$ (1.6 mM) for 48 h.*** *MTS analysis took place on spheroid maturity days 3, 5, 7, 9, 11 and 13. A single experiment consisting of triplicate spheroids were analysed on each day. Analysis was done using a 2-way ANOVA with Tukey's multiple comparisons test: control vs treated (for each analysis day), values are mean ±SD, * ($P \leq 0.05$), n=1.*

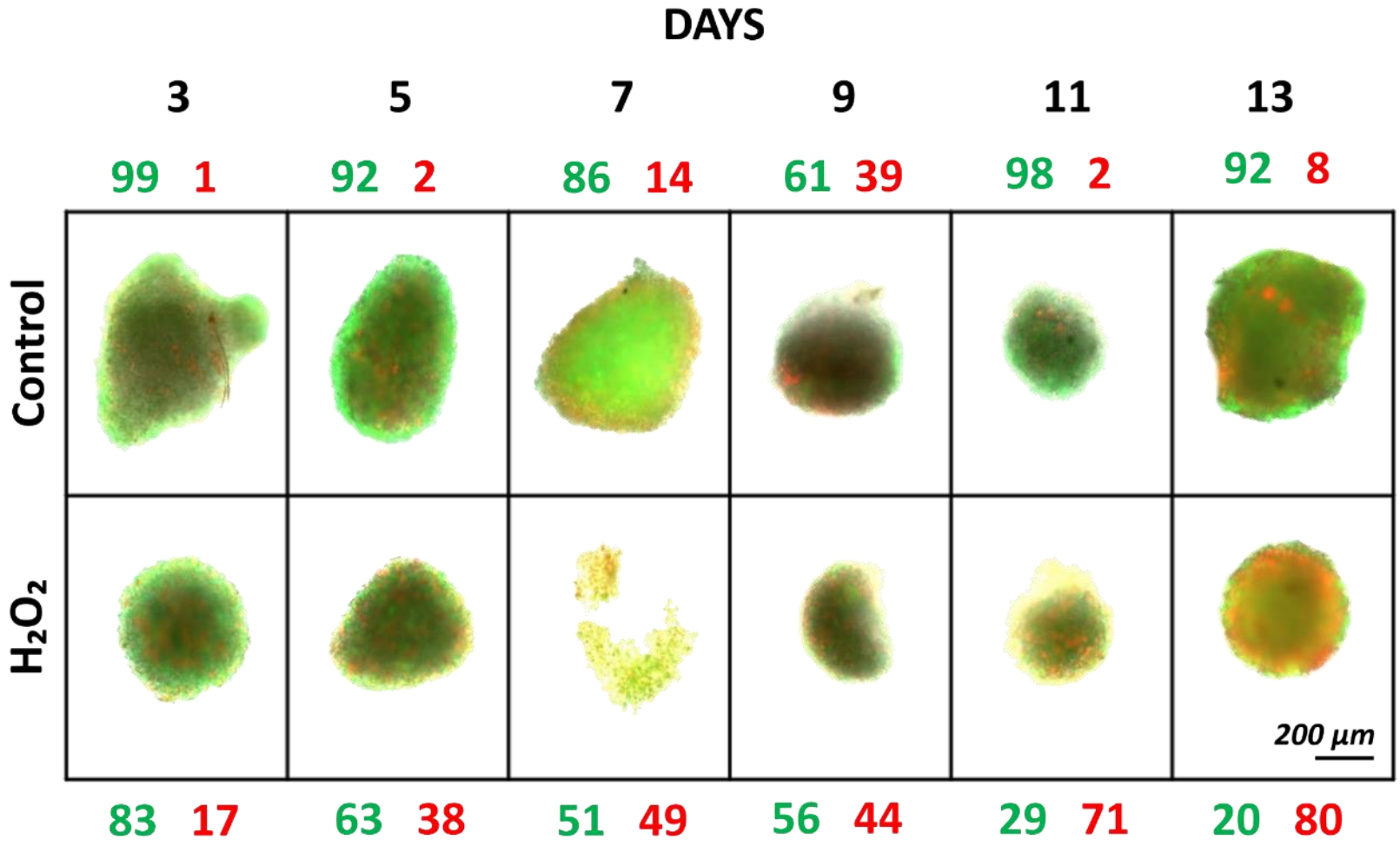


***Figure 4.6 Fluorescent images of FDA/PI stained K1 (20,000 cells/well) spheroids post 48 h $H_2O_2$ (1.6 mM) treatment.*** *Images were taken using a Zeiss fluorescent microscope at 10x magnification. Untreated spheroids (top row) and treated spheroids (bottom row). Images are representative of a single investigation with triplicates for each timepoint (days 3, 5, 7, 9, 11 and 13). ImageJ was used to produce the percentages of live to dead cells (green – live, red – dead).*

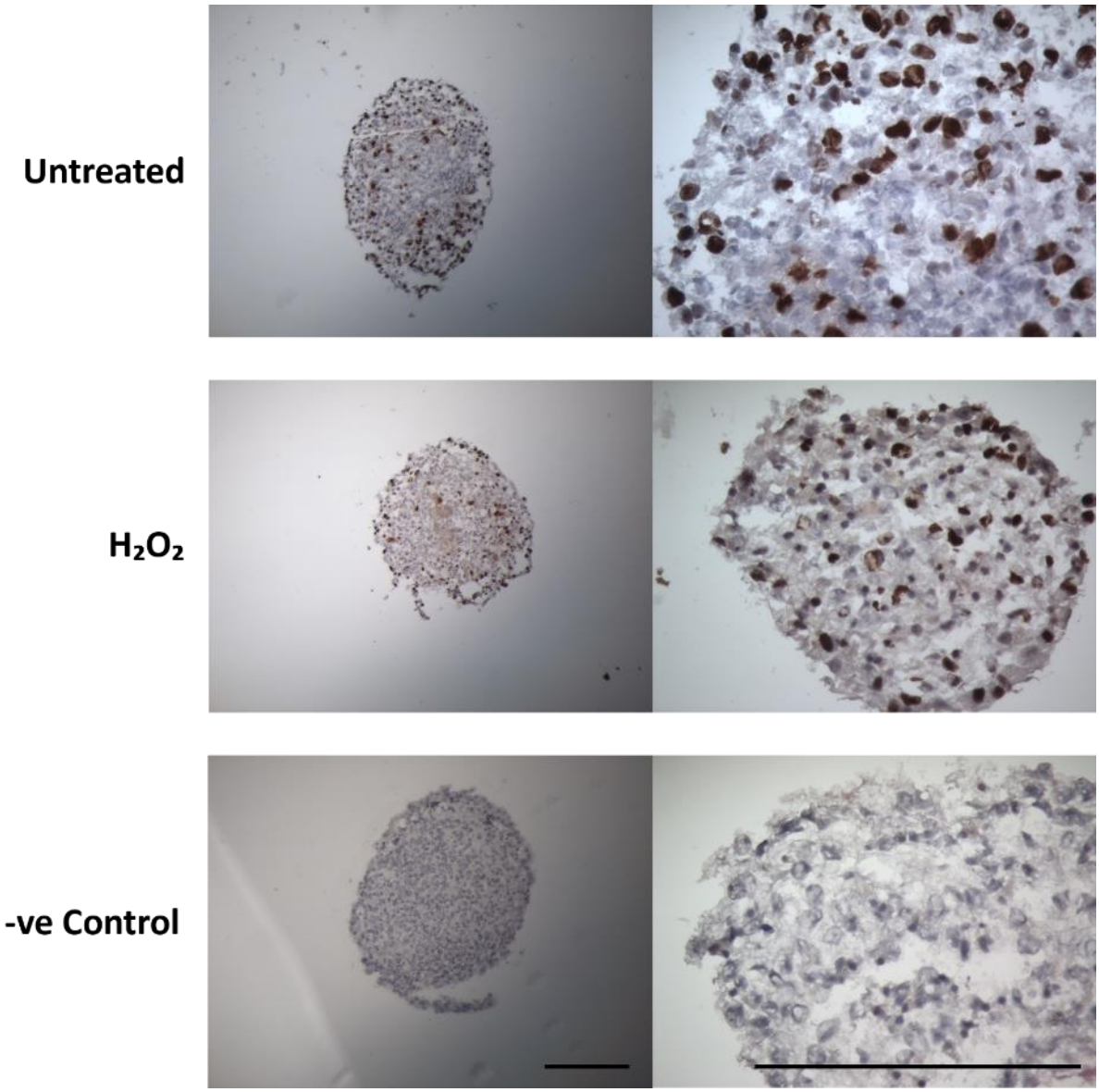


**Figure 4.7** ***K1 20K spheroids post 48 h $H_2O_2$ (1.6 mM) treatment stained with marker Ki67 for IHC.*** *Images were taken using brightfield light microscope at 10 and 40x magnification. Untreated spheroids (top row), $H_2O_2$ treated spheroids (middle row), and a negative control* (isotype control, IgG1, bottom row). *Triplicates for each timepoint were examined (days 3, 5, 7, 9, 11 and 13), images are representative of a single experiment. Scale bar 250 µm.*

### 4.5.1 Trialling $NaN_3$ as a potential cell death agent alternative on K1 spheroids

As a result of $H_2O_2$ not producing the expected amount of kill and the inability to penetrate the spheroids effectively, affecting only the cells covering the outer layers of the spheroid, $NaN_3$ (30 mM) was trialled, using the 48 h timepoint which was previously determined to be most effective.

A preliminary trial was conducted in order to determine whether $NaN_3$ was capable of penetrating the spheroid. To confirm this, six spheroids were incubated until they had reached a maturity of 5 days before a triplicate of spheroids were treated with $NaN_3$ whereas the remainder were left untreated with only a medium exchange and incubated for 48 h. At the 24 h mark Hoechst (20 mM) stain was added to each well. Once spheroids completed the treatment period, the medium was removed, and the wells were washed three times and replenished with 200 µL of PBS. Using confocal microscopy, a Z-stack was compiled (section 2.3.5.3/Figure 4.8). The confocal investigation revealed successful penetration of $NaN_3$ to the core of the spheroid, as highlighted by the observably fewer Hoechst-stained cells at the centre of the treated spheroids. This indicated that the stain was not effectively taken up by cells in this region, likely due to membrane compromise caused by $NaN_3$ with cells being unable to retain the stain. In contrast, the untreated spheroids clearly showed more Hoechst staining throughout the centre, indicating the presence of viable cells.

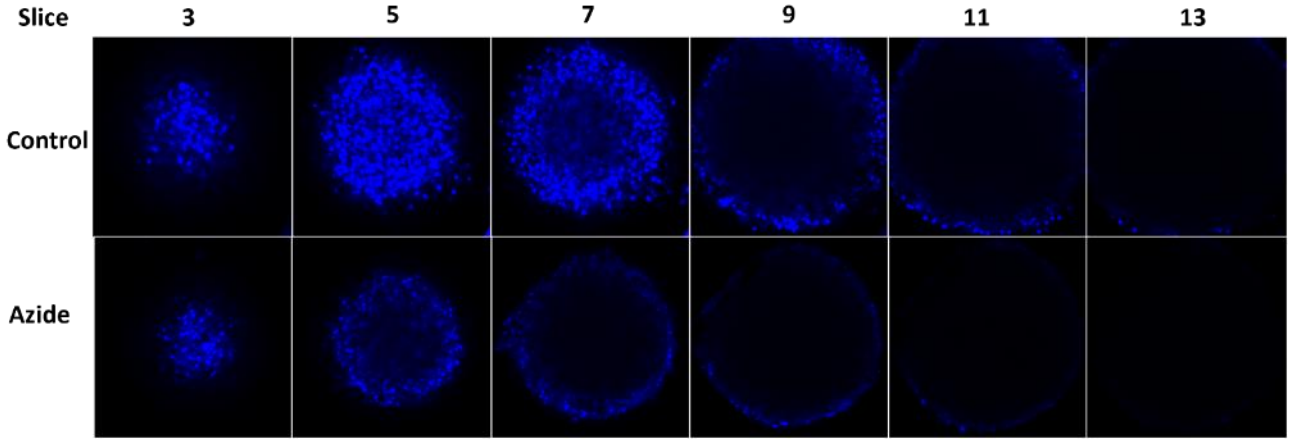


***Figure 4.8 Z-stack of K1 Hoechst-stained spheroids un/treated with $NaN_3$.*** *Images were captured using a confocal microscope (379 nm excitation, with images taken at different depths (slice every 5 µm) of the spheroid structure to assess $NaN_3$ penetration. Representative slices chosen to highlight stain presence at the centre of the spheroid. Three treated and three untreated spheroids were examined in a single experiment.*

Following the initial trials with $NaN_3$, MTS data revealed absorbance values showing a consistent trend of being lower in the treated groups compared to the controls, with a significant reduction being seen on the final day of the experiment (Figure 4.9). In addition, each bar had wide error bars due to the high variability in values when analysed using MTS. It is important to note that throughout the three repeats, on analysis day 5, two spheroids were lost and on days 9 and 11, a single spheroid, which may explain the similar values between the control and treated groups. All four of these lost spheroids disaggregated rendering them untestable, which was not experienced with the $H_2O_2$ investigations, although only a single experiment was possible.

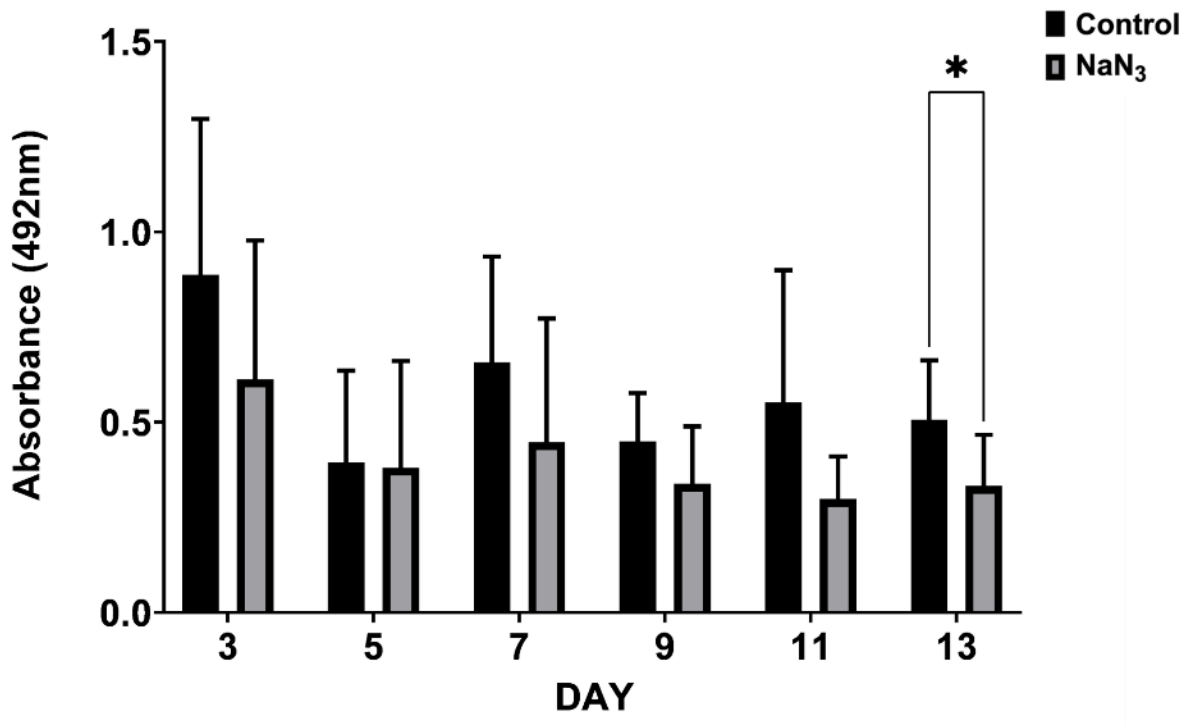


***Figure 4.9 MTS absorbance values for untreated and treated K1 20K spheroids with $NaN_3$ (30 mM) for 48 h.*** *MTS analysis took place on spheroid maturity days 3, 5, 7, 9, 11, and 13. Three independent experiments consisting of triplicates were conducted. A 2-way ANOVA with Tukey's multiple comparisons test was used; control vs treated (for each analysis day), values are mean ±SD, * ($P \leq 0.05$), n=3.*

The fluorescent images did not reflect the small reductions in viability observed with the MTS assays. However visually, there was a noticeable difference in staining patterns between the treated and untreated spheroids (Figure 4.10). Prominent red staining was seen for all of the spheroids in the treated $NaN_3$ group, with virtually complete death being observed in spheroids grown for 7 days or longer. This was contrary to the observations following $H_2O_2$ treatment, where minimal red (dead cell) staining was seen after 24 and 48 h of incubation. . The control spheroids maintained at least 96% viability at all time points. Even the "youngest" spheroid grown for 3 days showed over 80% dead cells following treatment with $NaN_3$, and although the percentage dropped to 61% at 5 days following treatment, this was most likely due to the shrinkage of the spheroid making it challenging to capture a clear image, therefore potentially skewing percentage readings.

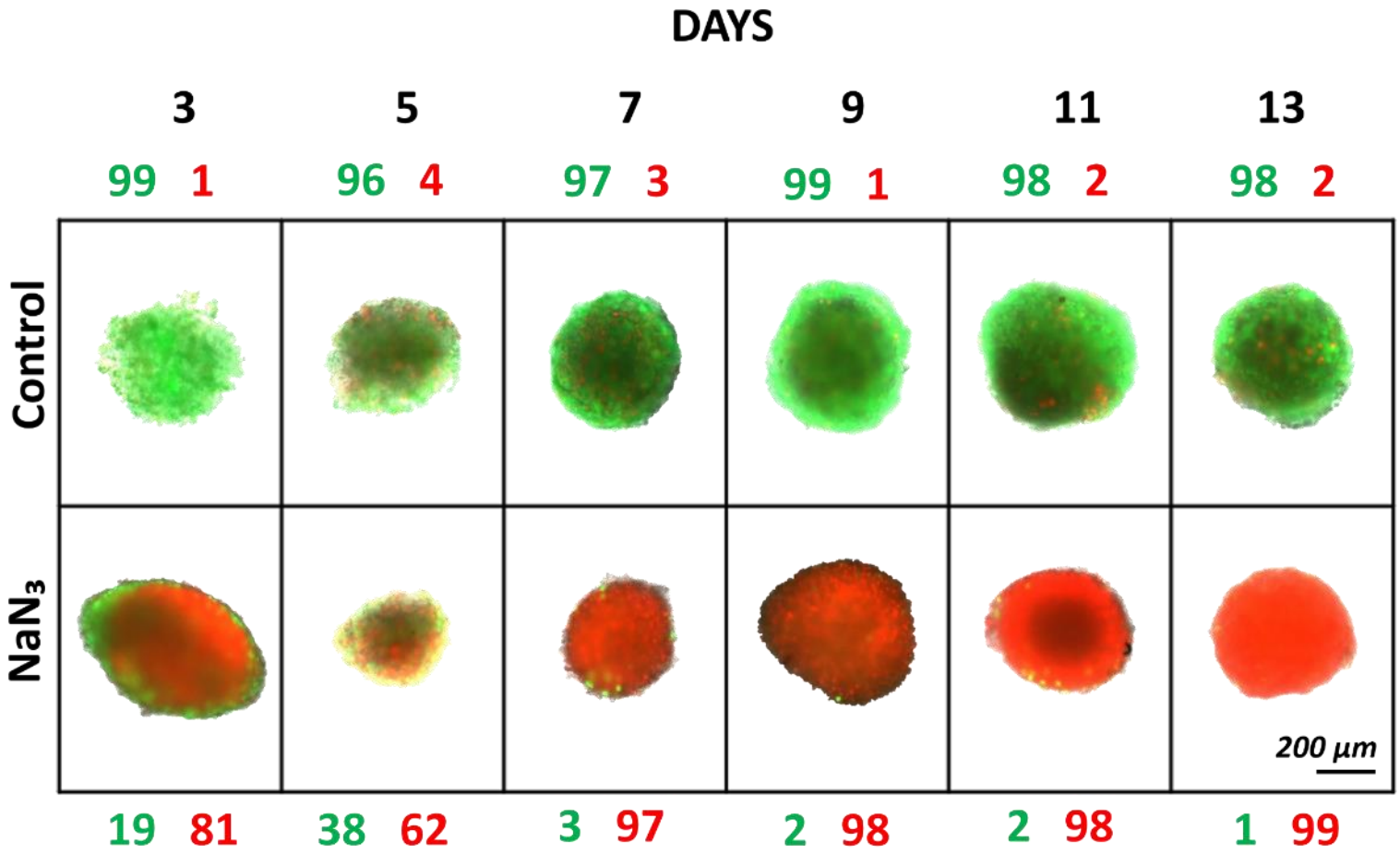


***Figure 4.10 Fluorescent images of FDA/PI stained K1 20K spheroids post 48 h $NaN_3$ (30 mM) treatment.*** *Images were taken using a Zeiss fluorescent microscope at 10x magnification. Untreated spheroids (top row) and treated spheroids (bottom row). Images are representative of a single investigation with triplicates for each timepoint (days 3, 5, 7, 9, 11 and 13). ImageJ was used to produce the percentages of live to dead cells (green – live, red – dead).*

Based solely, on the fluorescent images, it appeared that $NaN_3$ was a highly effective cell death inducer which was capable of permeating the dense spheroidal structure, which was confirmed by confocal microscopy. This finding was also congruent with IHC staining which showed the absence of staining near the centre of the sample indicating cells were not proliferating, with positive staining only being seen round the outer layers of the spheroid (Figure 4.11). The MTS assay however did not demonstrate this pattern of damage and as a result an alternative viability assay was trialled.

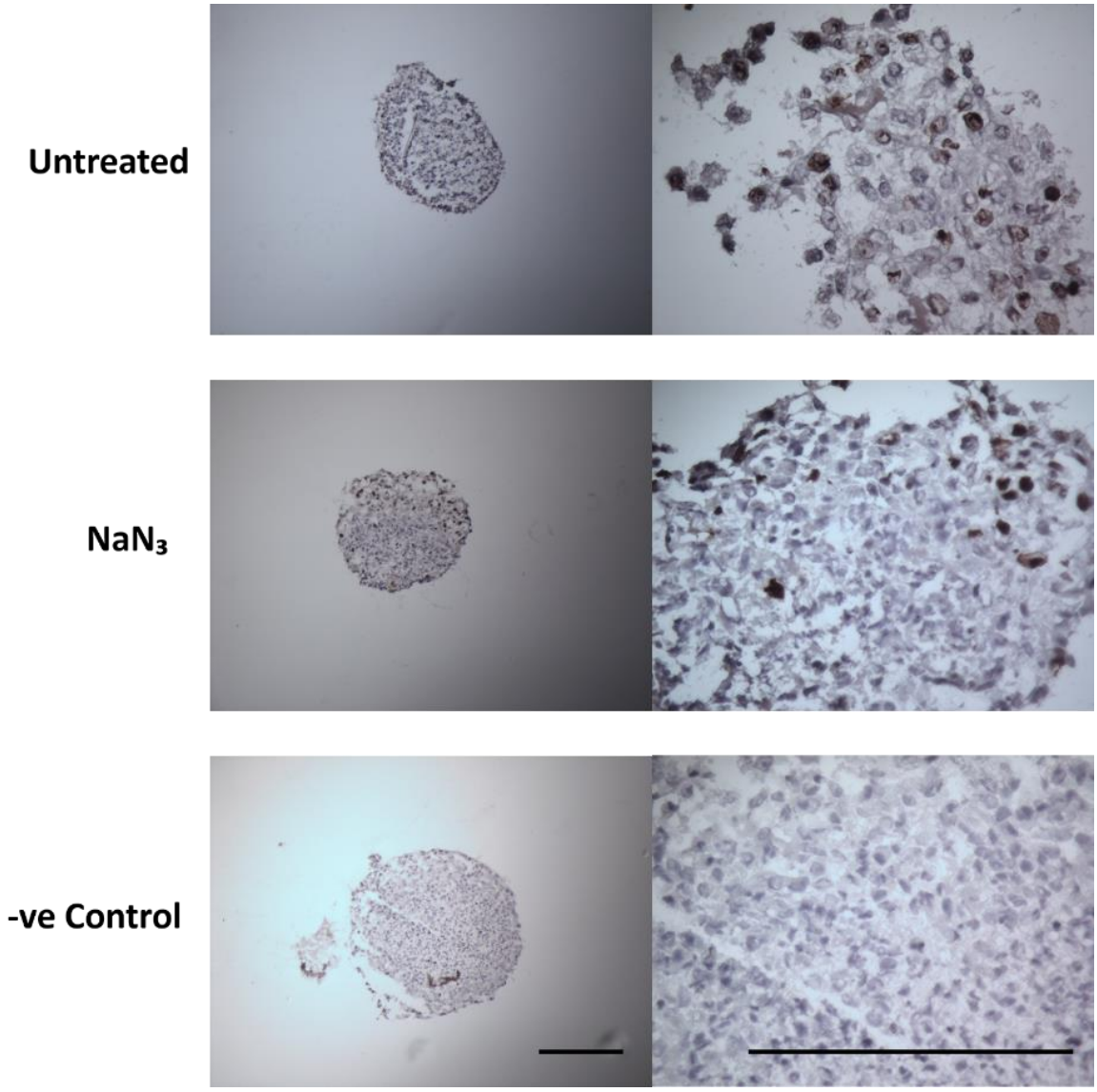


***Figure 4.11 K1 20K spheroids post 48 h $NaN_3$ (30 mM) treatment stained with marker Ki67 for IHC.*** *Images were taken using brightfield light microscope at 10 and 40x magnification. Untreated spheroids (top row), $H_2O_2$ treated spheroids (middle row), and a negative control (isotype control, IgG1, bottom row). Triplicates for each timepoint were examined (days 3, 5, 7 ,9, 11 and 13), images are representative of a single experiment. Scale bar 250 µm.*

Due to the discrepancy between the MTS data and FDA/PI staining, the CTG assay was employed to evaluate a different parameter, ATP production, as a potentially more informative and accurate measure of cell viability as $NaN_3$ inhibits ATP production by cellular mitochondria leading to cell death. The CTG assay was conducted three times on separate occasions using spheroids grown for 3, 5, 7, 9, 11, and 13 days, which were then incubated with $NaN_3$ for 48 h.

At all time points, there was a reduction in luminescence relating to reduced ATP production, following treatment with $NaN_3$ (Figure 4.12). Between the treatment groups, treated spheroids grown for 3, 5, and 9 days displayed marginal but not significant reductions in viability, whereas the spheroids grown for 7, 11 and 13 days had shown significant declines in luminescence values compared to the controls. Spheroids treated and analysed on day 7 had exhibited extremely low values, either $NaN_3$ was highly effective in killing spheroids or some were absent from CTG analysis, potentially through human error during relocation into a new plate.

Given the reproducibility of the CTG data and its better correlation with the live/dead fluorescent and IHC imaging analyses, $NaN_3$ was confirmed as the most suitable cell death inducer whereas CTG was selected as the preferred assay for assessing treatment effects for the remaining experiments. Moreover, CTG findings, along with the MTS results, indicated that days 7-9 consistently exhibited the highest viability readings, which helped determine the optimal time period for treating K1 spheroids seeded at 20,000 cells/well.

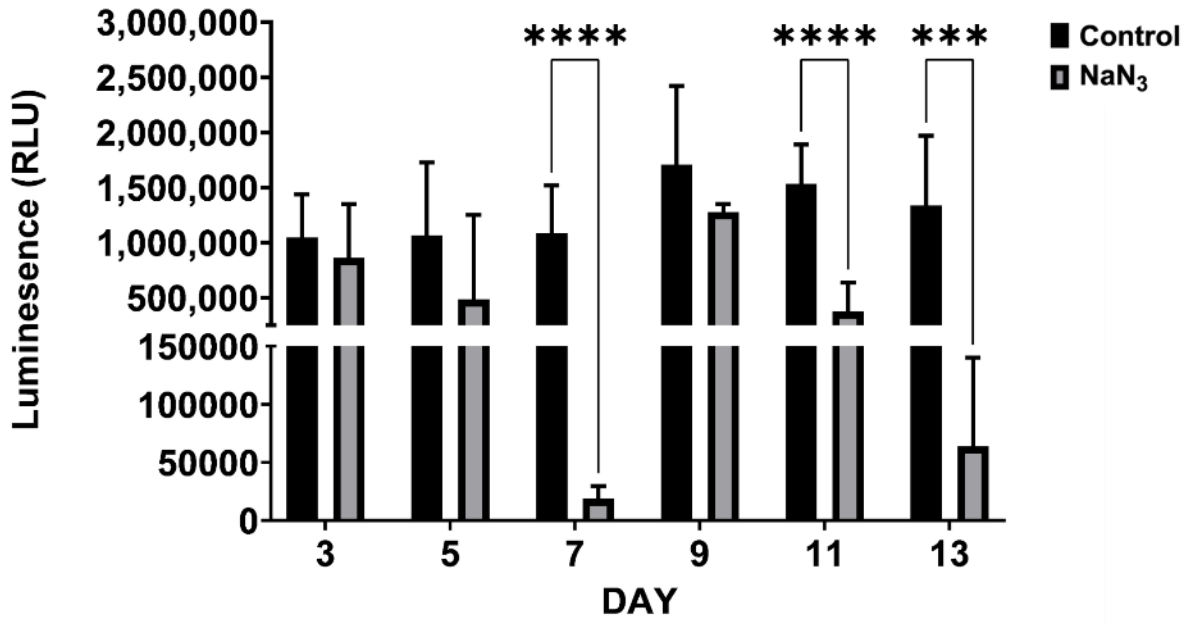


***Figure 4.12 Luminescent values from the CTG assay for untreated and treated (30mM $NaN_3$ for 48 h) K1 spheroids (seeded at 20,000 cells).*** *Three independent experiments consisting of triplicates were conducted whereby CTG analysis took place on spheroid maturity days 3, 5, 7, 9, 11, and 13. Data were analysed using a 2-way ANOVA with Tukey's multiple comparisons test; control vs treated (for each analysis day) values are mean ± SD, *** ($P \leq 0.001$) and **** ($P \leq 0.0001$), n=3.*

### 4.5.2 Effects of $NaN_3$ Treatment on K1 1000 cell/well Spheroids with and without Matrigel®

K1 spheroids were seeded at 1,000 cells/well in ULA plates, one with the inclusion of 1% (v/v) Matrigel® and one without; for two independent repeats (analysed using either MTS or CTG) as described in section 2.2.1. This was done to observe their response to treatment with $NaN_3$, and to see how effective each assay was at producing reliable results with the smaller spheroids. As previously discovered (Chapter 3), the inclusion of 1% (v/v) Matrigel® significantly aided the growth of the spheroids (section 3.7.4). The aim was to see whether the inclusion of Matrigel® had any impact on viability and thus determine the optimal treatment timeframe for these smaller spheroids.

Based on the 20,000 cells/well investigations analysed using MTS a more restricted treatment course (only days 5, 7 and 9) was determined to be the ideal window for treatment. Despite, CTG having replaced the MTS assay, it was important for comparative reasons to see how smaller spheroids responded to MTS analysis. It was thought that the small size of these spheroids might allow for better penetration of the MTS reagent to occur, that would provide a more sensitive assessment of viability and any drug effects.

Very minimal difference was observed in the treated spheroids grown without Matrigel®, compared to the control throughout the analysis period. However, when the K1 spheroids were grown on 1% (v/v) Matrigel®, spheroids cultured for 5 and 9 days showed a reduction in metabolic activity when treated compared to the controls, with a significant drop on day 5, whereas those grown for 7 days showed similar metabolic activity whether treated or not. Based on MTS readings, it would appear that $NaN_3$ was ineffective in inducing damage to smaller K1 spheroids.

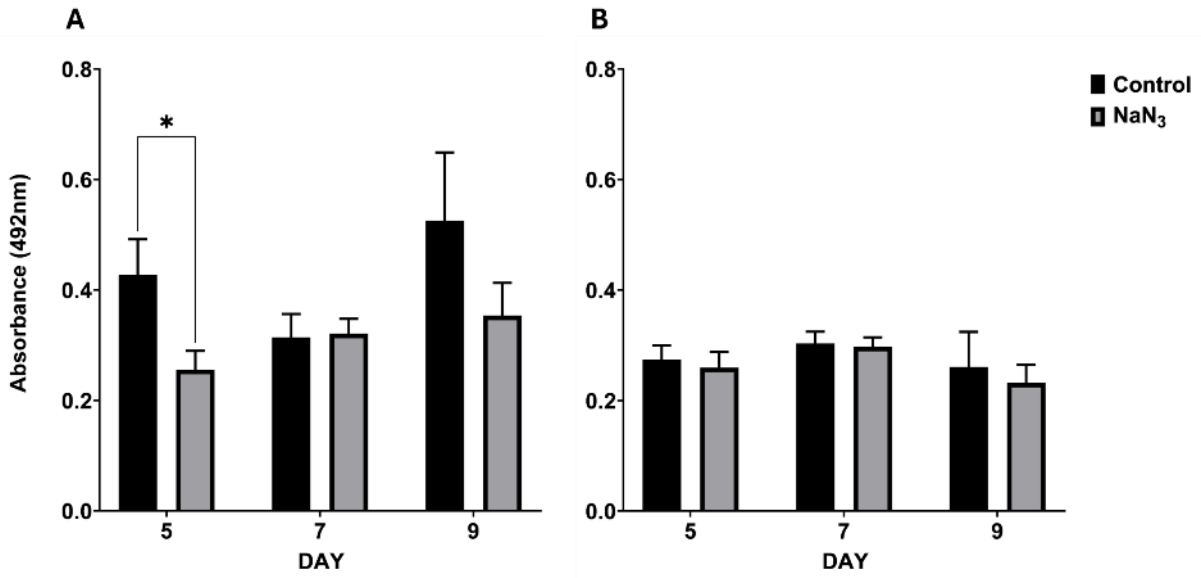


***Figure 4.13 MTS absorbance values for untreated and treated K1 1K spheroids (with and without 1% (v/v) Matrigel®) with $NaN_3$ (30 mM) for 48 h.*** *A single experiment with triplicates was conducted whereby MTS analysis took place on spheroid maturity days 5,7 and 9.* ***A*** *- spheroids supplemented with 1% (v/v) Matrigel®,* ***B*** *– without Matrigel®. Date was analysed using a 2-way ANOVA with Tukey's multiple comparisons test; control vs treated (for each analysis day) values are mean ±SD, * ($P \leq 0.05$), n=1.*

However, the fluorescent images were at odds with the MTS data as with the case involving 20,000 cells/well spheroids. The vast majority of the spheroid appears dead in every treated spheroid, regardless of the inclusion of Matrigel® (Figure 4.14). In the fluorescence assay the treated spheroids grown on Matrigel® appeared to be more sensitive to the cell death agent with high dead cell percentages of 91 and 98% on days 7 and 9 whereas, the non-supplemented treated spheroids recorded slightly lower percentages of 88 and 71% for days 7 and 9, respectively. Although not as high, the non-supplemented treated spheroids more consistently showed a high cell death percentage above 76% for all analysis days. Most importantly, the fluorescent images demonstrated that regardless of Matrigel® supplementation, these smaller (1000 cells/well) spheroids were highly susceptible to $NaN_3$.

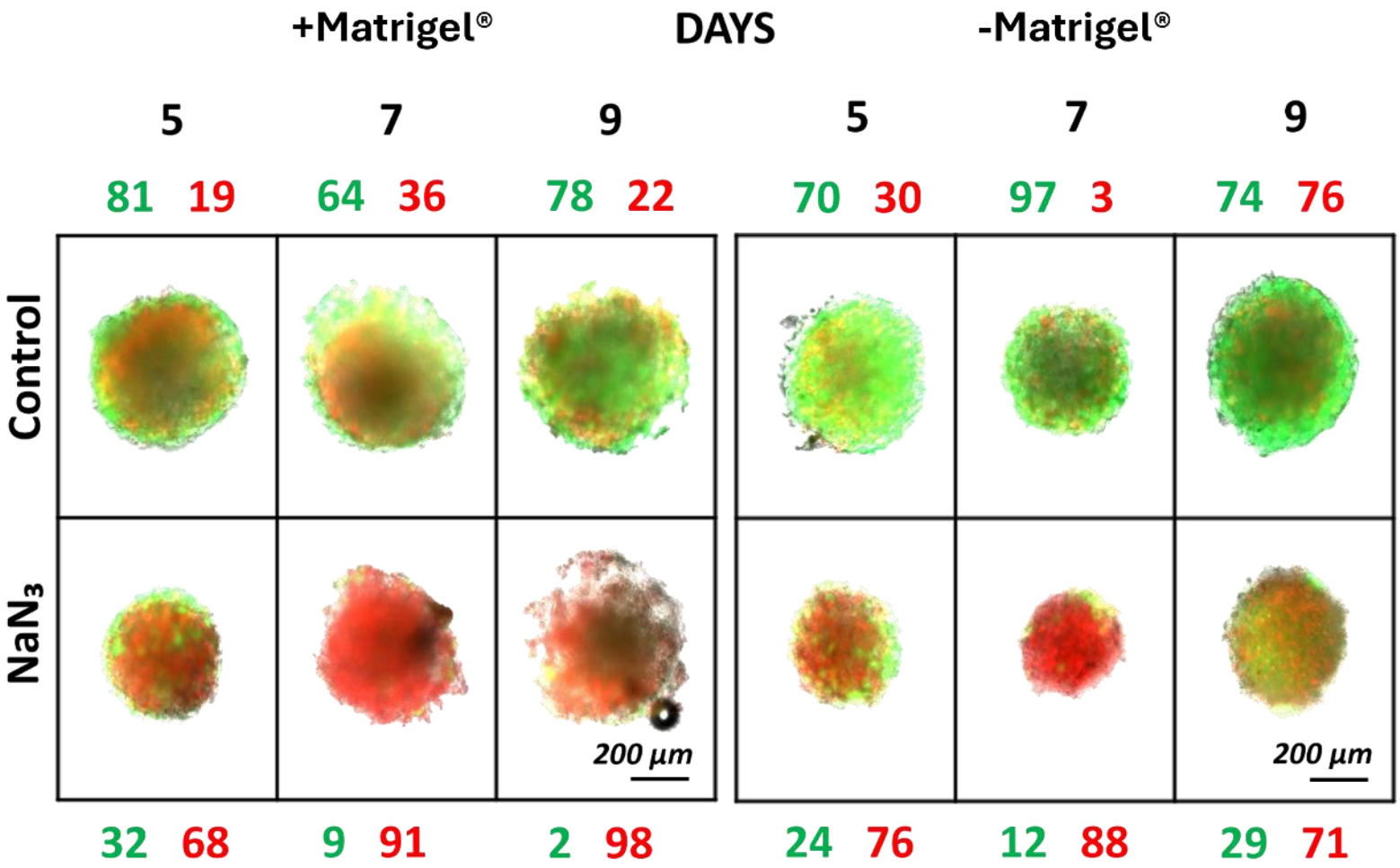


***Figure 4.14 Fluorescent images of FDA/PI stained K1 20K spheroids post 48 h (30 mM) $NaN_3$ treatment***. *Images were taken using a Zeiss fluorescent microscope at 10x magnification. Untreated spheroids (top row) and treated spheroids (bottom row) left table - with 1% (v/v) Matrigel® and right table – without. Images are representative of a single investigation with triplicates for each timepoint (days 5, 7, and 9). ImageJ was used to produce the percentages of live to dead cells (green – live, red – dead).*

As the CTG assay proved to be more accurate when investigating spheroids cultured from seeding 20,000 cells/well, the experiment involving 1000 cells/well spheroids was repeated this time with the new viability assay. Spheroids were grown for a total of 13 days and analysed on days 3, 5, 7, 9, 11 and 13. It was found that CTG data again conflicted with the MTS results and supported what was seen with the stained spheroids, i.e. that there was significant cell death (Figure 4.15). A much greater disparity was seen in luminescence values between the treated and control groups regardless of the presence of Matrigel®, including significant differences in values between treatment groups on day 3, 5 and 11 in the Matrigel® set whereas it was recorded on days 3, 9, 11 and 13 in the non-Matrigel® set. Based on CTG data, spheroids plated without Matrigel® were more sensitive compared to ones supplied with it.

Notable reductions in viability compared to the controls were observed on each analysis day with the exception of day 9 in the Matrigel® set and day 5 in the non-supplemented group. However, only a single repeat was carried out and therefore this was most likely due to issues with the spheroids and requires further repeat experiments. Despite analysis, the day 7 spheroids readings for non-supplemented spheroids did not produce a significant difference between the treated and control groups due to the presence of outliers.

From the CTG experiment, the group with Matrigel® appeared to have consistently higher viability values on average compared to the spheroids without supplementation. Even for the treated spheroids, viability values were highest among the Matrigel® supplemented spheroids. This was also observed in the optimisation investigations, whereby on average spheroid diameter was greater in Matrigel® supplemented spheroids compared to the non-Matrigel® spheroids (Chapter 3) which may correlate with improved viability.

Taking the data together it supports the greater reliability of using CTG over MTS for accurately analysing the viability of spheroids. A further consistent finding is that both the 1000 and 20,000 cells/well spheroids displayed the highest viability values on days 7-9, therefore the same treatment window would be used for these spheroids.

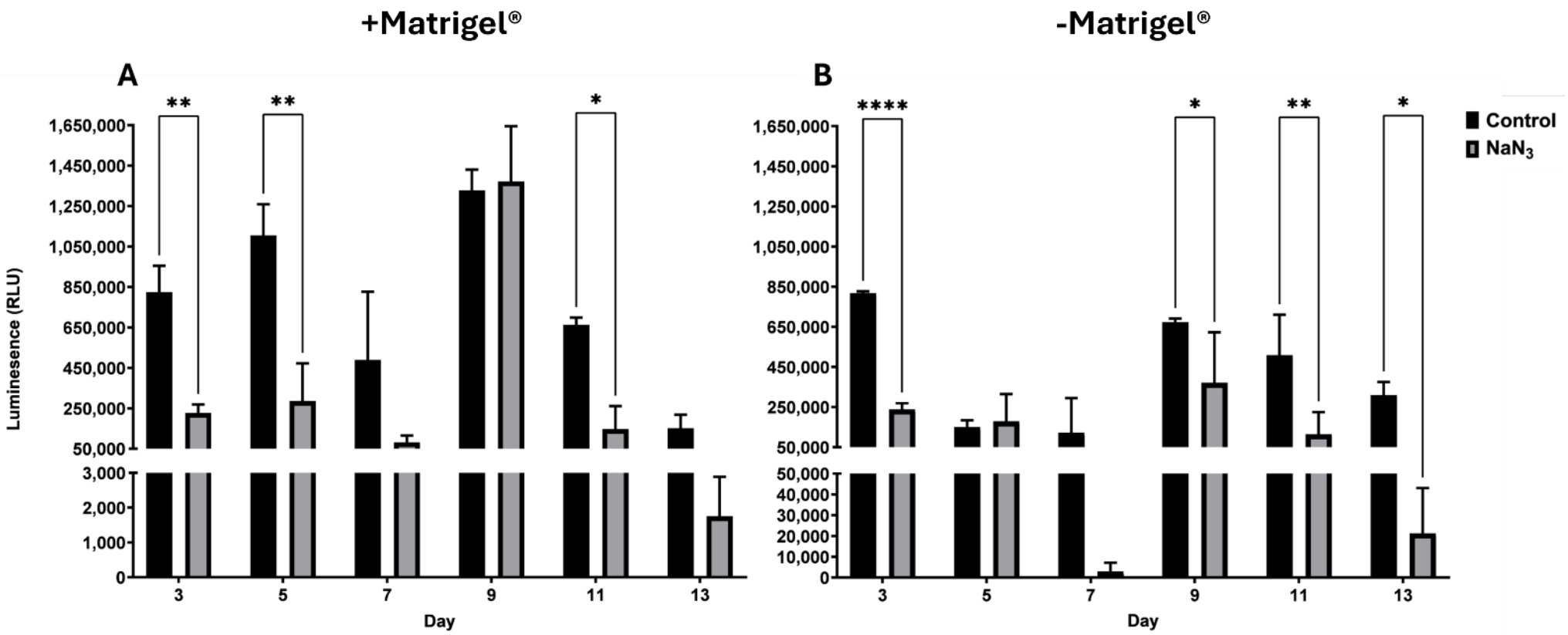


***Figure 4.15 CTG luminescent values for untreated and treated K1 1000 cells/well spheroids (with and without 1% (v/v) Matrigel®) with $NaN_3$ (30 mM) for 48 h.*** A single experiment with triplicates was conducted whereby *CTG analysis took place on spheroid maturity days 3, 5, 7, 9, 11, and 13. **A** - spheroids supplemented with 1% (v/v) Matrigel®, **B** – without Matrigel®. Data was analysed using a 2-way ANOVA with Tukey's multiple comparisons test;* control vs treated (for each analysis day) *values are mean ±SD,* * (P ≤ 0.05), ** (P ≤ 0.01), and **** (P ≤ 0.0001), *n=1.*

## 4.6 Investigating $NaN_3$ treatment on 8305c spheroids seeded at 10,000 cells/well

Three repeats involving 8305c spheroids, plated at 10,000 cells/well, treated with $NaN_3$ were conducted to see how these cells responded to the same concentration and treatment protocol used for the K1 spheroids.

Every analysis day displayed significantly lower values for the treated spheroids compared to their respective controls, excluding day 3 results; luminescence values never exceeded half of their control counterparts' values (Figure 4.16). In addition, the treated values were similar to one another and significantly lower than their respective control throughout the course of treatment from days 5 to 13, implying that $NaN_3$ treatment was more effective and consistent in inducing cell death in 8305c spheroids compared to K1 spheroids.

To confirm what was found with the CTG values, fluorescent images were analysed (Figure 4.17). A gradual decrease in recorded live cells was seen in the control as time progressed from 83 down to 59% whereas a general increase in the percentage of dead cells was seen in the treated spheroids, with an abnormally low reading on day 3 and 9, most probably due to an issue in setting up the spheroids. On days 5 and beyond the treated spheroids showed a higher dead cell than viable cell percentage with an almost 100% kill seen by day 13. It would also appear the 8305c spheroids succumb to "natural" cell death at a slightly earlier stage compared to the K1 which consistently had values above 85% throughout the observation period (Figure 4.4/6/10). Overall, CTG values had strongly correlated with the FDA/PI staining analysis further supporting the decision of changing the primary cell viability assay from MTS to CTG.

The analysed images displayed the effectiveness of $NaN_3$ entry into the 8305c spheroids as it did in the K1 spheroids. As seen in the K1 spheroids analysed with CTG, 8305c values were considerably lower by day 11 through to day 13, with control values on the final day resembling those of the treated group on day 3. Implying substantial cell death by that time, meaning investigations had to be completed before this time point. Therefore, for consistency

it was decided that the optimal treatment window for this cell line would be days 7-9. The same would be applied to the 1000 cells/well 8305c spheroids which due to time constraints, growth trends were not investigated.

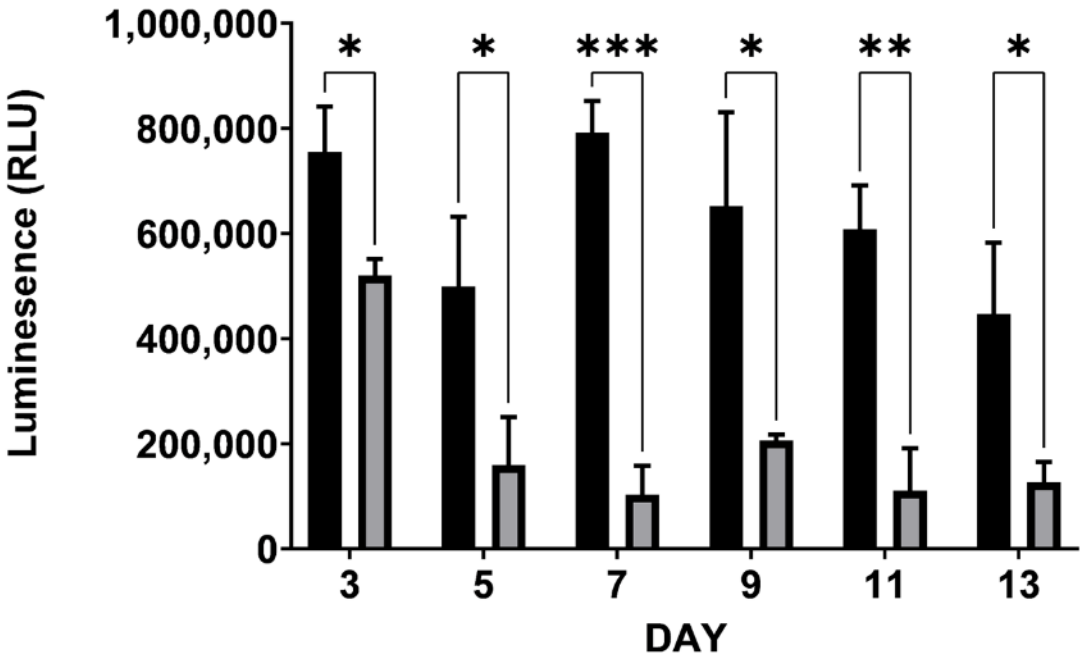


***Figure 4.16 CTG luminescent values for untreated and treated 8305c 10,000 cells/well spheroids with $NaN_3$ (30 mM) for 48 h.*** *Three independent experiments consisting of triplicates were conducted whereby CTG analysis took place on spheroid maturity days 3, 5, 7, 9, 11, and 13. Data were analysed using a 2-way ANOVA with Tukey's multiple comparisons test; control vs treated (for each analysis day) values are mean ± SD, * (P ≤ 0.05), ** (P ≤ 0.01), and *** (P ≤ 0.001), n=3.*

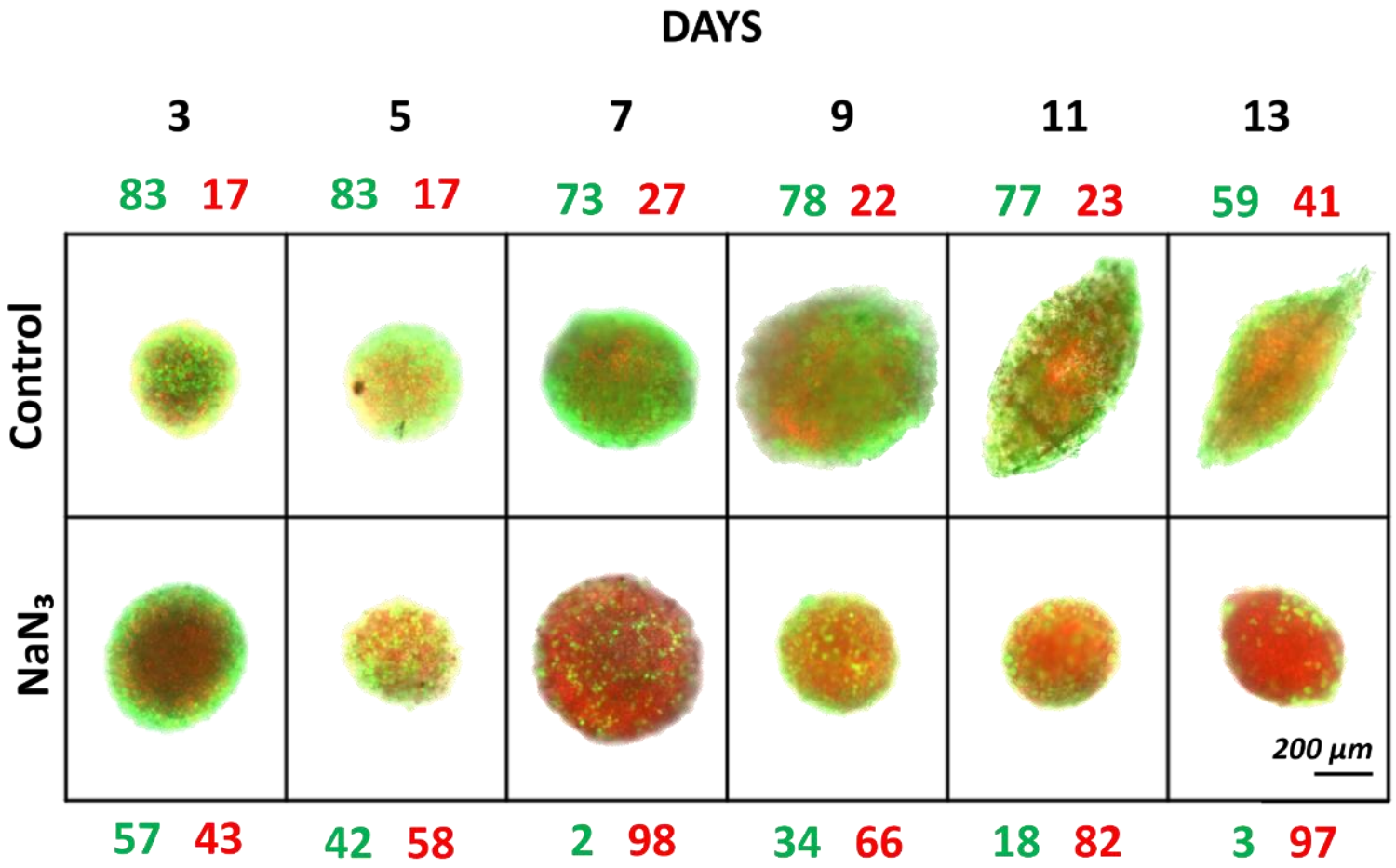


***Figure 4.17 Fluorescent images of FDA/PI stained 8305c 10,000 cells/well spheroids post 48 h $NaN_3$ (30 mM) treatment***. *Images were taken using a Zeiss fluorescent microscope at 10x magnification. Untreated spheroids (top row) and treated spheroids (bottom row). Images are representative of a single investigation with triplicates for each timepoint (days 3, 5, 7, 9, 11 and 13). ImageJ was used to produce the percentages of live to dead cells (green – live, red – dead).*

## 4.7 Discussion

The aim of these experiments was to determine whether it was possible to induce cell death in spheroids and to monitor their viability over a specified time period which would identify a window for spheroid treatment with TKI drugs.

### 4.7.1 $H_2O_2$ and Its Challenges in Spheroid Models

Initial investigations utilised $H_2O_2$ as the cytotoxic agent, but minimal cell death was observed in K1 spheroids when analysed using the MTS assay. Fluorescent microscopy indicated that $H_2O_2$ only affected the outer lining of the spheroids, implying poor penetration into the structure. Even increasing the incubation time from 24 to 48 h yielded little improvement in reducing viability, as confirmed by fluorescent images and IHC staining which showed no difference in the proliferation of cells when compared to the untreated samples.

$H_2O_2$ primarily induces oxidative damage to the outer lining of the spheroid, with limited diffusion across the cell membrane possibly due to the dense structure and lack of vascularisation in this model, which could have led to the poor distribution of the agent (Shen *et al.,* 2024). Moreover, in spheroids the outer proliferating layers exhibit higher metabolic activity which rapidly consume $H_2O_2$ to generate the ROS, therefore reducing its availability for cells in the deeper regions (Grimes *et al.,* 2014). For instance, the necrotic core, which is created due to hypoxic conditions, forces cells to adapt and alter processes in turn reducing ROS production, allowing the cells to be less susceptible to oxidative damage (Fuhrmann & Brüne, 2017). This could explain why cells other than the external layers within the spheroid remained majorly unaffected. However, it has been described by Guzy & Schumacker (2006) that cells can experience an increase in ROS production in response to hypoxic conditions, meaning that spheroids would be expected to have shown gradually stronger red staining the closer the cells were to the core. No changes were seen however in the current work, with only slightly higher percentages of dead cells after the incubation increase to 48 h, so affects may also be cell type specific.

### 4.7.2 $NaN_3$ as a Spheroid Cell Death Inducer

Due to the limitations associated with $H_2O_2$, $NaN_3$ was trialled. Initial investigations utilising confocal microscopy revealed that $NaN_3$ successfully penetrated the spheroids and induced significant damage, as evidenced by fluorescent images which showed considerably more red staining than the $H_2O_2$ administration, along with live/dead percentages which indicated significant death of the spheroids. Although, larger than $H_2O_2$ molecules, the findings suggested that $NaN_3$ was more effective in penetrating the spheroid structure, possibly due to not becoming saturated in the outer layers as $NaN_3$ inhibits mitochondrial activity in contrast to $H_2O_2$ which relies on mitochondria for ROS production to induce damage (Juan *et al.,* 2021). As a result, the more metabolically demanding outer cells were most likely more concentrated with $H_2O_2$ whereas the $NaN_3$ inhibited the functionality of the mitochondria within any cells allowing the remaining molecules to permeate the spheroid more easily.

Despite confocal and fluorescent images indicating $NaN_3$ effectively induced damage to spheroids, MTS did not appear to support these observations Conversely CTG, an assay that is tailored for use on 3D structures such as spheroids, lyses the structure for easier access to cells and measures the quantity of ATP produced as a measure of viability. With this change, clear reduction in viability was seen in K1 spheroids regardless of seeding density. The most observable example was seen in the 1000 cells/well spheroids, which according to the MTS assay, $NaN_3$ did not induce significant cellular damage with similar values in both the control and treated groups. However, when analysed using CTG it was clear this was not the case, showing major reductions in viability readings across most times in treated spheroids compared to controls. An intriguing observation was that spheroids supplied with Matrigel® appeared more sensitive to $NaN_3$ when analysed using FDA/PI staining, possibly due to the hydrogel retaining the agent within the spheroid for a longer period of time compared to the non-supplemented spheroids, leading to greater cellular damage. This has been described previously by Schmidt *et al.,* (2008) who explained that hydrogels can limit influx of molecules but in turn also limit or prevent the efflux of these molecules once inside the encapsulated cells.

The 8305c spheroids seeded at 10,000 cells/well exhibited greater susceptibility to $NaN_3$ compared to K1 spheroids, significant damage was observed in the treated spheroid groups on each analysis day unlike the other cell line regardless of plating density and also displayed clear penetration into the structure and spheroid death when analysed using FDA/PI staining with fluorescent microscopy.

### 4.7.3 Limitations of the spheroid models

Due to supply issues and time constraints, only the 10,000 cells/well 8305c spheroids were investigated which meant treatment on 8305c spheroids seeded at 1000 cells/well were not conducted. Therefore, choice of the optimal window for treatment was based on the experiments involving the K1 cell line and the larger 8305c spheroids.

Moreover, lack of a CTG assay on $H_2O_2$ treated spheroids meant comparisons between the two assays were not possible. However, this would not have impacted the decision to use $NaN_3$, as the fluorescent images involving $H_2O_2$ treated spheroids were not convincing. When juxtaposed with $NaN_3$ treated spheroids, the damage was stark and unequivocal, with observably more intense red staining indicating cell death and further confirmed by CTG analysis.

Furthermore, image processing using the ImageJ program was labour-intensive. Although there are macro settings that allow for speedy processing with set commands and thresholds, spheroidal images often require manual adjustment for each image, especially when out of focus or when the software does not accurately detect individual cells (Venter & Niesler, 2019).

### 4.7.4 Chosen Experimental Parameters

CTG and dead/live staining findings confirmed that K1 and 8305c spheroids could be effectively killed by $NaN_3$, but also through this investigative process it was discovered that the MTS assay was not appropriate for analysis on 3D models and allowed for the prompt adjustments for the use of CTG prior to the initiation of the main experiments involving sorafenib. Furthermore, these observations described in this chapter highlighted the

importance of the cytotoxic molecules ability to navigate the complex structure of spheroids to induce damage, meaning a range of concentrations would need to be tested.

Based on viability readings from all the experiments analysed by the CTG assay it was decided that the optimal time for spheroid treatment prior to natural (looking at untreated spheroid observations) viability decline, would be between days 7-11. Days 7 and 9 were chosen, meaning treatment would commence on days 5 and 7, respectively. Furthermore, 1% (v/v) Matrigel® would be added to the 1000 cells/well spheroids, which not only doubled the size of the spheroids (section 3.7.4) but also improved their overall viability.

Addition of Matrigel® was based on recommendations from a commercial collaborator (CN-BIO) who successfully had grown spheroids at a density of 1000 cells/well. This study did not explore other options due to the very convincing results, that being the improved viability and size increase compared to those without the matrix. Many researchers have incorporated the use of Matrigel® for their spheroid's generation protocols such as Hu *et al.,* (2024) who manufactured ATC spheroids (8505c similar cell line to 8305c) and determined viability using the CTG assay. They found that using Matrigel®-coated plates the matrix facilitated better cell attachment and a more open arrangement of the cells, allowing cells to adequately absorb nutrients from the medium. This was seen in Chapter 3 whereby Matrigel® supplemented spheroids were consistently larger than the spheroids without the hydrogel, making identification easier which is crucial for fluorescent microscopy examination. Another valuable supplement for spheroid growth appears to be the addition of agarose, which is commonly associated with spheroid development, and although agarose is the more cost effective option (Oh *et al.,* 2022), to the best knowledge of the author it does not simulate growth to the extent that Matrigel® had in the current study.

With the wide variety of experimental parameters utilised in association with thyroid spheroids and drug testing, there is a pressing need for standardisation especially with viability analysis. As previously described in Table 4.1 and section 4.1, investigations involving sorafenib testing on TC cell lines identical to those used in the current study demonstrated variability in the types of assays, cell death agents and concentrations employed. The most common assays used were CCK-8, MTT, XTT or the CTG assay (Table 4.1), all of which have

been optimised for use on monolayers. Despite the gradual transition to 3D models for drug testing, due to their greater predictive prowess compared to 2D models, researchers often continue to use assays optimised for monolayer cultures. This can adversely affect the reproducibility and reliability of results, as well as their accuracy in predicting drug effects *in vivo*. Dominijanni *et al.,* (2021) examined this issue by evaluating commercially available cell viability assays optimised for 2D applications, such as Promega's CellTiter-Glo®, CellTiter 96® MTS Assay, and Thermo Fisher's PrestoBlue™ assay, within 3D cultures. The study found that these assays often produce inaccurate viability outputs in 3D models when compared to their performance in 2D cultures. Assay such as MTS are unsuitable for use on 3D models as even distribution of the reagent within the structure can be hindered which can lead to inaccurate results (Costa *et al.,* 2016). This strongly reflected what was experienced in the current study with inconsistent and contradictory findings when comparing viability readings against FDA/PI staining analysis which further supported the decision to use the CTG assay which reflected the damage observed in the fluorescent images.

The decision to use FDA/PI staining analysis with fluorescent microscopy allowed for discovery of the unreliability of the MTS assay, and also highlighted the importance of a secondary confirmation tool to ensure findings corroborate viability measurements. Kwapiszewska *et al.,* (2014) advocates for the use of microscopic imaging in combination with viability assays to validate results. They had employed spectrofluorimetric analysis and fluorescence-based live/dead cell analysis using Calcein-AM and Propidium Iodide to evaluate the viability of spheroids on-chip and determine the optimal window for treatment (12 days). This method also eliminated the need to transfer spheroids to a new plate which is a requirement for CTG analysis.

In the current study, a 48 h treatment window when viability was the highest was chosen, in this case on days 7 to 11 meaning analysis would take place when spheroids had reached a maturity of 7 or 9 days. Ghiandai *et al.,* (2024) investigating SW1736 (ATC) spheroids also incorporated Matrigel® into their generation protocol had found that between 7-10 days was the best window for viability testing. Another study, manufacturing K1 spheroids on ULA plates had used the CTG assay and PI staining once spheroids were around 7 days old (Sekhar

*et al.,* 2022). Showcasing that despite the differences in cell lines, spheroids from this study and those used in the literature were mature enough for testing when around a week in age.

Overall, there is substantial literature which supports the choice of the selected analytical tools, and highlights the importance of validating techniques, i.e. using fluorescent imaging alongside the standard biological assays, to ensure accurate and reliable measurements of cell viability in 3D cultures allowing the creation of a suitable treatment plan.

# Chapter 5 Investigating sorafenib-Induced Cytotoxicity in Thyroid Cancer Spheroids

## 5.1 Introduction

With constantly rising thyroid cancer incidence rates worldwide, many individuals unfortunately develop radioiodine (RAI)-refractive tumours (5-15% of all DTC, with 50% of metastatic DTC becoming refractive), leaving the gold standard treatment of surgery plus radio/chemotherapy ineffective (Aashiq *et al*., 2019). Further investigations into the best treatments for these individuals are urgently needed. Currently the most promising type of treatment are tyrosine kinase inhibitors, such as sorafenib; this type II inhibitor is the first-line treatment option for advanced DTC that are refractory to RAI therapy (Dadu *et al.,* 2014). This class of drug work by targeting and inhibiting multiple kinase pathways involved in tumour cell proliferation and angiogenesis (section 1.5.1).

Although thyroid cancers such as papillary carry a good prognosis, once it becomes RAI refractory the mean life span falls to less than 5 years (Liu *et al*., 2020). The most aggressive and most likely to gain refractory properties is the anaplastic thyroid carcinoma, which frequently does not respond to traditional treatments of surgery and radiotherapy, and such patients frequently show poor responses to sorafenib (Thomas *et al.,* 2014, Wu *et al.,* 2020). Regardless of thyroid tumour type, there is great variability in behaviour and response of thyroid cancer to treatment which is why it is important to establish the mechanisms by which it reacts to treatment.

With the gradual transition from 2D to 3D models in drug therapy analysis, an increasing number of studies have highlighted the superior properties of more complex 3D models (Fitzgerald *et al.* 2015; Carragher *et al.,* 2018). These models offer more reproducible and translational results compared to traditional monolayers, which often fail to accurately replicate outcomes in animal and human trials (Kimlin *et al.,* 2011; Melissaridou *et al.,* 2019). Specifically, these models recapitulate aspects of the *in vivo* tumour microenvironment,

including differences in metabolism, hypoxia tolerance, and drug penetration heterogeneity, which contribute to their superior ability to predict therapeutic resistance and thus efficacy.

However, in the realm of thyroid cancer research, few spheroidal models have been described which prompted the following investigations. Spheroids provide greater complexity including a microenvironment and more intricate cell-cell interactions over traditional monolayer models (Pinto *et al.,* 2020). Thus, 3D models are thought to offer a better understanding of drug-tissue interactions, especially in relation to factors such as drug penetration with a generally greater translational relevance to *in vivo* human responses over 2D models (Berrouet *et al*., 2020).

Two immortalised human cell lines were used in the current study, papillary (K1) and anaplastic (8305c) to generate spheroids, which would undergo treatment with sorafenib. These two types of cancer have very different characteristics in terms of behaviour and associated mortality. Using spheroids with differing morphologies will potentially give an insight into drug response and resistance mechanisms which is currently something that has not been well explored or documented.

Although spheroid use is advantageous in drug analysis over traditional monolayers, they still lack certain properties meaning they also fall short of truly replicating tumour morphology *in vivo.* The most important of which is vascularity, especially with the heightened angiogenic properties of tumours, which significantly alters and influences tumour cell metabolism as well as drug delivery (Padera *et al*., 2004). Microfluidic on-chip devices have the potential to bridge that gap, by simulating the vascular microenvironment by providing dynamic perfusion, accurately replicating the nutrient and oxygen gradients present in *in vivo* tumour microenvironments (Feng *et al.,* 2023). Culture under flow, improves the physiological relevance of spheroids, leading to more predictive drug responses and tissue behaviours for greater translational accuracy (van Duinen *et al.,* 2015). Microfluidic devices offer manipulation of mechanical forces at the cellular and subcellular levels. This includes applying the desired pressures, tensions, or shear forces to spheroids. In addition, microfluidic chips can be tailored to specific experimental needs, enhancing experimental flexibility (Sonnen & Merten, 2019). The use of microfluidic devices to culture spheroids under flow conditions

represents a significant advancement in enhancing the translational potential of *in vitro* models to *in vivo* systems (section 1.6.2).

Many publications have used the methylthiazolyldiphenyl-tetrazolium bromide (MTT) assay or an alternative such as a dead cell apoptosis assay when analysing viability of TKI thyroid cells/spheroids (Mortensen *et al.,* 2023 and Lin *et al*., 2021). However, the emergence and inclusion of 3D models when investigating drug effectiveness has prompted the review of how well these cell viability assays, that have been used primarily for monolayers, translate to use for 3D. One study found that viability assays specifically designed for analysing more complex models such as the CellTiter-Glo® 3D (CTG) assay by Promega, performed better compared to the standard MTT assay on 3D cultures. However, both suffered inaccuracies leading the authors to recommend including microscopic assessment as an additional validation tool (Dominijanni *et al.,* 2021).

The CTG assay, measuring the presence of ATP in live cells was chosen for the current study along with fluorescent imaging, to visualise how the drug affects the spheroid and whether it aligns with the quantitative data (CTG, diameter readings and FDA/PI analysis). An additional measure of spheroid diameter was incorporated to see if there was any impact of drug treatment on gross spheroidal size. CTG has been shown to have a higher signal:background ratio compared to the MTT assay allowing for more sensitive readings (Riss *et al*., 2014); a similar observation was also observed in this study (Chapter 4). A recent paper by Sarıyar *et al.,* (2023) also used the 3D CTG assay when analysing TKI therapy resistance in spheroids, which hopefully marks the beginning of a gradual adoption of cell viability assays that are better suited for analysing 3D models rather than utilising assays outside their intended use.

Another issue when exploring what others have done with TKI and thyroid spheroids is the wide variability in concentrations that have been tested. As a result, this study performed a preliminary test to determine the optimal concentration range based on literature and work done with sorafenib on K1 and 8305c monolayers at the University (personal communication Miss Hannah Beattie). As data on K1 and sorafenib was very limited a decision was made initially to create a range based on what had been used for the 8305c cell line, which ranged from 0 – 30 µM (Zhu & Xie, 2023 and Mortensen *et al.,* 2023). Given that previous findings

were based on monolayer cultures, a concentration range of 25-200 µM was initially set. This would help determine if higher concentrations would be necessary for 3D models. Incubation times with sorafenib were quite similar across studies ranging from 24-72 h, therefore a median of 48 h was chosen for this study.

## 5.2 Aims and Objectives

Sorafenib efficacy was explored using a wide range of concentrations and two thyroid cancer cell lines differing in proliferation rates. K1, the papillary cell line represents the most abundantly diagnosed thyroid cancer while the anaplastic (8305c) cell line, although rare, is highly aggressive with high incidence of becoming metastatic. The two differing cell lines were used to observe how different tumour types would respond to sorafenib. Furthermore, the feasibility of utilising spheroid cultures within microfluidic chip devices was tested as a novel platform for drug testing.

## 5.3 Methods and Materials

### 5.3.1 Spheroid generation

Spheroids were generated based on protocols outlined in section 2.2. For the preliminary investigation a ULA plate was seeded with 20,000 cells/well (in 100 µL of medium), two wells for each drug concentration used, the control, and DMSO groups. The plate was incubated for 48 h, with the drug treated spheroids having their medium replenished with their respective concentrations at 24 h. The controls also had a medium change at the same time point. This was to attempt to mimic the *in vivo* scenario as the half-life of sorafenib *in vivo*, when taken orally by patients, is 20 to 25 h; daily doses are required when given clinically (Huh *et al.,* 2021).

For subsequent experiments with sorafenib, two ULA plates for each repeat were used, one for CTG assay analysis whereby triplicates for each concentration were analysed, including the controls. The second plate, identical to the first in terms of arrangement and treatment procedures, was used for analysis via fluorescent staining and subsequent imaging, which also

allowed for diameter measurements and percentage of live/dead cells to be established using ImageJ.

### 5.3.2 Sorafenib treatment

Based on work done with 2D models using sorafenib by the research group, and the limited data from literature, 4 initial concentrations were selected: 25, 50, 100 and 200 µM, but this was altered, following preliminary experiments to 3.13, 6.25, 12.5, 25, 50 and 100 µM and remained the standard range for subsequent experiments.

Further experiments consisted of using a different cell line (8305c) seeded at 10,000 cells/well and also smaller models for both cell lines consisting of 1,000 cell/well spheroids (including 1% w/v Matrigel®; section 2.2.1) in order to investigate responses of tumour models lacking a necrotic core. Procedures were consistent across the cell lines and models.

### 5.3.3 $IC_{50}$ calculation

To determine the $IC_{50}$ values, cell viability was assessed using the CTG assay on days 7 and 9 post 48 h sorafenib treatment. The raw viability data for these two time points were combined and normalised using GraphPad Prism software. Normalisation was performed to account for any variations between the different experimental runs and to standardize the data for accurate comparison. Following normalisation, non-linear regression analysis with a variable slope was applied to the combined data plotted against the concentration to determine the $IC_{50}$ values. Representing the concentration at which 50% of the maximum inhibition of cell viability was achieved.

### 5.3.4 On-chip setup

In accordance with previous research conducted at the University of Hull, spheroids were cultured according to the protocol outlined in section 2.2, with K1 cells seeded into a 96 well plate, at a density of 20,000 and 8305c cells at 10,000. Following a cultivation period of 7 days for K1 spheroids and 5 days for 8305c spheroids. PMMA carriers were laser-cut and coated with Matrigel® (section 2.5). Subsequently, syringes were prepared for the administration of sorafenib, with each cell line necessitating 4 devices, totalling 8 syringes. Sorafenib was

prepared from a 100 µM stock solution in DMSO and serially diluted (0, 25, 50 and 100 µM). Spheroids were then added to each of the three culture areas, with 3 spheroids introduced per area, 9 per device, totalling 27 spheroids across 4 devices. Following perfusion for 24 h at a rate of 2 µL/min, syringes were replaced, and the devices were further incubated for 24 h with medium alone. At the end of the experiment, carriers were carefully removed from the devices and spheroids were transferred to ULA plates for examination, allowing for analysis via CTG or FL microscopy.

### 5.3.5 Cell viability analysis

Spheroid viability was analysed by measuring ATP production using the CTG assay as described in section 2.3.4. Post sorafenib treatment, spheroids were transferred and incubated in an opaque, white-walled 96-well flat-bottom plate with CTG reagents, before reading on the luminometer. Using a plate dedicated for staining did not necessitate transfer of spheroids to another plate, instead, spheroids were washed with PBS (200 µL) and stained with PI/FDA in their respective wells (section 2.3.5). The fluorescent images were taken at x10 magnification using a Zeiss microscope on pre-set filters (2.3.5.2). Although triplicates of spheroids for each concentration were prepared for staining analysis, complete sets were not always attained. Using ImageJ software live/dead cell compositions within spheroids were able to be determined along with their diameters to gain an estimate of average sizes (section 2.2.2;4.5).

## 5.4 Statistical Analysis

CTG, diameter and percentage readings were analysed in GraphPad v9.5.1, utilising a 2-way ANOVA, followed by a Dunnett's multiple comparison test. Fluorescent images were analysed with ImageJ software to determine live/dead cell percentages and diameter measurements.

# Results

## 5.5 Assessing sorafenib effects on thyroid cell line spheroids

### 5.5.1 Analysing sorafenib potency on K1 spheroids seeded at 20,000 cells/well

This investigation was undertaken with the aim of determining a dose response curve for sorafenib. Additionally, as the TKI was diluted in DMSO it was crucial to verify whether the solvent had any effect on spheroid viability, analysed using the CTG assay.

The preliminary experiment showed that sorafenib concentrations of 100 and 200 µM were highly potent resulting in the expected cytotoxic effect (Figure 5.1). However, significant reduction in spheroid viability at a concentration of 25 µM sorafenib was also observed, every concentration for both analysis at days, 7 and 9 produced statistically significant decreases in viability when compared to the control, $p<0.0001$. This prompted the incorporation of an extended range of concentrations as low as 3.13 µM, whilst 200 µM was discarded as it had very similar results to the 100 µM concentration and it was clear that both were capable of killing the spheroids very effectively.

Another important observation was that DMSO, at an equivalent concentration to that used in the 100 µM sorafenib, had no adverse effects on spheroid viability, strongly mimicking luminescence values of the control group. Also, both day 7 and 9 tested spheroids displayed similar values for each concentration and shared a homogenous trend of decreasing viability as TKI concentrations increased. Due to the 25 µM sorafenib still having a significant effect, the concentrations were lowered further and the 200 µM concentration was omitted.

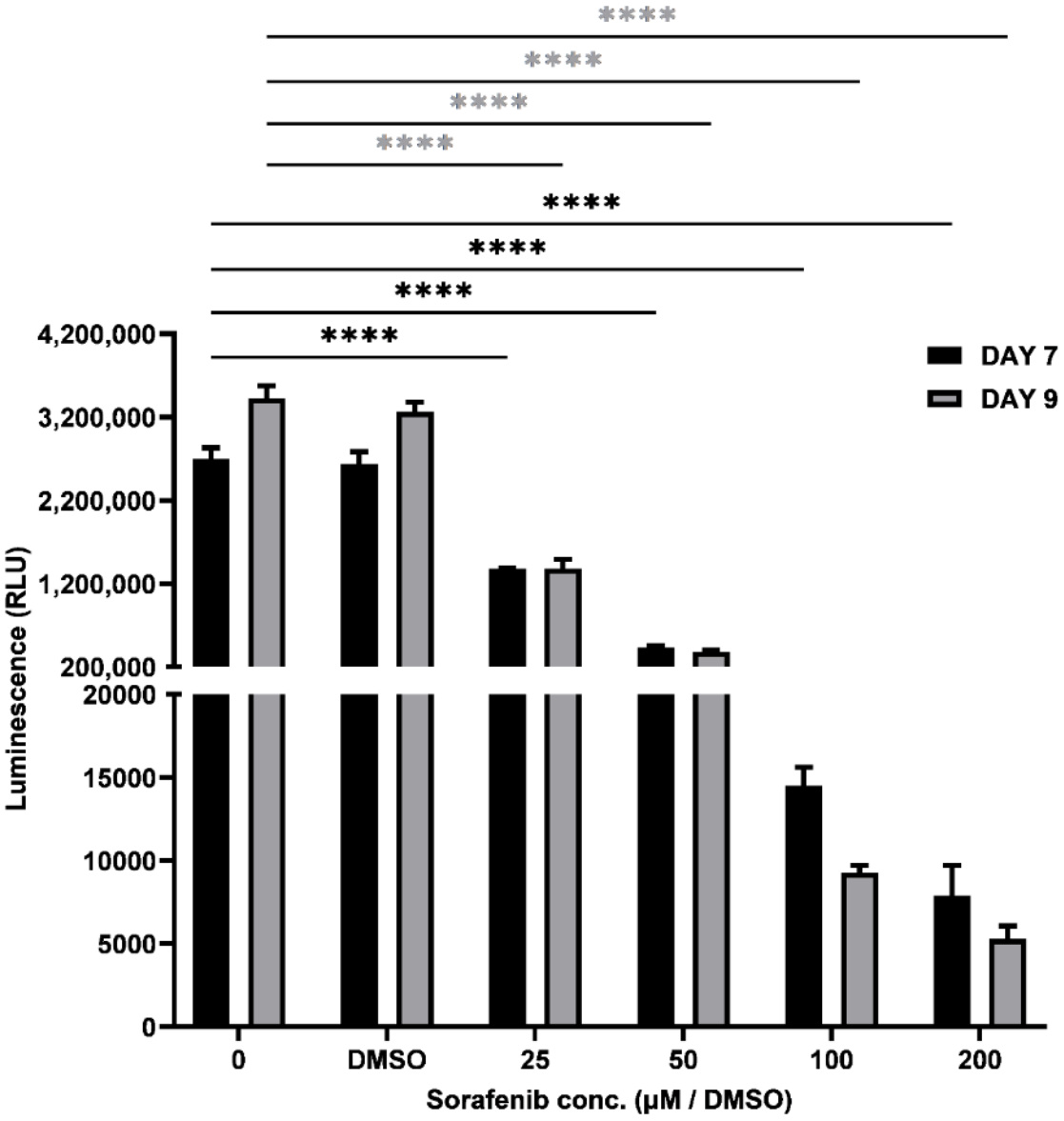


***Figure 5.1 Luminescence values from the CTG assay for untreated and treated (sorafenib for 48 h) K1 spheroids (seeded at 20,000 cells).*** *A single experiment was conducted with triplicates for each treatment group. CTG values were determined post 48 h incubation with the TKI, with replenishment after 24 h, day 7 spheroids began treatment when spheroids were 5 days old, day 9 spheroids when they were 7 days mature. Significant differences determined by a 2-way ANOVA with Dunnett's multiple comparison test, between control and treated groups. Values are mean ±SEM, **** (P ≤ 0.0001), n =1. DMSO: dimethyl sulfoxide, diluted to match the highest concentration of sorafenib [1% (v/v)].*

A considerable reduction in spheroid viability was observed at a concentration as low as 6.25 µM, whereby viability compared to control had dropped by 10.5% for the day 7 group and by 8.3% for day 9 spheroids. The least potent concentration of 3.13 µM still managed a discernible, if small, drop in viability (Figure 5.2). Also, a concentration of 12.5 µM and beyond, all displayed a highly significant decrease in viability regardless of spheroid age when compared to the control group. The most potent concentration (100 µM) had induced an almost complete kill for both day groups, a reduction in viability of 98.1% for day 7 and 98.3% for day 9 when compared to their respective control groups. Indicating sorafenib was extremely effective in killing spheroids at the higher concentrations.

A reassuring observation was the similar values given for the control (cells alone) and DMSO groups for both days, which was a strong indication that DMSO, at this percentage (10%), does not affect spheroid growth. From this investigation, it was clear that the older (Day 9) spheroids, consistently retained marginally higher viability values across all groups compared to 7-day-old spheroids, possibly indicating a slightly larger spheroid where the drug diffusion distance to the centre will be increased, creating an elevated level of resistance to the TKI.

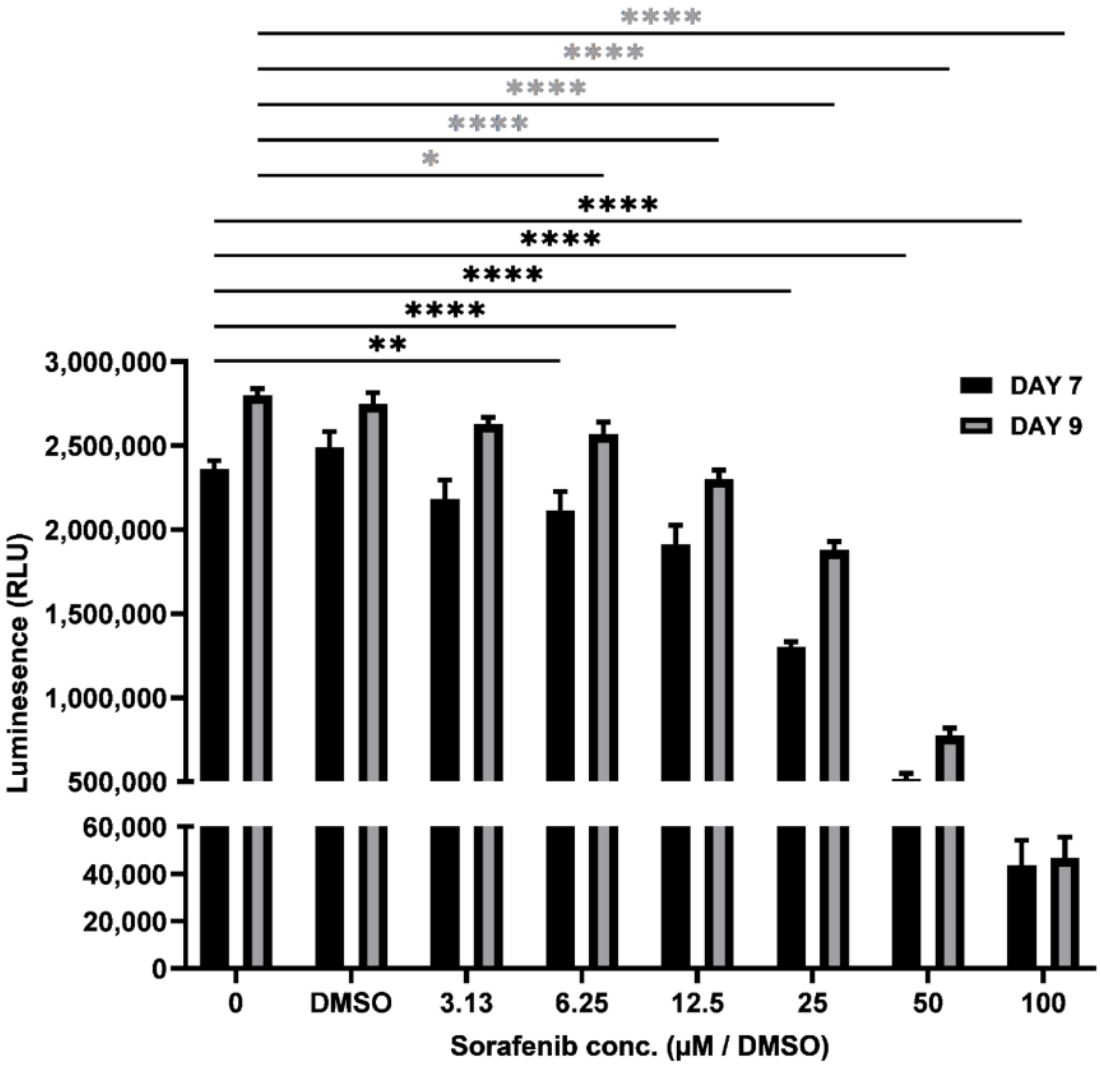


***Figure 5.2 Luminescence values from the CTG assay for untreated and treated (sorafenib for 48 h) K1 spheroids (seeded at 20,000 cells).*** *Three independent experiments with triplicates for each treatment group were conducted. CTG values were determined post 48 h incubation with the TKI, with replenishment after 24 h. Day 7 spheroids began treatment when spheroids were 5 days old, day 9 spheroids when they were 7 days mature. Significant differences determined by a 2-way ANOVA with Dunnett's multiple comparison test, between control and treated groups. Values are mean ±SEM,* * ($P \leq 0.05$), ** ($P \leq 0.01$), and **** ($P \leq 0.0001$), *n =3. DMSO: dimethyl sulfoxide, diluted to match the highest concentration of sorafenib [1% (v/v)].*

The day 7 spheroid diameters gave a consistent size of about 870 µm, with two atypically sized spheroids in the 50 µM drug group, slightly skewing the overall trend (Figure 5.3). With the day 9 spheroids, there was a gradual decline in spheroid size as the concentration of sorafenib increased, more notably at concentrations greater than 12.5 µM. Day 9 spheroids subjected to 100 µM sorafenib saw an average diameter of 740 µm, which was considerably lower compared to the control values (900 µm). A Dunnett's multiple comparisons test revealed significant differences in spheroid sizes of treated spheroids compared to the control, when treated with a concentration of 12.5 µM and above. This correlates with the CTG results in Figure 5.2, but not in the case of the day 7 spheroids which lacked any great deviation from the average size throughout the treatment period.

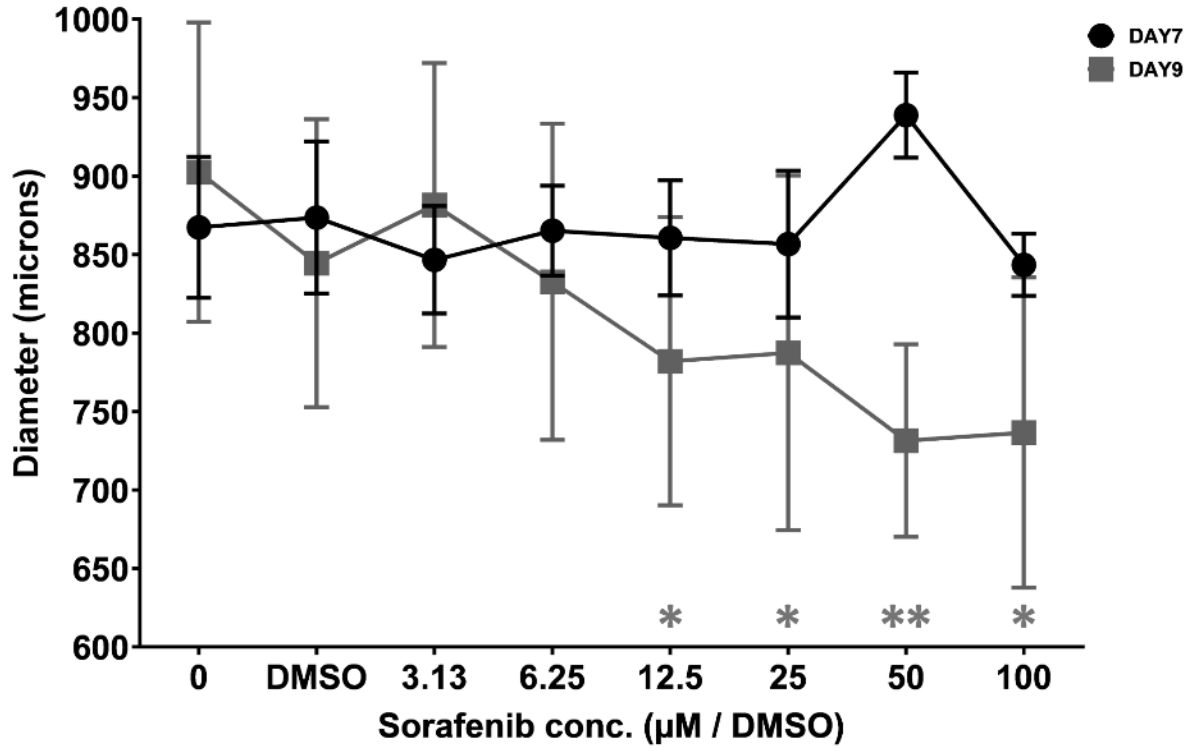


***Figure 5.3 Diameter measurements for K1 spheroids (seeded at 20,000 cells) post 48 h sorafenib treatment.*** *Images were taken using a Zeiss fluorescent microscope at 10x magnification and then average diameter readings of spheroids for each concentration were determined using ImageJ, triplicates (three repeats, incomplete sets for some) for each concentration. Significant differences determined by 2-way ANOVA with Dunnett's multiple comparison test, between control and treated groups. Values are mean ±SEM, * (P ≤ 0.05), and ** (P ≤ 0.01), n=3. DMSO: dimethyl sulfoxide, diluted to match the highest concentration of sorafenib [1% (v/v)].*

A similar trend was observed when measuring the percentage of live and dead cells within the spheroids using FDA/PI staining, although not as pronounced as in the CTG and diameter readings. The only significant results post Dunnett's analysis were seen following treatment with 50 and 100 µM sorafenib, whereby percentages of live cells fell below the 50% mark (Figure 5.4). Day 7 spheroids had very high live cell percentages that only dropped significantly once treated with the top 100 µM concentration of sorafenib whilst, a significant decline in live cell percentages in the day 9 spheroids was seen in the 50 and 100 µM groups. Thus, these readings did not truly mirror results from previous tests but did once again highlight how the older day 9 spheroids appeared more sensitive to the treatment.

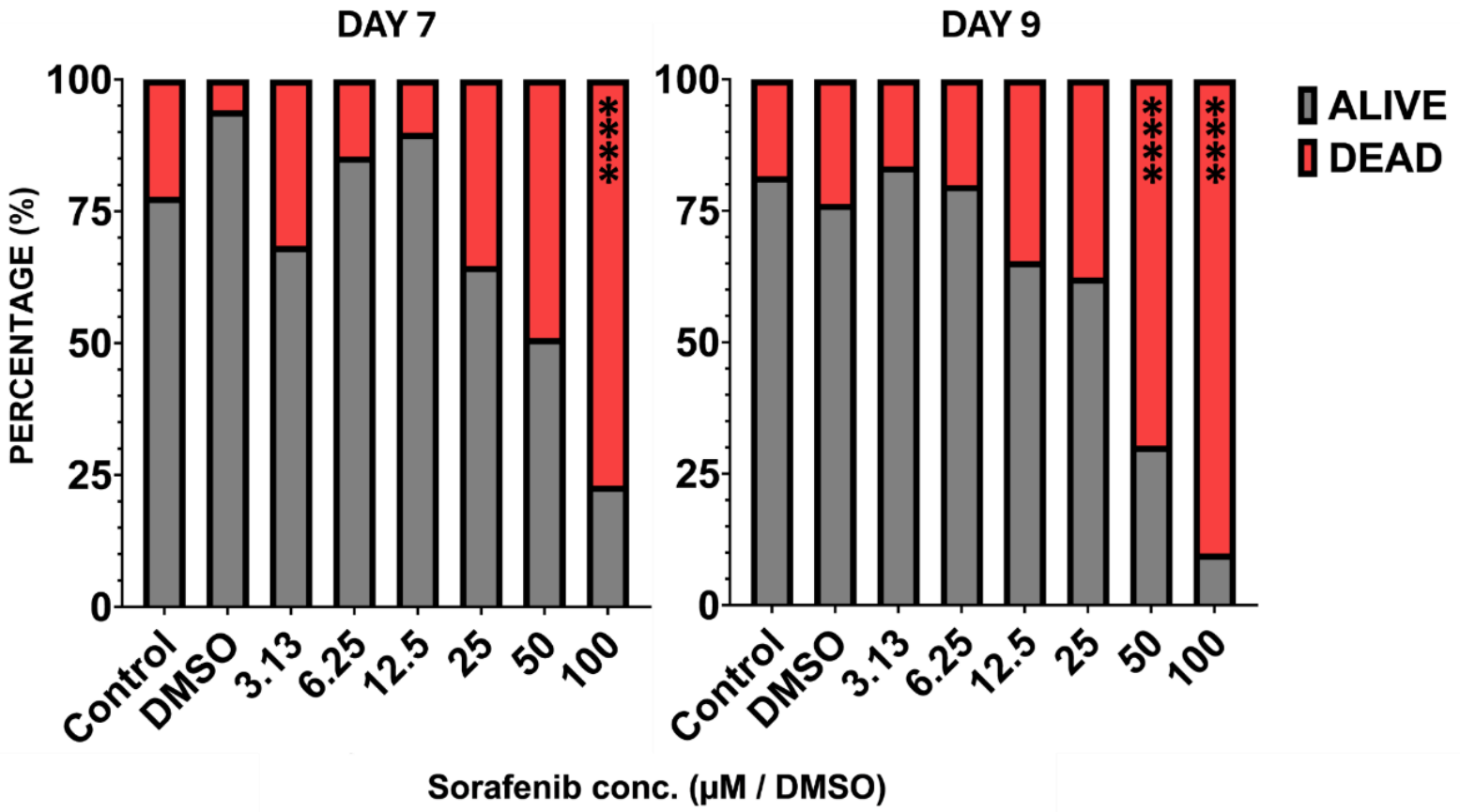


***Figure 5.4 Median Live/Dead percentage readings for K1 spheroids post 48 h sorafenib treatment. Day 7 (left) and Day 9 (right) K1 spheroids (seeded at 20,000 cells).*** *Images were taken using a Zeiss fluorescent microscope at 10x magnification and percentages of live and dead cells for each spheroid were determined using ImageJ, triplicates (three repeats in total, incomplete sets for some) for each concentration. Median values were plotted to compensate for abnormal readings, although significant differences were determined using mean values by utilising a 2-way ANOVA with Dunnett's multiple comparison test, between control and treated groups, **** ($P \leq 0.0001$), n=3. DMSO: dimethyl sulfoxide, diluted to match the highest concentration of sorafenib [1% (v/v)].*

When comparing the quantitative results to the fluorescent images in the control and treated groups, there was no visual difference in staining up to 6.25 µM. At 6.25 µM and below, the spheroids maintain a dominant green colour with a high percentage of live cells (Figure 5.5). It is only following treatment with 12.5 µM sorafenib and above that more spheroids display more of an orange/red colour resulting from the damage induced by sorafenib. This was seen for both groups of spheroids (day 7 and 9) which is congruent with the CTG results and diameter analysis specifically for day 9 spheroids, whereby significant reductions in ATP production and size were observed in the spheroids treated with 12.5 µM sorafenib group and above. The 50 and 100 µM treated spheroids displayed the most pronounced damage with high percentages of cell death, and the percentage of live cells fell below 50% which corroborates all the results derived from the earlier tests.

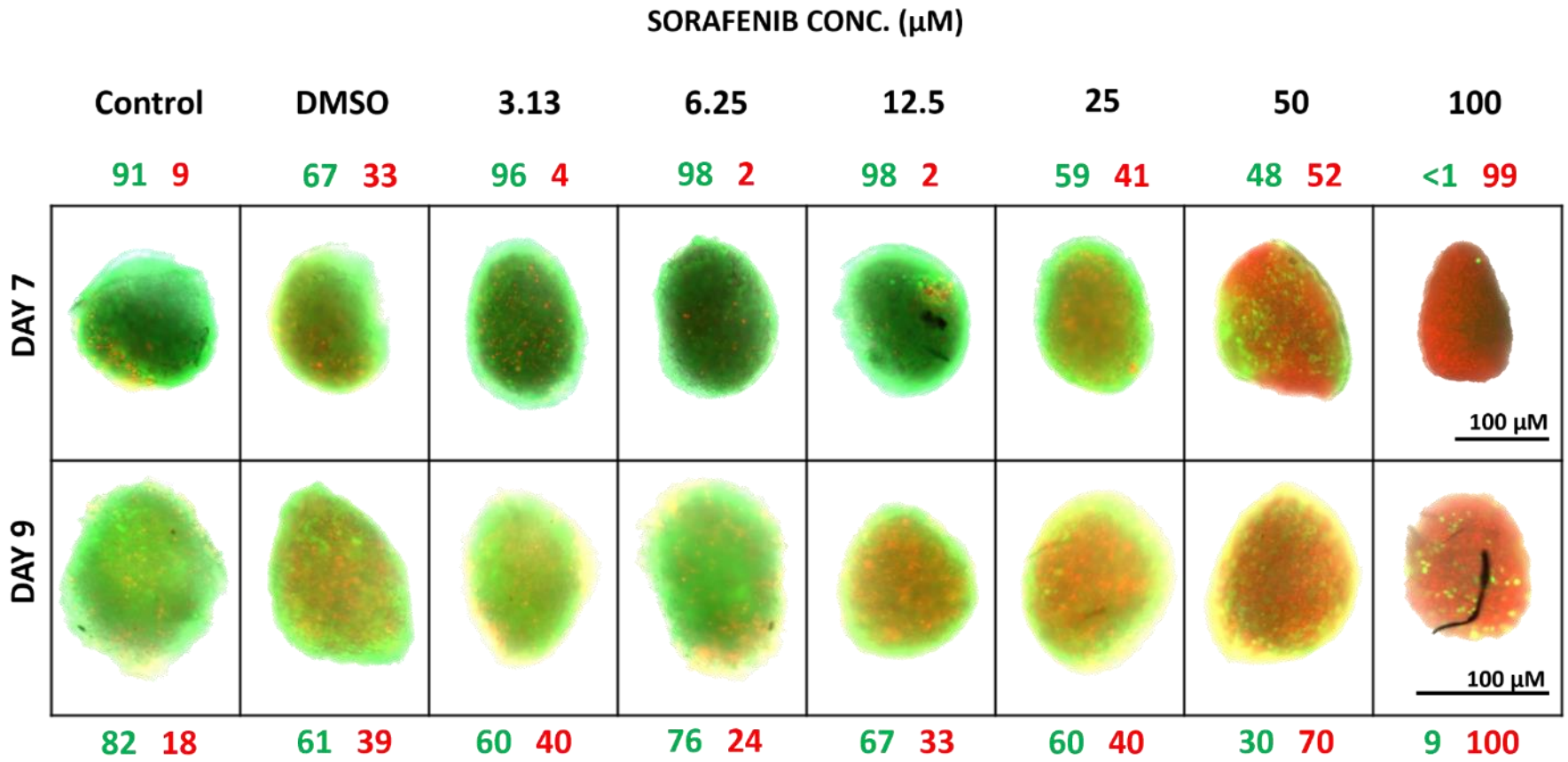


***Figure 5.5 Fluorescent images of Fluorescein Diacetate and Propidium Iodide (FDA/PI) stained K1 spheroids post 48 h sorafenib treatment. Day 7 and Day 9 spheroids were seeded at 20,000 cells.*** *Images were taken using a Zeiss fluorescent microscope at 10x magnification. ImageJ was used to produce the percentages of live (green) and dead (red) cells. Images are representative of three independent repeats, whereby 3 spheroids for each concentration group were imaged and analysed per repeat, n=3. DMSO: dimethyl sulfoxide, diluted to match the highest concentration of sorafenib [1% (v/v)].*

### 5.5.2 Analysing sorafenib potency on K1 spheroids seeded at 1,000 cells/well

Sorafenib was also tested on K1 spheroids seeded at 1,000 cells/well plus 1% (w/v) Matrigel® on a ULA plate in order to see how the effects of the TKI differed on a much smaller 3D model, which potentially lacked a necrotic core and exhibited higher viability compared to non-supplemented spheroids (section 3.5.1). It is important to note that these spheroids were supplied with Matrigel® for structural integrity support, however it is not believed to have had any effect on how cells reacted to the TKI as investigations with $NaN_3$, a metabolic poison, displayed that spheroids with and without Matrigel® had very similar responses to the drug (section 4.5.2).

A significant reduction in viability when compared to the control, was seen at concentrations of 25 µM (47% drop) and above for day 7 spheroids and as low as 6.25 µM (28.6% drop) and beyond for the day 9 spheroids (Figure 5.6). Noticeably, the day 9 spheroids were more sensitive than the 7 day old spheroids and also retained consistently higher values of viability reflecting the trend seen in the larger spheroids (seeded at 20,000 cells/well). It would seem the smaller spheroids, more specifically when younger (7 days in this case), had a greater resistance to sorafenib compared to the K1 spheroids plated at 20,000 cells/well, having shown a significant decline in viability at 25 µM whereas for the larger spheroids these were highly vulnerable even at 6.25 µM, which was observed with the day 9 spheroids seeded at 1000 cells/well. Both spheroid age groups (1000 cells/well) when treated with the top concentration showed highly effective reductions in viability, by 99.5% for day 7 spheroids and 99.2% for day 9 spheroids, values which are slightly higher compared to the larger spheroids again showcasing sorafenib could induce an almost complete 'kill'. As before the control and DMSO groups showed similar values meaning that DMSO had no undesirable effects on the spheroids.

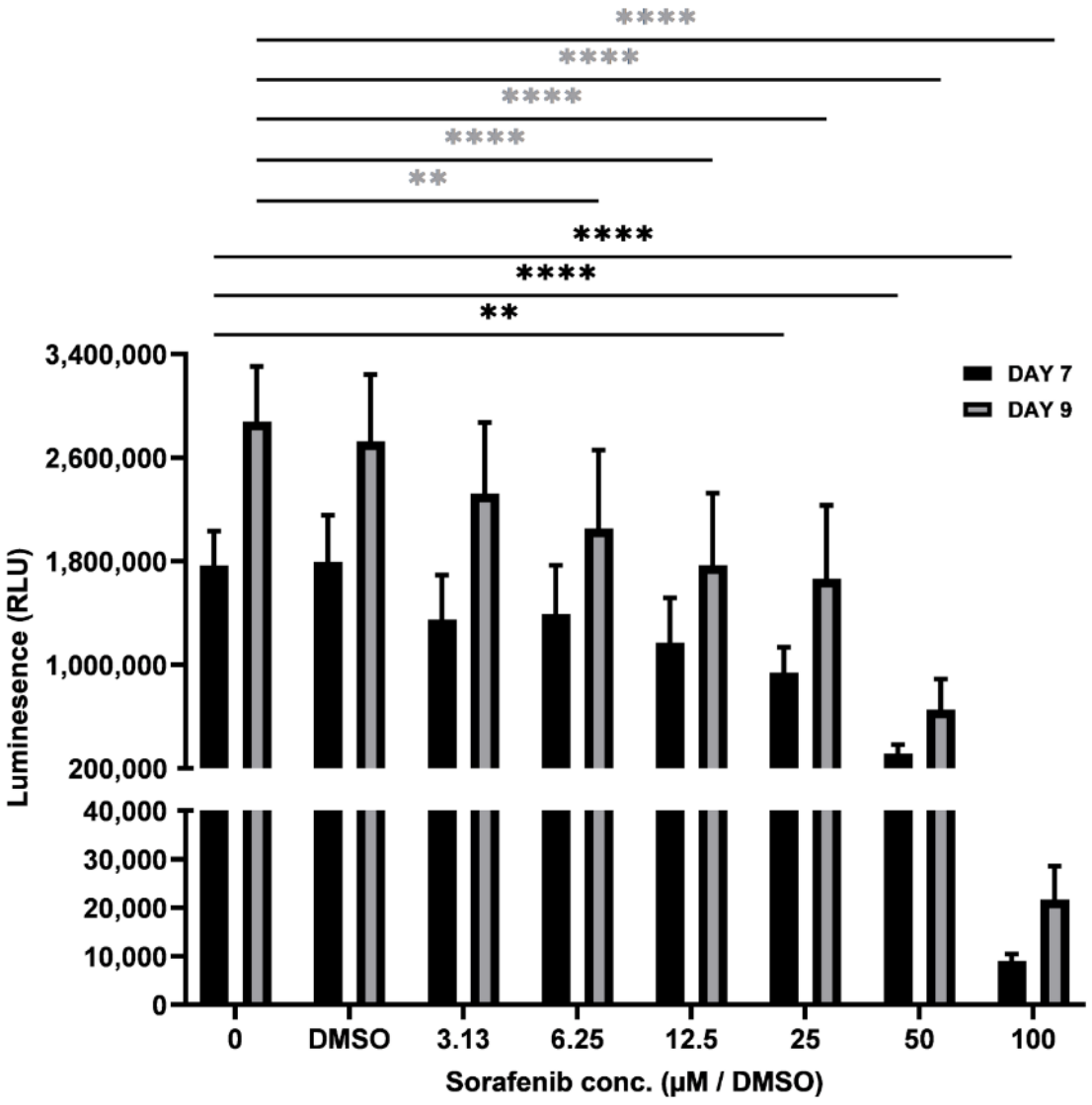


***Figure 5.6 Luminescence values from the CTG assay for untreated and treated (sorafenib for 48 h) K1 spheroids (seeded at 1000 cells).*** *Three independent experiments with triplicates for each treatment group were conducted. CTG values were determined post 48 h incubation with the TKI, with replenishment after 24 h. Day 7 spheroids began treatment when spheroids were 5 days old, day 9 spheroids when they were 7 days mature. Significant differences determined by a 2-way ANOVA with Dunnett's multiple comparison test, between control and treated groups. Values are mean ±SEM, ** (P ≤ 0.01), and **** (P ≤ 0.0001), n =3. DMSO: dimethyl sulfoxide, diluted to match the highest concentration of sorafenib [1% (v/v)].*

In contrast to the diameter measurements of spheroids plated at 20,000 cells/well which reflected the CTG readings, these spheroids (1000 cells/well) did not. For day 7 spheroids both the control groups (including DMSO) along with the 3.13 µM group had shown similar diameter averages of 1200 µm (Figure 5.7). Interestingly, the average diameter readings had increased to an average of 1300 µm for groups treated with 6.25, 12.5 and 25 µM before dropping down to 1140 µm for the 50 µM treated group and 955 µm for 100 µM. Whereas, day 9 spheroids had retained an average diameter of 1450 µm before dropping to 1370 µm in the 50 µM group and 1185 µm for 100 µM. Dunnett's multiple comparisons revealed no significant decreases for any of the groups or sets despite observable reductions, particularly, at the two most potent concentrations.

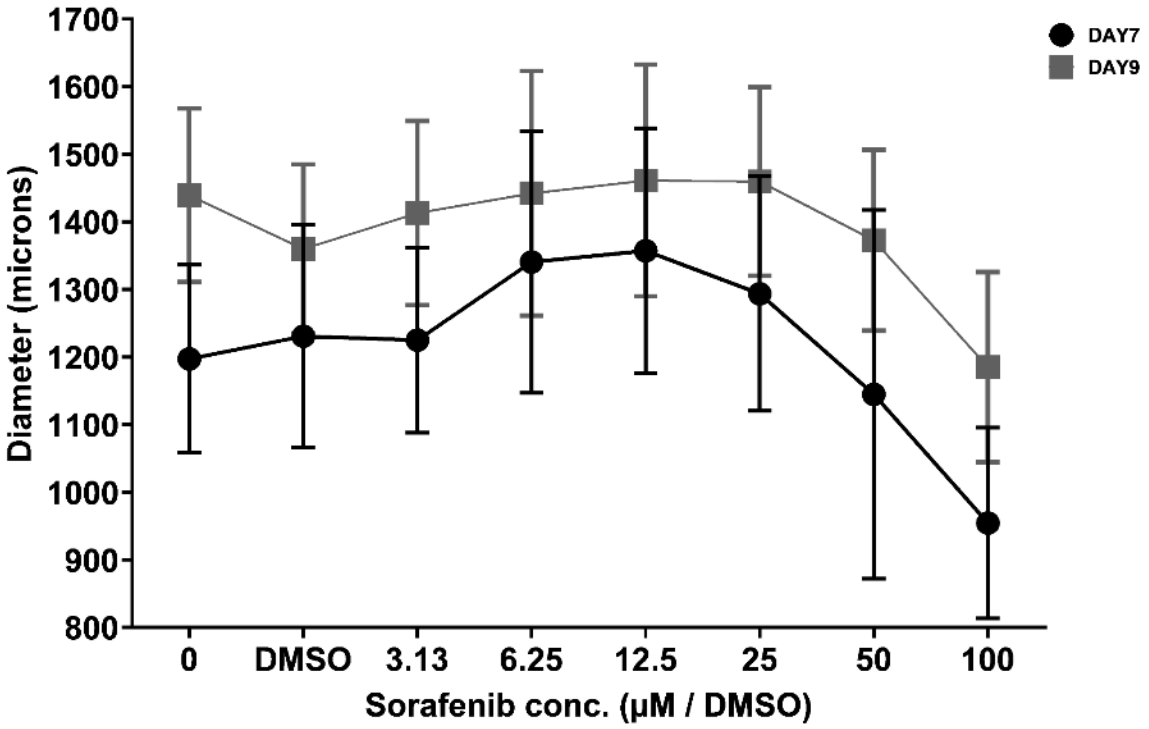


***Figure 5.7 Diameter measurements for K1 spheroids (seeded at 1000 cells) post 48 h sorafenib treatment.*** *Images were taken using a Zeiss fluorescent microscope at 10x magnification and then average diameter readings of spheroids for each concentration were determined using ImageJ, triplicates (three repeats, incomplete sets for some) for each concentration. Significant differences determined by 2-way ANOVA with Dunnett's multiple comparison test, between control and treated groups. Values are mean ±SEM, n=3. DMSO: dimethyl sulfoxide, diluted to match the highest concentration of sorafenib [1% (v/v)].*

For the percentage measurements, following FDA/PI staining, a considerable proportion of dead cells was again only seen at the top concentrations similar to the results observed with the K1 spheroids seeded at 20,000 cells/well (Figure 5.8). However, in this case day 7 spheroids appeared more sensitive than day 9 spheroids which only produced significant declines in live cell percentages post Dunnett's analysis in the 50 and 100 µM groups. Whereas significant drops had been recorded in much lower concentrations of 12.5 µM and above for the younger day 7 spheroids.

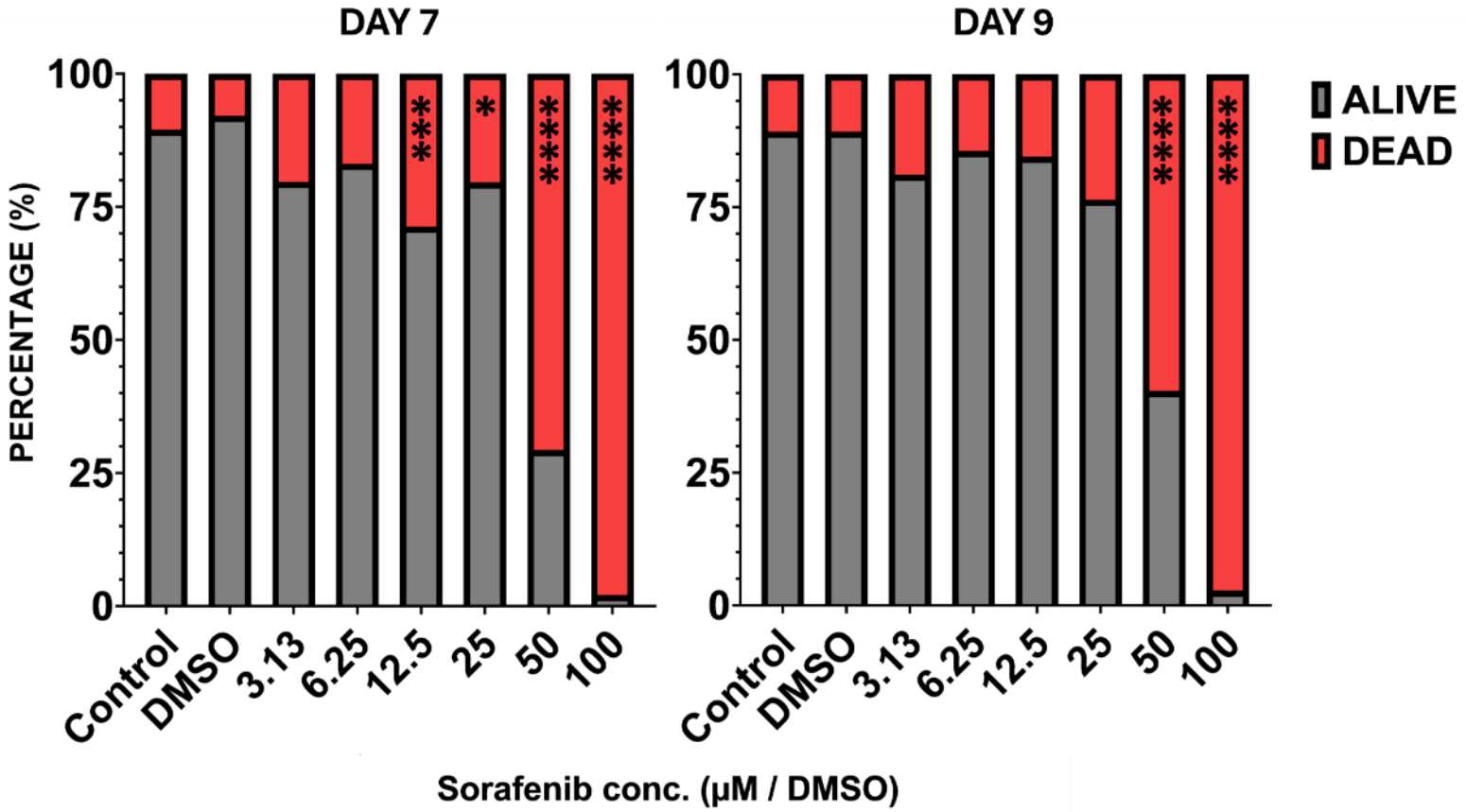


***Figure 5.8 Median Live/Dead percentage readings for K1 spheroids post 48 h sorafenib treatment. Day 7 (left) and Day 9 (right) K1 spheroids (seeded at 1000 cells).*** *Images were taken using a Zeiss fluorescent microscope at 10x magnification and percentages of live and dead cells for each spheroid were determined using ImageJ, triplicates (three repeats in total, incomplete sets for some) for each concentration. Median values were plotted to compensate for abnormal readings, although significant differences were determined using mean values by utilising a 2-way ANOVA with Dunnett's multiple comparison test, between control and treated groups, * (P ≤ 0.05), *** (P ≤ 0.001) and **** (P ≤ 0.0001), n=3. DMSO: dimethyl sulfoxide, diluted to match the highest concentration of sorafenib [1% (v/v)].*

Fluorescent images only strongly resembled what was seen in the quantitative results for the day 9 spheroids, i.e. only the highest concentrations induced significant kill, driving live cell percentages below 50%, with complete spheroidal death observed at 100 µM for both days (Figure 5.9). As with the 20,000 cells/well spheroid images, the pronounced red staining identifying cell death was seen only at the 50 µM and 100 µM groups. Based on these representative fluorescent images, day 7 spheroids also only experienced considerable cell death emphasising the importance of the previous tests which highlighted spheroids were affected at the lower concentrations.

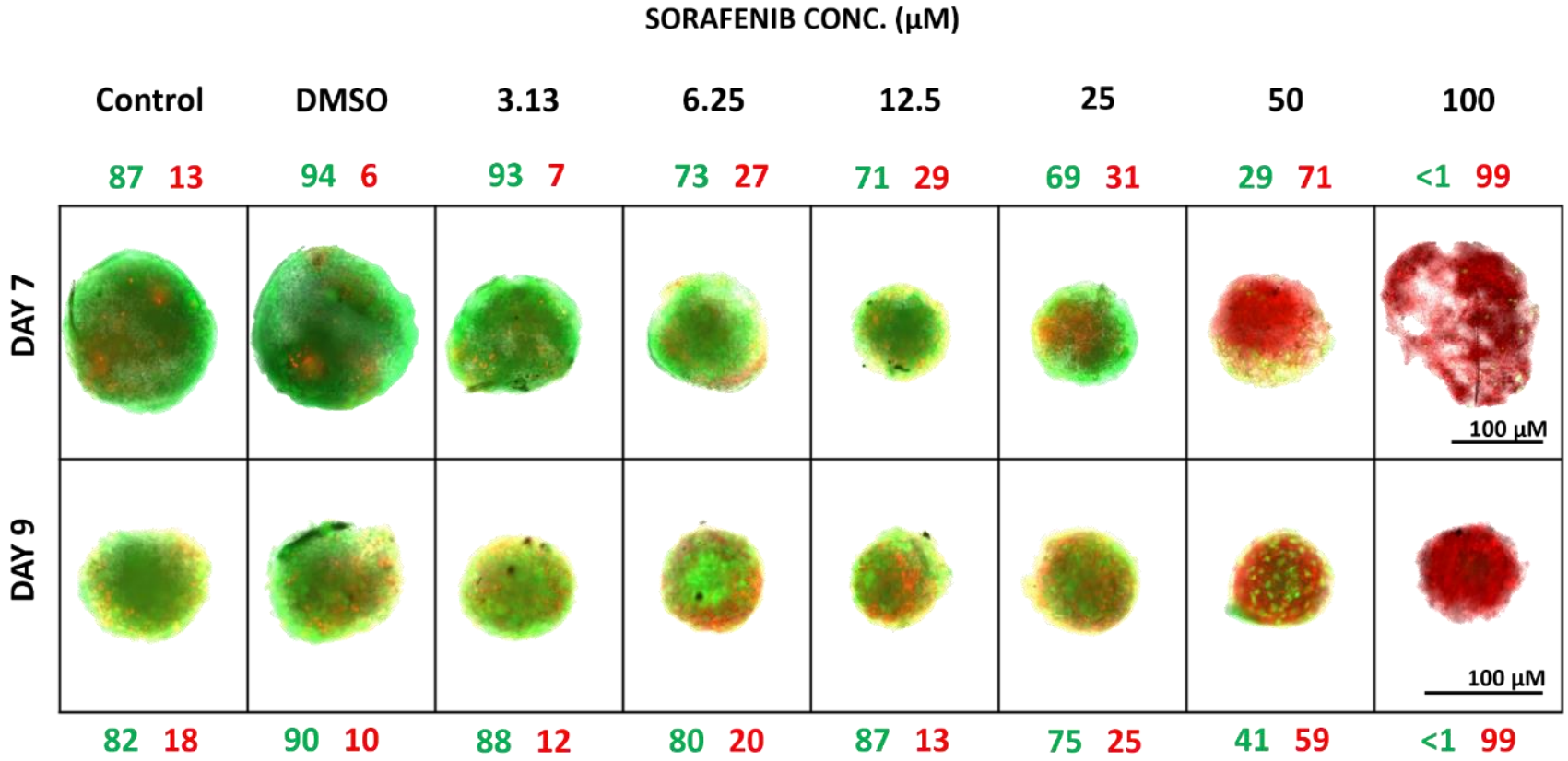


***Figure 5.9 Fluorescent images of Fluorescein Diacetate and Propidium Iodide (FDA/PI) stained K1 spheroids (seeded at 1000 cells/well) post 48 h sorafenib treatment.*** *Images were taken using a Zeiss fluorescent microscope at 10x magnification. ImageJ was used to produce the percentages of live (green) and dead (red) cells. Images are representative* of three independent repeats*, whereby 3 spheroids for each concentration group were imaged and analysed per repeat*, n=3. DMSO: dimethyl sulfoxide, diluted to match the highest concentration of sorafenib [1% (v/v)].

### 5.5.3 Investigating sorafenib effects on 8305c 10K spheroid viability

This experiment was conducted to see how a different cell line would respond to sorafenib treatment. The more aggressive 8305c cell line was investigated (section 5.2) utilising the preliminary experiments in section 3.6, which determined that the optimal number of cells required to form a good spheroid was 10,000 cells/well.

Following treatment of day 5 and day 7 8305c spheroids for 48 h the results from the CTG assay suggest that the anaplastic cell line (8305c) is surprisingly more sensitive to sorafenib than the papillary cell line (K1), as a significant reduction in ATP production was observed, following treatment with 3.13 µM sorafenib in the day 9 group with a drop in viability of 15.3% compared to the control (Figure 5.10). This is in contrast to the K1 cell line where an effect was not observed until treatment with 6.25 µM sorafenib. Control and DMSO for both days demonstrated a high degree of congruence, again demonstrating that this cell line is, like the K1 cell line, was unaffected by the presence of DMSO at the concentration used to dissolve the highest concentration of sorafenib. A noticeable difference between groups treated on different days was that day 9 ATP production decreases were more pronounced than those from day 7 spheroids, especially evident in the day 9 spheroids following 50 µM sorafenib where luminescent readings were reduced by 81.2% in the day 7 spheroids but by a much larger 93.4% in the day 9 spheroids.

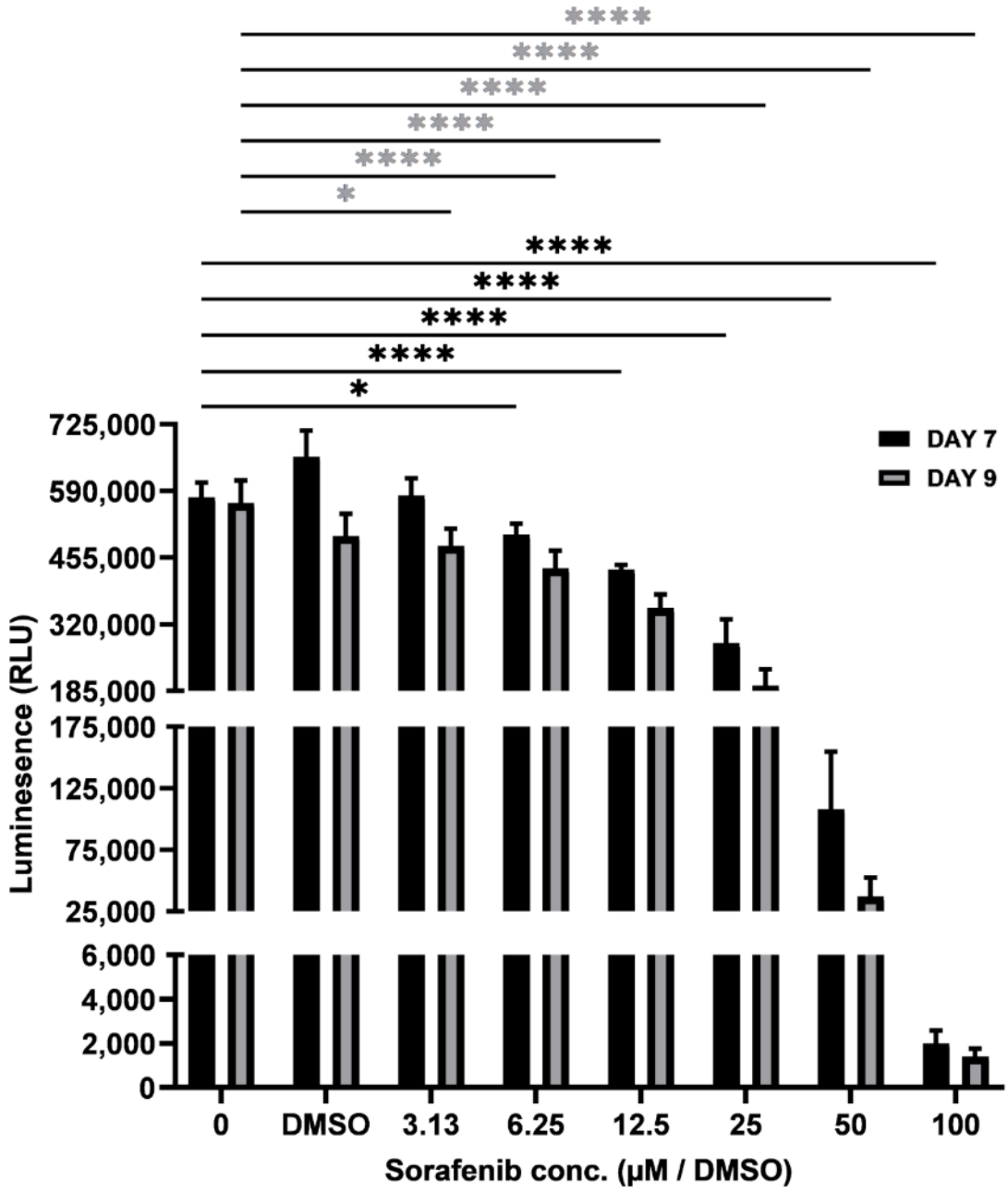


***Figure 5.10 Luminescence values from the CTG assay for untreated and treated (sorafenib for 48 h) 8305c spheroids (seeded at 10,000 cells).*** *Three independent experiments with triplicates for each treatment group were conducted. CTG values were determined post 48 h incubation with the TKI, with replenishment after 24 h. Day 7 spheroids began treatment when spheroids were 5 days old, day 9 spheroids when they were 7 days mature. Significant differences determined by a 2-way ANOVA with Dunnett's multiple comparison test, between control and treated groups. Values are mean ±SEM, * (P ≤ 0.05), and **** (P ≤ 0.0001), n =3. DMSO: dimethyl sulfoxide, diluted to match the highest concentration of sorafenib [1% (v/v)].*

In terms of spheroid size, the day 7 control and DMSO spheroids were on average 132 µm larger than the day 9 spheroids from the same conditions, however sizes remained fairly consistent for the spheroids treated with the lower concentrations of sorafenib (3.13-25 µM) at around 610-640 µm (Figure 5.11). Whereas, day 9 spheroids had dropped to an average of 630 µm (3.13-25 µM) whereby control and DMSO averages were at around 720 µm with visible drops at the top two concentrations. The diameter trend decreases between the top concentrations and controls were quite similar for both day 9 and day 7 spheroids: day 7 control spheroids were on average 590 µm shrinking to a diameter of approximately 510 µm following treatment with 100 µM sorafenib, while the day 9 spheroids treated with 100 µM sorafenib were on average 415 µm in diameter compared to the controls at 720 µm. A Dunnett's test had confirmed that the only significant reduction in diameter size for the day 7 spheroids was seen in the 100 µM group. Whereas, for the day 9 a significant reduction when compared to the control was observed for every single treatment group, strongly replicating the viability decline trend post CTG analysis.

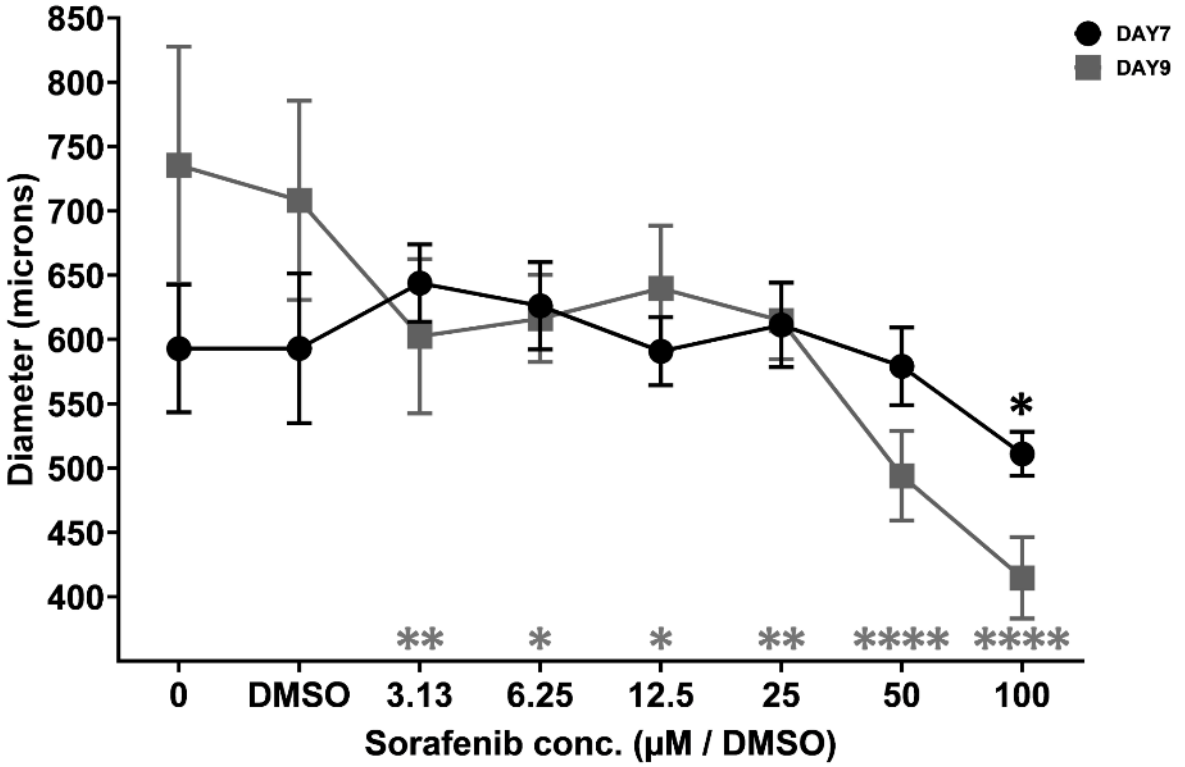


***Figure 5.11 Diameter measurements for 8305c spheroids (seeded at 10,000 cells) post 48 h sorafenib treatment.*** *Images were taken using a Zeiss fluorescent microscope at 10x magnification and then average diameter readings of spheroids for each concentration were determined using ImageJ, triplicates (three repeats, incomplete sets for some) for each concentration. Significant differences determined by 2-way ANOVA with Dunnett's multiple comparison test, between control and treated groups. Values are mean ±SEM, * (P ≤ 0.05), ** (P ≤ 0.01), and **** (P ≤ 0.0001), n=3. DMSO: dimethyl sulfoxide, diluted to match the highest concentration of sorafenib [1% (v/v)].*

Live-dead cell percentages, determined following FDA/PI staining, displayed very similar measurements to those observed for the K1 spheroids (Figure 5.12). Only the top two concentrations of sorafenib (50 and 100 µM) for both 7 and 9 day spheroids induced a greater percentage of dead cells with those being the only groups demonstrating significant declines in live cell percentages post Dunnett's analysis. This does not correlate well with the CTG values which showed a pronounced decline in viability at concentrations as low as 3.13 µM.

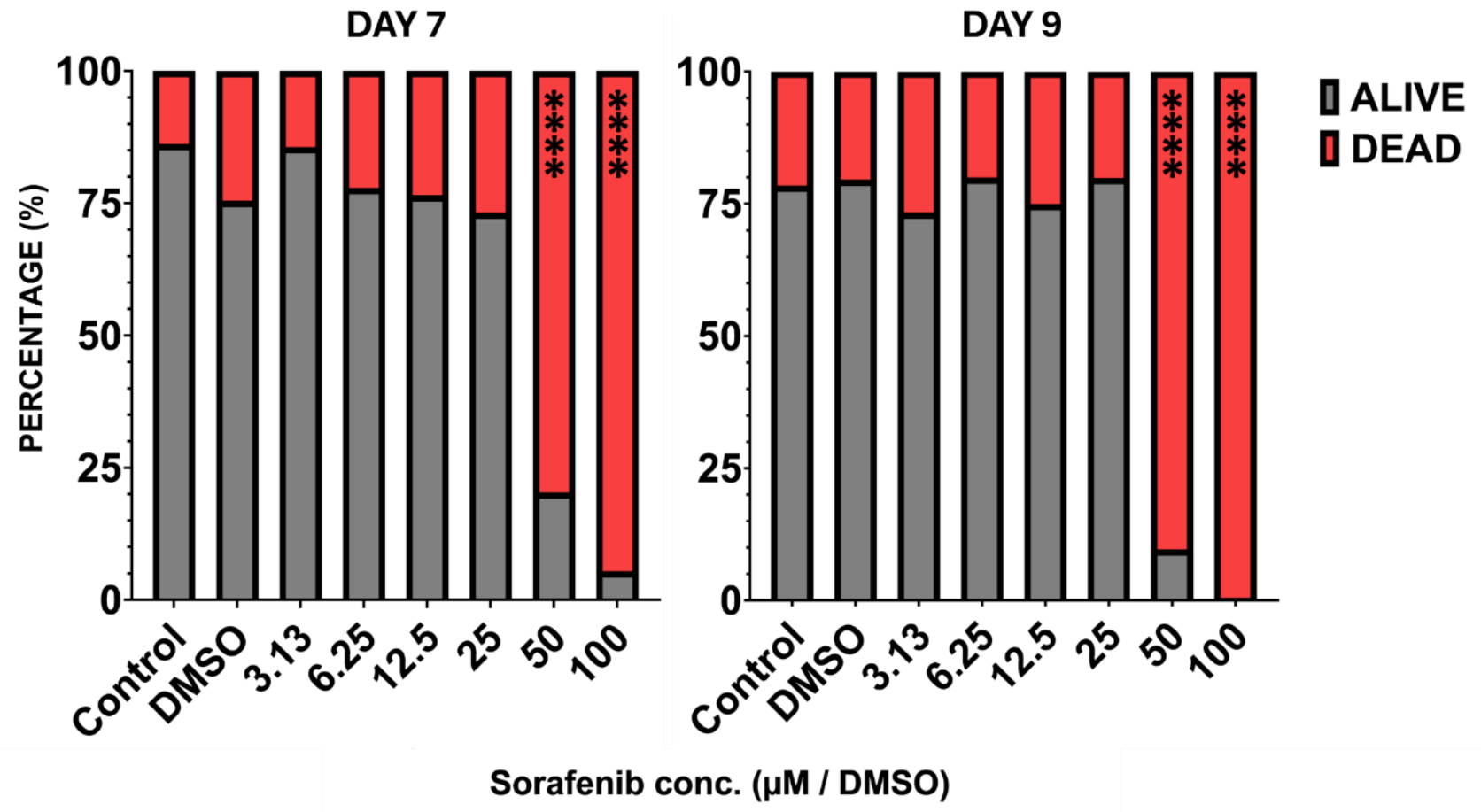


***Figure 5.12 Median Live/Dead percentage readings for 8305c spheroids post 48 h sorafenib treatment****. Day 7 (left) and Day 9 (right) K1 spheroids (seeded at 10,000 cells). Images were taken using a Zeiss fluorescent microscope at 10x magnification and percentages of live and dead cells for each spheroid were determined using ImageJ, triplicates (three repeats in total, incomplete sets for some) for each concentration. Median values were plotted to compensate for abnormal readings, although significant differences were determined using mean values by utilising a 2-way ANOVA with Dunnett's multiple comparison test, between control and treated groups, **** (P ≤ 0.0001), n=3. DMSO: dimethyl sulfoxide, diluted to match the highest concentration of sorafenib [1% (v/v)].*

The fluorescent images demonstrate a pronounced red stained centre in all spheroids, presumably a necrotic core characteristic of a tumour-like structure (Figure 5.13), a feature which was not as consistently seen in the 20,000 cells/well spheroids. Despite that in a similar fashion to the large K1 spheroids, 8305c spheroids plated at 10,000 cells/well at the top two concentrations (50 and 100 μM) were the only sets showing a visible reduction in the live cells (green stain) and an increase in the dead (red stain) cells, which do not reflect what was seen in the previous tests. This highlights the importance of including FDA/PI staining with fluorescent microscopy as a secondary analysis tool in addition to the primary assay for determining spheroid cell viability. It would appear that sorafenib is more potent at the lower concentrations in 8305c spheroids compared to K1, as there is more intense red staining and noticeably lower live cell percentages across all treatment groups and days.

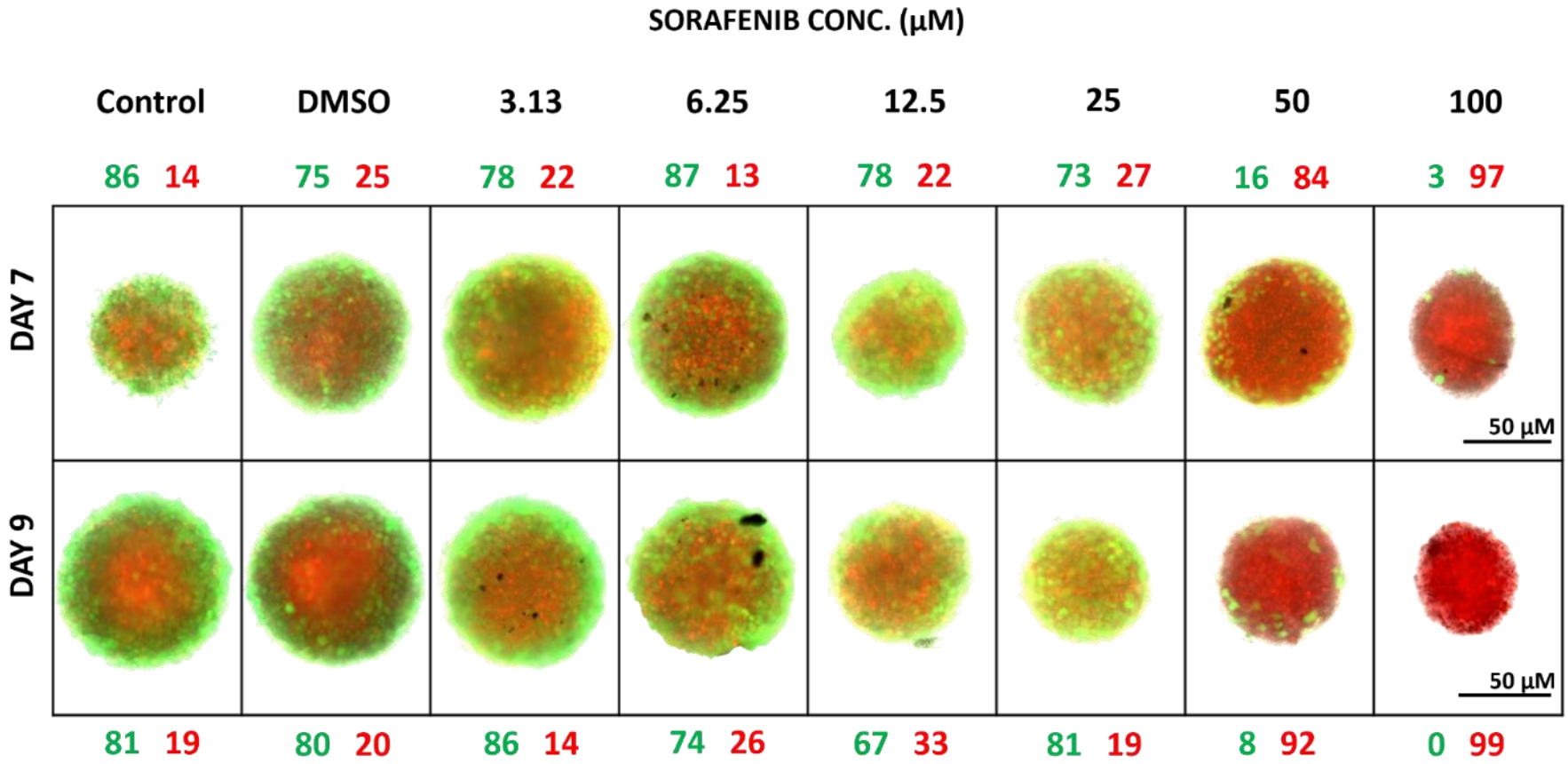


***Figure 5.13 Fluorescent images of Fluorescein Diacetate and Propidium Iodide (FDA/PI) stained 8305c spheroids (seeded at 10,000 cells) post 48 h sorafenib treatment.*** *Images were taken using a Zeiss fluorescent microscope at 10x magnification. ImageJ was used to produce the percentages of live (green) and dead (red) cells. Images are representative* of three independent repeats*, whereby 3 spheroids for each concentration group were imaged and analysed per repeat*, n=3. DMSO: dimethyl sulfoxide, diluted to match the highest concentration of sorafenib [1% (v/v)].

### 5.5.4 Investigating sorafenib effects on 8305c 1K spheroid viability

As with the K1 cell line, the smaller spheroid model was investigated for the 8305c cell line, to determine whether a smaller spheroid, which potentially has a smaller or non-existent necrotic core, responds differently to the larger spheroids. As mentioned in the optimisation Chapter (section 3.3), 1000 cells/well 8305c spheroids had not been investigated via fluorescent microscopy to verify the presence/lack of a necrotic core and as a result confirmation took place during imaging analysis post sorafenib administration.

Following sorafenib treatment (3.13 – 100 µM), the same trend in ATP production, measured by the CTG assay was observed as in the K1 spheroids plated at 1,000 cells/well, where the day 9 spheroids had shown greater sensitivity to sorafenib than the day 7 spheroids (Figure 5.14). The lowest concentration to induce a significant reduction in viability compared to the control in the day 7 spheroids was at 50 µM (drop of 94.3%) and above, whereas for day 9 spheroids it was seen at the lowest concentration of 3.13 µM with a decline by 26.5%. Interestingly, the CTG values for the 6.25 and 12.5 µM groups had more or less matched those of the control. Both day 7 spheroids (K1 and 8305c) seeded at 1000 cells/well had shown greater resistance to sorafenib compared to their larger counterparts and older spheroid groups suggesting younger and smaller spheroids were less susceptible to the cytotoxic effects.

Based on the day 9 DMSO readings it would seem that the solvent had a negative effect on spheroid viability, noted by the significant difference in viability when compared to the control. However, for the day 7 spheroids significantly higher luminescence values were observed in the DMSO group, highlighting the need for further future repeats in order to say for certain whether the presence of DMSO had any damaging effects on spheroid viability.

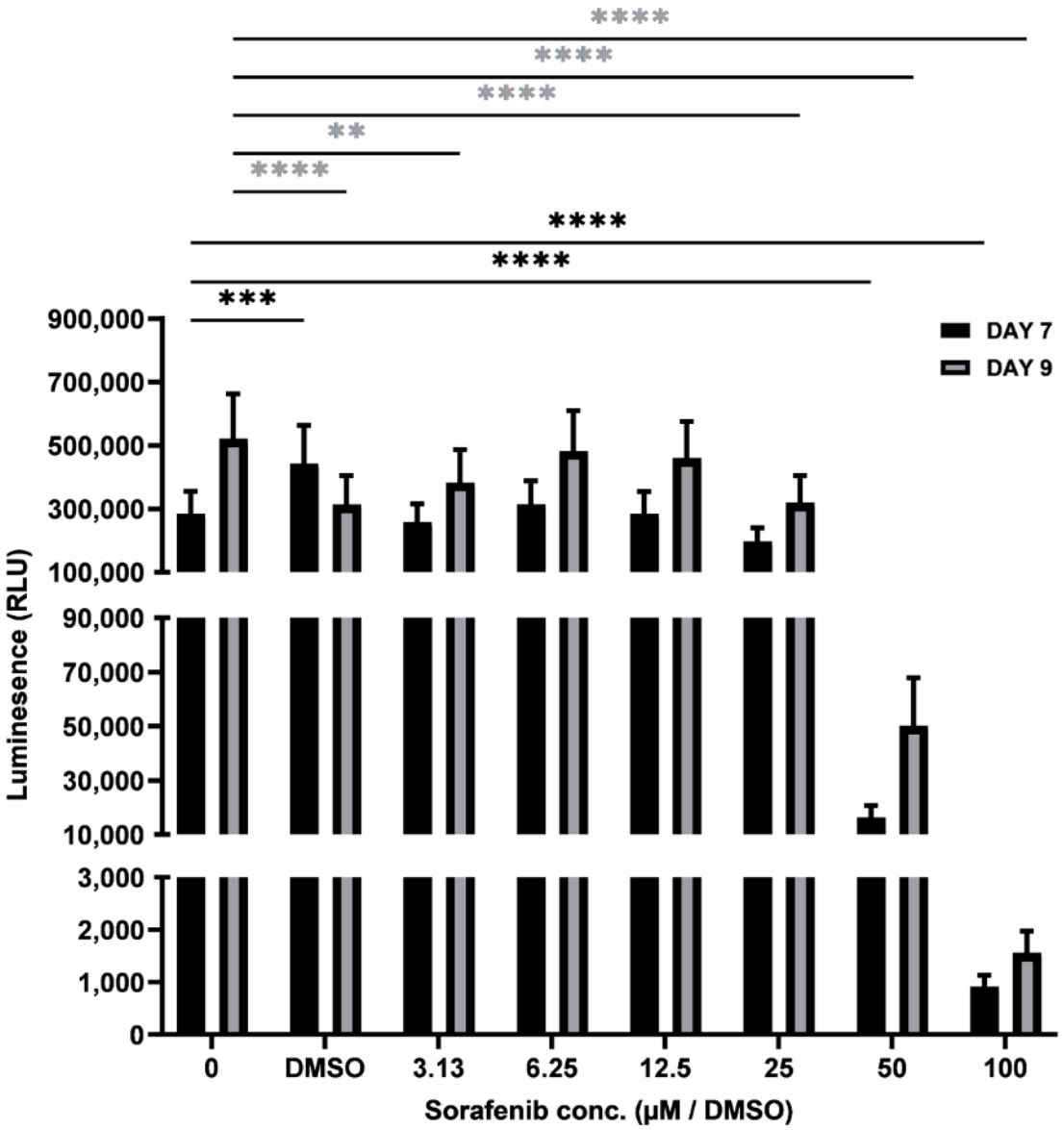


***Figure 5.14 Luminescence values from the CTG assay for untreated and treated (sorafenib for 48 h) 8305c spheroids (seeded at 1000 cells).*** *Three independent experiments with triplicates for each treatment group were conducted. CTG values were determined post 48 h incubation with the TKI, with replenishment after 24 h. Day 7 spheroids began treatment when spheroids were 5 days old, day 9 spheroids when they were 7 days mature. Significant differences determined by a 2-way ANOVA with Dunnett's multiple comparison test, between control and treated groups. Values are mean ±SEM, ** (P ≤ 0.01), *** (P ≤ 0.001) and **** (P ≤ 0.0001), n=3. DMSO: dimethyl sulfoxide, diluted to match the highest concentration of sorafenib [1% (v/v)].*

Spheroid diameter measurements showed almost identical spheroidal sizes in the DMSO group for both day 7 and day 9 spheroids (around 650 µm), whereas the day 9 spheroids were roughly 128 µm larger than the day 7 ones for the control group (Figure 5.15). In the day 9 set-up, all groups maintained a diameter reading of around 670 µm with a significant reduction in size only being observed in the 100 µM group following a Dunnett's test, where the average diameter decreased to 490 µm. In contrast day 7 spheroids decreased in diameter from the average 560 µm size, following treatment with both 50 and 100 µM sorafenib down to 520 µm and 455 µm with no significant reductions recorded.

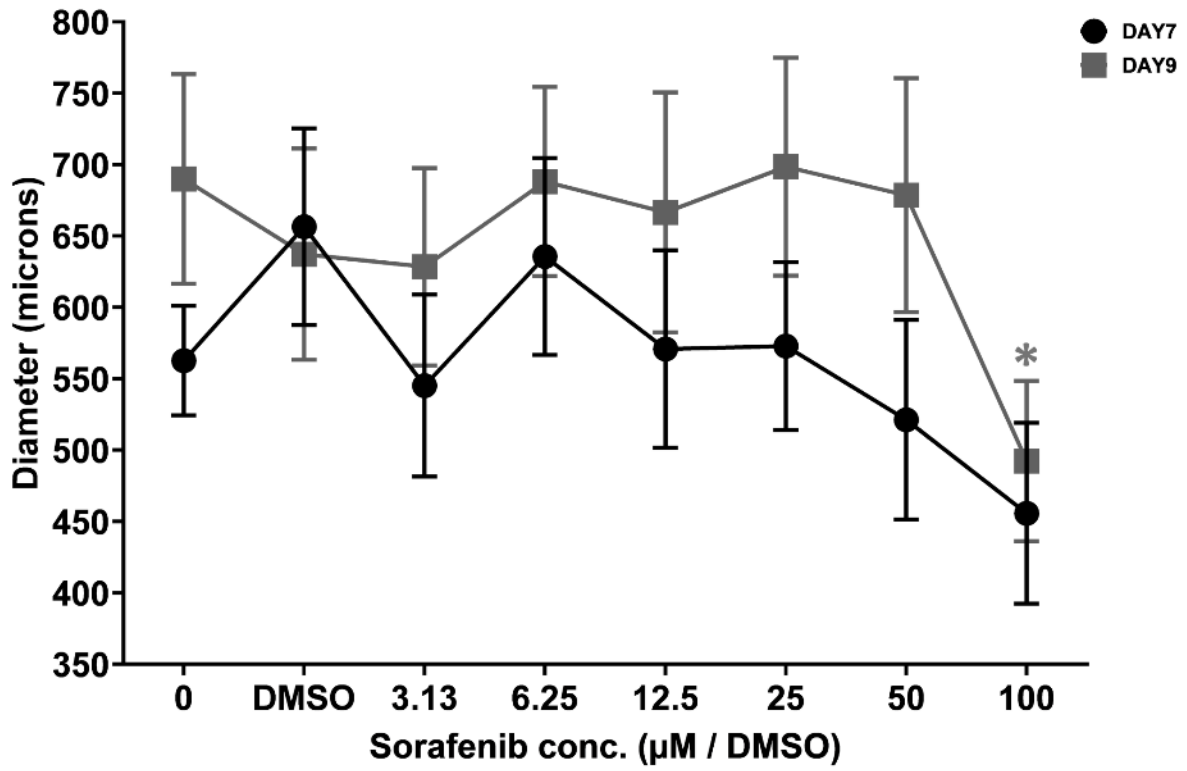


***Figure 5.15 Diameter measurements for 8305c spheroids (seeded at 1000 cells) post 48 h sorafenib treatment.*** *Images were taken using a Zeiss fluorescent microscope at 10x magnification and then average diameter readings of spheroids for each concentration were determined using ImageJ, triplicates (three repeats, incomplete sets for some) for each concentration. Significant differences determined by 2-way ANOVA with Dunnett's multiple comparison test, between control and treated groups. Values are mean ±SEM, * (P ≤ 0.05), n=3. DMSO: dimethyl sulfoxide, diluted to match the highest concentration of sorafenib [1% (v/v)].*

Continuing the trends seen in previous measurements for 8305c spheroids (plated at 10,000 cells/well), the 1000 cells/well 8305c spheroid model showed, the percentage of dead cells was only greater in both the day 7 and day 9 spheroids treated with 50 (mean dead cell percentage - 87% for day 7 and 77% for day 9) and 100 µM sorafenib dead cell percentage - 97% for day 7 and 98% for day 9) (Figure 5.16). Every group except for the top two concentrations regardless of age retained a live to dead cell percentage greater than 75%, with the only significant reductions recorded in the 50 and 100 µM groups for both analysis days.

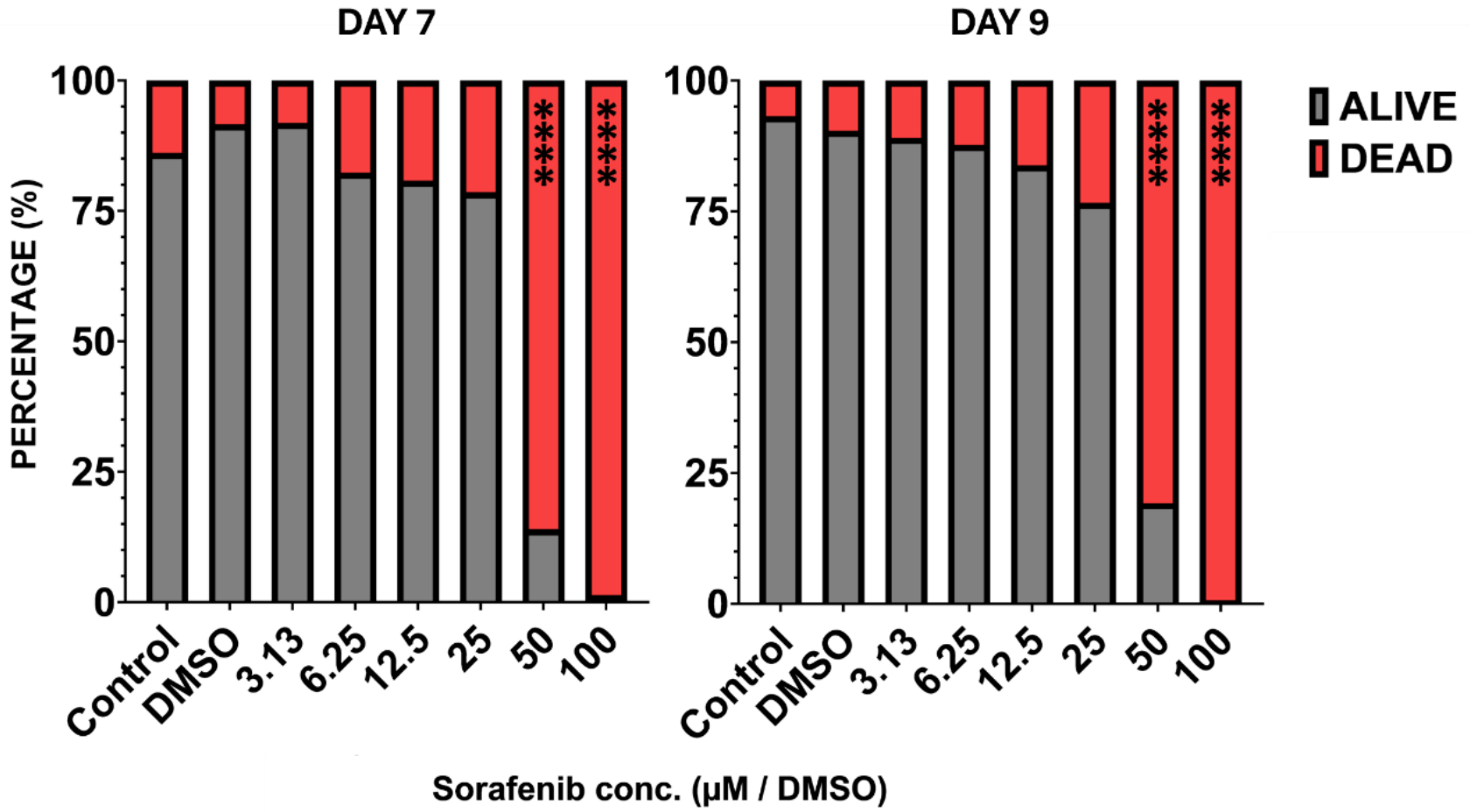


***Figure 5.16 Median Live/Dead percentage readings for 8305c spheroids post 48 h sorafenib treatment.*** *Day 7 (left) and Day 9 (right) K1 spheroids (seeded at 1000 cells). Images were taken using a Zeiss fluorescent microscope at 10x magnification and percentages of live and dead cells for each spheroid were determined using ImageJ, triplicates (three repeats in total, incomplete sets for some) for each concentration. Median values were plotted to compensate for abnormal readings, although significant differences were determined using mean values by utilising a 2-way ANOVA with Dunnett's multiple comparison test, between control and treated groups, **** ($P \leq 0.0001$), n=3. DMSO: dimethyl sulfoxide, diluted to match the highest concentration of sorafenib [1% (v/v)].*

The fluorescent images of the spheroids demonstrated different staining behaviours compared to the larger (10,000 cells/well) 8305c spheroids and the other K1 cell line, in that many unstained areas were evident in some of the spheroids (Figure 5.17). It is unclear whether the cell type and number resulted in these incomplete images, or the spaces were induced by damage inflicted by the sorafenib, however, the latter is unlikely as there is some evidence of the unstained areas in the control spheroids. Despite this observation it is clear that sorafenib had a pronounced impact on the spheroids, but only at the top concentrations (50 and 100 µM), where an increase in dead cells (red) was observed and a reduction in size at the top concentration for the day spheroids further supporting what was found in the other tests.

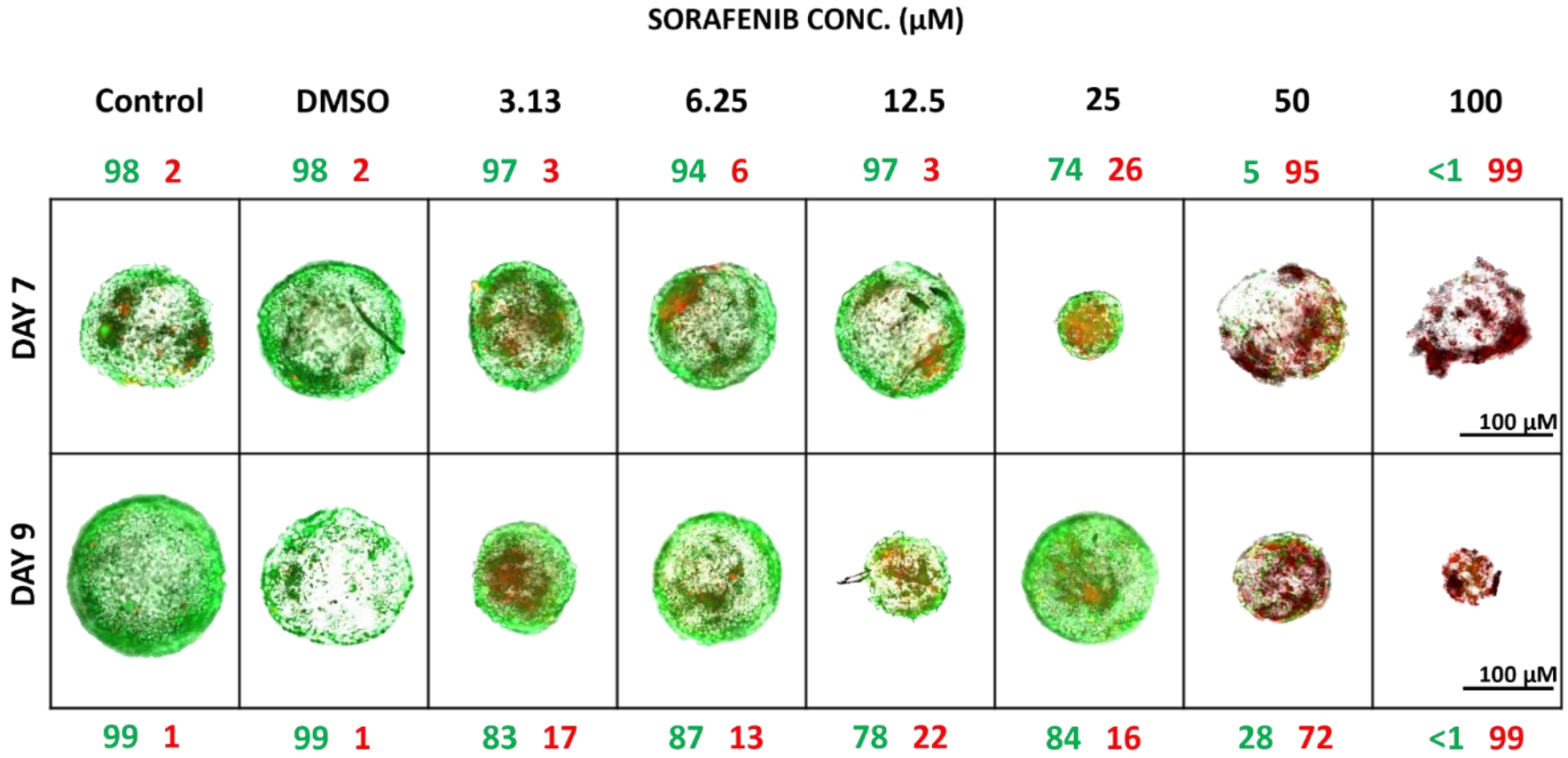


***Figure 5.17 Fluorescent images of Fluorescein Diacetate and Propidium Iodide (FDA/PI) stained 8305c spheroids (seeded at 1000 cells) post 48 h sorafenib treatment.*** *Images were taken using a Zeiss fluorescent microscope at 10x magnification. ImageJ was used to produce the percentages of live (green) and dead (red) cells. Images are representative of three independent repeats, whereby 3 spheroids for each concentration group were imaged and analysed per repeat, n=3. DMSO: dimethyl sulfoxide, diluted to match the highest concentration of sorafenib [1% (v/v)].*

### 5.5.5 Calculation of $IC_{50}$ values

An $IC_{50}$ value represents the concentration of a drug or inhibitor (i.e. sorafenib) required to reduce the activity of a biological system in this case TC spheroids by 50% relative to a control (Sebaugh, 2011). Measurements were based on the viability values derived from both analyses' days (7+9) post CTG examination against a sorafenib concentration range of 0, 3.13, 6.25, 12.5, 25, 50 and 100 µM.

The analysis of sorafenib's efficacy across the two cell lines (K1 and 8305c) and spheroid densities yielded the following $IC_{50}$ values: K1 spheroids seeded at 20,000 cells/well exhibited an $IC_{50}$ of 28.30 µM (Figure 5.18). In contrast, K1 spheroids at a lower density of 1,000 cells/well demonstrated a lower $IC_{50}$ of 18.66 µM, suggesting increased sensitivity compared to the higher-density spheroids, a stark contrast to previous findings. For the 8305c cell line the opposite was observed, larger spheroids seeded at 10,000 cells/well showed an $IC_{50}$ of 18.61 µM, reflecting a similar level of sensitivity as the K1 spheroids at the lower density. Whereas 8305c spheroids seeded at 1,000 cells/well had a higher $IC_{50}$ of 28.49 µM, which closely mirrored the recorded value for the larger K1 spheroids, and the trend seen of the smaller spheroids exhibiting greater resistance as shown throughout this Chapter. In the case of the 8305c cell line, larger spheroids showcased heightened sensitivity to sorafenib compared to smaller spheroids.

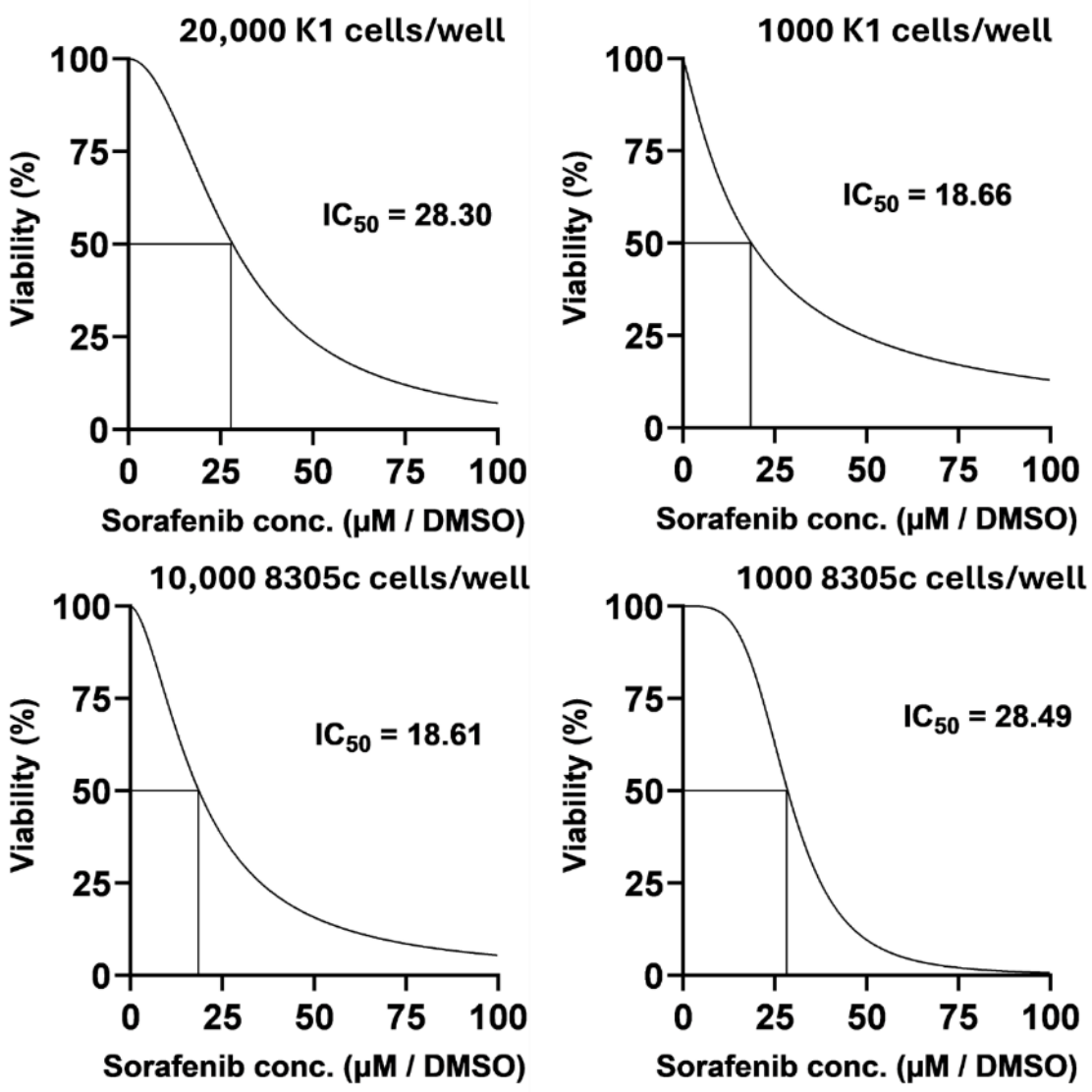


***Figure 5.18 Calculated $IC_{50}$ values for K1 and 8305c spheroids.*** *Normalised Day 7 and Day 9 spheroid viability values post CTG analysis were combined and plotted against sorafenib concentrations (0, 3.13, 6.25, 12.5, 25, 50 and 100 µM) to determine an $IC_{50}$ value for each cell line and seeding density using GraphPad prism. Each graph represents the established $IC_{50}$ value for each seeding density and cell line using triplicate CTG values for each analysis day after three independent repeats.*

## 5.6 Spheroid On-chip investigations

Based on literature recommendations for better simulating the *in vivo* environment (section 1.6.2), spheroids were placed onto on-chip devices and treated with sorafenib for 48 h with replenishment after 24 h to mimic patient dosing in clinic. Both the K1 and 8305c cells lines were investigated, seeded at 20,000 and 10,000 cells respectively and grown for 5 days in 96-well ULA plates, before transfer onto chip. The concentrations of sorafenib used were reduced to 0, 25, 50, and 100 µM, based on the results of the static experiments and CTG was used to analyse spheroid viability post treatment.

The first and only successful experiment out of a total of four repeats involved K1 spheroids with 4 replicates for 0 µM, 6 for both 25 µM and 50µM, and 5 for 100 µM which were analysed with CTG, revealing values reminiscent of those obtained from spheroids grown in static ULA plates, with decreasing viability (luminescence) observed with increasing sorafenib concentrations, which were all significantly less than the control (medium containing DMSO; Figure 5.19). The reason for the odd number of replicates is due to the challenges faced with recovering spheroids from the chips into the opaque-walled plates for CTG analysis as spheroids could be lost either through spontaneous disaggregation or human error.

The only major difference observed between static and on-chip experiments, was that the spheroids on-chip appeared to be more sensitive to the TKI compared to the static cultures. For example, all the treated on-chip spheroids had less than 10,000 RLU values compared to those maintained in static culture, where following treatment with the highest concentration of sorafenib (100 µM), the RLU value was around 50,000 RLU. Whereas the control CTG value was complementary to the untreated values for the K1 20,000 cells/well spheroids under no-flow conditions.

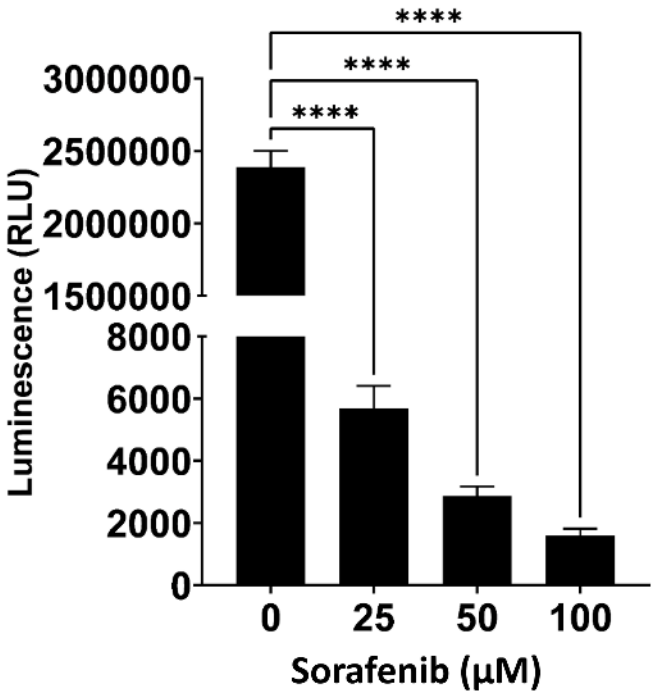


***Figure 5.19 Luminesce values from the CTG assay for untreated and treated (sorafenib for 48 h) K1 spheroids (seeded at 20,000 cells) post on-chip treatment.*** *Spheroids were placed on-chip when 5 days old, CTG values were determined post 48 h incubation with TKI replenishment after 24 h. 4 replicates for 0 µM, 6 for 25 µM + 50µM and 5 for 100 µM were analysed. Significant differences determined by a 2-way ANOVA with Dunnett's multiple comparison test, between control and treated groups. Values are mean ± SEM, **** (P ≤ 0.0001), n=1.*

The fluorescent images, obtained after staining the on-chip spheroids with FDA/PI demonstrate that most of the damage induced by the TKI appeared to have been done to the outer layer of the spheroid (Figure 5.19). However, when analysed using ImageJ, it was revealed that hardly any cells had retained the green stain except for the control spheroids, hence very low live/dead cell readings. A background staining issue would explain why despite the 100 µM treated spheroid displaying a large area of green staining which would normally indicate a population of viable cells, is actually just a facade with the majority of cells in fact picking up the PI stain when the colour channels are split during ImageJ analysis, thus a very high cell death percentage of 99% which corroborates the CTG readings. Moreover, the control, which retained a high percentage (96%) of viable cells post incubation on-chip further confirms that damage inflicted to the treated spheroids was in fact due to the TKI rather than incubation on-chip with viability values matching those of the static K1 spheroids. Regardless,

a gradual decline in live cell percentages was observed with 21% for the 25 µM spheroid and drastically dropping to 5 and <1% for the 50 and 100 µM spheroids, respectively.

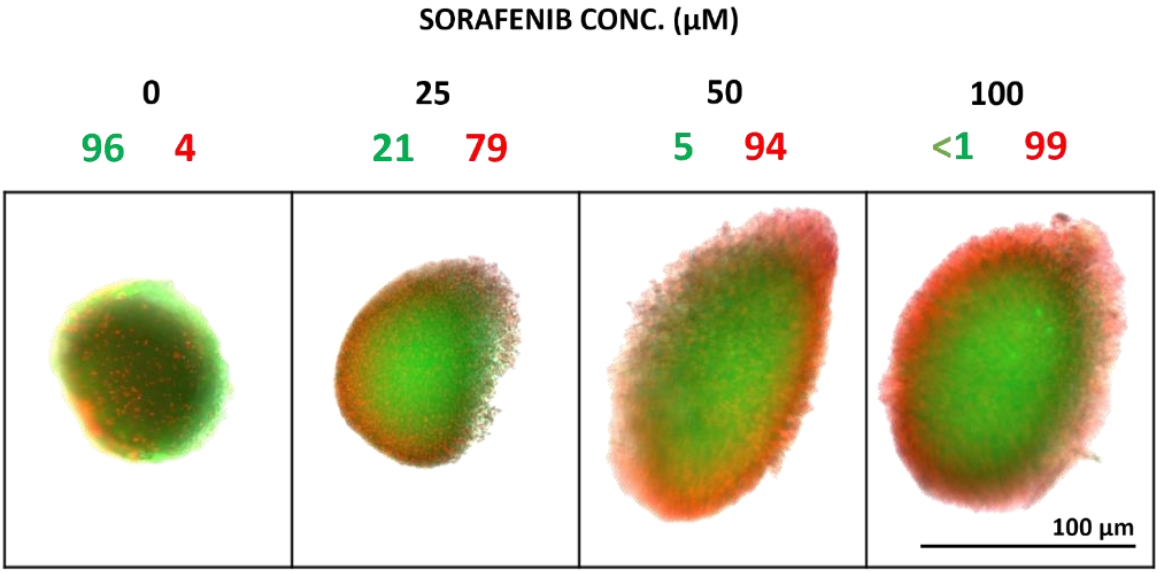


***Figure 5.20 Fluorescent images of Fluorescein Diacetate and Propidium Iodide (FDA/PI) stained K1 spheroids (seeded at 20,000 cells) post 48 h sorafenib treatment on-chip.*** *Images were taken using a Zeiss fluorescent microscope at 4x magnification. ImageJ was used to produce the percentages of live to dead cells, green – live, red – dead cells. Images are representative, whereby 2 spheroids for each concentration group were imaged and analysed, n=1.*

The investigation with K1 spheroids was repeated once more however after analysis with CTG assay, but it was discovered that all spheroids had perished as they showed less than 1000 RLU values. When 8305c spheroids were investigated on-chip, CTG results revealed that all spheroids were dead regardless of treatment, demonstrating less than 800 RLU values (Figure 5.20). Unfortunately, the same result was produced when another attempt was conducted. Both the K1 and 8305c images revealed extensive damage to the spheroidal structures with very high dead cell percentages (above 80%) despite the presence of green staining (mostly likely background staining as revealed by ImageJ analysis) (Figure 5.21).

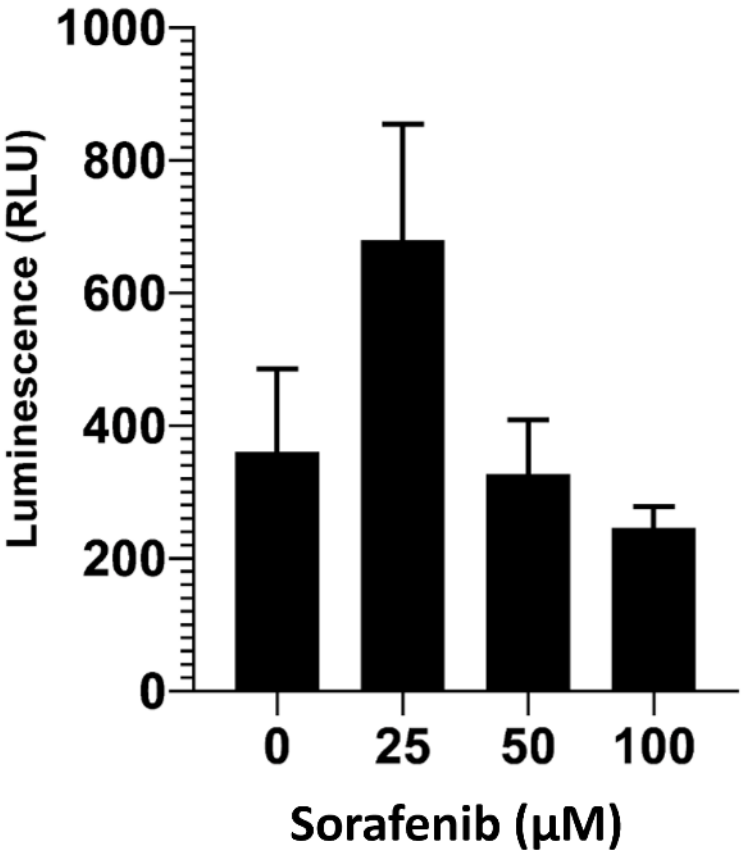


***Figure 5.21 Luminesce values from the CTG assay for untreated and treated (sorafenib for 48 h) 8305c spheroids (seeded at 10,000 cells) post on-chip treatment.*** *Spheroids were placed on-chip when 5 days old, CTG values were determined post 48 h incubation with TKI replenishment after 24 h. 4 replicates for 0 µM, 10 for 25 µM, 8 for 50µM and 5 for 100 µM were analysed. Analysed using a 2-way ANOVA with Dunnett's multiple comparison test, between control and treated groups. Values are mean ± SEM, n =1.*

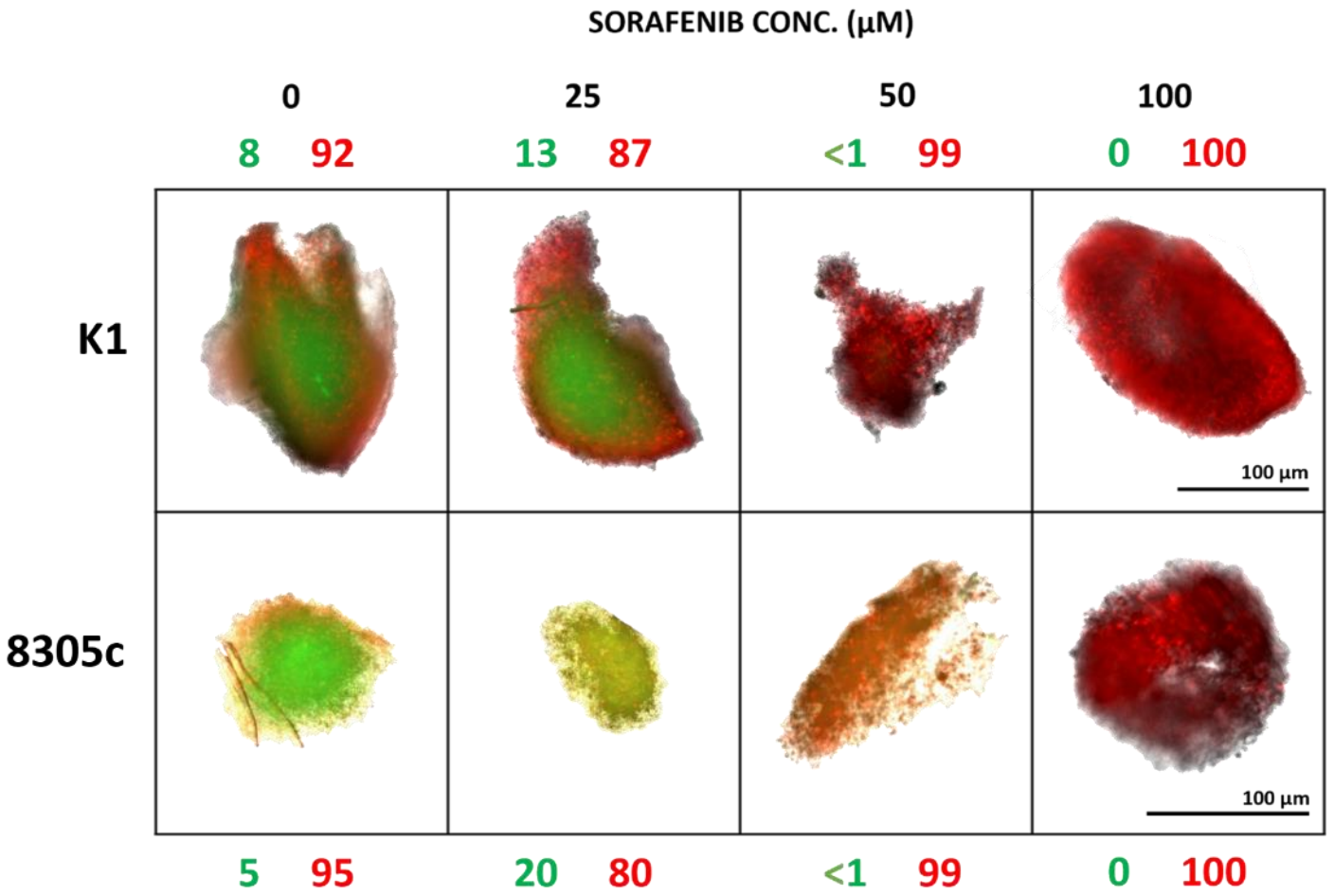


***Figure 5.22 Fluorescent images of Fluorescein Diacetate and Propidium Iodide (FDA/PI) stained K1 (seeded at 20,000 cells/well) and 8305c (seeded at 10,000 cells/well) spheroids post 48 h sorafenib treatment on-chip.*** *Images were taken using a Zeiss fluorescent microscope at 10x magnification. ImageJ was used to produce the percentages of live to dead cells, green – live, red – dead cells. Images are representative from a single repeat which included duplicate images for each treatment group (top row - K1), two repeats for the 8305c spheroids (bottom row).*

## 5.7 Discussion

The aim of the investigations conducted in this Chapter, was to examine the effects of sorafenib on spheroids using two different thyroid cancer cell lines, with varying properties. To further the understanding of how different tumour cell types respond to treatment with TKI, progressing the development of the thyroid tumour model for drug testing.

### 5.7.1 Effects of sorafenib on Thyroid Carcinoma Spheroids

In the current study, spheroid age significantly affected their response to sorafenib treatment. Older K1 and 8305c spheroids (Day 9) were more sensitive to the drug compared to younger (Day 7) spheroids, with substantial reductions in viability observed at lower concentrations. Moreover, younger and smaller (1000 cells/well) spheroids displayed greater resistance, in contrast with the older and larger spheroids which showed heightened sensitivity, especially at higher drug concentrations.

Eilenberger *et al.,* (2019) looked into the effects of spheroidal age on sorafenib penetration. They seeded S-layer coated 96-well U-bottom plates with 3000 HepG2 (liver carcinoma cell line) cells/well, incubated for 2 days before sorafenib (100 µM) treatment with varying lengths of time, from a minimum of 24 h to a maximum of 12 days, to observe how long-term exposure affects cell toxicity. For determining spheroid viability AlamarBlue® and LIVE/DEAD® Viability/Cytotoxicity assays were utilised, although live/dead (FDA/PI) staining was employed in the current study, viability readings were generated via the CTG assay. Eilenberger *et al.,* found that the older, and larger the spheroid, the greater resistance to treatment was observed. This increased resistance was attributed to the spheroids' growth, which enhances cell density and interstitial pressure, thereby limiting drug penetration. Larger spheroids impose higher interstitial fluid pressure which creates more severe hypoxic and acidic conditions, further impeding drug diffusion and contributing to treatment resistance (Nunes *et al.,* 2018). This provides a possible explanation for the heightened resistance of the smaller (1000 cells/well) spheroids compared to the larger (10/20,000 cells/well) which matched or surpassed the size of their larger seeding density counterparts. Smaller spheroids were supplemented with 1% Matrigel® which were found to have doubled the size of these structures when compared to those without the matrix (Chapter 3), moreover, these

spheroids exhibited on par or larger sizes for instance 1000 K1 cells/well (roughly >1100 µm on average across treatment groups) compared to the 20,000 cells/well spheroids (870-900 microns). Thus, a greater diffusion distance has to be achieved by sorafenib, meaning increased resilience. Moreover, smaller spheroids had not been observed to possess a necrotic core meaning central cells continued to proliferate and the agent at less potent doses most likely could not reach them, especially with the spread out arrangement in due part to the addition of Matrigel®. In terms of age, this result contrasts with Eilenberger *et al. (2019),* as in the current study, younger day 7 spheroids tended to display heightened resistance so it may be the size as opposed to age that is the decisive factor in whether the spheroid develops resistance.

Another study investigated the effects of Sirtuin inhibitors (cambinol and EX-527) on stimulating the efficacy of sorafenib (Ceballos *et al.,* 2021); by utilising hepatocellular carcinoma cells (HepG2 and Huh7 cell lines). Spheroids were seeded at a density of 1500 cells/well and began treatment (2 or 4 µM sorafenib) when spheroids were 4 days old for a duration of 72 h. Although a much lower concentration of the TKI, they had used a similar seeding density and window of treatment however they opted for using an Acid Phosphatase (APH) assay to measure spheroid viability, APH activity is proportional to the number of viable cells as opposed to the CTG assay, which measures levels of ATP. Ceballos *et al. (2021),* found sorafenib treatment reduced spheroid volume in a concentration-dependent manner, and combining it with cambinol or EX-527 led to even greater volume reductions in HepG2 and Huh7 spheroids. They had also utilised ImageJ software to determine spheroid sizes however, Ceballos *et al.,* converted spheroid volumes into percentages relative to control cells hindering in depth comparisons with spheroids from the current study despite that they observed significant reductions in spheroid volume at every concentration tested much like the day 9, 10,000 cells/well 8305c spheroids. Another, similarity between the studies was the morphological change in spheroids which exhibited visually smaller structures with rougher edges and an irregular shape post treatment whereas controls maintained spherical bodies.

Although, fluorescent imaging using FDA/PI staining is highly insightful, depicting the arrangement of non/viable cells within the spheroids it suffers greatly in terms of reliability when used for viability analysis, especially on more complex models. Viability investigations

using FDA/PI staining can be compromised by several factors: spectral overlap between fluorescein (from FDA) and PI can obscure accurate detection; FDA's susceptibility to hydrolysis and instability affect the stain's sensitivity. In addition, external factors such as residual esterase activity in dead cells complicate the assessment of cell viability as despite being dead, they are identified as viable during analysis (Boyd *et al.,* 2008). Consequently, while FDA/PI staining provided some confirmation of cell death at higher concentrations, the CTG assay detected significant viability declines at lower concentrations (3.13 µM), underscoring the need for using multiple analytical methods to obtain a more sensitive and accurate assessment of cell viability.

To the knowledge of the author, no data involving K1 spheroids and sorafenib is available in the literature. The lack of studies in this area maybe due to the fact that radioiodine refractive DTCs such as papillary carcinomas are relatively rare (Jannin *et al*., 2022), hence more work has been published on the more aggressive and more commonly RAI refractive anaplastic cell lines (e.g. 8305c). For that reason, limited comparisons can be made to what others have done.

Unfortunately, only a single study (Mortensen *et al.,* 2023) has been identified utilising 8305c spheroids to measure response to sorafenib. Spheroids had been seeded at 1000 cells/well and cultured for three days before treatment commenced with no replenishment throughout a 25-day observation. Researchers compared sorafenib response in eight different TC cell lines (CAL-62, B-CPAP, 8505c, 8305c, MDA-T32, FTC-238, ACT-1, and SW1736) and found that the 8305c spheroids were the second most resistant cell line when treated with the TKI (10 µM). All the PTC cell lines showcased much greater susceptibility to sorafenib which contrasts with findings from the current study where K1 spheroids did not respond significantly to treatment with the lowest dose of 3.13 µM whereas both the larger and smaller 8305c spheroids had. The greatest difference between methodologies was the fact that Mortensen *et al.* had utilised XTT an assay optimised for monolayers whereas in the current study an assay deemed more suitable (CTG) was used to determine spheroid viability which produces more reliable results when used on the appropriate model type (described in section 4.7.4). Moreover, their investigation lasted 25 days with only a single treatment (10 µM) event when spheroids were three days old compared to only a 48 h incubation with sorafenib with a

broader range of concentrations (3.13 -100 µM) in the current study. This may have allowed for the spheroids to gain resistance over time or due to Mortensen *et al. (2023),* use of agarose-coated wells may have influenced the interaction between the cells and the agent. However, the current study used Matrigel® for the smaller 8305c spheroids, but the larger ones plated at 10,000 cells/well lacking any hydrogel supplementation still showcased greater sensitivity.

### 5.7.2 Comparison of $IC_{50}$ values

Based on the limited studies available looking specifically at the responses of K1 and 8305c cell lines to a range of different concentrations of sorafenib there was a general trend of the 8305c cell line exhibiting greater resistance to the TKI compared to the K1 cell line. With $IC_{50}$ values reported between 20-26.4 µM for 8305c cells (Talezadeh Shirazi *et al.,* 2022 and Lin *et al.,* 2021) and 4.24-16.28 µM for K1 (Ya *et al.,* 2022 and Ruan *et al.,* 2015).

For the 8305c investigations Talezadeh Shirazi *et al. (2022),* had plated 8305c cells at 20,000 cells/well in flat-bottom 96-well plates, incubated with a sorafenib range of 5-64 µM sorafenib for 24 h with viability of the cells determined using the MTT assay. Compared to Lin *et al (2021).,* who seeded a 24-well plate with 20,000 8305c cells/well, allowed it to incubate overnight and was then treated with sorafenib for a total of 4 days using an identical concentration range to the current study (3.13 - 100 µM), with viability analysis on the 4$^{th}$ day using the CytoTox96 kit with spectrophotometry. For the K1 investigations 3000 cells/well were incubated in 96-well plates for a total of 10 days before 48 h treatment with sorafenib concentrations of 0.5 - 20 µM with viability analysed using the CCK-8 assay (Ya *et al.*, 2022). Whereas Ruan *et al.,* (2015), examined the 48 h culture of 96-well flat-bottom plates seeded with 4000 K1 cells/well, with a range of sorafenib concentrations (5nM, 50nM, 500nM, 5µM) including replenishment of medium supplied with a fresh dose of the TKI after 24 h of incubation. Cell viability was determined using the CCK-8 assay.

These findings closely resemble the $IC_{50}$ values determined in the current study but only in relation to the smaller spheroids. K1 spheroids plated at 1000 cells/well presented an $IC_{50}$ of 18.66 µM compared to the literature max value reporting of 16.28 µM whereas 8305c spheroids seeded at 1000 cells/well displayed an $IC_{50}$ of 28.49 µM almost mirroring the $IC_{50}$

value determined by the aforementioned studies which presented a top value of 26.4 µM. Despite methodological differences between the current study and those previously described, such as the use of 3D spheroid models versus 2D monolayer cultures with variations in seeding densities and plate types, comparable $IC_{50}$ values were achieved. Notably, Ruan *et al.,* (2015), was the only study to incorporate dose replenishment of the TKI to better simulate patient dosing ensuring a stable concentration of sorafenib for the duration of the treatment period. Coincidently, the $IC_{50}$ findings were roughly 2 µM above the stated top end of the described literature range for both 1000 cells/well spheroids (K1 and 8305c). This discrepancy is likely attributable to the fact that the mentioned $IC_{50}$ calculations were conducted using monolayer cultures, whereas the current study utilised 3D models, which present a greater drug diffusion distance.

It has been reported that 2D models exhibit heightened responsiveness to treatment compared to 3D models as found by Rodríguez-Hernández *et al.,* (2020), where the 2D (hepatocellular carcinoma (HCC) cells) model appeared to be more sensitive to sorafenib, compared to the 3D model (HCC spheroids). Spheroids were generated by seeding 5000 cells/well and allowed to reach a maturity of 8 days when treatment with 10 µM sorafenib began and viability was measured using Caspase-Glo® on days 8, 10, 12 and 15. Rodríguez-Hernández and colleagues, had only used a single dose of 10 µM in contrast with the current study which used a broad range of concentrations, two differing seeding densities and 24 h sorafenib replenishment. In spite of this, similar cell viability assays were used in terms of establishing spheroid viability by lysing the dense structure and measuring the luminescent produce. Moreover, the study had begun treatment when spheroids were 8 days old resembling the current study's treatment window of 7-9 days. Rodríguez-Hernández *et al.,* (2020) suggested that the enhanced sensitivity in 2D cultures might be due to better drug penetration, as all cells have equal access to the drug immediately upon application, compared to spheroids where the drug needs time to access the cell in the centre of the spheroid. The findings of slightly higher sorafenib $IC_{50}$ spheroid readings when compared to those determined using monolayers could potentially be attributed to this.

Moreover, the current study observed that the 8305c spheroids seeded at 10,000 cells/well were more consistent in generating a necrotic core compared to the larger K1 spheroids

despite that K1 spheroids plated at 20,000 cells/well were less susceptible to the TKI than the larger 8305c spheroids. This contrasts with Rodríguez-Hernández *et al*., (2020), explanation that a lack of a hypoxic environment in the monolayer cultures compared to 3D spheroids which possess a necrotic core and dense structure, are more susceptible to the cytotoxic effects. However, this would have meant that the 8305c spheroids seeded at 10,000 cells/well should have been more resistant suggesting that cell type may have had a considerable effect. Further work would be required to investigate this aspect.

### 5.7.3 On-chip investigations

For on-chip investigations, spheroids were placed on microfluidic devices and treated with sorafenib for 48 hours, with replenishment after 24 hours to mimic patient dosing (Fallahi *et al.,*2013). Both K1 and 8305c cell lines were investigated, seeded at 20,000 and 10,000 cells, respectively. With only one successful run, it was challenging to definitively assess the effectiveness of this method in simulating *in vivo* responses to the TKI. Regardless, several interesting observations were gleaned particularly the heightened susceptibility of K1 spheroids post sorafenib treatment on-chip compared to static.

Spheroids have been demonstrated to be superior models for studying drug sensitivity compared to monolayer cultures (Clevers, 2016). However, they still lack important features such as vascularisation which is compensated for when incorporated into a microfluidic device. This dynamic environment allows for a more realistic representation of *in vivo* conditions through the continuous supply of fresh media simulating blood circulation. Thereby enhancing spheroid capabilities as an effective model for drug screening (Białkowska *et al.,* 2020).

The on-chip control K1 spheroids had matched the viability readings when compared to the static K1 spheroids. This contrasts with the study by Lee *et al.,* (2013) who found that spheroids cultured under flow conditions possessed superior viability compared to static cultures using hepatocyte spheroids (HSC cell line) which were grown on the device by injecting 100 µL of 2,000,000 HSC cells/mL into the concave chambers of the chip. Viability was determined after 13 days of incubation using live/dead staining, Calcein AM (for live cells), and ethidium homodimer-1 (for dead cells) while still on the chip. As there was only one

successful run in the current study, further repeats would be required to establish whether flow conditions improve spheroid viability or not.

In addition, based on a single repeat there was an observed heightened sensitivity of on-chip spheroids to sorafenib when comparing CTG values. This however opposes the general consensus of spheroid on-chip drug screening literature, as a review of multiple studies by Tevlek *et al*., (2023) all revealed that greater drug resistance was seen in microfluidic cultures compared to those grown under static, no-flow conditions.

Moreover, treated spheroids also showed an elongated shape, possibly due to the TKI disturbing the outer structure enough to be manipulated by the flow as the control's structure remained unbothered. A similar observation by Mishra *et al.,* (2023) found that untreated periodontal ligament stem cell spheroids-on-chip had their structure remodelled, reflecting the stretched-out spheroids in the current study, resembling an oval rather than spherical shape, regardless of the flow rate.

Sadly, in a repeat of the investigation, all K1 spheroids had perished confirmed by CTG assay with sub-1000 RLU values. Similarly, 8305c spheroids showed extensive damage with high dead cell percentages and lower RLU values compared to the K1. Subsequent attempts with both cell lines yielded the same result, prompting the need for a protocol/device review before further repeats would be attempted. A possible explanation for the death of spheroids post incubation on-chip may be due to the process of transporting cells out of the devices for cell viability analysis. Moshksayan *et al.,* (2018) described the benefits of analysing spheroid vitality on a chip directly without disturbing the cultures as they mentioned removal of spheroids for analysis, affected viability negatively. Future repeats would involve the incorporation of on-chip examinations in an attempt to not damage the spheroids during transport which is required for CTG analysis.

### 5.7.4 Limitations

When working on spheroids it is important for cells to be able to self-assemble into spherical structures. However, in many cases including work mentioned in this chapter, occurrences of spontaneous disaggregation and formation of irregular structures were fairly common which

has also been observed in other studies for instance Hu *et al.,* (2024) who worked with 8505c spheroids which would break up, particularly after 21 days of culture. They overcame this issue through Matrigel® encapsulation which may explain why the current study observed greater losses amongst the larger spheroids which lacked this supplement.

Disaggregation was more frequent, for spheroids receiving the higher doses of sorafenib regardless of cell line, especially when attempting to transfer the cells from one plate to another, such as in the case of CTG analysis, where spheroids were transferred to an opaque plate. Also, during the fluorescent staining procedure spheroids were subject to additional stresses in the form of multiple washes with PBS and the staining step itself, along with human error whereby spheroids were taken up by the pipette and retrieval was not possible. This made it difficult to generate complete triplicate sets of images for each concentration and control group. The difficulty of handling spheroids was mentioned by Sirenko *et al.,* (2015), who found that spheroids post-treatment with anticancer drugs made it challenging to produce readings that would reflect the expected concentration-dependent response. While they found live/dead staining to be an effective workaround, a recurrent issue in the current study was the inability to retain cells in the wells during FDA/PI staining due to multiple washing steps inadvertently removing cells.

The observed high mortality rate of spheroids cultured on PMMA inserts whereby a single repeat was successful out of a total of four repeats suggests a possibly damaging interaction between spheroids and the insert material. The PMMA surface is inherently hydrophobic, which can disrupt the spheroid structure, weakening cell adhesion and ultimately leading to cell death. Unlike PMMA, PVA-coated surfaces offer a hydrophilic environment that better supports spheroid formation and stability. As demonstrated by Chen *et al.,* (2015) who showcased superior results compared to the current study in terms of maintaining viable cells, using human colon (HCT116), breast cancer (T47D) and hepatocellular carcinoma cell line (HepG2) spheroids injected into the wells of their chips at a density $1 \times 10^6$ cells $mL^{-1}$. Chen *et al.,* (2015) were able to consistently grow spheroids on-chip for a duration of 8 days, suggesting that PVA may be a more suitable material for cultivating and maintaining spheroids for longer periods of time. A major difference was that the spheroids were transferred onto the chip when they were 5 days old as opposed to Chen *et al.,* (2015) which were grown on-

chip from the start. It is possible the transport of spheroids into a new environment may have had disruptive effects on the spheroids. Future experiments would include the exploration of alternative materials, such as PVA, to improve spheroid culture conditions.

Although rare, spheroids would sometimes aggregate into highly irregular shapes rather than the expected uniform and round form, in addition, the presence of inter-plate variability through which each plate varies in terms of spheroid size made representative conclusions more challenging, an issue commonly mentioned in spheroid literature (Zanoni *et al*., 2016 and Han *et al*., 2021). To overcome these challenges, greater amounts of replicates could be grown followed by microscopic examination to identify abnormal spheroids, removing them thus ensuring all spheroids ready for treatment would have a strong spherical shape. In addition, a different method for cultivating spheroids could be explored for instance the hanging drop method optimised by Kelm *et al.,* (2003). They were able to generate homogenous in shape and size spheroids for various cell lines notably HepG2 and a mammary gland adenocarcinoma cell line, (MCF-7) with almost 100% efficacy.

# Chapter 6 Generation of Thyroid Organoids from Patient-Derived Tissue

## 6.1 Introduction

Following on from the spheroids which were an amalgamation of homogenous cells, this section focuses on organoids; multicellular aggregates derived from animal and human tissue, grown under varying conditions and supplementations to stimulate proliferation, allowing for subsequent testing and analysis (Song *et al.,* 2024). The key motivation for the development of thyroid tumour-derived organoids is the quest for a more reliable and personalised therapy analysis model. Organoids have the potential to capture the variation in drug response between individuals, allowing for predictions to be made on how the patient may react to certain treatments, reducing the risks of exposing individuals to potentially harmful or unsuccessful regimens (Jabs *et al.,* 2017).

A key aspect of the current study was the willingness of patients to consent to donating their resected thyroid tissue for research purposes. Excess resected thyroid tissue, not required for pathological determination is usually discarded, so utilising this excess tissue to generate more relevant 3D models to streamline treatment, has the potential to benefit patients in the future (Thasler *et al.,* 2003).

The construction of organoids and techniques surrounding their maintenance are still in their infancy stage for many tissues. Each different tumour type requires specific optimisation procedures to establish standardised methods for generating and preserving organoids (Tang *et al.,* 2022). Following a search of the literature, to the author's knowledge, established tumour-derived organoid models for different types of thyroid cancer are still unavailable (Samimi *et al.,* 2021), however, research is ongoing. One drawback that needs to be considered however, is the reproducibility of these organoids. The main issues surrounding organoids other than acquisition of the sample, is their consistent generation and high patient variability (Kim *et al.,* 2020).

### 6.1.1 Applications and advantages of organoids

Organoids are capable of recapitulating the *in vivo* tumour environment with greater accuracy compared with spheroids, due to the presence of heterogenous cells, whereas spheroids are usually generated from homogenous immortalised cell lines lacking the diverse nature of cells seen within tumours. In addition, Chen *et al.,* (2021) found that prevalent genetic mutations and mutational patterns observed in human PTC specimens were detected in organoid cultures, thus establishing a correlation between the genetic characteristics observed in clinical specimens and those replicated in *in vitro* models. Something that, due to their simplicity and lack of histological resemblance to the primary cancer, is not seen in spheroidal cultures, although genetic manipulation within these models is possible (Ishiguro *et al.,* 2017).

Many anticancer drugs, which are developed from screening 2D cancer cell lines and animal subjects, fail in clinical trials, signifying the weak preclinical predictions that current testing procedures offer. This is largely attributed to factors such as the inability of 2D models to accurately replicate drug diffusion distances, hydrostatic/interstitial pressure, and the development of necrotic cores, all of which significantly influence how tumours respond to therapeutics, affecting both drug sensitivity and resistance patterns (Verjans *et al.,* 2017). Organoids may provide greater predictive power, with studies utilising patient-derived PTC organoids showing intra- and inter-patient specific drug responses (Barbosa *et al;* Chen *et al.,* 2021), a valuable indicator of how effective the drug would be in clinical trials. Furthermore, developing viable and reproducible 3D models before clinical testing could significantly reduce the reliance on laboratory animals. This is particularly relevant for thyroid research, where there is a scarcity of animal models for the various histopathologic types of thyroid cancer, and these models often fail to accurately predict human drug responses (Samimi *et al.,* 2021).

Not only would organoids serve as platforms for testing mono and combination therapies prior to administration to patients, there is promising research into developing these models to better understand tumorigenesis of thyroid pathologies, something that is still not well understood (Samimi *et al.,* 2021).

### 6.1.2 Challenges surrounding organoid development

Organoids do suffer from a few limitations, which currently render the model unsuitable for preclinical testing. The time-consuming and multifaceted nature surrounding tissue acquisition, dissociation, generation and maintenance in its current state makes this model highly inefficient (Yang *et al.,* 2023). Especially when compared to spheroids, which possess high-throughput capabilities and are much easier to set up with very strong self-assembling properties (Scalise *et al.,* 2021). A study carried out by Sondorp *et al.,* (2020), reported an organoid forming efficiency for stable PTC-derived organoids was approximately 7%, highlighting the inconsistent and limited potential of patient-derived tissue in forming viable organoids.

Further problems lie with the procurement of human tissue for organoid generation which is faced with both ethical and consensual issues. The current study which received ethical approval ahead of commencing the study (section 2.4), observed an enthusiastic willingness of patients to participate. However, the number of samples available for use in research is highly dependent on clinical cooperation and will vary significantly based on location and prevalence of thyroid cancer in that area. In addition, rare subtypes such as anaplastic carcinomas are more difficult to attain due to their scarcity.

Within the literature there is great variability in tissue dissociation processes, encompassing primary cell extraction from tissue samples (Table 6.1), their supplementations, as well as when these organoid-like structures are suitable for harvesting and testing. This highlights the need for more standardised approaches to generating these complex models.

When examining drug effectiveness, spheroids and organoids offer distinct advantages and limitations. Spheroids are better suited for high-throughput screening and initial drug discovery studies due to their simplicity, reproducibility, and ease of production. On the other hand, organoids provide a more physiologically relevant model with greater potential for predicting *in vivo* drug responses. The decision between the use of spheroids and organoids should be based on specific research objectives, available resources, and the desired level of complexity and relevance to human physiology.

### 6.1.3 Matrigel® and VitroGel®

Matrigel® is a hydrogel derived from the extracellular matrix of Engelbreth-Holm-Swarm (EHS) mouse sarcoma cells which can effectively mimic the *in vivo* environment, with the inclusion of ECM proteins and growth factors such as laminin, collagen IV, and entactin (Cherne *et al.,* 2021). It is one of the most commonly used hydrogels in organoid culture providing a supportive environment for cell attachment, proliferation, and differentiation.

Whereas VitroGel® hydrogels also mimic the ECM but are synthetic, lacking the biological components offered by Matrigel®. VitroGel® slowly becoming an alternative for Matrigel® use due to its lower costs and not relying on animals for its production (Xiao *et al.,* 2019). For the current study, the Discovery Kit (Cat# VHM04-K) offered by TheWell Bioscience was trialled, which consists of a range of VitroGel ORGANOID hydrogels (V1-V4) designed specifically for organoid culture (TheWell Bioscience, 2024). Each hydrogel varies in bio-functional ligands, mechanical strengths, and biodegradability which allows researchers to screen and select the optimal hydrogel for their specific organoid needs.

## 6.2 Aims

To develop and characterise robust *ex vivo* thyroid cancer models using patient-derived tissue samples with different scaffold supports. This entailed evaluating the growth and morphology of organoids and primary spheroids. In addition, observe and determine the suitability of co-culturing immortalised thyroid cancer cells with primary cells.

***Table 6.1 Recent studies investigating human derived thyroid tissue and their preferred dissociation and culture methods.*** *Selection based on recent studies (2004-2024) utilising patient-derived thyroid tissue for culture and/or organoid generation.*

| Study | Tissue | Dissociation | Thyroid tissue/organoid supplementation |
|---|---|---|---|
| **Fierabracci *et al.,* 2008** | Thyroid adenoma, normal thyroid tissue and tissue affected by Graves' disease | Dissociated using centrifuge, enzymatically<br><br>digested in Collagenase IV | Thyroid primary cells were collected, plated and cultured in spheroid medium (1:1 mixture of DMEM and F12, supplemented with glucose, sodium bicarbonate, L-glutamine, penicillin, streptomycin, a defined hormone and salt mixture, β-mercaptoethanol, EGF, and bFGF). Primary cell aggregates resembling spheroids were harvested after 7–10 days |
| **Riley *et al.,* 2019** | Thyroid tissue both malignant and benign | Tissues was sliced using a vibratome. Minced using scalpels. Enzymatic digestion using Collagenase IV and DNase I | Thyroid tissue was maintained on microfluidic devices supplied with medium (DMEM with FBS, penicillin/streptomycin, glutamine, amphotericin B, thyrotropin and sodium iodide) |
| **Sondorp *et al.,* 2020** | Classified papillary thyroid carcinoma. | Mechanically digested using the GentleMACS Dissociator<br><br>Digested in HBSS, BSA, Dispase and<br><br>Collagenase II | Primary cells were plated with Matrigel® in organoid culture medium (50% Wnt3a and 10% R-spondin conditioned medium, DMEM with HEPES, ROCK inhibitor Y-27632, Nicotinamide, Noggin, EGF, TGF-β inhibitor, FGF-2, and VEGF-121)<br><br>Organoids cultured for 7 days before collection |
| **van der Vaart *et al.,* 2021** | Thyroid follicular cells | Tissue chopped into small ~1-mm pieces using a scalpel Digested in Collagenase I, ROCK inhibitor Y-27632, Primocin in AdDMEM/F12 | Thyroid cells plated in basement membrane extract (BME) supplied with organoid expansion medium (AdDMEM/F12, B27, Glutamax, HEPES, Penicillin-Streptomycin, Primocin, N-acetylcysteine, Nicotinamide, R-spondin 3 conditioned medium, A83-01, FSK, EGF, FGF10, p38 Inhibitor, Wnt Surrogate, and TSH<br><br>Organoids first formed 1 to 2 weeks, collected after 21-40 days |
| **Ogundipe *et al.,* 2021** | Non-malignant thyroid gland tissue | Mechanical digestion using the GentleMACS dissociator followed by enzymatic digestion in Dispase and Collagenase I | Primary cells seeded in Matrigel® (DMEM-F12 with 50% Wnt and 10% R-spondin1 conditioned media, penicillin/streptomycin, glutamax, EGF, FGF-2, B27, heparin sodium salt, nicotinamide, A83-01, and noggin)<br><br>Organoids cultured for 7 days were ready for collection |
| ***Yi et al.,* 2022** | Normal thyroid tissue, differentiated thyroid carcinoma tissue, and anaplastic tissue | Tissue cut using forceps and scissors followed by chemical digestion in Trypsin and Collagenase IV | Primary cells incubated in (HBSS, RPMI-1640, FBS) |

## 6.3 Materials and Methods

### 6.3.1 Sample Collection

Thyroid samples were collected directly from the operating theatre and transported to the laboratory in complete DMEM within 15 min of resection, for immediate dissociation into primary cells (section 2.4.1). Samples were named using THY followed by a numerical value based on the order they were received to pseudo anonymise the samples. Additional information on patient recruitment, age, tumour stage and ethical approval can be found in section 2.4.

### 6.3.2 Organoid generation protocol

Biopsy samples were minced with scalpels until gel-like (section 2.4.1) and digested in a mix of DNase, Collagenase IV, and complete DMEM at 37°C for 2 h. After digestion, samples were triturated, filtered, and centrifuged. The cell pellet was treated with RBC lysis solution (section 2.4.1), followed by another centrifugation, resuspension in complete DMEM, and cell counting using trypan blue exclusion (section 2.1.3). For organoid generation, cells were seeded in Matrigel® (section 2.4.2.1) or VitroGel® (section 2.4.2.2) and maintained in a 37°C, 5% $CO_2$ incubator with medium replenished every three days. Organoid growth was monitored by light microscopy, and TSH and iodine were added later to enhance growth (section 2.4.2.2). An overview of the organoid generation process can be seen in Figure 6.1. VitroGel® samples were processed using VitroGel® recovery solution (section 2.4.2.3), stained, and examined under a fluorescent microscope (section 2.3.5.2).

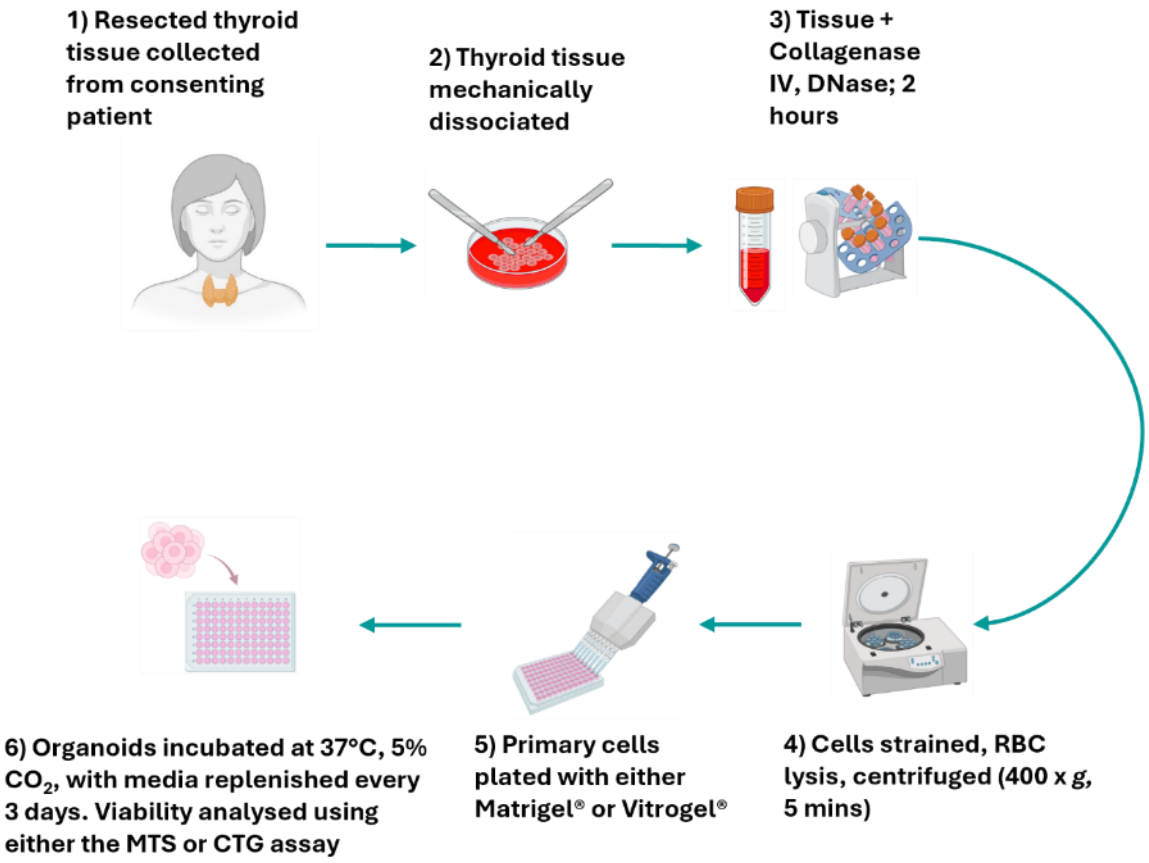


***Figure 6.1 Overview of the organoid generation process****. Minced biopsy samples were digested with DNase and Collagenase IV. Cells were then filtered, centrifuged, and subjected to RBC lysis. Cells were counted and plated. Organoids were generated using either Matrigel® or VitroGel® matrices followed by regular observations and viability analysis. Created using Biorender.*

### 6.3.3 Primary spheroid generation protocol

To utilise the remaining cell suspension, 100 µL was added to multiple wells of a round-bottom ULA plate (section 2.4.3) to assess spheroid formation without Matrigel® or VitroGel®. Growth was monitored via light and fluorescent microscopy after FDA/PI staining, with periodic imaging (section 2.3.5). Due to limited organoid growth, K1 cells were co-cultured with primary cells in a ULA plate (section 2.4.3.1). CytoPainter Cell Tracking Green Dye was used for microscopy after initial CFSE labelling challenges (section 2.4.3.3;2.4.3.2).

### 6.3.4 Cell viability analysis

Initially, primary spheroid viability post treatment with sorafenib was investigated utilising the MTS assay, conducted in an identical way to the cell line spheroids (section 2.3.3). As mentioned in Chapter 4, the assay of choice was switched to the CTG assay including for primary spheroid experiments. Following the same protocol as was used in the cell line spheroids (section 2.3.4).

## 6.4 Statistical Analysis

CTG and MTS readings were analysed using GraphPad v9.5.1, For THY30 a one-way ANOVA with Dunnett's multiple comparison test was conducted. For THY31 CTG readings a 2-way ANOVA was conducted with Dunnett's multiple comparison test. Fluorescent images were analysed with ImageJ software to determine live/dead cell percentages.

# Results

## 6.5 Characterisation of patient-derived organoids and primary spheroid growth and morphology

The approach to organoid generation was iterative, with each phase of the study informing and refining the next investigation. Initial experiments provided insights that were used to optimise conditions, such as modifying hydrogel types and adjusting cell culture parameters. This patient-by-patient methodology allowed for progressive improvements in the protocol.

The initial three attempts at generating organoids (with Matrigel®) from patient-derived tissue, served as preliminary experiments aimed at refining the procedures and observing growth dynamics. The first patient sample, classified as papillary microcarcinoma (THY26), exhibited minimal cell aggregation on day 3 of incubation. On day 7, larger structures indicative of successful proliferation/cell aggregation or both were observed (Appendix 6.1). By day 21, these structures had amplified slightly in both size and number (Figure 6.2). However, growth stagnated following day 21, with no organoid-like structures visible. Even when the plate was left for an additional 20 days, with regular medium replenishment, no observable changes were noted.

Similar growth patterns were observed in the subsequent two samples, THY27 (papillary microcarcinoma) and THY28 (medullary carcinoma) for days 3 and 7 (Appendix 6.2/3). However, by day 21, THY26 and THY27, exhibited observably more small cell clusters compared to THY28, suggesting differential growth dynamics between samples (Figure 6.2). Not one of the three samples however showed any growth past 21 days of incubation. As all three samples exhibited limited growth, it was hypothesised that maybe Matrigel® was not the optimal matrix for promoting thyroid organoid formation. For this reason and due to supply issues associated with Matrigel®, alternative matrices for growing the organoids were sourced.

An excess of primary cells remaining after seeding all three samples allowed for an additional observation test into how well these cells can form multicellular spheroids in ULA plates. On

day 3, cells appeared dispersed with some aggregation, which developed into a more unified structure by day 7, closely resembling the structures seen in Figure 6.2. Post 21 days of incubation the cells seemed to disperse even more losing any clustered structure they possessed and returned to an arrangement of multiple minute cell clusters (Figure 6.2).

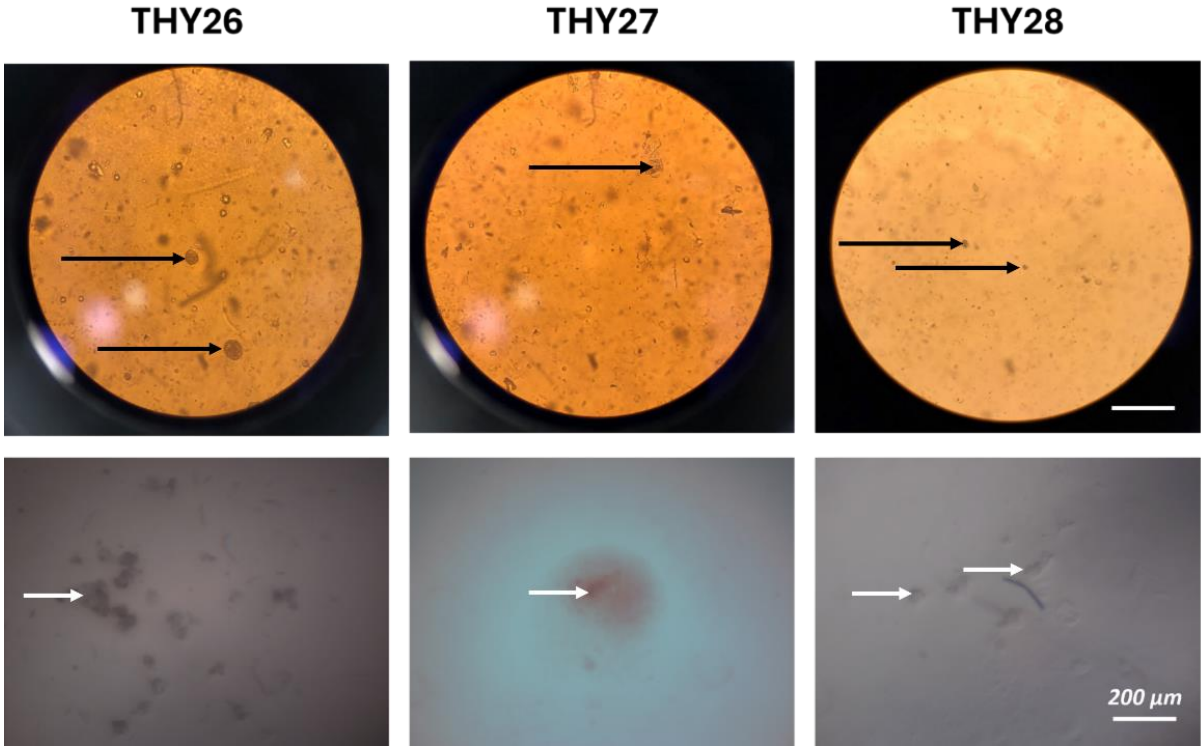


***Figure 6.2 Images of primary thyroid tissue cultures (3 x $10^5$ cells/ml) seeded in a 24-well plate on a Matrigel® base (Top row) and 3 x $10^5$ cells/ml, 100 µL/well, seeded in a ULA plate without Matrigel® (Bottom row).*** *Images are representative of 8 replicate wells; 3 images were taken per sample for both organoids and primary spheroids post 21-day incubation, taken using a brightfield microscope at 10x magnification. THY26 and THY27– Papillary microcarcinoma and THY28 – Medullary carcinoma. Black arrows point to potential cell clusters whereas white arrows point to potential primary spheroids. Scale bar – 200 µm.*

## 6.6 Using VitroGel® as an alternative to Matrigel® in generating thyroid organoids

THY30 (a follicular adenoma) was the first sample to be grown on the new hydrogel. The sample size was substantial, which enabled further investigations beyond growth observations. Samples were minced, digested and plated following the protocol for VitroGel® encapsulation (four wells were prepared for each VitroGel® sample) found in section 2.4.2.2. Additional tests for organoids included 24 h treatment with sorafenib at doses of 25 and 75 µM, along with a control group (medium only) and a Cytospin investigation with fluorescent staining analysis. Spheroid formation tests in ULA plates were also performed.

Similar growth trends by day 10 for all 4 of the VitroGel® samples were observed, with cells scattered across the hydrogel layer displaying no real aggregation. Small structures were more prevalent by day 13, after which there was a slight increase in the size of these cell clusters (Appendix 6.4). Nevertheless, most cells appeared to remain isolated with no sign of deliberate and organised aggregation. By day 24 some structures in VitroGel® samples 1 and 4 acquired a darker hue potentially indicating a denser collection of cells (Figure 6.3).

Two different tissue samples were collected from patient THY31, one was classified as a papillary carcinoma (follicular variant), the other was benign (B) thyroid. The benign organoid cultures exhibited very little growth across any of the VitroGel® samples; from days 6 -12 there were a few visible, albeit individual cells for all the VitroGel® samples, with no presence of a unified structure. There was very little presence of any cell clusters by day 24 (Figure 6.3). For the follicular organoid cultures produced from THY31, growth was observably greater, with more visible cell aggregates in all VitroGel® samples, that grew in size throughout the 24 day culture period but lacked any tangible organoids structure.

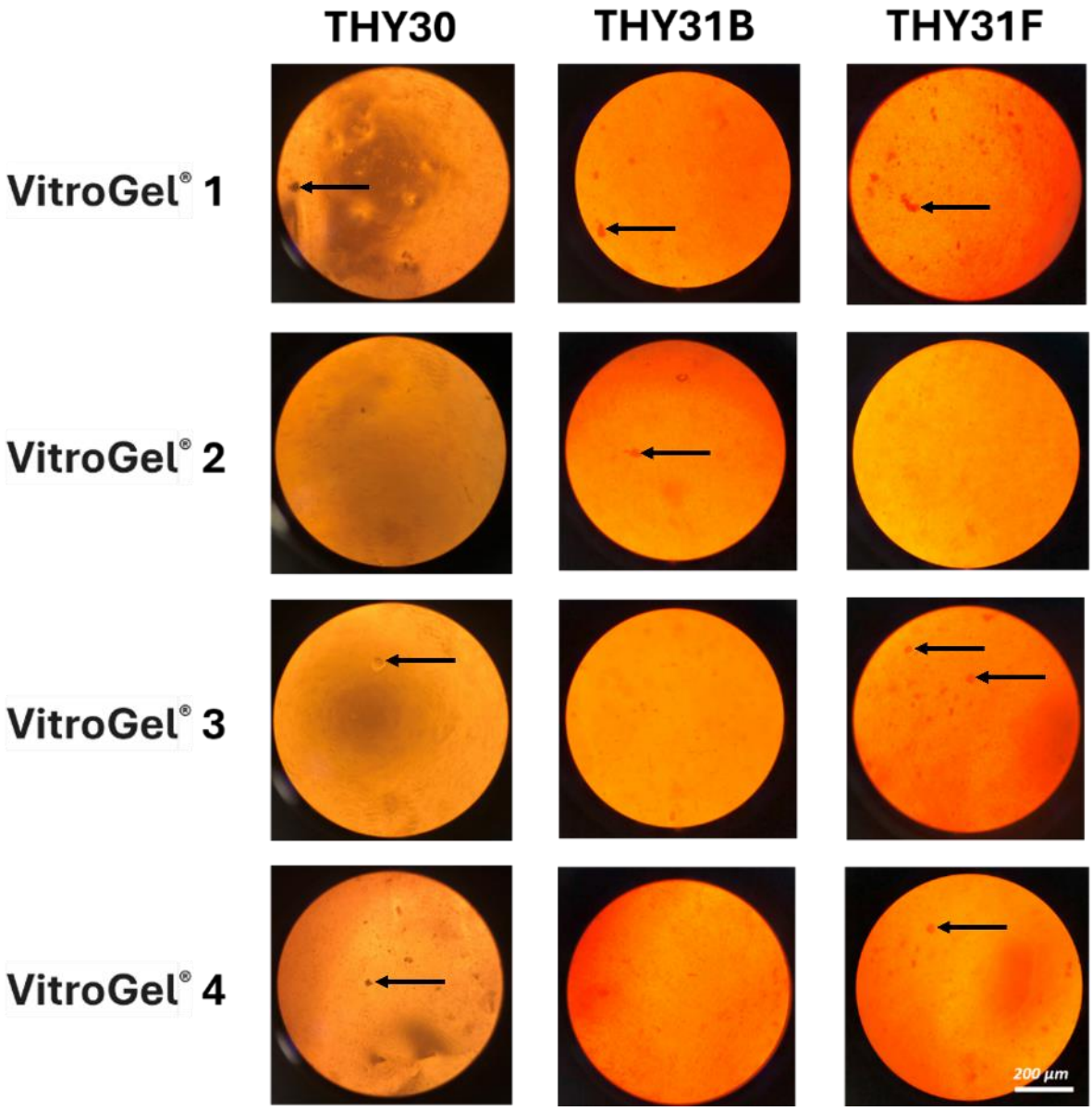


***Figure 6.3 Images of primary thyroid tissue cultures (8 x $10^5$ cells/mL) seeded in a 96-well flat bottom plate with one of four VitroGel® samples.*** *Images are representative of 4 replicate wells; 3 images were taken per VitroGel® sample post 24-day incubation, taken using a brightfield microscope at 10x magnification. THY30 – Follicular adenoma, THY31B – Benign and THY31F – Papillary carcinoma (Follicular variant). Black arrow to potential cell clusters. Scale bar – 200 µm.*

Cytospins of THY30 cells recovered from the VitroGel® (one well per VitroGel® sample) were carried out to identify and confirm the presence of primary cells, as it was difficult to do so under the microscope while the cells were still in the well and encapsulated within the hydrogel, scattering cells across multiple layers in the gel. The first attempt at Cytospin demonstrated that the recovery solution appeared to not have fully dissolved the VitroGel®, as no cells were identified (Figure 6.4).

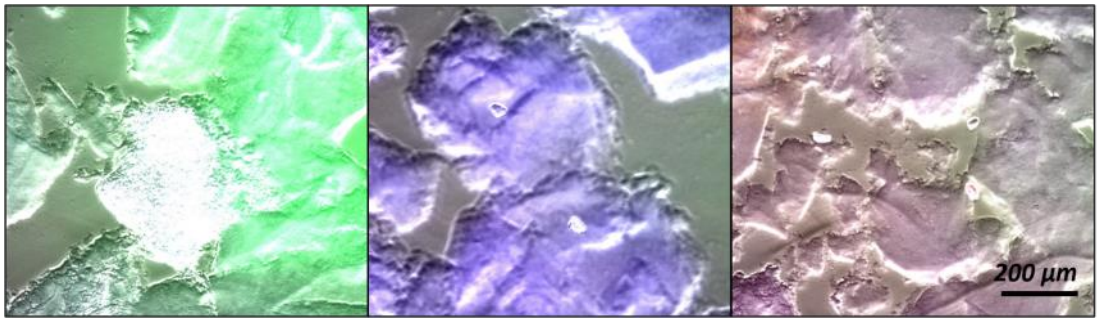


***Figure 6.4 Images of primary thyroid tissue cultures, THY30 (8 x $10^5$ cells/mL) seeded in a 96-well flat bottom plate with one of four VitroGel® samples following Cytospin.*** *Images are representative; 3 images were taken per VitroGel® sample following 15 days of incubation and subsequent Cytospin. Images taken using a Zeiss fluorescent microscope at 10x magnification. THY30 – Follicular adenoma. Scale bar – 200 µm.*

As with the Matrigel® investigations, spheroid formation in ULA plates (without Matrigel® or VitroGel®) was monitored using the remaining primary cells from the THY30 sample. More dense spherical structures were seen compared to the attempts with THY26/7/8 (Figure 6.5). On day 5, cells were concentrated near the centre of the well, with structures resembling a spheroid as seen by day 15. The day 15 structures were observed with a halo surrounding the central mass. It was uncertain what this mass consisted of, but it was most likely to be a combination of red blood cells (RBC) and debris, prompting the inclusion of a RBC lysis solution to the dissociation procedure.

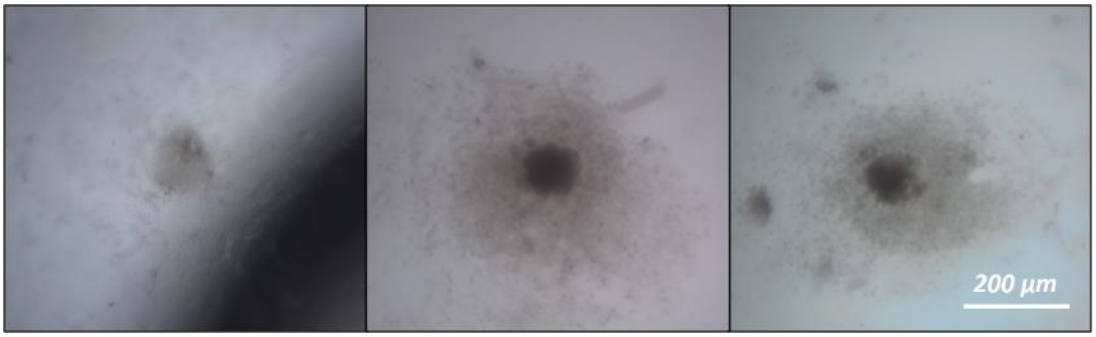


***Figure 6.5 Images of primary thyroid spheroid cultures, THY30 (8 x $10^5$ cells/mL, 100 µL/well) seeded in a 96-well ULA plate.*** *The best representative images of 9 replicates were taken after 15 days of incubation using a brightfield microscope at 10x magnification. THY30 – Follicular adenoma. Scale bar – 200 µm.*

ULA plates were also seeded with the remaining primary cell suspension from the THY31 sample. The benign cells did appear to have very small aggregates by day 7 which appeared to be growing in size. Unfortunately, both the benign and follicular primary spheroids succumbed to a bacterial infection preventing growth observations and comparisons between the two samples, therefore a single set of images for day 5 were acquired (Appendix 6.5).

THY30/31 primary cells seeded in a 96-well ULA plate were treated with sorafenib for subsequent analysis with MTS, CTG and IHC once spheroids reached a maturity of 21 days. It was soon realised that it was challenging to transfer the spheroid-like structures into an opaque plate for CTG analysis. The most common issue was the disaggregation of cells when attempting to lift the cells using a pipette and secondly, in some cases cells were firmly attached to the bottom of the wells, which hindered the ability of picking these cells up for OCT embedding, sectioning and staining for IHC investigations, which meant IHC was not performed.

As a result, the cells were treated within their wells and additional care was taken when performing washes with PBS, which was limited to one per primary spheroid as they were highly prone to disaggregation with each consecutive wash attempt. Attaining fluorescent images for these cells was challenging, allowing for only a handful of images to be collected. In the 25 µM treated group, very few of the THY30 primary cells survived the staining

procedure, most likely due to additional stress exerted following treatment. Whilst the 75 µM treated and control group both exhibited very strong red staining indicting cell death (Figure 6.6), which is congruent with the MTS data (Figure 6.7), which displayed very low levels of absorbance across all groups. Despite the control having a higher absorbance than the treated samples this difference was not significantly different, indicting cells may have been dead prior to treatment.

Sorafenib treatment (25 and 75 µM) was attempted with both the benign and the follicular adenoma primary spheroid cultures (THY31), followed by FDA/PI staining. Both samples displayed similar images displaying very strong green staining, with high levels of background staining in some instances and an absence of red staining (Figure 6.6). This would have indicated that the cells remained viable post treatment. However, analysis with the CTG assay revealed that the treated primary spheroids, including the control, consisted of very low RLU values of around 60, meaning that cells were either dead or not present. Based on these initial observations involving THY30/31 samples, little progress was made in generating viable organoids.

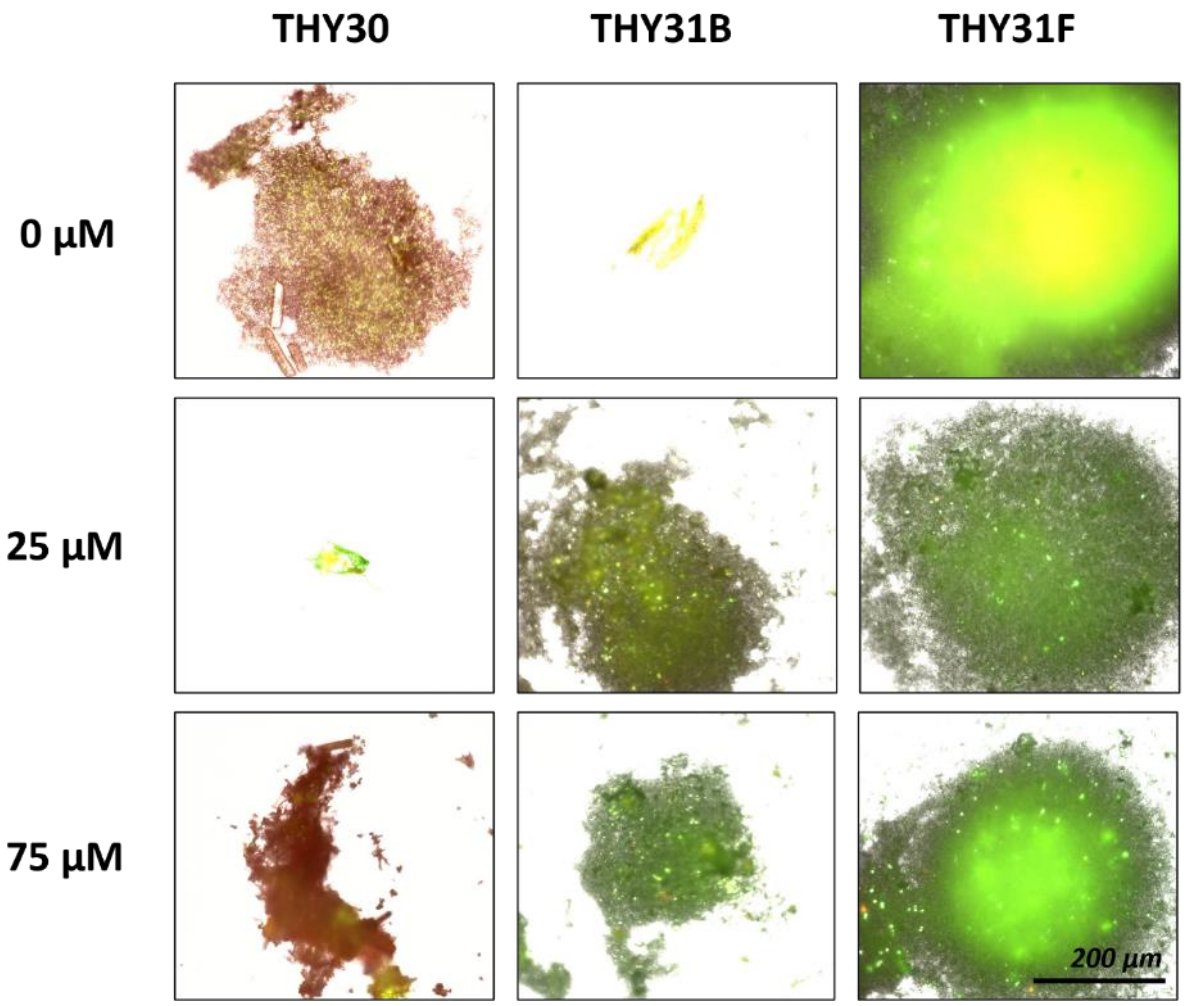


***Figure 6.6 Images of primary thyroid tissue cultures, THY30 and THY31 (8 x $10^5$ cells/mL, 100 µL/well) seeded in a 96-well ULA plate following treatment with sorafenib (25 and 75 µM) and FDA/PI staining.*** *Images are representative of triplicates; 3 images were taken per THY sample following 21 days of incubation and subsequent treatment and staining. Images taken using a Zeiss fluorescent microscope at 10x magnification. THY30 – Follicular adenoma, THY31B – Benign and THY31F – Papillary carcinoma (Follicular variant). Scale bar – 100 µm.*

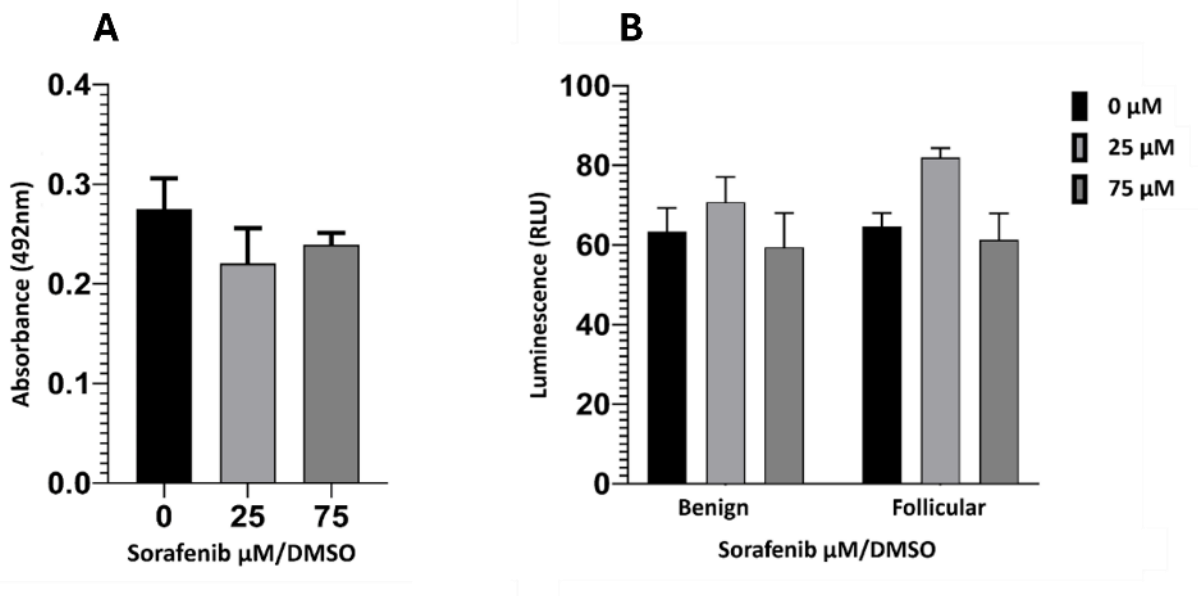


***Figure 6.7 Primary spheroid absorbance and luminescent values after treatment with sorafenib. A:*** *MTS absorbance values (492nm) for untreated (Medium with DMSO) and treated THY30 primary 'spheroid' (seeded at 8 x $10^5$ cells/ml, 100 µL/well) with sorafenib (25 and 75 µM) for 24 h. MTS analysis took place post 24 h treatment. THY30 – Follicular carcinoma. Triplicate wells were analysed. Values are mean ±SEM, n=1 with triplicates for each treatment group.* ***B:*** *Luminescence values for untreated and treated primary spheroid from sample THY31B/F (seeded at 8 x $10^5$ cells/ml, 100 µL/well) with sorafenib (25 and 75 µM) for 24 h. CTG analysis took place post 24 h treatment. THY31 B – Benign, F - Follicular carcinoma. Triplicate wells were analysed. Values are mean ±SEM, n=1., with triplicates for each treatment group.*

THY34 was classified as a papillary carcinoma, it had succumbed to a fungal infection and therefore growth observations were not possible. Remaining primary cells from the THY34 sample had been seeded into a ULA plate and combined with either 1000, 10,000 or 20,000 K1 cells/well, which were labelled with CFSE making them fluoresce green (section 2.4.3.3). This was attempted in order to determine if there was an optimal density of K1 cells, which could support the aggregation of primary cells into spheroids. However, there was a very strong presence of background staining in the primary spheroids with no possibility of identifying any cells.

The co-culture of primary cells, with CFSE labelled K1 cells was repeated with cells dissociated from THY37 (papillary carcinoma), with varying densities of K1 cells per well (1,000, 10,000,

or 20,000 cells/well). The primary cells combined with 1000 K1 cells/well, appeared to form the best spheroids as early as day 4, however, many small 'satellite' spheroids were also present at this time point (Figure 6.8). By day 9 these gradually began to amalgamate and by day 14 only singular spheroidal structures were evident. Primary cells combined with 10,000 K1 cells/well revealed a lack of cellular aggregation with a mass observed at the centre of the well, fluorescent imaging however revealed no staining, suggesting the mass did not consist of viable cells but debris/dead cells. Although the primary cells with 20,000 K1 cells/well did show a small amount of aggregation of cells, they failed to form any spheroid resembling structures over the course of the observations. For instance, by day 14 of observations many small and chaotic clusters of cells, containing lots of debris or dead cells that failed to aggregate were visible. Therefore, the first successful trial of combining primary and immortalised cells, implied that the combination of primary cells with 1000 K1 cells provided the greatest value in aiding primary cell aggregation. Despite images showing good spheroid formation, the labelling dye appeared to command a dominant presence under the microscope making identification of primary cells very challenging. Combined with the high background staining experience in the THY34 experiment, another labelling dye was trialled.

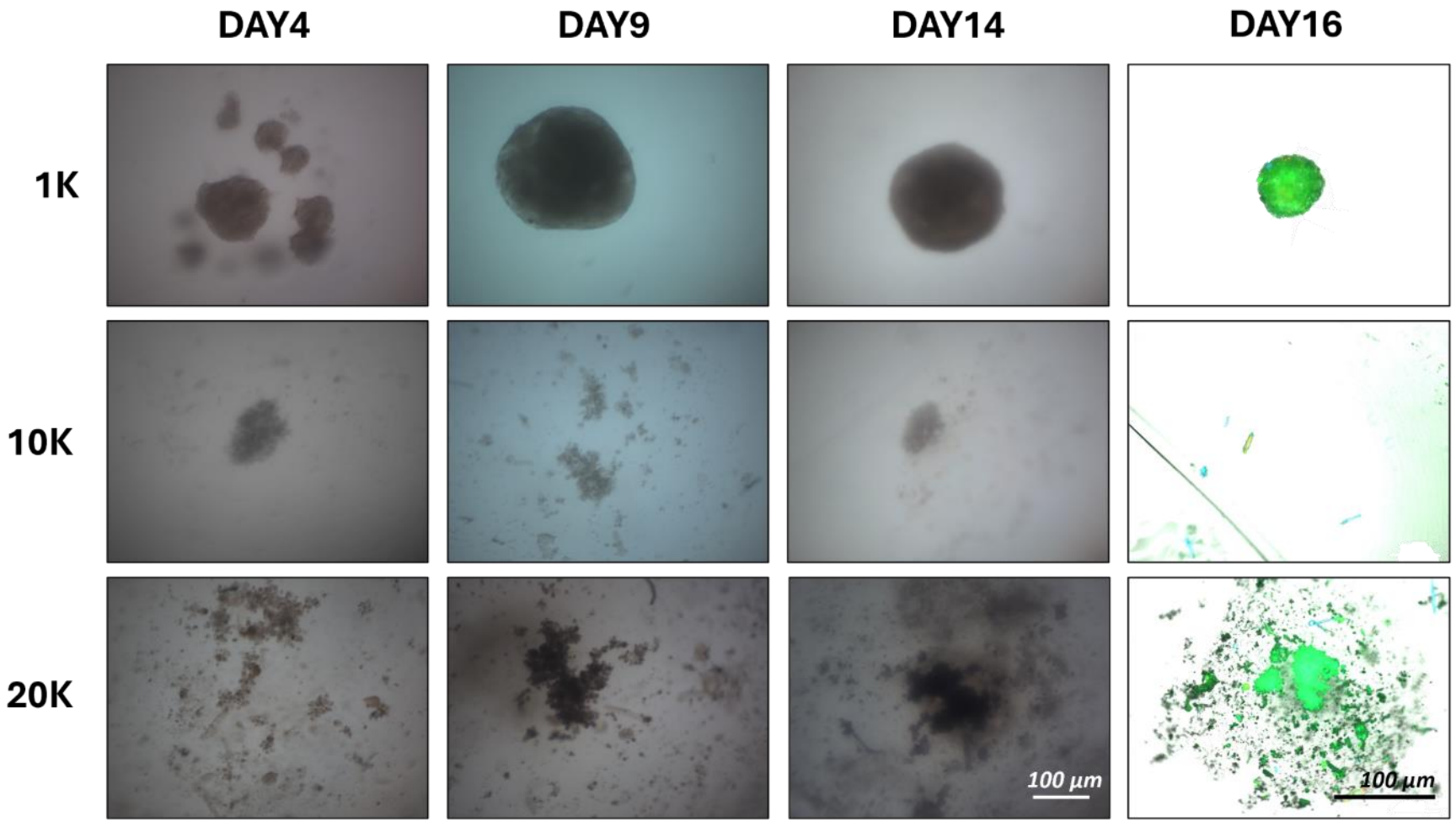


***Figure 6.8 Images of primary thyroid tissue cultures, THY37 (1000 cells/well) seeded in a 96-well ULA plate and cocultured with either 1,000, 10,000, or 20,000 CFSE stained K1 cells/well).*** *Images are representative of 3 replicates per seeding density; 3 images were taken for each THY + K1 cells 'spheroid' replicate throughout the 16 days of incubation followed by fluorescent imaging. Images taken using a brightfield microscope and Zeiss fluorescent microscope at 10x magnification. THY37 – papillary carcinoma. Scale bar – 100 µm.*

THY 38 was classified as benign thyroid tissue. The sample received was small (less than 2 $mm^3$) and so was only processed for spheroid development rather than the VitroGel® organoid study. In addition to the co-culture of primary tumour cells with K1 cells, TSH and iodine (section 2.4.2.2) were added to the medium for the first time in an attempt to encourage spheroid formation and growth.

Co-cultured spheroid formation was tested using 1000 and 20,000 K1 cells, combined with 1000 dissociated primary cells, based on the findings from the previous investigation. CytoPainter green dye (section 2.4.3.3), was used instead of CFSE, in an attempt to limit the background staining. With CytoPainter no background staining was observed, however, no cell presence was detected in the control (Primary+K1 cells without CytoPainter) (Figure 6.9) and only a small number of the labelled K1 cells could be observed with no primary cells following co-culture, most likely due to the poor formation of any spheroidal structures, therefore observing the arrangement of K1 cells within the confines of the primary spheroids was not possible.

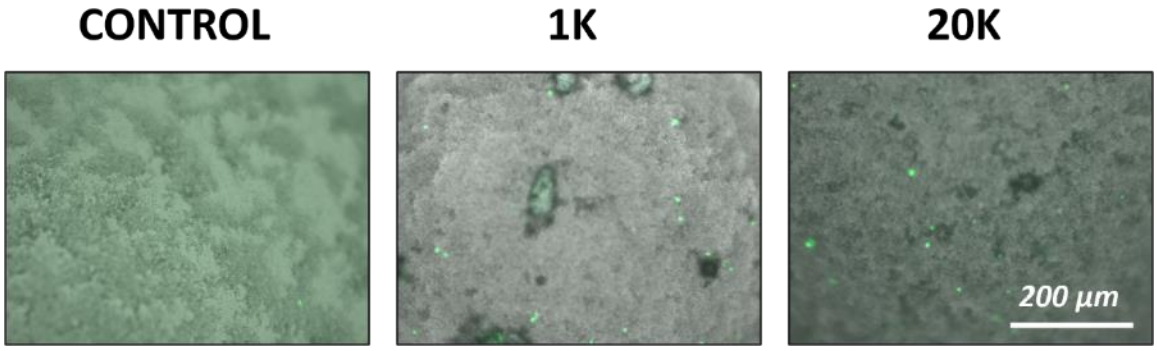


***Figure 6.9 Images of primary thyroid tissue cultures, THY38 (1000 cells/well) seeded in a 96-well ULA plate and cocultured with either 1,000 or 20,000 CytoPainter green stained K1 cells/well).*** *Images are representative of triplicates per seeding density; 3 images were taken per THY + K1 cells 'spheroid' after 14 days of incubation using a Zeiss fluorescent microscope at 10x magnification. THY38 – Benign thyroid tissue. Scale bar – 100 µm.*

THY39 was the final patient derived tissue sample studied and was classified as a follicular adenoma. The sample was dissociated and plated (8 x $10^5$ cells/ml) with each of the four VitroGel® samples (four wells per hydrogel sample). Samples were analysed much earlier in their growth period (up to day 7), compared to the previous investigations due to findings frequently indicating that most cells were dead by day 14. The primary cells cultured in the various VitroGel® samples were imaged periodically on days 3, 5 and 7. Images from cultures in VitroGel® were largely consistent with what was seen in previous repeats, with cells arranged in small aggregates where the vast majority of cells were in isolation from one another, with no indication of organoid formation (Appendix Figure 6.11).

ULA plates were seeded with the remaining primary cell suspension from the THY39 samples. Although a greater cell density was possible in comparison to previous attempts, these cells did not appear to form any spherical structures at the centre of the well (Appendix Figure 6.12). Instead, the cells assumed a scattered arrangement.

After the 7 day growth observations, one well per VitroGel® sample from the organoid plate was recovered using VitroGel® recovery solution, for a Cytospin investigation and fluorescent imaging in an attempt to identify and confirm the presence of cells. Cytospin was attempted, however no cells were identified with only the VitroGel® base being seen in the majority of images, which would indicate the hydrogel had not dissolved fully. A further well from each of the VitroGel® samples was retrieved with the recovery solution, however Incubation times were doubled ensuring the VitroGel® had completely dissolved with additional PBS washes to effectively remove the hydrogel. Although the presence of the VitroGel® in the background had decreased in intensity, there were still no cells evident.

In addition to the organoid generation experiment, CytoPainter green-labelled K1 cells were co-cultured with the primary cells (THY39, section 2.4.3.3) and seeded at 1000 cell/well in combination with 1000 primary cells, as this density of cells generally produced the most uniform spheroidal structures. The co-cultured cells were incubated for a total of 9 days in ULA plates before fluorescent imaging. Hoechst stain was also utilised in an attempt to highlight all cells. Images revealed the K1 cells favoured the centre of the well (Figure 6.10). In contrast, the primary cells appeared much larger than the K1 cells, although it is difficult to

determine confidently whether the structures seen are singular primary cells or groups. The primary cells were largely isolated from each other in a formation encircling the central mass of K1 cells.

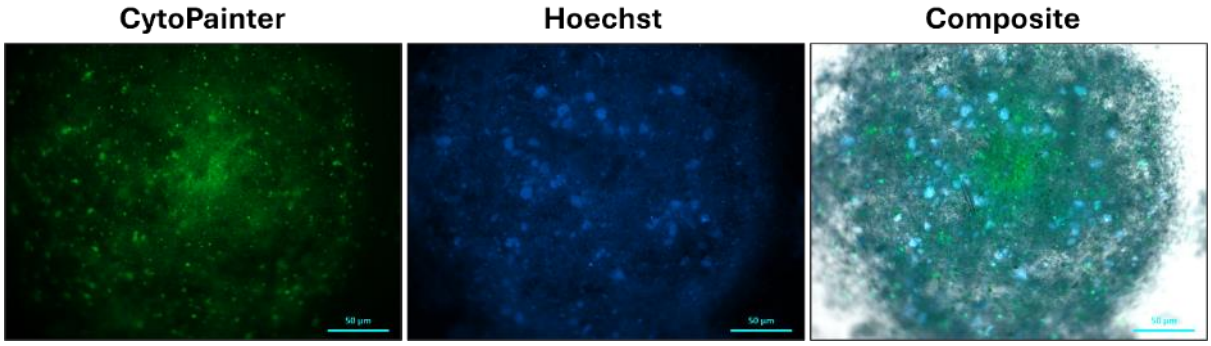


***Figure 6.10 Images of primary thyroid tissue cultures, THY39 (1000 cells/well) seeded in a 96-well ULA plate and cocultured with 1,000 CytoPainter green stained K1 cells/well).*** *Images are representative of a triplicate set; 3 images for each replicate were taken after 9 days of incubation using a Zeiss fluorescent microscope at 10x magnification. THY39 – Follicular adenoma. Scale bar – 50 µm.*

For comparisons, monocellular CytoPainter green labelled K1 spheroids were also imaged (Figure 6.11). Revealing a more defined spheroidal formation, which would suggest that the primary cells had possibly hindered the aggregation capabilities of the K1 cells. These final two figures highlight the preliminary nature of the organoid study, underscoring the need for further investigation and refinement to substantiate the findings.

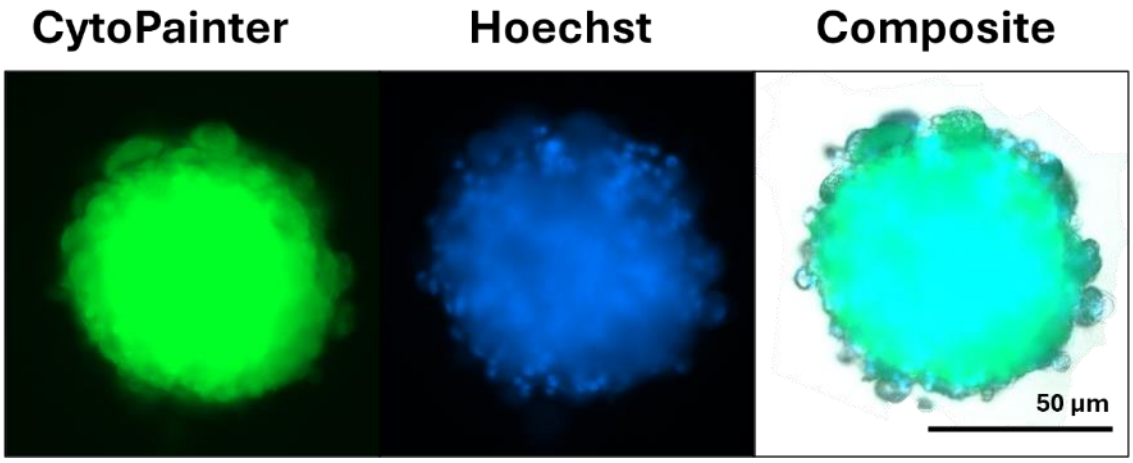


***Figure 6.11 Fluorescent images of a K1 spheroid (1000 cells/well) seeded in a 96-well ULA plate following labelling with CytoPainter and Hoechst.*** *Images are representative of a triplicate set; 3 images for each replicate were taken following 9 days of incubation and subsequent staining. Images taken using a Zeiss fluorescent microscope at 10x magnification. Scale bar – 50 µm.*

## 6.7 Discussion

The aim of the work in this chapter was to develop and optimise organoid generation using patient derived tissue. In the literature, there is no standard protocol for the dissociation of thyroid tissue and generation of organoids, which is understandable considering the extensive number and variety of thyroid tissue types. The profound number of additives used for organoid cultures (Table 6.1) can result in organoid cultivation becoming extremely expensive. For instance, van der Vaart *et al.,* (2021)*,* described the incorporation of at least 20 additional supplements for stimulating organoid growth resulting in a highly costly investigation, especially as these cultures require frequent medium replenishment. In the case of van der Vaart and colleagues*,* these costs were even greater as they ran their organoid observations for almost a year, with fresh medium exchange every three days along with the removal of organoids that were roughly a month old, mechanically dissociating them into individual cells and re-plating for continued organoid generation. Therefore, in the current study only the most commonly used supplements were added to the protocol initially, with additional supplements included as needed, when limited growth was observed. This approach aimed to reduce costs and make organoid manufacture a more efficient and cost-effective model for predictive toxicology research.

### 6.7.1 A Comparative Analysis of VitroGel® and Matrigel® for the Generation of Organoids

The ECM is important in supporting cell attachment, proliferation, and differentiation, making the choice of using a certain hydrogel vital for the success of maintaining tissue cultures and to encourage further growth. The limited success observed in organoid formation within this study poses challenges for comparisons, however certain insights can be made.

The generation of thyroid organoids from patient-derived tissue faced significant challenges, including minimal growth and difficulties in cell analysis. Observations of primary cell cultures within VitroGel® and Matrigel® revealed similar limited growth patterns. However, while both matrices supported cell aggregation and proliferation, initial samples that were incubated with Matrigel® lacked the formation of any tangible structures resembling organoids,

regardless of the tissue of origin. VitroGel® cultures exhibited visibly slower growth kinetics compared to Matrigel®. Notably, with Matrigel® cultures consisting of small cell clusters as early as day 3 of incubation, compared to the VitroGel® cultures which required at least 12 days before any structures worth noting were observed. In the case of long-term culture, both hydrogels demonstrated comparable results, capable of maintaining these small aggregate cultures for prolonged periods of time (~1 month) but without any improved growth in size.

The use of Matrigel® in organoid culture is widely reported, but it alone does not contribute significantly to the generation of these structures. Ogundipe *et al.,* (2021) investigated the creation of human thyroid organoids using Matrigel®, but struggled with organoid formation when lacking the supplements, Wnt and R-spondin, which significantly propagated growth. Interestingly, murine thyroid cells were able to form organoids without them, although the addition of Wnt and R-spondin enhanced their self-renewal capacity. The incorporation of both of these supplements were of common trend as shown in Table 6.1 with every study involving organoids including them.

Wnt are a family of proteins heavily involved in stem cell differentiation, cell proliferation and tissue regeneration through the activation of downstream β-catenin signalling pathways that regulate cell development. Miao *et al.,* (2020) found that Wnt was able to prolong the lifespan of human kidney tubular epithelial organoids (tubuloids) beyond the typical passage limit and enhance the outgrowth of organoids from single cells. On the other hand, R-spondins which are also proteins, amplify Wnt signalling by binding to receptor LRP6 and enhancing its interaction with frizzled receptors, which stabilises β-catenin and boosts the signalling pathway (ter Steege & Bakker, 2021). A study looking into the effects of R-spondin for organoid cultivation over 30 days found that the inclusion of the supplement significantly increased the size and survival rate of intestinal organoids. Specifically, organoids supplied with R-spondin were 2.7 times larger after 3 days and 5.7 times larger after 6 days compared to control organoids (lacking R-spondin). Moreover, the survival rate of these organoids was doubled by day 6 compared to the controls (Levin *et al.,* 2020). The synergistic effect of Wnt and R-spondin demonstrate the valuable interactions between the two proteins and their involvement in signalling pathways which can significantly improve the maintenance and proliferation of organoids.

The findings of Ogundipe *et al.,* highlighted that Matrigel® alone does not support growth and thus required the incorporation of additional and more expensive supplements. One such study conducted by Liang *et al.,* (2022), looked at human foetal thyroid organoids grown on Matrigel® and found that Forskolin, in conjunction with Wnt and R-spondin, stimulated their maturation leading to larger structures and expression of thyroxine secretion, closely mimicking mature thyroid tissue. Another example of how further supplements on top of the standard ones can have more of an effect and support on organoid generation than the hydrogel itself, underscoring the plethora of supplements available and how important and expensive the optimisation stage can be for manufacturing organoids.

Due to supply issues surrounding Matrigel®, four different VitroGel® hydrogels were utilised, however, a search of the literature for studies utilising this novel hydrogel for thyroid organoid growth yielded none. VitroGel® has however, been used for development of organoids from other tissue, and in the same way that Wnt and R-spondin work across multiple tissue types it was hoped the Vitrogel would work. For instance, Cherne *et al.,* (2021) used the same VitroGel® kit, containing four samples, for the generation of human gastric organoids, which showed comparable performance to Matrigel® in supporting organoid culture. Interestingly, Cherne *et al.,* also included Wnt and R-spondin in their growth medium. In particular, VitroGel® V-ORG-3, showed stimulated organoid growth by allowing monocyte-derived dendritic cell (MoDC) migration through its permeable matrix. This finding is especially important in the fact that VitroGel® has a xeno-free composition as opposed to Matrigel®, this VitroGel® aligns with ethical standards and regulatory requirements, meaning it could be a valuable and more cost-effective alternative to Matrigel® in the future. In the current study, there were no noticeable differences observed between the VitroGel® samples and subsequent organoid growth was unfortunately not achieved, regardless of the changes in protocol i.e. the addition of RBC lysis, TSH and iodine to the medium. Although this was the only study in the literature using VitroGel® for organoid development, a master's thesis compared various animal-free matrices as alternatives to traditional animal-derived matrices like Matrigel® and Basement membrane extract, for culturing liver organoids and kidney tubuloids. They also used the same four VitroGel® samples and found that all the VitroGel® samples generally supported organoid growth but showed slower growth rates and smaller

sizes compared to Matrigel®, more noticeably in liver organoids. (Scarlat, 2023). It is clear that VitroGel® is a promising alternative to Matrigel®, as it is considerably cheaper and more ethical, with less batch-to-batch variability (Hughes *et al.,* 2010) essential for experimental reproducibility.

### 6.7.2 Thyroid tissue-derived primary spheroids

This study was not capable of creating tangible primary spheroid models from thyroid tissue alone, which would have allowed for reliable testing with sorafenib and subsequent comparative analysis with static and on-chip investigations. Despite that, preliminary experiment success was observed in cultivated primary spheroids through the co-culture of primary cells with the K1 cell line. This shows promise, and thus with the inclusion of additional supplements such as Wnt and R-spondin and further optimisation this may become a valuable multicellular model for drug screening. The generation of primary thyroid spheroids using primary cells cocultured with K1 cells, at a density of 1,000 K1 cells/well provided the best primary spheroids, as higher densities resulted in less structured or chaotic clusters, indicating overcrowding. However, the primary spheroids were not suitable for removal out of their wells as the structure would easily crumble, which may be fixed through the use of hydrogel encapsulation to provide a scaffold for improved structural integrity. In addition, when culturing mono K1 cells, these cultures formed more defined spheroids, suggesting primary cells may have a negative interaction with K1 cells hindering cell aggregation.

Cirello *et al.,* (2016) had investigated the benefits of developing spheroids from thyroid tissue on 6 well-ULA plates for drug testing and found spheroids responded differently based on their tissue of origin (e.g. papillary *vs*. follicular thyroid cancer). When treated with compound SP600125, the JNK inhibitor was able to induce cell death and reduced size of spheroids derived from malignant tissue which displayed selective responses in comparison to normal thyroid tissue derived spheroids, the latter not showing significant cell death. Unfortunately, sorafenib experiments in the current study were unsuccessful which do not allow for comparisons to be made on how these respond to treatment. Although, ultra-low attachment plates had been used, Cirello *et al.,* (2016) found 6-well flat-bottom ULA plates to be an

effective platform for organoid growth which may have provided a better growth environment for primary cell aggregation than the use of 96-well round-bottom plates, especially as the dissociation protocols and cultivation processes were akin to one another. In addition, similar seeding densities; 300,000/800,000 compared to Cirello *et al.,* (2016)*,* 500,000 cells/well were used, also without the use of a hydrogel with spheroids ready for collection/testing after a week of incubation. This suggests that the difference in plates may have a major influence on spheroid cultivation and future repeats would need to look at testing a variety of plates to find which is most suitable for thyroid tissue.

Another study, successfully established and characterised patient-derived tumour spheroids as models for anaplastic thyroid cancer using Matrigel® drops, AggreWell and Matrigel® embedding (Hu *et al.,* 2024). These spheroids exhibited tissue-specific architecture based on the type of tumour tissue, with gene expression profiles consistent with parental tumours, and increased resistance to targeted therapies compared to monolayer cultures. They had used a very similar method of tissue dissociation and maintenance to *Cirello et al.,* (2016)*,* and had not added either Wnt or R-spondin into the media. However, they did underscore their use of Matrigel® which was particularly impactful in stimulating growth of spheroids where the number of starting viable cells was low. Moreover, they had utilised 6-well flat-bottom plates just like Cirello *et al.,* (2016), illuminating the possibility that the limited success in growing primary spheroids in the current study may have stemmed from the improper choice of culture plates. However, during primary spheroid investigations, the incorporation of any hydrogels into the protocol was not possible due to low supply which was reserved for the organoid investigations. Regardless, all the aforementioned studies vary in methodologies with not all requiring the addition of a hydrogel which highlights the challenging aspect of creating a standardised protocol for the generation of both primary organoids and spheroids.

The partial success in the current study combined with the Cirello *et al.,* (2016) and Hu *et al.,* (2024) studies highlights the importance of these multicellular models, who (Cirello and Hu) also found that the patient-derived thyroid spheroids had an identical genetic pattern to its tissue of origin. Further showcasing how these models can more accurately represent the inter-patient variable nature of tumour structure and composition and its effect on drug response, which cannot be effectively measured on homogenous 3D models or monolayers.

### 6.7.3 Implications of thyroid organoid generation

Currently the most challenging aspect of generating organoids is the reliability of production, which would be required for future mass scale manufacture. Clinical samples are limited, with a plethora of obstacles surrounding collection, use and availability of rare malignant thyroid tissue samples. In addition, running a single organoid experiment can be highly costly and lacks the high throughput aspect that cell line-derived spheroids possess (Lasolle *et al.,* 2023).

In an effort to minimise costs and to simplify the process, the current study reduced the number of additives and supplements that many other studies had used (Table 6.1), with a view to establishing a list of only the essential additives required for organoid generation. Currently, every study identified that investigated thyroid organoid generation had their own personalised supplement lists and dissociation techniques, emphasising the need for a standardised protocol for the culture of thyroid organoids (Harrison *et al.,* 2021). It is essential to reduce the costs of generating these models, which would then allow for effective use as a preclinical screening tool, offering better prediction capabilities compared to monolayers (Matsui & Shinozawa, 2021).

It is also difficult to classify exactly what constitutes an 'organoid', the general description is tissue that possesses qualities and forms a structure resembling that of organs in the human body (Huch *et al.,* 2017). However, in the current study, the creation of thyroid-like structures that can mimic the *in vivo* organ was not achieved. It has been reported previously that many issues surrounding successful aggregation, proliferation and maintenance plague the generation of patient tissue derived organoids (Andrews & Kriegstein, 2022). The most common reason being low-grade maturation, leading to very lethargic growth, which seldom reaches a stage where they can offer an accurate recapitulation of the *in vivo* organ. As mentioned in Table 6.1 and the current section, organoids/primary spheroids generally require at least a week to develop into viable structures for testing with some necessitating almost a full month. This poses great reproducibility and throughput capability concerns. An organoid literature review by Rossi *et al.,* (2018) suggests a possible solution for enhancing organoid architecture and promotion of growth, by introducing stem cell culture scaffolds, featuring a topography mirroring the specific tissue. This would allow the organoid to

progress in maturity but also stimulate the differentiation of cells within the organoid as well as providing structural support, allowing for stronger aggregation of primary cells. Most organoids, especially those created from patient derived thyroid tissue, develop into small clusters (Cherne *et al.,* 2021; Ogundipe *et al.,* 2021 and Cirello *et al.,* 2016), which was not achieved in the current study as although the formation of small aggregates of cells was noted, these were considerably smaller than those from the aforementioned studies especially as it was not possible to retrieve them from their wells.

Organoids lack vascularisation, immune cells and neuronal structures which play an important role in how the tumour responds to drugs *in vivo* are essential in the tumorigenesis process (Chew *et al.,* 2020). Meaning, organoids are not currently capable of ideally mimicking the microenvironment, however in a review by Samimi *et al.,* (2021), a potential solution was proposed to overcome the aforementioned obstacle. The use of organoids on microfluidic devices has shown to provide organoids with mechanical, electrical, and hydrodynamic cues stimulating organoid functionality and which can also emulate flow conditions experienced in vascularised tissue, allowing for a more realistic response to treatment (Carvalho *et al.,* 2023).

Another option is the use of microfluidic devices, to maintain biopsies of viable thyroid tissue for subsequent analysis. For example, Riley *et al.,* (2019), successfully preserved PTC-derived tissue on a tissue-on-chip device for 96 h, including the perfusion of the chemotherapy drug etoposide and JNK inhibitor (SP600125) which significantly increased apoptosis levels compared to the control tissue (no treatment) which maintained high viability throughout the observation period. While tissue-on-chip provides a more accurate representation of the tumour microenvironment, it lacks throughput capabilities. However, organoids are anticipated to offer improved scalability and high-throughput analysis in the future, making them a promising alternative for extensive drug testing and treatment evaluation. For example, Cherne *et al.,* (2021) designed a microfluidic platform (GOFlowChip) which showed that it was capable of maintaining human gastric organoids cocultured with MoDC's, simulating precise cellular interactions and migration dynamics in a controlled microenvironment. The GOFlow set-up mimics physiological conditions such as vascularity for more accurate investigations into how the *in vivo* tumour may respond to treatment.

Furthermore, due to the 3D structure of the matrices used in the current study, imaging of the cluster of cells was challenging, as individual cells/clusters were present at different planes within the matrices. Another obstacle was the lack of tangible structures in both the organoid and spheroids investigations which heavily hindered transport out of their wells and the possibility of additional testing other than observatory ones.

### 6.7.4 Future applications

Despite the lack of success in the current project, organoid models derived from patient-derived thyroid tissue not only offers a promising platform for predicting drug response, but also the study of disease mechanisms, especially when no study currently exists utilising these novel models to pursue a deeper understanding of thyroid tumorigenesis (Samimi *et al.,* 2021).

A change in the approach of a novel drug in entering clinical testing is long overdue, there have been minimal revisions to the models used, which still heavily rely on 2D monolayers and laboratory animals. A meta-analysis has shown that only 5% of agents showing significant anticancer activity in preclinical testing are eventually licensed after successfully demonstrating efficacy in Phase III trials (Hutchinson & Kirk, 2011). With a more recent review indicating that 52% of drug failures in clinical trials occur due to poor efficacy (Kiriiri *et al.,* 2020). Out of 5154 cancer-related clinical trials, with 73% of those focused on developing cancer treatments, very few progress to Phase III and beyond, only 8.6% made it to Phase III and 0.6% to Phase IV (Liu *et al.,* 2017). This low number is concerning and highlights the waste of money spent on these trials, but with the rapid development of 3D models, their implementation in preclinical testing is likely to increase over time, by providing greater predictive accuracy and examine how these changes affect performance in phase III trials. With several clinical trials currently taking place looking to present their findings on the use of organoid analysis to determine the most appropriate therapy for individual patients within the next decade (Table 6.2) This provides optimism for the future of more accurate drug development and preclinical tools (Hofmann *et al.,* 2022).

***Table 6.2 Ongoing clinical trials involving organoids****. Created using information from the clinicaltrials.gov database.*

| Principal investigator | Title | Type of organoid | Design | Status | Planned completion | Patients needed |
|---|---|---|---|---|---|---|
| **Quan Liu, Jiangsu, China** | A Single-arm, Single-center Clinical Trial of Patient-derived Lung Cancer Organoids for Predicting Therapeutic Response in Patients with Multiline Drug-resistant Lung Cancer | Lung cancer | Randomised<br>Parallel<br>Phase 2 | Recruiting | 2026-05-31 | 50 |
| **Shiwei Guo, Shanghai, China** | A Prospective, Randomized, Controlled Trial of Adjuvant Chemotherapy for Pancreatic Cancer Based on Organoid Drug Sensitivity Test | Pancreatic cancer | Randomised<br>Parallel<br>Phase 3 | Recruiting | 2025-05-31 | 200 |
| **Veronique Serre-Beinier, Geneva, Switzerland** | Patient-derived Organoids of Lung Cancer to Test Drug Response | Lung cancer | Observational;<br>Cohort | Recruiting | 2029-12-30 | 50 |
| **Roland Seiler, Biel, Switzerland** | Guidance of Adjuvant Instillation in Intermediate Risk Non-muscle Invasive Bladder Cancer by Drug Screens in Patient Derived Organoids. A Single Center, Open-label, Phase II Trial with a Feasibility Endpoint. (GAIN-INST-TRIAL) | Bladder cancer | Non-randomised<br>Single group<br>Interventional | Recruiting | 2026-11-16 | 33 |
| **Jun Yan, Guangdong, China** | Precision Chemotherapy Based on Organoid for Colorectal CancerPatient-Derived Tumor Organoid Drug Sensitivity for Colorectal Cancer: A Prospective, Multicentre, Randomized, Controlled Trial | Colorectal cancer | Randomised<br>Parallel | Recruiting | 2025-12-01 | 186 |
| **Summer Swearingen, California, USA** | An Organoid-based Functional Precision Medicine Trial in Osteosarcoma: PREMOST | Bone cancer | Observational;<br>Prospective | Recruiting | 2027-01-01 | 40 |
| **Alba Di Leone, Rome, Italy** | Breast Cancer Subtype Characterization Through Patient's Derived Organoids". (BCinsightPDO) | Breast cancer | Observational;<br>Prospective | Recruiting | 2027-06-15 | 306 |

# Chapter 7 Discussion

RAI-R, or resistance to RAI treatment has proven to be a challenging obstacle in the management of thyroid cancers. Given the prevalence of TC subtypes that manage to evade the effects of conventional therapy, TKI have emerged as a promising second-line treatment and in some cases, the first-line choice. In recent years, the adoption of more complex 3D models, such as spheroids and organoids has significantly advanced the understanding of tumorigenesis, tumour progression and therapeutic alternatives.

One such alternative, in terms of thyroid cancer, is sorafenib which other than Lenvatinib, is currently the only approved first-line treatment of advanced RAI-R DTC (Chen *et al.,* 2023). However, high incidences of dose reductions and adverse side effects post-sorafenib therapy for thyroid and renal cancer patients have been reported in three separate randomised phase III trials. These trials observed a 13-35% incidence of dose reductions and 10-38% of treatment discontinuation due to serious adverse events (Li *et al.,* 2015). Improving the understanding on why individual responses are so varied, could allow drug selection to be tailored to give the most appropriate treatment to patients, while identifying patients that might experience these adverse events, allowing for a more reliable and personalised approach, through the use of cell line/patient derived - spheroid/organoid models (Gong *et al.,* 2017).

The current study, focused on optimising and establishing spheroid models utilising two thyroid cancer cell lines of differing cellular characteristics and behaviour, in order to provide a reliable and consistent platform for the analysis of drug treatment.

Both K1 and 8305c spheroids were successfully grown and optimised to provide two model types; spheroids which presented with a necrotic core and spheroids which did not, allowing for insights into how a hypoxic environment influences drug response. Moreover, it was shown that a homogeneous 3D model could be consistently generated using a reproducible protocol, allowing for high-throughput screening. The protocol involved seeding cells into 96-well ultra-low attachment plates, where a density as low as 1,000 cells/well reliably produced spheroids.

Furthermore, it was demonstrated that the incorporation of the ECM supplement, Matrigel® significantly influenced spheroid development in several key ways. Firstly, inclusion of this additive significantly increased spheroid size, which was particularly notable given the initial low seeding density. Interestingly, the sizes of the Matrigel® supplemented spheroids matched, or even surpassed, those of larger spheroids with much greater starting cell numbers. This enhancement facilitated easier identification of spheroids under the microscope and created a more spacious cellular arrangement within the 3D model, which was likely to enhance nutrient and gas exchange. This improved exchange prevented the formation of a hypoxic core, allowing for comparisons against necrotic tumour spheroids. Overall, Matrigel®-supplemented spheroids exhibited greater viability compared to those without the additive, highlighting its role in supporting more robust and viable spheroid cultures.

Regarding sorafenib therapy, 8305c spheroids derived from the characteristically aggressive anaplastic thyroid carcinoma interestingly exhibited greater sensitivity to sorafenib compared to the papillary thyroid carcinoma derived K1 spheroids. Furthermore, 1000 cells/well spheroids appeared more resistant to therapy compared to the larger 10/20,000 cells/well spheroids. The observed sensitivity differences highlight the complexity of therapeutic responses in different thyroid cancer subtypes and suggest that factors beyond the primary drug-target interactions are at play, such as the unique tumour microenvironments and spheroid structures. Regardless, both cell line $IC_{50}$ values at the lower plating density highly resembled those described in the literature which had utilised monolayers, showcasing that the 3D spheroid approach not only validates previous findings but also enhances the understanding of drug behaviour in a more physiologically relevant context.

Preliminary trials have demonstrated the potential of utilising microfluidic devices to culture spheroid models, representing a significant advancement by integrating static cultures with dynamic, flow-based systems. Microfluidic devices provide a more sophisticated and controlled environment, allowing for continuous perfusion and the simulation of *in vivo*-like conditions. Spheroids cultured in these dynamic conditions exhibited increased sensitivity to TKI therapy, consistent with observations reported in the literature. By incorporating microfluidic technology, 3D models can be enhanced in their predictive accuracy and offer

more relevant insights into how tumours may react to treatments in clinical scenarios (Lapizco-Encinas & Zhang, 2022).

## 7.1 Future work

In this study, immortalised PTC and ATC cell line spheroids (homogenous) were optimised for high-throughput simple drug screening, using straightforward procedures, ready for experimentation within less than a week.

The limitations of homogeneous spheroids in cancer research have highlighted the need for multicellular spheroids (MCS) to better recapitulate the heterogeneous TME. MCS offer superior mimicry of TME features, including tumour hypoxia and complex cell-cell interactions, which are crucial for understanding cancer progression and treatment resistance (Nath & Devi, 2016).

Breast cancer research has demonstrated the potential of MCS models. Reynolds *et al.* (2017) developed MCS incorporating cancer stem cells (CSC) by combining triple-negative (MDA-MB-231) and luminal (MCF7) breast cancer cell lines in Matrigel® and collagen gels. Their study revealed spatially-dependent drug responses, highlighting the influence of cellular spatial arrangement on drug efficacy and resistance. Notably, treatment with Paclitaxel resulted in the selective elimination of non-stem-like cancer cells while sparing or enriching the CSC population within the core, underscoring the importance of tumour architecture in drug resistance mechanisms. Further exemplifying the value of MCS models, Balsa *et al.* (2020) utilised MCS generated from MCF-7 and MDA-MB-231 cell lines to evaluate the anti-cancer and anti-metastatic potential of a novel copper-tropolone compound, [Cu(trp)2]. Their study reported a remarkable 26-fold lower $IC_{50}$ for [Cu(trp)2] compared to the clinically used chemotherapy drug Cisplatin in MCS models. Moreover, [Cu(trp)2] effectively inhibited both migration and invasion of breast cancer cells within MCS, suggesting its potential as a drug candidate for further testing in *in vivo* cancer models.

A significant advancement in addressing the lack of vascularisation in *in vitro* models has been the incorporation of endothelial and perivascular cells in 3D co-culture spheroid models (Vakhrushev *et al.,* 2021). Ascheid *et al*. (2024) created complex MCS models that included

various breast cancer cell lines (MCF7, MDA-MB-231/435s, Sk-Br3, ZR75-1, MDA-MB-468, AT3), human monocytic cells (THP-1), normal human dermal fibroblasts (NHDF), and human umbilical vein endothelial cells (HUVEC-2). These MCS successfully recreated complex TME features, including perivascular niches and tumour-stromal interactions, with spheroids forming mature vascular networks after 9 days with high reliability and reproducibility.

To advance TC research using MCS models, several key areas should be addressed. Standardising criteria for spheroid size, viability, and ECM mimicry is crucial for improving result reliability (Ryu *et al.,* 2019; Arora *et al.,* 2024). The development of high-throughput screening platforms, as demonstrated by Lee *et al.* (2018) using poly(ethylene glycol) (PEG)-based hydrogel microwells for uniform-sized MCS generation, can facilitate more efficient and precise studies. Incorporating diverse cell types relevant to the thyroid TME, such as thyroid-specific fibroblasts, immune cells, and endothelial cells, would create more physiologically relevant models for TC research. With ongoing improvements, MCS models have the potential to become an established drug screening platform with greater predictive capability over the next decade, especially as numerous studies continue to enhance their accuracy and reliability.

Another emerging model involves the use of adipose-derived stem cells (ADSC), which offer a novel approach for assessing individual risk and treatment responses in TC. Culturing ADSCs from a patient's fat tissue enables the analysis of genetic mutations, chromosomal abnormalities, and other relevant biomarkers associated with the disease (Zhang *et al.,* 2020). These stem cells have the ability to differentiate into thyroid-like cells, providing a platform for drug response testing and potentially aiding in early detection. Although still in the experimental stage, this method could lead to a minimally invasive strategy for identifying thyroid cancer-related biomarkers or genetic aberrations and developing tailored treatment plans based on patient-specific profiles.

Patient-derived organoids represent a promising model for personalised medicine in TC research, despite challenges in their formation. Vlachogiannis *et al*. (2018) demonstrated that metastatic gastrointestinal organoids closely mirror the molecular and phenotypic profiles of original tumours, indicating their potential value in predicting patient responses to

treatments. The integration of factors such as Wnt and R-spondin into organoid development has been shown to enhance their morphology, viability, and cellular composition, improving their resemblance to *in vivo* tumours and predictive accuracy (Urbischek *et al.,* 2019; Sprangers *et al.,* 2020; Wilson *et al.,* 2021).

While organoids excel in case-by-case studies due to their ability to mimic patient-specific tumour characteristics, they face limitations as preclinical drug screening platforms. Traditional organoid systems require extended cultivation periods of one to four weeks and most rely on Matrigel® embedding, which introduces batch-to-batch variability and impairs reproducibility (Ren *et al.,* 2022). To address these challenges, Jung *et al*. (2021) developed a novel Hydro-plate system for culturing colorectal cancer organoids. This system produces hydro-organoids (HO) from dissociated healthy and neoplastic colonic tissues, resulting in consistent size and morphology compared to Matrigel®-embedded organoids. Notably, HO were treated with chemotherapy drugs such as Doxifluridine, Oxaliplatin, or their combination after only six days of cultivation, significantly reducing the time required for drug screening. The enhanced efficiency and consistency of the Hydro-plate system suggest its potential as a more effective preclinical drug screening platform, overcoming the prolonged incubation times associated with traditional organoid culture. However, the high costs of organoid use, along with patient tumour heterogeneity, indicate the need for further optimisation to improve scalability and reduce expenses.

Microfluidic devices integrated with 3D tumour models offer significant advancements in drug screening and personalised treatment by more accurately replicating the *in vivo* TME compared to traditional 2D cultures and animal models. Fevre *et al.* (2023) demonstrated the potential of this approach using Ewing's Sarcoma (A673) spheroids, where microfluidic platforms revealed novel drug synergies and enhanced efficacy through specific drug combination sequences. Adapting this methodology to TC research could uncover similar therapeutic interactions and optimise treatment strategies. Mehta *et al.* (2024) developed a microfluidic system generating oral cancer spheroids on the device from resected squamous cell carcinomas, preserving inter-patient tumour heterogeneity and mimicking solid tumour histology. Their system effectively tested a tri-chemo drug panel (Paclitaxel, 5 Fluorouracil, and cisplatin) on three-day-old spheroids, with responses correlating well with clinical

histopathological reports. This approach, allowing for viability and imaging analysis without spheroid manipulation, could be adapted for future primary spheroid investigations as in the current study, primary cultures were too fragile for transport/testing. The potential of effluent analysis from these systems remains largely unexplored. Effluents from malignant tissue contain valuable biomarkers such as extracellular vesicle miRNAs (e.g., miR-375-3p, miR-7-5p, miR-382-5p) and cell surface markers (e.g., CD3+ and CD4+) associated with thyroid-related diseases (Xi *et al.,* 2020; Feng *et al.,* 2020). Investigating these biomarkers could provide insights into prognosis and treatment efficacy in thyroid cancer.

Recent advancements in digital microfluidics (DMF) technology offer significant improvements for drug screening and personalised medicine, particularly in handling small primary cell populations. Zhai *et al*. (2024) demonstrated DMF efficacy by treating freshly obtained hepatectomy tissue with chemotherapy drugs (sorafenib, regorafenib, apatinib, and lenvatinib), assessing drug efficacy on-chip within 36 h, using fluorescent dyes. This approach accelerates drug screening while maintaining high precision in evaluating drug responses. DMF technology offers cost-effectiveness, portability, and potential savings in research and development costs—up to 25% compared to traditional methods (Ingber, 2022; Bouquerel *et al.,* 2023). However, DMF technology is still in its early stages and requires further optimisation to potentially incorporate 3D models such as organoids and spheroids on these devices, ensuring its broader application in clinical settings. The integration of these microfluidic technologies in TC research holds promise for advancing personalised treatment strategies and improving the understanding of tumour biology. Further research is needed to adapt and optimize these systems specifically for TC, potentially leading to more effective and targeted therapies for patients.

## 7.2 Conclusion

This study advances the understanding of 3D thyroid cancer models for drug screening, demonstrating high reproducibility and throughput, revealing significant differences in therapeutic responses between TC subtypes. Further research with patient-derived tissue is crucial to develop models that better reflect individual tumours and support personalised therapy approaches.

# References


Aashiq, M., Silverman, D.A., Na'ara, S., Takahashi, H. & Amit, M. (2019) Radioiodine-refractory thyroid cancer: Molecular basis of Redifferentiation Therapies, management, and novel therapies. *Cancers,* 11(9), 1382.

Abdelgalil, A.A., Alkahtani, H.M. & Al-Jenoobi, F.I. (2019) Sorafenib. *Profiles of Drug Substances, Excipients and Related Methodology*, 239–266.

Abdolahi, S., Ghazvinian, Z., Muhammadnejad, S., Saleh, M., Asadzadeh Aghdaei, H. & Baghaei, K. (2022) Patient-derived xenograft (PDX) models, applications and challenges in cancer research. *Journal of Translational Medicine*, 20(1), 206.

Abe, I. and Lam, A.K. (2021) 'Anaplastic thyroid carcinoma: Current issues in genomics and therapeutics', *Current Oncology Reports*, 23(3), 31.

ABOLS, A., DUCENA, K., ANDREJEVA, D., SADOVSKA, L., ZANDBERGA, E., VILMANIS, J., NARBUTS, Z., TARS, J., EGLITIS, J., PIRAGS, V. & LINE, A. (2015) Trefoil factor 3 is required for differentiation of thyroid follicular cells and acts as a context-dependent tumor suppressor. *Neoplasma,* 62(06), 914–924.

Aguilar Cosme, J.R., Gagui, D.C., Bryant, H.E. & Claeyssens, F. (2021) Morphological response in cancer spheroids for screening photodynamic therapy parameters. *Frontiers in Molecular Biosciences*, 8, 784962.

Akgönüllü, S., Bakhshpour, M., Pişkin, A.K. & Denizli, A. (2021) Microfluidic systems for cancer diagnosis and applications. *Micromachines,* 12(11), 1349.

Albi, E., Cataldi, S., Lazzarini, A., Codini, M., Beccari, T., Ambesi-Impiombato, F. & Curcio, F. (2017) Radiation and Thyroid Cancer. *International Journal of Molecular Sciences*, 18(5), 911.

Alemu, A., Terefe, B., Abebe, M. & Biadgo, B. (2016) Thyroid hormone dysfunction during pregnancy: A Review. *International Journal of Reproductive BioMedicine*, 14(11), 677–686.

Amaral, M., Afonso, R. A., Gaspar, M. M., & Reis, C. P. (2020). Anaplastic thyroid cancer: How far can we go? *EXCLI journal*, 19, 800–812.

Andrews, M.G. & Kriegstein, A.R. (2022) Challenges of Organoid Research. *Annual Review of Neuroscience*, 45(1), 23–39.

Anthon, S.G. & Valente, K.P. (2022) Vascularization strategies in 3D cell culture models: From scaffold-free models to 3D bioprinting. *International Journal of Molecular Sciences,* 23(23), 14582.

Antunes, N., Kundu, B., Kundu, S.C., Reis, R.L. & Correlo, V. (2022) In vitro cancer models: A closer look at limitations on translation. *Bioengineering,* 9(4), 166.

Apostolou, K., Zivaljevic, V., Tausanovic, K., Zoric, G., Chelidonis, G., Slijepcevic, N., Jovanovic, M. & Paunovic, I. (2020) Prevalence and risk factors for thyroid cancer in patients with multinodular goitre. *BJS Open*, 5(2), 14.

Aravindan, K. (2017) Papillary thyroid cancer: Why the increase and what can be done? Indian *Journal of Cancer*, 54(3), 491.

Armstrong, M., Asuka, E., & Fingeret, A. (2023). Physiology, Thyroid Function. *In StatPearls*. Retrieved from https://www.ncbi.nlm.nih.gov/books/NBK537039/

Arora, S., Singh, S., Mittal, A., Desai, N., Khatri, D.K., Gugulothu, D., Lather, V., Pandita, D. & Vora, L.K. (2024) Spheroids in cancer research: Recent advances and opportunities. *Journal of Drug Delivery Science and Technology,* 100, 106033.

Arrojo e Drigo, R. & Bianco, A.C. (2011) Type 2 deiodinase at the crossroads of thyroid hormone action. *The International Journal of Biochemistry & Cell Biology*, 43(10), 1432–1441.

Aung, T.N., Acs, B., Warrell, J., Bai, Y., Gaule, P., Martinez-Morilla, S., Vathiotis, I., Shafi, S., Moutafi, M., Gerstein, M., Freiberg, B., Fulton, R. & Rimm, D.L. (2021) A new tool for technical standardization of the KI67 immunohistochemical assay. *Modern Pathology,* 34(7), 1261–1270.

Babić Leko, M., Gunjača, I., Pleić, N. & Zemunik, T. (2021) Environmental factors affecting thyroid-stimulating hormone and thyroid hormone levels. *International Journal of Molecular Sciences*, 22(12), 6521.

Badea, M.A., Balas, M., Hermenean, A., Ciceu, A., Herman, H., Ionita, D. & Dinischiotu, A. (2019) Influence of Matrigel® on single- and multiple-spheroid cultures in breast cancer research. *SLAS Discovery*, 24(5), 563–578.

Balsa, L.M., Ruiz, M.C., Santa Maria de la Parra, L., Baran, E.J. & León, I.E. (2020) Anticancer and antimetastatic activity of copper(ii)-tropolone complex against human breast cancer cells, breast multicellular spheroids and mammospheres. *Journal of Inorganic Biochemistry*, 204, 110975.

Barbosa, M.A., Xavier, C.P., Pereira, R.F., Petrikaitė, V. & Vasconcelos, M.H. (2021) 3D cell culture models as recapitulators of the tumor microenvironment for the screening of anti-cancer drugs. *Cancers,* 14(1), 190.

Bargahi, N., Ghasemali, S., Jahandar-Lashaki, S. & Nazari, A. (2022) Recent advances for cancer detection and treatment by microfluidic technology, review and update. *Biological Procedures Online*, 24(1), 5.

Basolo, A., Matrone, A., Elisei, R. & Santini, F. (2022) Effects of tyrosine kinase inhibitors on thyroid function and thyroid hormone metabolism. *Seminars in Cancer Biology*, 79, 197–202.

Bath, S. C., Steer, C. D., Golding, J., Emmett, P. & Rayman, M. P. (2013) 'Iodine deficiency in UK pregnant women and its association with adverse neurodevelopmental outcomes in their children: results from the Avon Longitudinal Study of Parents and Children (ALSPAC)', *The Lancet*, 382(9889), pp. 331-337.

Bath, S.C., Verkaik-Kloosterman, J., Sabatier, M., ter Borg, S., Eilander, A., Hora, K., Aksoy, B., Hristozova, N., van Lieshout, L., Tanju Besler, H. & Lazarus, J.H. (2022) A systematic review of iodine intake in children, adults, and pregnant women in Europe—comparison against dietary recommendations and evaluation of dietary iodine sources. *Nutrition Reviews,* 80(11), 2154–2177.

Benvenga, S., Tuccari, G., Ieni, A. & Vita, R. (2018) Thyroid gland: Anatomy and physiology. *Encyclopedia of Endocrine Diseases*,382–390.

Bergdorf, K., Bauer, J.A., Westover, D., Phifer, C., Murphy, B., Tyson, D.R., Lee, E. & Weiss, V.L. (2022) Utilizing three-dimensional culture methods to improve high-throughput drug screening in anaplastic thyroid carcinoma. *Cancers,* 14(8), 1855.

Berrouet, C., Dorilas, N., Rejniak, K.A. & Tuncer, N. (2020) Comparison of drug inhibitory effects (IC50) in monolayer and spheroid cultures. *Bulletin of Mathematical Biology*, 82(6).

Białkowska, K., Komorowski, P., Bryszewska, M. & Miłowska, K. (2020) Spheroids as a type of three-dimensional cell cultures—examples of methods of preparation and the most important application. *International Journal of Molecular Sciences*, 21(17), 6225.

Boltze, C., Brabant, G., Dralle, H., Gerlach, R., Roessner, A. & Hoang-Vu, C. (2002) Radiation-induced thyroid carcinogenesis as a function of time and dietary iodine supply: An in vivo model of tumorigenesis in the rat. *Endocrinology,* 143(7), 2584–2592.

Bouquerel, C., Dubrova, A., Hofer, I., Phan, D.T., Bernheim, M., Ladaigue, S., Cavaniol, C., Maddalo, D., Cabel, L., Mechta-Grigoriou, F., Wilhelm, C., Zalcman, G., Parrini, M.C. & Descroix, S. (2023) Bridging the gap between tumor-on-chip and Clinics: A systematic review of 15 years of studies. *Lab on a Chip*, 23(18), 3906–3935.

Boyd, V., Cholewa, O.M. and Papas, K.K., 2008. Limitations in the use of fluorescein diacetate/propidium iodide (FDA/PI) and cell permeable nucleic acid stains for viability measurements of isolated islets of Langerhans. *Current trends in biotechnology and pharmacy*, 2(2), p.66.

Brancato, V., Oliveira, J.M., Correlo, V.M., Reis, R.L. & Kundu, S.C. (2020) Could 3D models of cancer enhance drug screening*? Biomaterials*, 232, 119744.

British Dietetic Association (2021) Iodine Food Fact Sheet. Available at: https://www.bda.uk.com/resource/iodine.html (Accessed: 18 May 2024).

Brito, J.P., Yarur, A.J., Prokop, L.J., McIver, B., Murad, M.H. & Montori, V.M. (2013) Prevalence of thyroid cancer in multinodular goiter versus single nodule: A systematic review and meta-analysis. *Thyroid*, 23(4), 449–455.

Brose, M.S., Nutting, C.M., Jarzab, B., Elisei, R., Siena, S., Bastholt, L., de la Fouchardiere, C., Pacini, F., Paschke, R., Shong, Y.K., Sherman, S.I., Smit, J.W., Chung, J., Kappeler, C., Peña, C., Molnár, I. & Schlumberger, M.J. (2014) Sorafenib in radioactive iodine-refractory, locally advanced or metastatic differentiated thyroid cancer: A randomised, double-blind, phase 3 trial. *The Lancet,* 384(9940), 319–328.

Browning, A.P., Sharp, J.A., Murphy, R.J., Gunasingh, G., Lawson, B., Burrage, K., Haass, N.K. & Simpson, M. (2021) Quantitative analysis of tumour spheroid structure. *eLife,* 10, e73020.

Brüningk, S.C., Rivens, I., Box, C., Oelfke, U. & ter Haar, G. (2020) 3D tumour spheroids for the prediction of the effects of radiation and hyperthermia treatments. *Scientific Reports,* 10(1), 1653.

Buranaamnuay, K. (2021) The MTT assay application to measure the viability of spermatozoa: A variety of the assay protocols. *Open Veterinary Journal*, 11(2), 251.

Byrne, A.T., Alférez, D.G., Amant, F., Annibali, D., Arribas, J., Biankin, A.V., Bruna, A., Budinská, E., Caldas, C., Chang, D.K., Clarke, R.B., Clevers, H., Coukos, G., Dangles-Marie, V., Eckhardt, S.G., Gonzalez-Suarez, E., Hermans, E., Hidalgo, M., Jarzabek, M.A., de Jong, S., Jonkers, J., Kemper, K., Lanfrancone, L., Mælandsmo, G.M., Marangoni, E., Marine, J.-C., Medico, E., Norum, J.H., Palmer, H.G., Peeper, D.S., Pelicci, P.G., Piris-Gimenez, A., Roman-Roman, S., Rueda, O.M., Seoane, J., Serra, V., Soucek, L., Vanhecke, D., Villanueva, A., Vinolo, E., Bertotti, A. & Trusolino, L. (2017) Interrogating open issues in cancer precision medicine with patient-derived xenografts. *Nature Reviews Cancer*, 17(4), 254–268.

Cabanillas, M.E., Ryder, M. and Jimenez, C. (2019) 'Targeted therapy for advanced thyroid cancer: Kinase inhibitors and beyond', *Endocrine Reviews*, 40(6), pp. 1573–1604.

Campos, A. de, Cruz Carvalho, I., Sarmento, S. & Fonseca, T. (2023) Iodine-induced hypothyroidism after chemoembolization with Ethiodized Oil: A Case of failure to escape from Wolff-Chaikoff Effect (WCE*). Cureus.* 15(5), e39352.

Capdevila, J., Mayor, R., Mancuso, F.M., Iglesias, C., Caratù, G., Matos, I., Zafón, C., Hernando, J., Petit, A., Nuciforo, P., Cameselle-Teijeiro, J.M., Álvarez, C., Recio, J.A., Tabernero, J., Matias-Guiu, X., Vivancos, A. & Seoane, J. (2018) Early evolutionary divergence between papillary and anaplastic thyroid cancers. *Annals of Oncology*, 29(6), 1454–1460.

Cappellacci, F., Canu, G., Lai, M., Lori, E., Biancu, M., Boi, F. & Medas, F. (2022) Association between Hashimoto Thyroiditis and differentiated thyroid cancer: A single-center experience. *Frontiers in Oncology*, 12, 959595.

Carragher, N., Piccinini, F., Tesei, A., Jr, O.J., Bickle, M. & Horvath, P. (2018) Concerns, challenges and promises of high-content analysis of 3D cellular models. *Nature Reviews Drug Discovery,* 17(8), 606–606.

Carvalho, D.J., Kip, A.M., Romitti, M., Nazzari, M., Tegel, A., Stich, M., Krause, C., Caiment, F., Costagliola, S., Moroni, L. & Giselbrecht, S. (2023) Thyroid-on-a-chip: An organoid platform for in vitro assessment of endocrine disruption. *Advanced Healthcare Materials,* 12(8), e2201555.

Ceballos, M.P., Angel, A., Delprato, C.B., Livore, V.I., Ferretti, A.C., Lucci, A., Comanzo, C.G., Alvarez, M. de, Quiroga, A.D., Mottino, A.D. & Carrillo, M.C. (2021) SIRTUIN 1 and 2 inhibitors enhance the inhibitory effect of sorafenib in hepatocellular carcinoma cells. *European Journal of Pharmacology*, 892, 173736.

Celano, M., Maggisano, V., Bulotta, S., Allegri, L., Pecce, V., Abballe, L., Damante, G. & Russo, D. (2019) Quercetin improves the effects of sorafenib on growth and migration of thyroid cancer cells. *Endocrine,* 67(2), 496–498.

Chaker, L., Cooper, D.S., Walsh, J.P. & Peeters, R.P. (2024) Hyperthyroidism. *The Lancet*, 403(10428), 768–780.

Chen, D., Tan, Y., Li, Z., Li, W., Yu, L., Chen, W., Liu, Y., Liu, L., Guo, L., Huang, W. & Zhao, Y. (2021) Organoid cultures derived from patients with papillary thyroid cancer. *The Journal of Clinical Endocrinology & Metabolism*, 106(5), 1410–1426.

Chen, D.W., Lang, B.H., McLeod, D.S., Newbold, K. & Haymart, M.R. (2023) Thyroid cancer. *The Lancet*, 401(10387), 1531–1544.

Chen, R., Li, Q., Xu, S., Ye, C., Tian, T., Jiang, Q., Shan, J. & Ruan, J. (2022) Modulation of the tumour microenvironment in hepatocellular carcinoma by tyrosine kinase inhibitors: From modulation to combination therapy targeting the microenvironment. *Cancer Cell International,* 22(1), 73.

Chen, S., Tang, J., Liu, F., Li, W., Yan, T., Shangguan, D., Yang, N. & Liao, D. (2023) Changes of tumor microenvironment in non-small cell lung cancer after TKI treatments. *Frontiers in Immunology*, 14, 1664-3224.

Chen, W., Wang, W., Xie, Z., Centurion, F., Sun, B., Paterson, D.J., Tsao, S.C., Chu, D., Shen, Y., Mao, G. & Gu, Z. (2023) Size-dependent penetration of nanoparticles in tumor spheroids: A multidimensional and Quantitative Study of Transcellular and paracellular pathways. *Small*, 20(8), 2304693.

Chen, X., Li, Y., Yao, T. & Jia, R. (2021) Benefits of zebrafish xenograft models in cancer research. *Frontiers in Cell and Developmental Biology*, 11(9), 616551.

Chen, Y., Gao, D., Liu, H., Lin, S. & Jiang, Y. (2015) Drug cytotoxicity and signaling pathway analysis with three-dimensional tumor spheroids in a microwell-based microfluidic chip for drug screening. *Analytica Chimica Acta*, 898, 85–92.

Cherne, M.D., Sidar, B., Sebrell, T.A., Sanchez, H.S., Heaton, K., Kassama, F.J., Roe, M.M., Gentry, A.B., Chang, C.B., Walk, S.T., Jutila, M., Wilking, J.N. & Bimczok, D. (2021) A Synthetic Hydrogel, VitroGel® organoid-3, improves immune cell-epithelial interactions in a tissue chip co-culture model of human gastric organoids and dendritic cells. *Frontiers in Pharmacology*, 12, 1663-9812

Chew, D., Green, V., Riley, A., England, R.J. & Greenman, J. (2020) The changing face of in vitro culture models for thyroid cancer research: A Systematic Literature Review. *Frontiers in Surgery,* 16(7), 43.

Chidawanyika, T. & Supattapone, S. (2021) Hydrogen peroxide-induced cell death in mammalian cells. *Journal of Cellular Signaling*, 2(3), 206-211.

Chou, R., Dana, T., Haymart, M., Leung, A.M., Tufano, R.P., Sosa, J.A. & Ringel, M.D. (2022) Active surveillance versus thyroid surgery for differentiated thyroid cancer: A systematic review. *Thyroid*, 32(4), 351–367.

Ciampi, R. & Nikiforov, Y.E. (2007) RET/PTC rearrangements and BRAF mutations in thyroid tumorigenesis. *Endocrinology,* 148(3), 936–941.

Cipriani, N.A., Nagar, S., Kaplan, S.P., White, M.G., Antic, T., Sadow, P.M., Aschebrook-Kilfoy, B., Angelos, P., Kaplan, E.L. & Grogan, R.H. (2015) Follicular thyroid carcinoma: How have histologic diagnoses changed in the last half-century and what are the prognostic implications? *Thyroid*, 25(11), 1209–1216.

Cirello, V., Vaira, V., Grassi, E.S., Vezzoli, V., Ricca, D., Colombo, C., Bosari, S., Vicentini, L., Persani, L., Ferrero, S. & Fugazzola, L. (2016) Multicellular spheroids from normal and neoplastic thyroid tissues as a suitable model to test the effects of multikinase inhibitors. *Oncotarget,* 8(6), 9752–9766.

Cléro, E., Ostroumova, E., Demoury, C., Grosche, B., Kesminiene, A., Liutsko, L., Motreff, Y., Oughton, D., Pirard, P., Rogel, A., Van Nieuwenhuyse, A., Laurier, D. & Cardis, E. (2021) Lessons learned from Chernobyl and Fukushima on thyroid cancer screening and recommendations in case of a future nuclear accident. *Environment International*, 146, 106230.

Clevers, H. (2016) Modeling development and disease with organoids. *Cell*, 165(7), 1586–1597.

Coca-Pelaz, A., Shah, J.P., Hernandez-Prera, J.C., Ghossein, R.A., Rodrigo, J.P., Hartl, D.M., Olsen, K.D., Shaha, A.R., Zafereo, M., Suarez, C., Nixon, I.J., Randolph, G.W., Mäkitie, A.A., Kowalski, L.P., Vander Poorten, V., Sanabria, A., Guntinas-Lichius, O., Simo, R., Zbären, P., Angelos, P., Khafif, A., Rinaldo, A. & Ferlito, A. (2020) Papillary thyroid cancer—aggressive variants and impact on management: A narrative review. *Advances in Therapy,* 37(7), 3112–3128.

Cohen, S.M., Mukerji, R., Timmermann, B.N., Samadi, A.K. & Cohen, M.S. (2012) A novel combination of Withaferin A and sorafenib shows synergistic efficacy against both papillary and anaplastic thyroid cancers. *The American Journal of Surgery*, 204(6), 895–901.

Costa, E.C., Moreira, A.F., de Melo-Diogo, D., Gaspar, V.M., Carvalho, M.P. & Correia, I.J. (2016) 3D tumor spheroids: An overview on the tools and techniques used for their analysis. *Biotechnology Advances,* 34(8), 1427–1441.

Cui, X., Hartanto, Y. & Zhang, H. (2017) Advances in multicellular spheroids formation. *Journal of The Royal Society Interface,* 14(127), 20160877.

Dadu, R., Devine, C., Hernandez, M., Waguespack, S.G., Busaidy, N.L., Hu, M.I., Jimenez, C., Habra, M.A., Sellin, R.V., Ying, A.K., Cote, G.J., Sherman, S.I. & Cabanillas, M.E. (2014) Role of salvage targeted therapy in differentiated thyroid cancer patients who failed first-line sorafenib. *The Journal of Clinical Endocrinology & Metabolism*, 99(6), 2086–2094.

Damiati, S., Kompella, U.B., Damiati, S.A. & Kodzius, R. (2018) Microfluidic devices for drug delivery systems and drug screening. *Genes,* 9(2), 103.

De Leo, S., Trevisan, M. and Fugazzola, L. (2020) 'Recent advances in the management of Anaplastic Thyroid Cancer', *Thyroid Research*, 13(1), 17.

de Souza, I.R., Canavez, A.D., Schuck, D.C., Gagosian, V.S., de Souza, I.R., Vicari, T., da Silva Trindade, E., Cestari, M.M., Lorencini, M. & Leme, D.M. (2021) Development of 3D cultures of zebrafish liver and embryo cell lines: A comparison of different spheroid formation methods. *Ecotoxicology*, 30(9), 1893–1909.

Delarue, M., Montel, F., Vignjevic, D., Prost, J., Joanny, J.-F. & Cappello, G. (2014) Compressive stress inhibits proliferation in tumor spheroids through a volume limitation. *Biophysical Journal,* 107(8), 1821–1828.

Derwahl, M. & Nicula, D. (2014) Estrogen and its role in thyroid cancer. *Endocrine Related Cancer,* 21(5), 273-83.

Dini, S., Binder, B.J., Fischer, S.C., Mattheyer, C., Schmitz, A., Stelzer, E.H., Bean, N.G. & Green, J.E. (2016) Identifying the necrotic zone boundary in tumour spheroids with pair-correlation functions. *Journal of The Royal Society Interface*, 13(123), 20160649.

Dominijanni, A.J., Devarasetty, M., Forsythe, S.D., Votanopoulos, K.I. & Soker, S. (2021) Cell viability assays in three-dimensional hydrogels: A comparative study of accuracy. *Tissue Engineering Part C: Methods,* 27(7), 401–410.

Ebrahimi, N., Fardi, E., Ghaderi, H., Palizdar, S., Khorram, R., Vafadar, R., Ghanaatian, M., Rezaei-Tazangi, F., Baziyar, P., Ahmadi, A., Hamblin, M.R. & Aref, A.R. (2023) Receptor tyrosine kinase inhibitors in cancer. *Cellular and Molecular Life Sciences*, 80(4), 104.

Eiermann, N., Stoecklin, G. & Jovanovic, B. (2022) Mitochondrial inhibition by $NaN_3$ induces assembly of eIF2α phosphorylation-independent stress granules in mammalian cells. *International Journal of Molecular Sciences*, 23(10), 5600.

Eilenberger, C., Rothbauer, M., Ehmoser, E.-K., Ertl, P. & Küpcü, S. (2019) Effect of spheroidal age on sorafenib diffusivity and toxicity in a 3D HEPG2 spheroid model. *Scientific Reports,* 9(1), 4863.

Enokida, T. & Tahara, M. (2021) Management of VEGFR-targeted TKI for Thyroid Cancer. *Cancers,* 13(21), 5536.

Fallahi, P., Ferrari, S.M., Santini, F., Corrado, A., Materazzi, G., Ulisse, S., Miccoli, P. & Antonelli, A. (2013) Sorafenib and thyroid cancer. *BioDrugs,* 27(6), 615–628.

Fallahi, P., Mazzi, V., Vita, R., Ferrari, S., Materazzi, G., Galleri, D., Benvenga, S., Miccoli, P. & Antonelli, A. (2015) New therapies for dedifferentiated papillary thyroid cancer. *International Journal of Molecular Sciences*, 16(12), 6153–6182.

Feldt-Rasmussen, U., Effraimidis, G. & Klose, M. (2021) The hypothalamus-pituitary-thyroid (hpt)-axis and its role in physiology and pathophysiology of other hypothalamus-pituitary functions. *Molecular and Cellular Endocrinology*, 525, 111173.

Feng, J., Neuzil, J., Manz, A., Iliescu, C. & Neuzil, P. (2023) Microfluidic trends in drug screening and Drug Delivery. *TrAC Trends in Analytical Chemistry,* 158, 116821.

Feng, K., Ma, R., Zhang, L., Li, H., Tang, Y., Du, G., Niu, D. & Yin, D. (2020) The role of exosomes in thyroid cancer and their potential clinical application. *Frontiers in Oncology*, 10, 2234-943X.

Fernández-Moncada, I. & Barros, L.F. (2014) Non-preferential fuelling of the na+/k+-atpase pump. *Biochemical Journal*, 460(3), 353–361.

Fevre, R., Mary, G., Vertti-Quintero, N., Durand, A., Tomasi, R.F.-X., Del Nery, E. & Baroud, C.N. (2023) Combinatorial drug screening on 3D Ewing sarcoma spheroids using droplet-based microfluidics. *iScience,* 26(5), 106651.

Fierabracci, A., Puglisi, M.A., Giuliani, L., Mattarocci, S. & Gallinella-Muzi, M. (2008) Identification of an adult stem/progenitor cell-like population in the human thyroid. *Journal of Endocrinology,* 198(3), 471–487.

Fierro-Maya, L.F., González, G.G., Rojas Melo, L.J., Cuéllar Cuéllar, A.A., Carreño, A. & Córdoba, C. (2021) Safety and efficacy of sorafenib in patients with advanced thyroid carcinoma: A phase II study (NCT02084732). *Archives of Endocrinology and Metabolism.* 65(4), 404–410.

Fitzgerald, K.A., Malhotra, M., Curtin, C.M., O' Brien, F.J. & O' Driscoll, C.M. (2015) Life in 3D is never flat: 3D models to optimise drug delivery. *Journal of Controlled Release*, 215, 39–54.

Flores-Torres, S., Peza-Chavez, O., Kuasne, H., Munguia-Lopez, J.G., Kort-Mascort, J., Ferri, L., Jiang, T., Rajadurai, C.V., Park, M., Sangwan, V. & Kinsella, J.M. (2021) Alginate–gelatin–Matrigel® hydrogels enable the development and multigenerational passaging of patient-derived 3D bioprinted cancer spheroid models. *Biofabrication,* 13(2), 025001.

Fritschen, A. & Blaeser, A. (2021) Biosynthetic, biomimetic, and self-assembled vascularized organ-on-a-chip systems. *Biomaterials*, 268, 120556.

Fuhrmann, D.C. & Brüne, B. (2017) Mitochondrial composition and function under the control of hypoxia. *Redox Biology*, 12, 208–215.

Gandhirajan, R.K., Rödder, K., Bodnar, Y., Pasqual-Melo, G., Emmert, S., Griguer, C.E., Weltmann, K.-D. & Bekeschus, S. (2018) Cytochrome c oxidase inhibition and cold plasma-derived oxidants synergize in melanoma cell death induction. *Scientific Reports*, 8(1), 12734.

Gaohong, Z. & Lijun, X. (2020) Research progress of DNA methylation in thyroid cancer. *DNA Methylation Mechanism*. 2, 91048.

Garcia, P.L., Miller, A.L. & Yoon, K.J. (2020) Patient-derived xenograft models of pancreatic cancer: Overview and comparison with other types of models. *Cancers,* 12(5), 1327.

Ge, J., Wang, J., Wang, H., Jiang, X., Liao, Q., Gong, Q., Mo, Y., Li, X., Li, G., Xiong, W., Zhao, J. & Zeng, Z. (2020) The braf v600e mutation is a predictor of the effect of radioiodine therapy in Papillary Thyroid Cancer. *Journal of Cancer*, 11(4), 932–939.

Geraldo, M.-N. (2016) Multinodular goiter. National Center for Biotechnology Information. Available online: https://pubmed.ncbi.nlm.nih.gov/25905424/ [Accessed 13/1/2024].

Ghiandai, V., Grassi, E.S., Gazzano, G., Fugazzola, L. & Persani, L. (2024) Characterization of epcam in thyroid cancer biology by three-dimensional spheroids in vitro model. *Cancer Cell International*, 24(1), 196.

Giczewska, A., Pastuszak, K., Houweling, M., Abdul, K.U., Faaij, N., Wedekind, L., Noske, D., Wurdinger, T., Supernat, A. & Westerman, B.A. (2023) Longitudinal drug synergy assessment using convolutional neural network image-decoding of glioblastoma single-spheroid cultures. *Neuro-Oncology Advances*, 5(5), 1.

Giverso, C. & Preziosi, L. (2019) Influence of the mechanical properties of the necrotic core on the growth and remodelling of tumour spheroids. *International Journal of Non-Linear Mechanics,* 108, 20–32.

Gong, L., Giacomini, M.M., Giacomini, C., Maitland, M.L., Altman, R.B. & Klein, T.E. (2017) Pharmgkb summary. *Pharmacogenetics and Genomics*, 27(6), 240–246.

Gorstein, J.L., Bagriansky, J., Pearce, E.N., Kupka, R. & Zimmermann, M.B. (2020) Estimating the health and economic benefits of universal salt iodization programs to correct iodine deficiency disorders. *Thyroid*, 30(12), 1802–1809.

Grimes, D.R., Kelly, C., Bloch, K. & Partridge, M. (2014) A method for estimating the oxygen consumption rate in multicellular tumour spheroids. *Journal of The Royal Society Interface,* 11(92), 20131124.

Groeneweg, S., van Geest, F.S., Peeters, R.P., Heuer, H. & Visser, W.E. (2019) Thyroid hormone transporters. *Endocrine Reviews*, 41(2), 146–201.

Guigon, C.J. & Cheng, S. (2009) Novel non-genomic signaling of thyroid hormone receptors in thyroid carcinogenesis. *Molecular and Cellular Endocrinology*, 308(1–2), 63–69.

Gunti, S., Hoke, A.T.K., Vu, K.P. & London, N.R. (2021) Organoid and spheroid tumor models: Techniques and applications. *Cancers,* 13(4), 874.

Guzy, R.D. & Schumacker, P.T. (2006) Oxygen sensing by mitochondria at complex III: The paradox of increased reactive oxygen species during hypoxia. *Experimental Physiology,* 91(5), 807–819.

Haase, J. (2020.) Dissertation. IGF2BP1 is the First Positive Marker for Anaplastic Thyroid Carcinoma and an Enhancer of a Targetable Gene Expression Signature. Available online:https://opendata.unihalle.de/bitstream/1981185920/35512/1/Dissertation_JacobHaase_2.pdf [Accessed 30/5/2024].

Habanjar, O., Diab-Assaf, M., Caldefie-Chezet, F. & Delort, L. (2021) 3D cell culture systems: Tumor application, advantages, and disadvantages. *International Journal of Molecular Sciences,* 22(22), 12200.

Hagemann, J., Jacobi, C., Hahn, M., Schmid, V., Welz, C., Schwenk-Zieger, S., Stauber, R., Baumeister, P., & Becker, S. (2017). Spheroid-based 3D cell cultures enable personalized therapy testing and drug discovery in head and neck cancer. *Anticancer Research*, 37(5), 2201–2210.

Hamilton, G. & Rath, B. (2019) Role of circulating tumor cell spheroids in drug resistance. *Cancer Drug Resistance 37*(5), 2201-2210.

Han, S.J., Kwon, S. & Kim, K.S. (2021) Challenges of applying multicellular tumor spheroids in preclinical phase. *Cancer Cell International*, 21(1), 152.

Harrison, S.P., Baumgarten, S.F., Verma, R., Lunov, O., Dejneka, A. & Sullivan, G.J. (2021) Liver organoids: Recent developments, limitations and potential. *Frontiers in Medicine*, 5(8), 574047.

Hofmann, B., Zinöcker, S., Holm, S., Lewis, J. & Kavouras, P. (2022) Organoids in the clinic: A systematic review of outcomes. *Cells Tissues Organs*, 212(6), 499–511.

Hofmann, M.-C., Kunnimalaiyaan, M., Wang, J.R., Busaidy, N.L., Sherman, S.I., Lai, S., Zafereo, M. & Cabanillas, M.E. (2022) Molecular mechanisms of resistance to kinase inhibitors in thyroid cancers. *Endocrine-Related Cancer* 29(11), 1351-0088.

Horgan, D., Führer-Sakel, D., Soares, P., Alvarez, C.V., Fugazzola, L., Netea-Maier, R.T., Jarzab, B., Kozaric, M., Bartes, B., Schuster-Bruce, J., Dal Maso, L., Schlumberger, M. & Pacini, F. (2022) Tackling thyroid cancer in Europe—the challenges and opportunities. *Healthcare,* 10(9), 1621.

Horn-Ross, P.L. (2001) Phytoestrogen consumption and breast cancer risk in a multiethnic population: The Bay Area Breast Cancer study. *American Journal of Epidemiology*, 154(5), 434–441.

Hsiao, V., Light, T.J., Adil, A.A., Tao, M., Chiu, A.S., Hitchcock, M., Arroyo, N., Fernandes-Taylor, S. & Francis, D.O. (2022) Complication rates of total thyroidectomy vs hemithyroidectomy for treatment of papillary thyroid Microcarcinoma. *JAMA Otolaryngology–Head & Neck Surgery*, 148(6), 531.

Hu, J., Liu, K., Ghosh, C., Khaket, T.P., Shih, H. & Kebebew, E. (2024) Anaplastic thyroid cancer spheroids as preclinical models to Test Therapeutics. *Journal of Experimental & Clinical Cancer Research,* 43(1), 85.

Hu, X., Wang, X., Liang, Y., Chen, X., Zhou, S., Fei, W., Yang, Y. & Que, H. (2022) Cancer risk in hashimoto's thyroiditis: A systematic review and meta-analysis. *Frontiers in Endocrinology*, 13, 937871.

Huang, W., Xing, Y., Zhu, L., Zhuo, J. & Cai, M. (2021) Sorafenib derivatives-functionalized gold nanoparticles confer protection against tumor angiogenesis and proliferation via suppression of EGFR and VEGFR-2. *Experimental Cell Research*, 406(1), 112633.

Huch, M., Knoblich, J.A., Lutolf, M.P. & Martinez-Arias, A. (2017) The hope and the hype of Organoid Research*. Development*, 144(6), 938–941.

Hughes, C.S., Postovit, L.M. and Lajoie, G.A. (2010) 'Matrigel: A complex protein mixture required for optimal growth of Cell Culture', *PROTEOMICS,* 10(9), 1886–1890.

Huh, K.-Y., Hwang, S., Park, S.-Y., Lim, H.-J., Jin, M., Oh, J., Yu, K.-S. & Chung, J.-Y. (2021) Population pharmacokinetic modelling and simulation to determine the optimal dose of nanoparticulated sorafenib to the reference sorafenib. *Pharmaceutics,* 13(5), 629.

Hutchinson, L. and Kirk, R. (2011) 'High drug attrition rates—where are we going wrong?', *Nature Reviews Clinical Oncology*, 8(4), 189–190.

Iglesias, M.L., Schmidt, A., Ghuzlan, A.A., Lacroix, L., Vathaire, F. de, Chevillard, S. & Schlumberger, M. (2017) Radiation exposure and thyroid cancer: A Review*. Archives of Endocrinology and Metabolism,* 61(2), 180–187.

Ingber, D.E. (2022) Human organs-on-chips for disease modelling, drug development and Personalized Medicine. *Nature Reviews Genetics*, 23(8), 467–491.

Inskip, P.D. (2001) Thyroid cancer after radiotherapy for childhood cancer**. Medical and Pediatric Oncology,* 36(5), 568–573.

Ishiguro, T., Ohata, H., Sato, A., Yamawaki, K., Enomoto, T. & Okamoto, K. (2017) Tumor-derived spheroids: Relevance to cancer stem cells and clinical applications. *Cancer Science,* 108(3), 283–289.

Jabs, J., Zickgraf, F.M., Park, J., Wagner, S., Jiang, X., Jechow, K., Kleinheinz, K., Toprak, U.H., Schneider, M.A., Meister, M., Spaich, S., Sütterlin, M., Schlesner, M., Trumpp, A., Sprick, M., Eils, R. & Conrad, C. (2017) Screening drug effects in patient-derived cancer cells links organoid responses to genome alterations. *Molecular Systems Biology*, 13(11), 955.

Jannin, A., Escande, A., Al Ghuzlan, A., Blanchard, P., Hartl, D., Chevalier, B., Deschamps, F., Lamartina, L., Lacroix, L., Dupuy, C., Baudin, E., Do Cao, C. & Hadoux, J. (2022) Anaplastic thyroid carcinoma: An update. *Cancers,* 14(4), 1061.

Jannin, A., Penel, N., Ladsous, M., Vantyghem, M.C. & Do Cao, C. (2019) Tyrosine kinase inhibitors and immune checkpoint inhibitors-induced thyroid disorders. *Critical Reviews in Oncology/Hematology,* 141, 23–35.

Jentzsch, V., Osipenko, L., Scannell, J.W. & Hickman, J.A. (2023) Costs and causes of oncology drug attrition with the example of insulin-like growth factor-1 receptor inhibitors. *JAMA Network Open*, 6(7).

Ji, D., Kamalden, T.A., del Olmo-Aguado, S. & Osborne, N.N. (2011) Light- and $NaN_3$-induced death of RGC-5 cells in culture occurs via different mechanisms. *Apoptosis,* 16(4), 425–437.

Jingtai, Z., Linfei, H., Yuyang, Q., Ning, K., Xinwei, Y., Xin, W., Xianhui, R., Dongmei, H., Weiwei, Y., Xiangrui, M., Tianze, Z., Wei, W. & Xiangqian, Z. (2023) Targeting Aurora-a inhibits tumor progression and sensitizes thyroid carcinoma to sorafenib by decreasing PFKFB3-mediated glycolysis. *Cell Death & Disease,* 14(3), 224.

Jonklaas, J. (2021) Optimal Thyroid Hormone Replacement. *Endocrine Reviews*, 43(2), 366–404.

Juan, C.A., Pérez de la Lastra, J.M., Plou, F.J. & Pérez-Lebeña, E. (2021) The chemistry of reactive oxygen species (ROS) revisited: Outlining their role in biological macromolecules (DNA, lipids and proteins) and induced pathologies. *International Journal of Molecular Sciences,* 22(9), 4642.

Jung, Y.H., Choi, D.-H., Park, K., Lee, S., Kim, J., Kim, H., Jeong, H.-W., Yang, J.H., Kim, J.-A., Chung, S. & Min, B.S. (2021) Drug screening by uniform patient derived colorectal cancer hydro-organoids. *Biomaterials*, 276, 121004.

Kaliszewski, K., Diakowska, D., Wojtczak, B., Forkasiewicz, Z., Pupka, D., Nowak, Ł. & Rudnicki, J. (2019) Which papillary thyroid microcarcinoma should be treated as “true cancer” and which as “precancer”? *World Journal of Surgical Oncology*, 17(1), e0244930.

Kamiloglu, S., Sari, G., Ozdal, T. & Capanoglu, E. (2020) Guidelines for cell viability assays. *Food Frontiers*, 1(3), 332–349.

Kapral, N. & Khot, R. (2022) Thyroid anatomy and ultrasound evaluation. *Techniques in Vascular and Interventional Radiology,* 25(2), 100818.

Karapanou, O., Simeakis, G., Vlassopoulou, B., Alevizaki, M. & Saltiki, K. (2022) Advanced Rai-refractory thyroid cancer: An update on treatment perspectives. *Endocrine-Related Cancer,* 29(5), 57-66.

Kasemsiri, P., Chaisakgreenon, P., Vatanasapt, P., Laohasiriwong, S., Teeramatwanich, W., Thongrong, C., Ratanaanekchai, T. & Suetrong, S. (2021) Survival benefit of intervention treatment in advanced anaplastic thyroid cancer. *International Journal of Surgical Oncology,* 2021, 1–8.

Kelm, J.M., Timmins, N.E., Brown, C.J., Fussenegger, M. & Nielsen, L.K. (2003) Method for generation of homogeneous multicellular tumor spheroids applicable to a wide variety of cell types. *Biotechnology and Bioengineering,* 83(2), 173–180.

Kim, J., Koo, B.-K. & Knoblich, J.A. (2020) Human organoids: Model Systems for Human Biology and Medicine. *Nature Reviews Molecular Cell Biology*, 21(10), 571–584.

Kim, M.-H., Lee, T.H., Lee, J.S., Lim, D.-J. & Lee, P.C.-W. (2020) HIF-1α inhibitors could successfully inhibit the progression of differentiated thyroid cancer in vitro. *Pharmaceuticals*, 13(9), 208.

Kimlin, L.C., Casagrande, G. & Virador, V.M. (2011) In vitro three-dimensional (3D) models in cancer research: An update. *Molecular Carcinogenesis*, 52(3), 167–182.

Kiriiri, G.K., Njogu, P.M. & Mwangi, A.N. (2020) Exploring different approaches to improve the success of drug discovery and Development Projects: A Review. *Future Journal of Pharmaceutical Sciences,* 6(1), 27.

Koibuchi, N. (2018) Molecular mechanisms of thyroid hormone synthesis and secretion. *Endocrinology*, 70(11), 1844-8.

Kuczynski, E.A. & Reynolds, A.R. (2019) Vessel co-option and resistance to anti-angiogenic therapy. *Angiogenesis*, 23(1), 55–74.

Kuczynski, E.A., Yin, M., Bar-Zion, A., Lee, C.R., Butz, H., Man, S., Daley, F., Vermeulen, P.B., Yousef, G.M., Foster, F.S., Reynolds, A.R. & Kerbel, R.S. (2016) Co-option of liver vessels and not sprouting angiogenesis drives acquired sorafenib resistance in hepatocellular carcinoma. *Journal of the National Cancer Institute,* 108(8), djw030.

Kurmann, A.A., Serra, M., Hawkins, F., Rankin, S.A., Mori, M., Astapova, I., Ullas, S., Lin, S., Bilodeau, M., Rossant, J., Jean, J.C., Ikonomou, L., Deterding, R.R., Shannon, J.M., Zorn, A.M., Hollenberg, A.N. & Kotton, D.N. (2015) Regeneration of thyroid function by transplantation of differentiated pluripotent stem cells. *Cell Stem Cell*, 17(5), 527–542.

Kwapiszewska, K., Michalczuk, A., Rybka, M., Kwapiszewski, R. & Brzózka, Z. (2014) A microfluidic-based platform for tumour spheroid culture, monitoring and drug screening. *Lab Chip*, 14(12), 2096–2104.

Laetitia, G., Sven, S. & Fabrice, J. (2020) Combinatorial therapies in thyroid cancer: An overview of preclinical and clinical progresses. *Cells*, 9(4), 830.

Lapizco-Encinas, B.H. & Zhang, Y.V. (2022) Microfluidic systems in clinical diagnosis. *ELECTROPHORESIS*, 44(1–2), 217–245.

Larsson, P., Engqvist, H., Biermann, J., Werner Rönnerman, E., Forssell-Aronsson, E., Kovács, A., Karlsson, P., Helou, K. & Parris, T.Z. (2020) Optimization of cell viability assays to improve replicability and reproducibility of cancer drug sensitivity screens. *Scientific Reports*, 10(1), 5798.

Lasolle, H., Schiavo, A., Tourneur, A., Gillotay, P., de Faria da Fonseca, B., Ceolin, L., Monestier, O., Aganahi, B., Chomette, L., Kizys, M.M., Haenebalcke, L., Pieters, T., Goossens, S., Haigh, J., Detours, V., Maia, A.L., Costagliola, S. & Romitti, M. (2023) Dual targeting of MAPK and PI3K pathways unlocks redifferentiation of braf-mutated thyroid cancer organoids. *Oncogene*, 43(3), 155–170.

Lee, J.M., Park, D.Y., Yang, L., Kim, E.-J., Ahrberg, C.D., Lee, K.-B. & Chung, B.G. (2018) Generation of uniform-sized multicellular tumor spheroids using hydrogel microwells for Advanced Drug Screening. *Scientific Reports*, 8(1), 17145.

Lee, M.A., Bergdorf, K.N., Phifer, C.J., Jones, C.Y., Byon, S.Y., Sawyer, L.M., Bauer, J.A. & Weiss, V.L. (2020) Novel three-dimensional cultures provide insights into thyroid cancer behavior. *Endocrine-Related Cancer,* 27(2), 111–121.

Lee, S.-A., No, D.Y., Kang, E., Ju, J., Kim, D.-S. & Lee, S.-H. (2013) Spheroid-based three-dimensional liver-on-a-chip to investigate hepatocyte–hepatic stellate cell interactions and flow effects. *Lab on a Chip*, 13(18), 3529.

Lee, S.H., Hu, W., Matulay, J.T., Silva, M.V., Owczarek, T.B., Kim, K., Chua, C.W., Barlow, L.J., Kandoth, C., Williams, A.B., Bergren, S.K., Pietzak, E.J., Anderson, C.B., Benson, M.C., Coleman, J.A., Taylor, B.S., Abate-Shen, C., McKiernan, J.M., Al-Ahmadie, H., Solit, D.B. & Shen, M.M. (2018) Tumor evolution and drug response in patient-derived organoid models of bladder cancer. *Cell*, 173(2).

LeSavage, B.L., Suhar, R.A., Broguiere, N., Lutolf, M.P. & Heilshorn, S.C. (2021) Next-generation cancer organoids. *Nature Materials*, 21(2), 143–159.

Levin, G., Zuber, S.M., Squillaro, A.I., Sogayar, M.C., Grikscheit, T.C. & Carreira, A.C. (2020) R-Spondin 1 (RSPO1) increases mouse intestinal organoid unit size and survival in vitro and improves tissue-engineered small intestine formation in vivo. *Frontiers in Bioengineering and Biotechnology*, 5(8), 476.

Li, Y., Gao, Z. & Qu, X. (2015) The adverse effects of sorafenib in patients with advanced cancers. *Basic & Clinical Pharmacology & Toxicology*, 116(3), 216–221.

Liang, J., Qian, J., Yang, L., Chen, X., Wang, X., Lin, X., Wang, X. & Zhao, B. (2022) Modeling human thyroid development by fetal tissue-derived organoid culture. *Advanced Science,* 9(9), 2105568.

Lin, S., Yeh, C., Huang, Y., Chou, T. & Wong, R.J. (2021) Therapeutic inhibition of polo-like kinases in Anaplastic Thyroid Cancer. *Cancer Science*, 112(2), 803–814.

Lin, S.-F., Lin, J.-D., Hsueh, C., Chou, T.-C. & Wong, R.J. (2018) Potent effects of roniciclib alone and with sorafenib against well-differentiated thyroid cancer. *Endocrine-Related Cancer*, 25(10), 853–864.

Liu, C., Liu, Z., Zhao, H., Cao, Y., Lin, Y. & Li, X. (2021) A VEGFR2 antagonist inhibits cell proliferation, migration, and invasion by blocking the PI3K-akt and MAPK signaling pathways in thyroid cancer. *Adv. Funct. Mater,* 30, 2003619.

Liu, H., Yang, D., Li, L., Tu, Y., Chen, C., & Sun, S. (2020). Appraisal of radioiodine refractory thyroid cancer: advances and challenges. *American journal of cancer research*, 10(7), 1923–1936.

Liu, J., Liu, Y., Lin, Y. & Liang, J. (2019) Radioactive iodine-refractory differentiated thyroid cancer and redifferentiation therapy. *Endocrinology and Metabolism*, 34(3), 215.

Liu, J., Xu, T., Ma, L. & Chang, W. (2021) Signal pathway of estrogen and estrogen receptor in the development of thyroid cancer. *Frontiers in Oncology*, 11, 593479.

Liu, T.-R., Xiao, Z.-W., Xu, H.-N., Long, Z., Wei, F.-Q., Zhuang, S.-M., Sun, X.-M., Xie, L.-E., Mu, J.-S., Yang, A.-K., Zhang, G.-P. & Fan, Y. (2016) Treatment and prognosis of anaplastic thyroid carcinoma: A clinical study of 50 cases. *PLOS ONE,* 11(10), e0164840.

Liu, Z., Delavan, B., Roberts, R. & Tong, W. (2017) Lessons learned from two decades of anticancer drugs. *Trends in Pharmacological Sciences,* 38(10), 852–872.

Lukowski, J.K. & Hummon, A.B. (2019) Quantitative evaluation of liposomal doxorubicin and its metabolites in spheroids. *Analytical and Bioanalytical Chemistry*, 411(27), 7087–7094.

Luo, H., Xia, X., Kim, G.D., Liu, Y., Xue, Z., Zhang, L., Shu, Y., Yang, T., Chen, Y., Zhang, S., Chen, H., Zhang, W., Li, R., Tang, H., Dong, B., Fu, X., Cheng, W., Zhang, W., Yang, L., Peng, Y., Dai, L., Hu, H., Jiang, Y., Gong, C., Hu, Y., Zhu, J., Li, Z., Caulin, C., Wei, T., Park, J. & Xu, H. (2021) Characterizing Dedifferentiation of thyroid cancer by Integrated Analysis. *Science Advances*, 7(31), 2003619.

Luo, Y., Kawashima, A., Ishido, Y., Yoshihara, A., Oda, K., Hiroi, N., Ito, T., Ishii, N. & Suzuki, K. (2014) Iodine excess as an environmental risk factor for autoimmune thyroid disease. *International Journal of Molecular Sciences,* 15(7), 12895–12912.

Ma, L., Liu, W., Xu, A., Ji, Q., Ma, Y., Tai, Y., Wang, Y., Shen, C., Liu, Y., Wang, T., Han, J. & Zhao, C. (2020) Activator of thyroid and retinoid receptor increases sorafenib resistance in hepatocellular carcinoma by facilitating the Warburg effect. *Cancer Science*, 111(6), 2028–2040.

Mass, T., Drake, J.L., Haramaty, L., Rosenthal, Y., Schofield, O.M., Sherrell, R.M. & Falkowski, P.G. (2012) Aragonite precipitation by "proto-polyps" in Coral cell cultures. *PLoS ONE*, 7(4), e35049.

Matsui, T. and Shinozawa, T. (2021) 'Human organoids for Predictive Toxicology Research and drug development'*, Frontiers in Genetics*, 12, 767621.

Mayson, S.E., Chan, C.M. and Haugen, B.R. (2021) 'Tailoring the approach to radioactive iodine treatment in thyroid cancer', *Endocrine-Related Cancer*, 28(10), 125-140.

McCain J. (2013). The MAPK (ERK) Pathway: Investigational Combinations for the Treatment Of BRAF-Mutated Metastatic Melanoma. *P & T : a peer-reviewed journal for formulary management,* 38(2), 96–108.

Mehta, V., Vilikkathala Sudhakaran, S., Nellore, V., Madduri, S. & Rath, S.N. (2024) 3D stem-like spheroids-on-a-chip for personalized combinatorial drug testing in oral cancer. *Journal of Nanobiotechnology*, 22(1), 344.

Melissaridou, S., Wiechec, E., Magan, M., Jain, M.V., Chung, M.K., Farnebo, L. & Roberg, K. (2019) The effect of 2D and 3D cell cultures on treatment response, EMT profile and stem cell features in head and neck cancer. *Cancer Cell International*, 19(1), 16.

Miao, Y., Ha, A., de Lau, W., Yuki, K., Santos, A.J.M., You, C., Geurts, M.H., Puschhof, J., Pleguezuelos-Manzano, C., Peng, W.C., Senlice, R., Piani, C., Buikema, J.W., Gbenedio, O.M., Vallon, M., Yuan, J., de Haan, S., Hemrika, W., Rösch, K., Dang, L.T., Baker, D., Ott, M., Depeille, P., Wu, S.M., Drost, J., Nusse, R., Roose, J.P., Piehler, J., Boj, S.F., Janda, C.Y., Clevers, H., Kuo, C.J. & Garcia, K.C. (2020) Next-generation surrogate WNTS support organoid growth and Deconvolute frizzled pleiotropy in vivo. *Cell Stem Cell,* 27(5), 840-851.

Mishra, A., Kai, R., Atkuru, S., Dai, Y., Piccinini, F., Preshaw, P.M. & Sriram, G. (2023) Fluid flow-induced modulation of viability and osteodifferentiation of periodontal ligament stem cell spheroids-on-chip. *Biomaterials Science*, 11(22), 7432–7444.

Mortensen, A.C., Berglund, H., Hariri, M., Papalanis, E., Malmberg, C. & Spiegelberg, D. (2023) Combination therapy of tyrosine kinase inhibitor sorafenib with the hsp90 inhibitor onalespib as a novel treatment regimen for thyroid cancer. *Scientific Reports*, 13(1), 16844.

Mortensen, A.C.L., Imgenberg-Kreuz, J., Spiegelberg, D., Botling, J. & Nestor, M. (2023) Utilizing CD44V6 and V600EBRAF-mutation for in vitro targeted combination therapy of thyroid carcinomas. *Heliyon*, 9(12), e22594.

Moshksayan, K., Kashaninejad, N., Warkiani, M.E., Lock, J.G., Moghadas, H., Firoozabadi, B., Saidi, M.S. & Nguyen, N.-T. (2018) Spheroids-on-a-chip: Recent advances and design considerations in microfluidic platforms for spheroid formation and culture. *Sensors and Actuators B: Chemical*, 263, 151–176.

Moya-Garcia, C.R., Okuyama, H., Sadeghi, N., Li, J., Tabrizian, M. & Li-Jessen, N.Y. (2022) In vitro models for head and neck cancer: Current status and future perspective. *Frontiers in Oncology,* 3(12), 960340.

Naoum, G.E., Morkos, M., Kim, B. & Arafat, W. (2018) Novel targeted therapies and immunotherapy for advanced thyroid cancers. *Molecular Cancer*, 17(1), 51.

Nath, S. & Devi, G.R. (2016) Three-dimensional culture systems in cancer research: Focus on tumor spheroid model. *Pharmacology & Therapeutics*, 163, 94–108.

National Cancer Institute (2024) An interactive website for SEER cancer statistics. Available online: [https://seer.cancer.gov/statistics-network/explorer/ [Accessed 21 May 2024].

NHS (2023) Causes of an overactive thyroid. NHS choices. Available online: https://www.nhs.uk/conditions/overactive-thyroid-hyperthyroidism/ [Accessed 16/05/2024].

Niciporuka, R., Nazarovs, J., Ozolins, A., Narbuts, Z., Miklasevics, E. & Gardovskis, J. (2021) Can we predict differentiated thyroid cancer behavior? role of genetic and molecular markers. *Medicina*, 57(10), 1131.

Nilsson, M. & Fagman, H. (2017) Development of the thyroid gland. *Development*, 144(12), 2123–2140.

North, A.J. (2006) Seeing is believing? A beginners' guide to practical pitfalls in image acquisition. *Journal of Cell Biology*, 172(1), 9–18.

Nuciforo, S., Fofana, I., Matter, M.S., Blumer, T., Calabrese, D., Boldanova, T., Piscuoglio, S., Wieland, S., Ringnalda, F., Schwank, G., Terracciano, L.M., Ng, C.K.Y. & Heim, M.H. (2018) Organoid models of human liver cancers derived from tumor needle biopsies. *Cell Reports*, 24(5), 1363–1376.

Nunes, A.S., Barros, A.S., Costa, E.C., Moreira, A.F. & Correia, I.J. (2018) 3D tumor spheroids as in vitro models to mimic in vivo human solid tumors resistance to therapeutic drugs. *Biotechnology and Bioengineering*, 116(1), 206–226.

Oba, T., Chino, T., Soma, A., Shimizu, T., Ono, M., Ito, T., Kanai, T., Maeno, K. & Ito, K. (2020) Comparative efficacy and safety of tyrosine kinase inhibitors for thyroid cancer: A systematic review and meta-analysis. *Endocrine Journal*, 67(12), 1215–1226.

Ogundipe, V.M.L., Groen, A.H., Hosper, N., Nagle, P.W.K., Hess, J., Faber, H., Jellema, A.L., Baanstra, M., Links, T.P., Unger, K., Plukker, J.T.M. & Coppes, R.P. (2021) Generation and differentiation of adult tissue-derived human thyroid organoids. *Stem Cell Reports,* 16(4), 913–925.

Oh, J.M., Gangadaran, P., Rajendran, R.L., Hong, C.M., Lee, J. & Ahn, B.-C. (2022) Different expression of thyroid-specific proteins in thyroid cancer cells between 2-dimensional (2D) and 3-dimensional (3D) culture environment. *Cells*, 11(22), 3559.

Padera, T.P., Stoll, B.R., Tooredman, J.B., Capen, D., Tomaso, E. di & Jain, R.K. (2004) Cancer cells compress intratumour vessels. *Nature*, 427(6976), 695–695.

Pavlacky, J. & Polak, J. (2020) Technical feasibility and physiological relevance of hypoxic cell culture models. *Frontiers in Endocrinology*, 21(11), 57.

Pavlidis, E., Galanis, I. & Pavlidis, T. (2023) Update on current diagnosis and management of anaplastic thyroid carcinoma. *World Journal of Clinical Oncology*, 14(12), 570–583.

Petreus, T., Kostrzewski, T., Singh, D. & Hughes, D. (2022) Abstract 182: Bridging Gaps in Translational biology: Exploring pharmacokinetic/pharmacodynamic/efficacy relationships and combination treatments in 3D tumor models using a microphysiological system. *Cancer Research,* 82(12), 182–182.

Pinto, B., Henriques, A.C., Silva, P.M. & Bousbaa, H. (2020) Three-dimensional spheroids as in vitro preclinical models for cancer research. *Pharmaceutics*, 12(12), 1186.

Prabhash, K., Saha, S., Joshi, A., Noronha, V., Patil, V., Menon, N., Singh, A., Shetty, O., Mittal, N., Chandrani, P. & Chougule, A. (2022) NRAS mutation in differentiated thyroid cancer. *Cancer Research, Statistics, and Treatment*, 5(4), 722.

Rahbari, R., Zhang, L. & Kebebew, E. (2010) Thyroid cancer gender disparity. *Future Oncology*, 6(11), 1771–1779.

Ralli, M., Angeletti, D., Fiore, M., D'Aguanno, V., Lambiase, A., Artico, M., de Vincentiis, M. & Greco, A. (2020) Hashimoto's thyroiditis: An update on pathogenic mechanisms, diagnostic protocols, therapeutic strategies, and potential malignant transformation. *Autoimmunity Reviews,* 19(10), 102649.

Raman, P. & Koenig, R.J. (2014) Pax-8–PPAR-γ fusion protein in thyroid carcinoma. *Nature Reviews Endocrinology*, 10(10), 616–623.

Ransy, C., Vaz, C., Lombès, A. & Bouillaud, F. (2020) Use of H2O2 to cause oxidative stress, the catalase issue. *International Journal of Molecular Sciences*, 21(23), 9149.

Rao, S.N. & Smallridge, R.C. (2023) Anaplastic Thyroid Cancer: An update. Best Practice & *Research Clinical Endocrinology & Metabolism*, 37(1), 101678.

Ravera, S., Nicola, J.P., Salazar-De Simone, G., Sigworth, F.J., Karakas, E., Amzel, L.M., Bianchet, M.A. & Carrasco, N. (2022) Structural insights into the mechanism of the sodium/iodide symporter. *Nature*, 612(7941), 795–801.

Ravera, S., Reyna-Neyra, A., Ferrandino, G., Amzel, L.M. & Carrasco, N. (2017) The sodium/iodide symporter (NIS): Molecular physiology and preclinical and clinical applications. *Annual Review of Physiology,* 79(1), 261–289.

Ravi, N., Yang, M., Mylona, N., Wennerberg, J. & Paulsson, K. (2020) Global RNA expression and DNA methylation patterns in primary anaplastic thyroid cancer. *Cancers*, 12(3), 680.

Ren, X., Chen, W., Yang, Q., Li, X. & Xu, L. (2022) Patient-derived cancer organoids for drug screening: Basic Technology and Clinical Application. *Journal of Gastroenterology and Hepatology,* 37(8), 1446–1454.

Resende de Paiva, C., Grønhøj, C., Feldt-Rasmussen, U. & von Buchwald, C. (2017) Association between Hashimoto's thyroiditis and thyroid cancer in 64,628 patients. *Frontiers in Oncology,* 10(7), 53.

Reyna-Neyra, A., Jung, L., Chakrabarti, M., Suárez, M.X., Amzel, L.M. & Carrasco, N. (2021) The iodide transport defect-causing Y348D mutation in the na+/i− symporter renders the protein intrinsically inactive and impairs its targeting to the plasma membrane. *Thyroid*. 31(8), 1272-1281.

Reynolds, D.S., Tevis, K.M., Blessing, W.A., Colson, Y.L., Zaman, M.H. & Grinstaff, M.W. (2017) Breast cancer spheroids reveal a differential cancer stem cell response to chemotherapeutic treatment. *Scientific Reports*, 7(1), 10382.

Riesco-Eizaguirre, G., Santisteban, P. & De la Vieja, A. (2021) The complex regulation of NIS expression and activity in thyroid and extrathyroidal tissues. *Endocrine-Related Cancer,* 28(10), 141-165.

Riley, A., Green, V., Cheah, R., McKenzie, G., Karsai, L., England, J. & Greenman, J. (2019) A novel microfluidic device capable of maintaining functional thyroid carcinoma specimens ex vivo provides a new drug screening platform. *BMC Cancer*, 19(1), 259.

Riss, T., Valley, M., Kupcho, K., Zimprich, C., Leippe, D., Niles, A., Vidugiriene, J., Cali, J., Kelm, J., Moritz, W. & Lazar, D. (2014) Validation of in vitro assays to measure cytotoxicity in 3D cell cultures*. Toxicology Letters*, 229.

Rodríguez-Hernández, M.A., Chapresto-Garzón, R., Cadenas, M., Navarro-Villarán, E., Negrete, M., Gómez-Bravo, M.A., Victor, V.M., Padillo, F.J. & Muntané, J. (2020) Differential effectiveness of tyrosine kinase inhibitors in 2D/3D culture according to cell differentiation, p53 status and mitochondrial respiration in liver cancer cells. *Cell Death & Disease,* 11(5), 339.

Romitti, M., Tourneur, A., de Faria da Fonseca, B., Doumont, G., Gillotay, P., Liao, X.-H., Eski, S.E., Van Simaeys, G., Chomette, L., Lasolle, H., Monestier, O., Kasprzyk, D.F., Detours, V., Singh, S.P., Goldman, S., Refetoff, S. & Costagliola, S. (2022) Transplantable human thyroid organoids generated from embryonic stem cells to rescue hypothyroidism. *Nature Communications*, 13(1), 7057.

Rossi, G., Manfrin, A. and Lutolf, M.P. (2018) 'Progress and potential in organoid research', *Nature Reviews Genetics*, 19(11), pp. 671–687.

Ruan, M., Liu, M., Dong, Q. & Chen, L. (2015) Iodide- and glucose-handling gene expression regulated by sorafenib or cabozantinib in papillary thyroid cancer. *The Journal of Clinical Endocrinology & Metabolism,* 100(5), 1771–1779.

Ryu, N.-E., Lee, S.-H. & Park, H. (2019) Spheroid culture system methods and applications for mesenchymal stem cells. *Cells*, 8(12), 1620.

Saiselet, M., Floor, S., Tarabichi, M., Dom, G., Hébrant, A., van Staveren, W.C. & Maenhaut, C. (2012) Thyroid cancer cell lines: An overview. *Frontiers in Endocrinology*, 16(3), 133.

Sakalem ME, De Sibio MT, da Costa FAdS, de Oliveira M. (2021) Historical evolution of spheroids and organoids, and possibilities of use in life sciences and medicine, *Biotechnology Journal*, 16(5), e2000463.

Samimi, H., Atlasi, R., Parichehreh-Dizaji, S., Khazaei, S., Akhavan Rahnama, M., Seifirad, S. & Haghpanah, V. (2021) A systematic review on thyroid organoid models: Time-trend and its achievements. *American Journal of Physiology-Endocrinology and Metabolism*, 320(3), 581-590.

Sant, S. & Johnston, P.A. (2017) The production of 3D tumor spheroids for Cancer Drug Discovery. Drug Discovery Today: *Technologies*, 23, 27–36.

Santoro, M., Moccia, M., Federico, G. & Carlomagno, F. (2020) Ret Gene Fusions in malignancies of the thyroid and other tissues. *Genes*, 11(4), 424.

Sarıyar, E., Karpat, O., Sezan, S., Baylan, S.M., Kıpçak, A., Guven, K., Erdal, E. & Fırtına Karagonlar, Z. (2023) EGFR and Lyn inhibition augments regorafenib induced cell death in sorafenib resistant 3D tumor spheroid model. *Cellular Signalling*, 105, 110608.

Scalise, M., Marino, F., Salerno, L., Cianflone, E., Molinaro, C., Salerno, N., De Angelis, A., Viglietto, G., Urbanek, K. & Torella, D. (2021) From spheroids to organoids: The next generation of model systems of human cardiac regeneration in a Dish. *International Journal of Molecular Sciences*, 22(24), 13180.

Scarlat, A. (1970) Animal-free matrix for organoids culturing. Utrecht University Student Theses Repository Home. Available online: https://studenttheses.uu.nl/handle/20.500.12932/43842 [Accessed 9/7/2024].

Schmidbauer, B., Menhart, K., Hellwig, D. & Grosse, J. (2017) Differentiated thyroid cancer—treatment: State of the art. *International Journal of Molecular Sciences,* 18(6), 1292.

Schmidt, J.J., Rowley, J. & Kong, H.J. (2008) Hydrogels used for cell-based drug delivery. *Journal of Biomedical Materials Research*, 87(4), 1113–1122.

Sebaugh, J.L. (2011) Guidelines for accurate EC50/IC50 estimation. *Pharmaceutical Statistics,* 10(2), 128–134.

Sekhar, K.R., Hanna, D.N., Cyr, S., Baechle, J.J., Kuravi, S., Balusu, R., Rathmell, K. & Baregamian, N. (2022) Glutathione peroxidase 4 inhibition induces ferroptosis and mtor pathway suppression in thyroid cancer. *Scientific Reports,* 12(1), 19396.

Shen, H., Zhu, R., Liu, Y., Hong, Y., Ge, J., Xuan, J., Niu, W., Yu, X., Qin, J.-J. & Li, Q. (2024) Radioiodine-refractory differentiated thyroid cancer: Molecular mechanisms and therapeutic strategies for Radioiodine Resistance. *Drug Resistance Updates*, 72, 101013.

Shen, X., Pan, D., Gong, Q., Gu, Z. & Luo, K. (2024) Enhancing drug penetration in solid tumors via nanomedicine: Evaluation models, strategies and Perspectives. *Bioactive Materials*, 32, 445–472.

Sies, H. & Jones, D.P. (2020) Reactive oxygen species (ROS) as pleiotropic physiological signalling agents. *Nature Reviews Molecular Cell Biology*, 21(7), 363–383.

Singh, A., Ham, J., Po, J.W., Niles, N., Roberts, T. & Lee, C.S. (2021) The genomic landscape of thyroid cancer tumourigenesis and implications for immunotherapy. *Cells*, 10(5), 1082.

Sirenko, O., Mitlo, T., Hesley, J., Luke, S., Owens, W. & Cromwell, E.F. (2015) High-content assays for characterizing the viability and morphology of 3d cancer spheroid cultures. *ASSAY and Drug Development Technologies*, 13(7), 402–414.

Smyth, P.P.A. (2021) Iodine, seaweed, and the thyroid. *European Thyroid Journal*, 10(2), 101–108.

Soares, M.N., Borges-Canha, M., Neves, C., Neves, J.S. & Carvalho, D. (2023) The role of graves' disease in the development of thyroid nodules and thyroid cancer. *European Thyroid Journal,* 12(4), e230055.

Sondorp, L.H.J., Ogundipe, V.M.L., Groen, A.H., Kelder, W., Kemper, A., Links, T.P., Coppes, R.P. & Kruijff, S. (2020) Patient-derived papillary thyroid cancer organoids for radioactive iodine refractory screening. *Cancers*, 12(11), 3212.

Song, K., Wang, Y., Wang, Y., Yao, W., Tang, Y., Tian, X., Song, X. & Zhou, J. (2024) Advances in thyroid organoids research and applications. *Endocrine Research*, 49(2), 86–91.

Song, Y., Driessens, N., Costa, M., De Deken, X., Detours, V., Corvilain, B., Maenhaut, C., Miot, F., Van Sande, J., Many, M.-C. & Dumont, J.E. (2007) Roles of hydrogen peroxide in thyroid physiology and disease. *The Journal of Clinical Endocrinology & Metabolism*, 92(10), 3764–3773.

Sonnen, K.F. & Merten, C.A. (2019) Microfluidics as an emerging precision tool in developmental biology. *Developmental Cell*, 48(3), 293–311.

Sorrenti, S., Baldini, E., Pironi, D., Lauro, A., D'Orazi, V., Tartaglia, F., Tripodi, D., Lori, E., Gagliardi, F., Praticò, M., Illuminati, G., D'Andrea, V., Palumbo, P. & Ulisse, S. (2021) Iodine: Its role in thyroid hormone biosynthesis and beyond. *Nutrients*, 13(12), 4469.

Sprangers, J., Zaalberg, I.C. & Maurice, M.M. (2020) Organoid-based modeling of intestinal development, regeneration, and Repair. *Cell Death & Differentiation*, 28(1), 95–107.

Srivastava, P., Braganca, J.M. & Kowshik, M. (2014) In vivo synthesis of selenium nanoparticles by halococcus salifodinae BK18 and their anti-proliferative properties against Hela Cell Line. *Biotechnology Progress*, 30(6), 1480–1487.

Suzuki, K., Kawashima, A., Yoshihara, A., Akama, T., Sue, M., Yoshida, A. & Kimura, H.J. (2011) Role of thyroglobulin on negative feedback autoregulation of thyroid follicular function and growth. *Journal of Endocrinology*, 209(2), 169–174.

Takamura, N., Orita, M., Saenko, V., Yamashita, S., Nagataki, S. & Demidchik, Y. (2016) Radiation and risk of thyroid cancer: Fukushima and Chernobyl. *The Lancet Diabetes & Endocrinology*, 4(8), 647.

Talezadeh Shirazi, P., Farjadian, S., Dabbaghmanesh, M.H., Jonaidi, H., Alavianmehr, A., Kalani, M. & Emadi, L. (2022) Eugenol: A new option in combination therapy with sorafenib for the treatment of undifferentiated thyroid cancer. *Iranian Journal of Allergy, Asthma and Immunology,* 21(3), 313-321

Tang, X.-Y., Wu, S., Wang, D., Chu, C., Hong, Y., Tao, M., Hu, H., Xu, M., Guo, X. & Liu, Y. (2022) Human organoids in basic research and clinical applications. *Signal Transduction and Targeted Therapy,* 7(1), 168.

Tarabanis, C., Banco, D., Keller, N.M., Bangalore, S. & Alviar, C.L. (2024) A case report of $NaN_3$-induced myopericarditis. *European Heart Journal - Case Reports*, 8(4), n.

ter Steege, E.J., Bakker, E.R.M (2021) The role of R-spondin proteins in cancer biology. *Oncogene*, 40(47), 6469–6478.

Tevlek, A., Kecili, S., Ozcelik, O.S., Kulah, H. & Tekin, H.C. (2023) Spheroid engineering in microfluidic devices. *ACS Omega,* 8(4), 3630–3649.

Thasler, W.E., Weiss, T.S., Schillhorn, K., Stoll, P.-T., Irrgang, B. & Jauch, K.-W. (2003) Charitable State-Controlled Foundation Human Tissue and Cell Research: Ethic and Legal Aspects in the Supply of Surgically Removed Human Tissue For Research in the Academic and Commercial Sector in Germany. *Cell Tissue Banking* 4, 49–56.

TheWell Bioscience (n.d.) VitroGel® organoid. TheWell Bioscience - 3D Cell Culture Hydrogel & Bioinks for 3D Bioprinting. Available online: https://www.thewellbio.com/product/3d-organoid-culture-hydrogel/ [Accessed 10/7/2024].

Thomas, L., Lai, S.Y., Dong, W., Feng, L., Dadu, R., Regone, R.M. & Cabanillas, M.E. (2014) Sorafenib in metastatic thyroid cancer: A systematic review. *The Oncologist*, 19(3), 251–258.

Thyroid cancer incidence statistics. (2024) Cancer Research UK. Available online: https://www.cancerresearchuk.org/health-professional/cancer-statistics/statistics-by-cancer-type/thyroid-cancer/incidence [Accessed 16/7/2024].

Urbischek, M., Rannikmae, H., Foets, T., Ravn, K., Hyvönen, M. & de la Roche, M. (2019) Organoid culture media formulated with growth factors of defined cellular activity. *Scientific Reports*, 9(1), 193.

Vakhrushev, I.V., Nezhurina, E.K., Karalkin, P.A., Tsvetkova, A.V., Sergeeva, N.S., Majouga, A.G. & Yarygin, K.N. (2021) Heterotypic multicellular spheroids as experimental and preclinical models of sprouting angiogenesis. *Biology*, 11(1), 18.

van der Vaart, J., Bosmans, L., Sijbesma, S.F., Knoops, K., van de Wetering, W.J., Otten, H.G., Begthel, H., Borel Rinkes, I.H., Korving, J., Lentjes, E.G., Lopez-Iglesias, C., Peters, P.J., van Santen, H.M., Vriens, M.R. & Clevers, H. (2021) Adult Mouse and human organoids derived from thyroid follicular cells and modeling of graves' hyperthyroidism. *Proceedings of the National Academy of Sciences*, 118(51), e2117017118.

van Duinen, V., Trietsch, S.J., Joore, J., Vulto, P. & Hankemeier, T. (2015) Microfluidic 3D cell culture: From tools to tissue models. *Current Opinion in Biotechnology*, 35, 118–126.

Veiga, L.H.S., Bhatti, P., Ronckers, C.M., Sigurdson, A.J., Stovall, M., Smith, S.A., Weathers, R., Leisenring, W., Mertens, A.C., Hammond, S., Neglia, J.P., Meadows, A.T., Donaldson, S.S., Sklar, C.A., Friedman, D.L., Robison, L.L. & Inskip, P.D. (2012) Chemotherapy and thyroid cancer risk: A report from the childhood cancer survivor study. *Cancer Epidemiology, Biomarkers & Prevention,* 21(1), 92–101.

Venter, C. & Niesler, C. (2019) Rapid quantification of cellular proliferation and migration using imagej. *BioTechniques,* 66(2), 99–102.

Verjans, E., Doijen, J., Luyten, W., Landuyt, B. & Schoofs, L. (2017) Three-dimensional cell culture models for anticancer drug screening: Worth the effort? *Journal of Cellular Physiology,* 233(4), 2993–3003.

Villanueva, I., Alva-Sánchez, C. & Pacheco-Rosado, J. (2013) The role of thyroid hormones as inductors of oxidative stress and neurodegeneration. *Oxidative Medicine and Cellular Longevity,* 2013, 1–15.

Vlachogiannis, G., Hedayat, S., Vatsiou, A., Jamin, Y., Fernández-Mateos, J., Khan, K., Lampis, A., Eason, K., Huntingford, I., Burke, R., Rata, M., Koh, D.-M., Tunariu, N., Collins, D., Hulkki-Wilson, S., Ragulan, C., Spiteri, I., Moorcraft, S.Y., Chau, I., Rao, S., Watkins, D., Fotiadis, N., Bali, M., Darvish-Damavandi, M., Lote, H., Eltahir, Z., Smyth, E.C., Begum, R., Clarke, P.A., Hahne, J.C., Dowsett, M., de Bono, J., Workman, P., Sadanandam, A., Fassan, M., Sansom, O.J., Eccles, S., Starling, N., Braconi, C., Sottoriva, A., Robinson, S.P., Cunningham, D. & Valeri, N. (2018) Patient-derived organoids model treatment response of metastatic gastrointestinal cancers. *Science*, 359(6378), 920–926.

Volante, M., Lam, A.K., Papotti, M. & Tallini, G. (2021) Molecular pathology of poorly differentiated and anaplastic thyroid cancer: What do pathologists need to know? *Endocrine Pathology*, 32(1), 63–76.

Wagner, I., Materne, E.-M., Brincker, S., Süßbier, U., Frädrich, C., Busek, M., Sonntag, F., Sakharov, D.A., Trushkin, E.V., Tonevitsky, A.G., Lauster, R. & Marx, U. (2013) A dynamic multi-organ-chip for long-term cultivation and substance testing proven by 3D human liver and skin tissue co-culture. *Lab on a Chip*, 13(18), 3538.

Wajapeyee, N. & Gupta, R. (2021) Epigenetic alterations and mechanisms that drive resistance to targeted cancer therapies. *Cancer Research*, 81(22), 5589–5595.

Wallace, D.I. & Guo, X. (2013) Properties of tumor spheroid growth exhibited by simple mathematical models. *Frontiers in Oncology*, 3, 2234-943X.

Wei, X., Wang, X., Xiong, J., Li, C., Liao, Y., Zhu, Y. & Mao, J. (2022) Risk and prognostic factors for BRAFV600E mutations in papillary thyroid carcinoma. *BioMed Research International,* 2022, 1–13.

What is a goiter? (2015) Northwest Thyroid Center. Available online: https://www.the-thyroid-surgeon.com/what-is-a-goiter/ [Accessed 17/7/2024].

Williams, D. (2015) Thyroid growth and cancer. *European Thyroid Journal,* 4(3), 164–173.

Wilson, S.S., Mayo, M., Melim, T., Knight, H., Patnaude, L., Wu, X., Phillips, L., Westmoreland, S., Dunstan, R., Fiebiger, E. & Terrillon, S. (2021) Optimized culture conditions for improved growth and functional differentiation of mouse and human colon organoids. *Frontiers in Immunology*, 11, 1664-3224.

World Health Organization (2013) Assessment of Iodine Deficiency Disorders and Monitoring their Elimination: A Guide for Programme Managers. Available online: https://www.who.int/nutrition/publications/micronutrients/iodine_deficiency/9789241595827/en/ [Accessed 16 May 2024].

Wu, J., Lin, C., Huang, C., Cheng, Y., Chien, C. & Sung, Y. (2020) Potential synergistic effects of sorafenib and CP-31398 for treating anaplastic thyroid cancer with P53 mutations. *Oncology Letters* 19(4), 3021-3026.

Wu, W., Li, X. & Yu, S. (2022) Patient-derived tumour organoids: A bridge between cancer biology and personalised therapy. *Acta Biomaterialia*, 146, 23–36.

Xi, C., Zhang, G.-Q., Sun, Z.-K., Song, H.-J., Shen, C.-T., Chen, X.-Y., Sun, J.-W., Qiu, Z.-L. & Luo, Q.-Y. (2020) Interleukins in thyroid cancer: From basic researches to applications in clinical practice. *Frontiers in Immunology*, 11, 1664-3224.

Xiang, J., Wan, C., Guo, R. & Guo, D. (2016) Is hydrogen peroxide a suitable apoptosis inducer for all cell types? *BioMed Research International*, 2016, 1–6.

Xiao, M., Qiu, J., Kuang, R., Zhang, B., Wang, W. & Yu, Q. (2019) Synergistic effects of stromal cell-derived factor-1α and bone morphogenetic protein-2 treatment on odontogenic differentiation of human stem cells from apical papilla cultured in the vitrogel 3D system. *Cell and Tissue Research,* 378(2), 207–220.

Xu, S., Huang, H., Qian, J., Liu, Y., Huang, Y., Wang, X., Liu, S., Xu, Z. & Liu, J. (2021) Prevalence of hashimoto thyroiditis in adults with papillary thyroid cancer and its association with cancer recurrence and outcomes. *JAMA Network Open*, 4(7), e2118526.

Ya, W., Li, H., Zhai, Z.-X., Yuan, S.-J., Xin, Y.-W., Yan, X.-H., Hao, Y.-H., Fan, W.-W. & Liu, L.-P. (2022) Silencing plasmacytoma variant translocation 1 promotes the anticancer activity of sorafenib in papillary thyroid carcinoma cells, PREPRINT (Version 1) available at *Research Square* [https://doi.org/10.21203/rs.3.rs-1493511/v1].

Yang, H., Liang, Q., Zhang, J., Liu, J., Wei, H., Chen, H., Wei, W., Chen, D. & Zhao, Y. (2023) Establishment of papillary thyroid cancer organoid lines from clinical specimens. *Frontiers in Endocrinology*, 14, 1664-2392.

Yang, Y., Li, S., Wang, Y., Zhao, Y. & Li, Q. (2022) Protein tyrosine kinase inhibitor resistance in malignant tumors: Molecular mechanisms and future perspective. *Signal Transduction and Targeted Therapy*, 7(1), 329.

Yasumura, S., Ohira, T., Ishikawa, T., Shimura, H., Sakai, A., Maeda, M., Miura, I., Fujimori, K., Ohto, H. & Kamiya, K. (2022) Achievements and current status of the Fukushima Health Management Survey. *Journal of Epidemiology,* 32(Suppl 12), S3–S10.

Yi, H., Ye, T., Ge, M., Yang, M., Zhang, L., Jin, S., Ye, X., Long, B. & Li, L. (2017) Inhibition of autophagy enhances the targeted therapeutic effect of sorafenib in thyroid cancer. *Oncology Reports*, 39(2), 711-720.

Yi, S., Kim, H.J., Koo, B.S., Lee, S.E., Choi, J. & Kang, Y.E. (2022) Efficient dissociation protocol for generation of single cell suspension from human thyroid tissue for single cell RNA sequencing. *Endocrinology and Metabolism*, 37(4), 698–700.

Yildirim Simsir, I., Cetinkalp, S. & Kabalak, T. (2019a) Review of factors contributing to nodular goiter and thyroid carcinoma. *Medical Principles and Practice*, 29(1), 1–5.

Zanoni, M., Piccinini, F., Arienti, C., Zamagni, A., Santi, S., Polico, R., Bevilacqua, A. & Tesei, A. (2016) 3D tumor spheroid models for in vitro therapeutic screening: A systematic approach to enhance the biological relevance of data obtained. *Scientific Reports*, 6(1), 19103.

Zarkesh, M., Arab, N., Abooshahab, R., Heydarzadeh, S., Sheikholeslami, S., Nozhat, Z., Salehi Jahromi, M., Fanaei, S.A. & Hedayati, M. (2022) CPG island status as an epigenetic alteration for NIS promoter in thyroid neoplasms; a cross-sectional study with a systematic review. *Cancer Cell International,* 22(1), 310.

Zhai, J., Liu, Y., Ji, W., Huang, X., Wang, P., Li, Y., Li, H., Wong, A.H.-H., Zhou, X., Chen, P., Wang, L., Yang, N., Chen, C., Chen, H., Mak, P.-I., Deng, C.-X., Martins, R., Yang, M., Ho, T.-Y., Yi, S., Yao, H. & Jia, Y. (2024) Drug screening on Digital Microfluidics for Cancer Precision Medicine. *Nature Communications,* 15(1), 2003619.

Zhai, M., Zhang, D., Long, J., Gong, Y., Ye, F., Liu, S. & Li, Y. (2021) The global burden of thyroid cancer and its attributable risk factor in 195 countries and territories: A systematic analysis for the global burden of disease study. *Cancer Medicine*, 10(13), 4542–4554.

Zhang, J., Liu, Y., Chen, Y., Yuan, L., Liu, H., Wang, J., Liu, Q. & Zhang, Y. (2020) Adipose-derived stem cells: Current applications and future directions in the regeneration of multiple tissues. *Stem Cells International*, 2020, 1–26.

Zhang, L., Zhou, M., Gao, X., Xie, Y., Xiao, J., Liu, T. & Zeng, X. (2023) Estrogen-related genes for thyroid cancer prognosis, immune infiltration, staging, and drug sensitivity. *BMC Cancer,* 23(1), 1048.

Zhang, W., Li, C., Baguley, B.C., Zhou, F., Zhou, W., Shaw, J.P., Wang, Z., Wu, Z. & Liu, J. (2016) Optimization of the formation of embedded multicellular spheroids of MCF-7 cells: How to reliably produce a biomimetic 3D model. *Analytical Biochemistry*, 515, 47–54.

Zhang, Y., Xing, Z., Liu, T., Tang, M., Mi, L., Zhu, J., Wu, W. & Wei, T. (2022) Targeted therapy and drug resistance in thyroid cancer. *European Journal of Medicinal Chemistry,* 238, 114500.

Zhang, Z., Liu, D., Murugan, A.K., Liu, Z. & Xing, M. (2013) Histone deacetylation of NIS promoter underlies braf v600e-promoted NIS silencing in thyroid cancer. *Endocrine-Related Cancer,* 21(2), 161–173.

Zhao, Y., Zhong, L. & Yi, H. (2019) A review on the mechanism of iodide metabolic dysfunction in differentiated thyroid cancer. *Molecular and Cellular Endocrinology,* 479, 71–77.

Zhao, Z., Chen, X., Dowbaj, A.M., Sljukic, A., Bratlie, K., Lin, L., Fong, E.L., Balachander, G.M., Chen, Z., Soragni, A., Huch, M., Zeng, Y.A., Wang, Q. & Yu, H. (2022) Organoids. *Nature Reviews Methods Primers*, 2(1), 94.

Zhu, W. & Xie, B. (2023) Plk4 inhibitor exhibits antitumor effect and synergizes sorafenib via arresting cell cycle and inactivating Wnt/β-catenin pathway in anaplastic thyroid cancer. *Cancer Biology & Therapy*, 24(1), n.

Zhu, Y., Zheng, B., Wang, H. & Chen, L. (2017) New knowledge of the mechanisms of sorafenib resistance in liver cancer. *Acta Pharmacologica Sinica*, 38(5), 614–622.

Zimmermann, M.B. & Galetti, V. (2015) Iodine intake as a risk factor for thyroid cancer: A comprehensive review of animal and human studies. *Thyroid Research*, 8(1), 8.

Zimmermann, M.B. (2008) Iodine requirements and the risks and benefits of correcting iodine deficiency in populations. *Journal of Trace Elements in Medicine and Biology,* 22(2), 81–92.

Zimmermann, M.B. (2009) Symposium on 'geographical and geological influences on nutrition' iodine deficiency in industrialised countries. *Proceedings of the Nutrition Society,* 69(1), 133–143.

Zygulska, A.L., Krzemieniecki, K. and Staszczak, A.S. (2013) 'The use of sorafenib in the thyroid cancer', *European Endocrinology*, 9(1), 28.

# Appendix 1

**1.1 TBS recipe:**

20x

121g Tris (Trizma Sigma T1503) 1M

170g NaCl (Sigma S3014) 3M

Make to 1L with $dH_2O$

Adjust pH to 7.6 with concentrated HCl (~80ml)

(If required add 0.1% Tween-20 for more stringent washing)

Dilute 20x in $dH_2O$ for use in IHC (50mM Tris, 150mM NaCl)

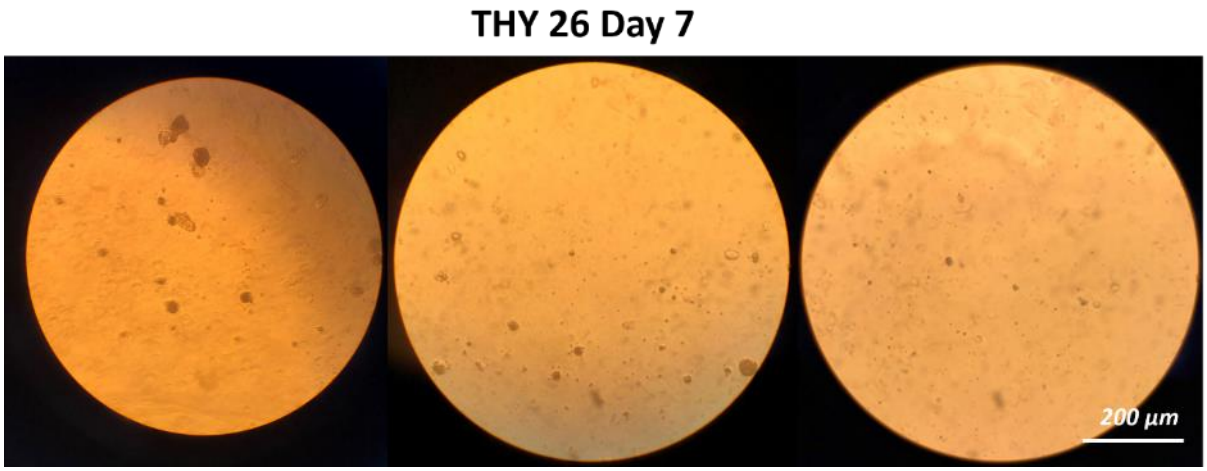


***Figure 6.1 Images of primary thyroid tissue cultures (3 x $10^5$ cells/ml) seeded in a 24-well plate on a Matrigel® base (Top row) and 3 x $10^5$ cells/ml, 100 µL/well, seeded in a ULA plate w/o Matrigel® (Bottom row).*** *Images are representative; 3 images were taken per sample for both organoids and primary spheroids post 7-day incubation, taken using a brightfield microscope at 10x magnification. THY26 – Papillary microcarcinoma. Scale bar – 200 µm.*

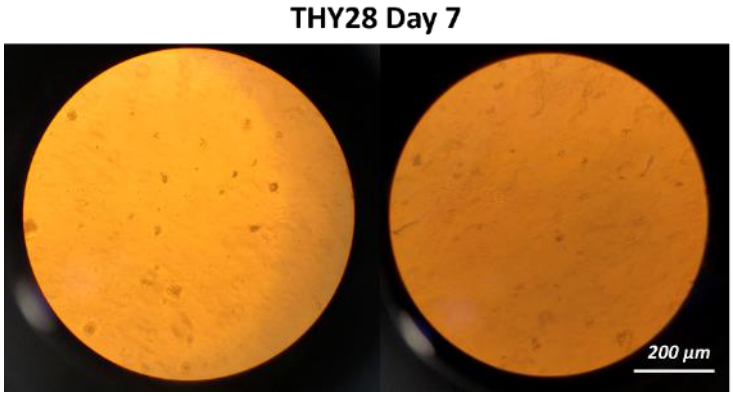


***Figure 6.2 Images of primary thyroid tissue cultures (3 x $10^5$ cells/ml) seeded in a 24-well plate on a Matrigel® base (Top row) and 3 x $10^5$ cells/ml, 100 µL/well, seeded in a ULA plate w/o Matrigel® (Bottom row).*** *Images are representative; 3 images were taken per sample for both organoids and primary spheroids post 7-day incubation, taken using a brightfield Microscope at 10x magnification. THY27– Papillary microcarcinoma. Scale bar – 200 µm.*


***Figure 6.3 Images of primary thyroid tissue cultures (3 x $10^5$ cells/ml) seeded in a 24-well plate on a Matrigel® base (Top row) and 3 x $10^5$ cells/ml, 100 µL/well, seeded in a ULA plate w/o Matrigel® (Bottom row).*** *Images are representative; 3 images were taken per sample for both organoids and primary spheroids post 7-day incubation, taken using a brightfield microscope at 10x magnification. THY28 – Medullary carcinoma. Scale bar – 200 µm.*

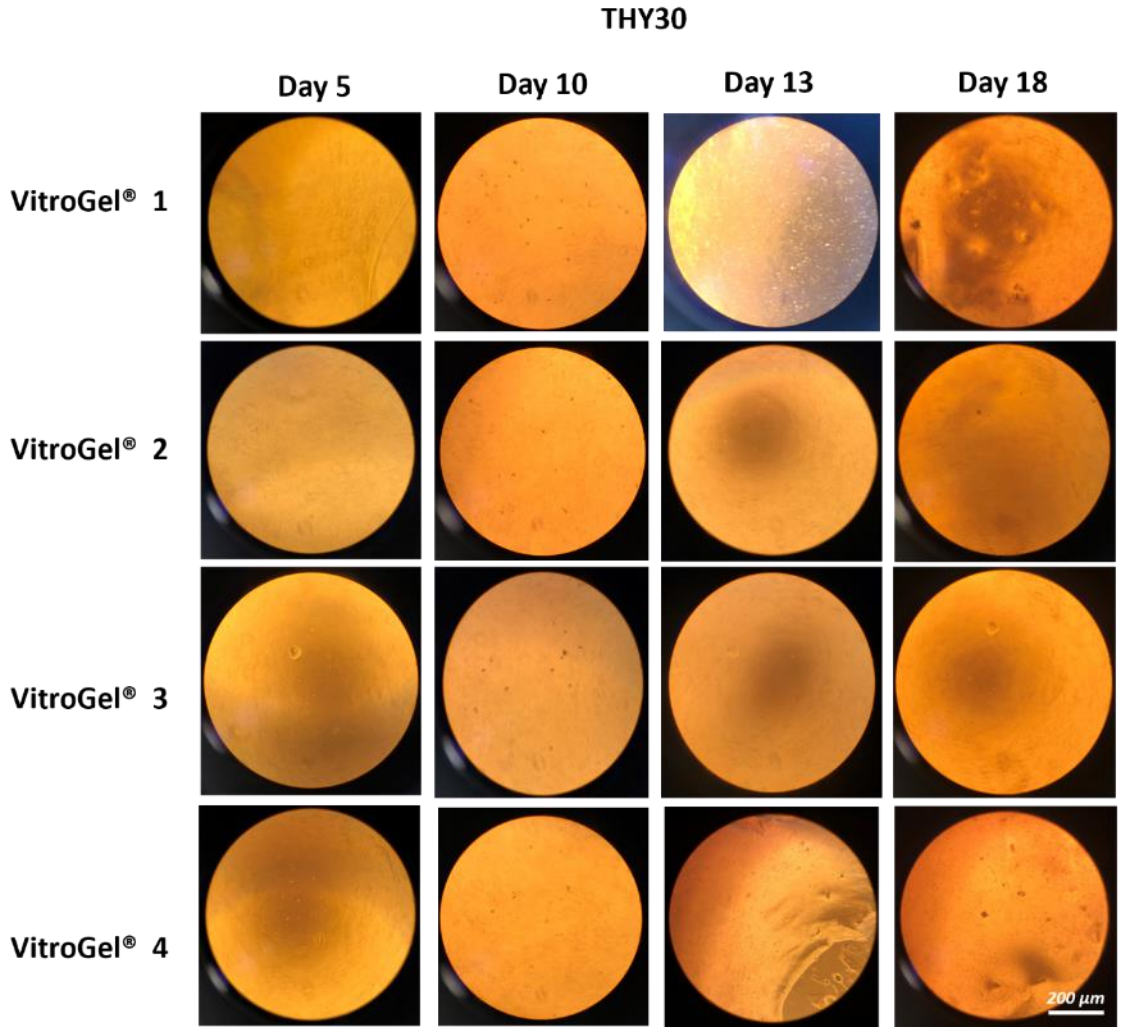


***Figure 6.4 Images of primary thyroid tissue cultures (8 x $10^5$ cells/mL) seeded in a 96-well flat bottom plate with one of four VitroGel® samples.*** *Images are representative; 3 images were taken per VitroGel® sample post 24-day incubation, taken using a brightfield microscope at 10x magnification. THY30 – Follicular adenoma. Scale bar – 200 µm.*

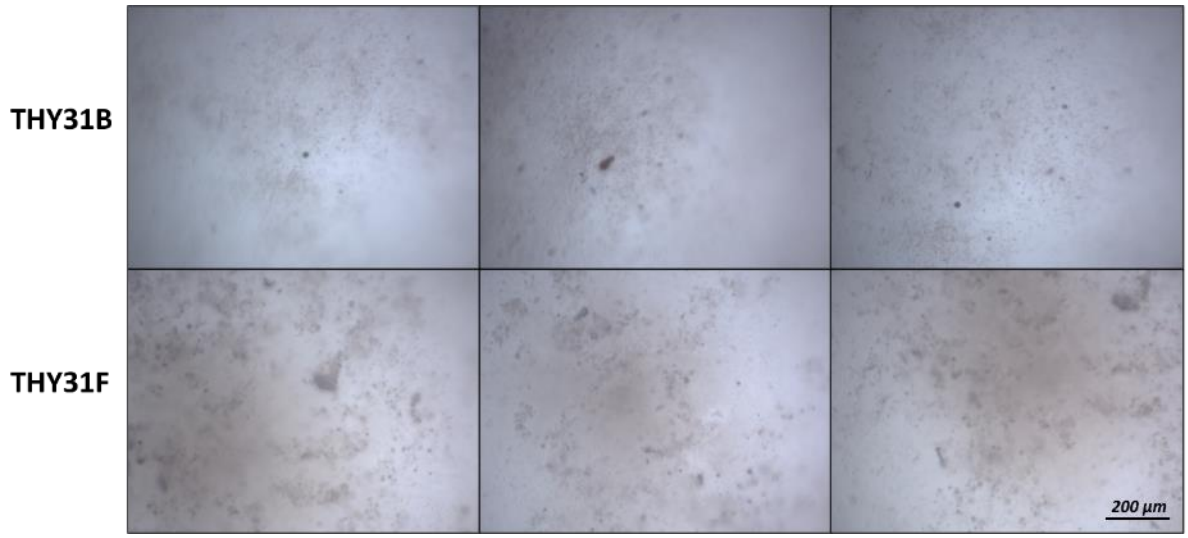


***Figure 6.5 Images of primary thyroid spheroid cultures, THY31 (8 x $10^5$ cells/mL, 100 µL/well) seeded in a 96-well ULA plate.*** *Three representative images were taken after 5 days of incubation using a brightfield microscope at 10x magnification. THY31B – Benign and THY31F – Papillary carcinoma (Follicular variant). Scale bar – 200 µm.*

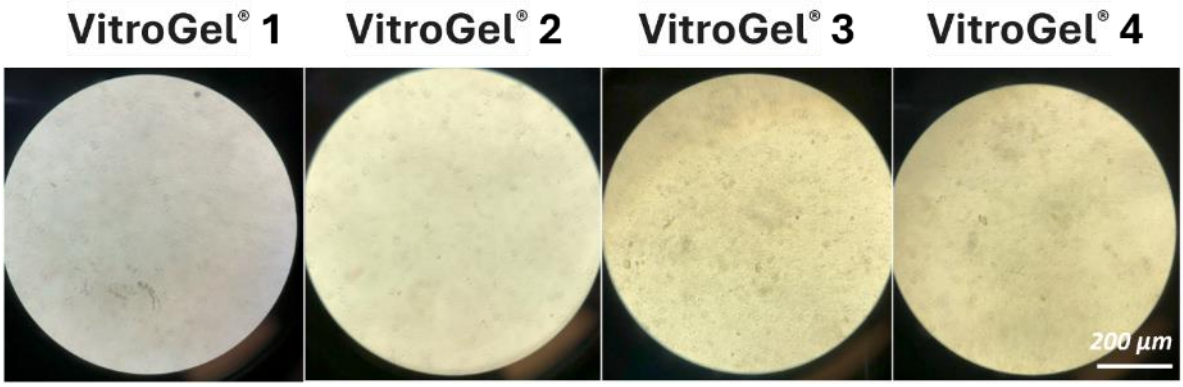


***Figure 6.11 Images of primary thyroid tissue cultures (8 x $10^5$ cells/mL) seeded in a 96-well flat bottom plate with one of four VitroGel® samples.*** *Images are representative of 4 replicate wells per VitroGel® sample; 3 images were taken per VitroGel® sample after 7 days of incubation using a brightfield microscope at 10x magnification. THY39 – Follicular adenoma. Scale bar – 200 µm.*

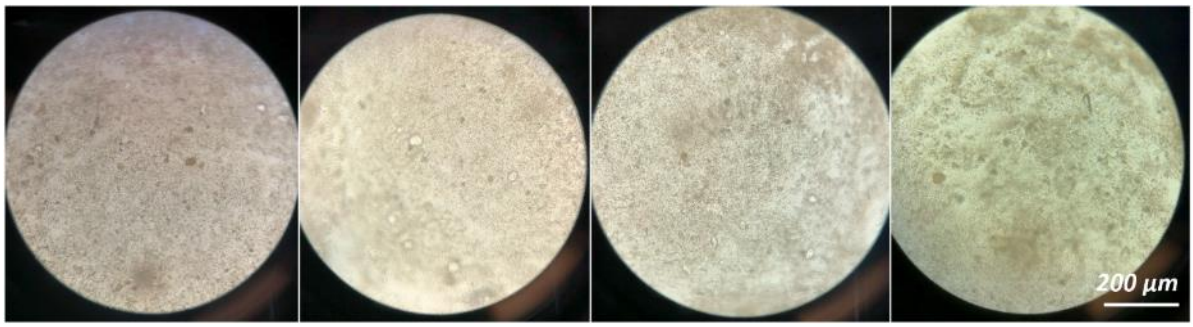


***Figure 6.12 Images of primary thyroid tissue cultures, THY39 (8 x $10^5$ cells/mL, 100 µL/well) seeded in a 96-well ULA plate.*** *Three representative images of 9 replicate wells were taken after 7 days of incubation using a brightfield microscope at 10x magnification. THY39 – Follicular adenoma. Scale bar – 200 µm.*